This electronic thesis or dissertation has been downloaded from Explore Bristol Research, http://research-information.bristol.ac.uk

Author:
Wakefield, Ross I

Title:
Creating and Simulating Parity-Time Symmetric Systems using Nonlinear Quantum Optics

General rights
Access to the thesis is subject to the Creative Commons Attribution - NonCommercial-No Derivatives 4.0 International Public License. A copy of this may be found at https://creativecommons.org/licenses/by-nc-nd/4.0/legalcode This license sets out your rights and the restrictions that apply to your access to the thesis so it is important you read this before proceeding.

Take down policy
Some pages of this thesis may have been removed for copyright restrictions prior to having it been deposited in Explore Bristol Research. However, if you have discovered material within the thesis that you consider to be unlawful e.g. breaches of copyright (either yours or that of a third party) or any other law, including but not limited to those relating to patent, trademark, confidentiality, data protection, obscenity, defamation, libel, then please contact collections-metadata@bristol.ac.uk and include the following information in your message:

- Your contact details
- Bibliographic details for the item, including a URL
- An outline nature of the complaint

Your claim will be investigated and, where appropriate, the item in question will be removed from public view as soon as possible.

Creating and Simulating Parity-Time Symmetric Systems using Nonlinear Quantum Optics

Ross Irwin Wakefield

School of Physics
University of Bristol

A dissertation submitted to the University of Bristol
in accordance with the requirements for award of the degree of
Doctor of Philosophy in the Faculty of Science.

December 2021

Word count: Twenty two thousand

Abstract

It is a typical assumption that closed quantum systems must have real eigenvalues and hence, be Hermitian. However, Parity-Time ($\mathcal{PT}$) symmetric systems are systems that, despite being non-Hermitian, can have real eigenvalues. They have a number of properties and applications that have been demonstrated using a variety of classical systems. To date, while several quantum simulations of $\mathcal{PT}$-symmetric systems have been performed, they all require postselection and no applications of physical quantum $\mathcal{PT}$-symmetric systems have been shown or demonstrated.

Here, we first look at simulating $\mathcal{PT}$-symmetric and non-Hermitian systems using postselection by embedding the non-Hermitian system into a larger Hermitian system, including using Halmos' dilation to simulate two coupled $\mathcal{PT}$-symmetric systems that are the time-reverse of each other using single photons input into a unitary interferometer.

With the realisation that there is a link between symplectic transformations inherent in nonlinear optical systems and $\mathcal{PT}$-symmetry, we then consider a nonunitary interferometer created using nonlinear optics in the form of squeezing that can perform postselection-free simulations of N-mode non-Hermitian systems and emulate this simulating a small 2-dimensional $\mathcal{PT}$-symmetric system.

Finally, we look at coupled microring resonators, which necessarily requires both squeezing and loss terms to function as a single photon source. In considering this from the viewpoint of $\mathcal{PT}$-symmetry and creating an Exceptional Point, we theoretically show that this system can create single photons with a purity above 99% at an enhanced efficiency compared with a single ring.

As a result of considering these systems, we will demonstrate that non-Hermitian and $\mathcal{PT}$-symmetric dynamics can be naturally created using Hermitian systems.

To my parents and grandparents

In memory of Granny

Acknowledgements

First of all, many thanks to Anthony for guiding me along along the way, encouraging me when I was unsure of what would work and most of all, offering kindness and support when I needed it most. Thanks also to Yogesh for getting involved from half-way round the world to introduce me to and teach me about $\mathcal{PT}$-symmetry.

Doing a PhD isn't made easier by life throwing obstacles in the way. Thanks to the wonderful QETLabs Admin Team for dealing with all things covid and non-covid related. In particular, thanks to Sorrel and Alex Martin for a being a constant source of support throughout everything.

Work is only worth whoever we work with, so thanks to Anthony (for all the orange juice), Nicola, Patrick, the Alexes, Rachel (for helping me move between flats), Konstantina, Owain, Dave (although may the Irish rugby team forever prevail), David and Levon for keeping me sane and Yogesh, Kaustubh and Jacob for making me so welcome from a computer screen across an ocean. From the wider QETLabs group, thanks to Pete, Dara, Will McCutcheon, Gary, Josh and Will Dixon for many interesting discussions about rings, solving lengthy equations and many other things. Thanks to my past teachers for teaching me all I know and getting me to this point.

I have been lucky to meet and know many amazing people on the journey here, both at Bristol and further afield. Thanks to all my friends for making my life in Bristol so vibrant and joyful. To my flatmates Lea, Conall, Jules and G for making it feel like home, to the Porridge Project crew, Jason, Lea, Sam, Teuntje, Conall and Hugh as well as Adam for letting it happen. Also to the Cambridge Space Dwarves, Austen, Dom, Jakub, MattF, TimF and TimShi for being amazing in every way. When covid struck, everything went online, so I can only thank Holly and her virtual pub quizes (also organising impressive online conferences) for injecting some joy into the week.

Many thanks to Mum and Dad, for supporting me in moving to and staying in England and encouraging me to continue along this path, as well as Granny, Victor and Jennifer, my aunts, uncles, cousins and other relatives who have been so encouraging over the years.

Author's Declaration

I declare that the work in this dissertation was carried out in accordance with the requirements of the University's Regulations and Code of Practice for Research Degree Programmes and that it has not been submitted for any other academic award. Except where indicated by specific reference in the text, the work is the candidate's own work. Work done in collaboration with, or with the assistance of, others, is indicated as such. Any views expressed in the dissertation are those of the author.

SIGNED: .... DATE:..........................

Table of Contents

List of Figures

Figure **Page**

Chapter 1

Introduction

A common assumption in quantum mechanics is that for an operator to have real eigenvalues (and hence be an observable), it must be Hermitian. However, it has been realised that this is not necessarily the case and that if a non-Hermitian operator satisfies a certain symmetry (referred to as Parity-Time, or $\mathcal{PT}$ symmetry) [1] or can be related to a Hermitian operator by a similarity transform (known as being pseudo-Hermitian) [2–4], it also can have real eigenvalues. When the eigenvalues are real, the symmetry is referred to as being unbroken and when they are complex, the symmetry is then broken.

These operators have a range of features, often related to the Exceptional Point (EP), a point between the broken and unbroken regimes where the eigenvectors (as well as the eigenvalues) of the operator coalesce. Where in the unbroken regime, the evolution of a $\mathcal{PT}$-symmetric Hamiltonian is oscillatory; and in the broken regime, the evolution decays or grows exponentially; at the EP, the evolution becomes polynomial. The eigenvalues and eigenvectors are also affected by the presence of a nearby EP, leading to different potential applications such as information retrieval [5] and reducing decoherence [6] if a quantum $\mathcal{PT}$-symmetric system could be created. As such, there is also interest in simulating such systems [7–9].

Classical $\mathcal{PT}$-symmetric systems, usually involving gain and loss, have been created and shown to have a variety of uses [10–20]. However, creating a quantum $\mathcal{PT}$-symmetric system relies on either creating a purely lossy system or using postselection [7, 21–23]. As such, no applications of quantum $\mathcal{PT}$-symmetry have yet been shown to be experimentally viable.

In this thesis, we look at using different methods of simulating non-unitary transformations to simulate $\mathcal{PT}$-symmetric Hamiltonians. One of these methods shows a link between nonlinear optics and $\mathcal{PT}$-symmetry, which we then use to show that quantum $\mathcal{PT}$-symmetric systems with gain and loss can exist and show that the enhancement typical of EPs in equivalent classical systems also exists in quantum systems and can be used to improve the generation of single photons.

1.1 Thesis Outline

Chapter 2 is a background chapter on $\mathcal{PT}$-symmetric and pseudo-Hermitian Hamiltonians, the simulation and creation of which is one of the goals of this thesis. This starts by looking at the fundamental ideas behind the postulates of quantum mechanics in section 2.2, leading to defining $\mathcal{PT}$-symmetric and pseudo-Hermitian Hamiltonians in section 2.3. Some features at and near exceptional points are looked at in section 2.4, how these systems can be simulated in section 2.5 and some applications and potential issues of them 2.6.

Chapter 3 is the second background chapter and is on quantum optics, which is used throughout this thesis to create and simulate $\mathcal{PT}$-symmetric Hamiltonians. This chapter starts by quantising the electromagnetic field to derive the photonic creation and annihilation operators in section 3.2. Transformations on these operators are then considered in section 3.3. These transformations can be split into linear/passive transformations, including unitary interferometers, looked at in section 3.4 and nonlinear/active transformations in section 3.5. This chapter then ends by considering microring resonators in the linear regime in section 3.6.

Chapter 4 is the first results chapter and primarily looks at the method of unitary dilation to simulate $\mathcal{PT}$-symmetric Hamiltonians. Before considering unitary dilation, we first look at embedding $\mathcal{PT}$-symmetric systems into open quantum systems using the Lindblad master equation in section 4.2, demonstrating that purely lossy $\mathcal{PT}$-symmetric systems can be created. This is also adapted to show that $\mathcal{PT}$-symmetric systems with gain and loss can be embedded into a non-Markovian open system, although the probability of a successful postselection may be small. Section 4.3 then looks at the various properties of using unitary dilation to simulate coupled $\mathcal{PT}$-symmetric systems, including different normalisation methods (section 4.3.2) and defining an effective Hamiltonian that gives the dilated unitary (section 4.3.3). This chapter ends by considering different applications of unitary dilation in section 4.4, such as simulating exotic non-Hermitian versions of particles (section 4.4.2) and considering unitary dilation as an extension of the HOM effect [24] to tune the coupling of the coupled systems by varying the distinguishability of the input photons (section 4.4.1).

Chapter 5 is the second results chapter and in looking at how unitary interferometers are created by being unitary transformations (using linear optics) on the creation and annihilation operators, considers how nonunitary interferometers could be created by using symplectic transformations (i.e. nonlinear optical transformations) on the creation and annihilation operators. By considering this transformation as the matrix exponential of what we here refer to as an 'effective Hamiltonian', shown in section 5.2, we show a connection between symplectic transformations and $\mathcal{PT}$-symmetry in section 5.3. That is, any symplectic transformation is necessarily a $\mathcal{PT}$-symmetric transformation. This idea is used in section 5.4 to design a nonunitary interferometer using the singular value decomposition with loss and gain (in the form of squeezing). Section 5.5 further shows that this design can be made more efficient using typical methods from (Hermitian) Hamiltonian simulation algorithms. We then create a model of a 2D $\mathcal{PT}$-symmetric lattice in section 5.6 and emulate the nonunitary interferometer from section 5.4 simulating this lattice in section 5.7 using code given in appendix A.

Chapter 6 is the final results chapter and focuses on creating a quantum $\mathcal{PT}$-symmetric system using coupled microring resonators as well as finding a well defined practical application of $\mathcal{PT}$-symmetry in quantum physics. At a fundamental level, this can be done by considering squeezing as gain, with loss arising naturally from the system, as well as from the coupling to a waveguide that is necessary for the system to have an output. In comparing with the typical idea of a $\mathcal{PT}$-symmetric system with gain and loss, this gives the design and Hamiltonian described in section 6.2. This section also gives a derivation of loss rates, the effective Hamiltonian of the system (as defined in section 5.2) and shows that there is a steady state solution when a continuous wave pump is input to the system. Section 6.3 calculates the eigenvalues and eigenvectors of this system and in doing so, demonstrates that it is a quantum $\mathcal{PT}$-symmetric system with exceptional point surfaces.

Having done this, we now aim to find a practical application of these coupled microring resonators. One typical application of a microring resonator is to create single photons by creating a two-mode squeezed state and heralding one of the modes. The correlation functions of this process are given for coupled rings in section 6.4 and in more detail in appendix C. Using the solutions to the equations of motion (the equations of motion are given in full in appendix B) calculated in section 6.5 using properties given in appendix D, these correlation functions are then calculated in section 6.6, demonstrating an enhancement in single photon generation typical of exceptional points in $\mathcal{PT}$-symmetric systems.

Chapter 7 ends this thesis, coming to a conclusion about using nonlinear quantum optics to create and simulate $\mathcal{PT}$-symmetric systems.

Chapter 2

Quantum Mechanics and Parity-Time Symmetry

> *Answers were always important, but they were seldom easy*
>
> — Patrick Rothfuss, *The Slow Regard of Silent Things*

This is a background chapter that summarises already existing results.

2.1 Introduction

The idea of Parity-Time ($\mathcal{PT}$) symmetry in quantum mechanics was first realised by Bender and Boettcher [1], who[1] considered the possibility of non-Hermitian Hamiltonians with real eigenvalues. Since then, $\mathcal{PT}$-symmetric systems have been created classically [10–12], often using some form of cavity or resonator [13–20] and simulated or recreated using postselection in quantum systems [7, 21–23]. Here, we review the main discoveries of quantum $\mathcal{PT}$-symmetry, starting with a brief discussion of the fundamental ideas behind the postulates of quantum mechanics in section 2.2, which leads into how the postulates can be adjusted to include (non-Hermitian) $\mathcal{PT}$-symmetric and pseudo-Hermitian Hamiltonians without necessarily having to change the fundamental principles in section 2.3. We then look at various properties of these Hamiltonians in section 2.4, how they can be simulated using quantum simulators (with postselection) in section 2.5 and some recent applications of and potential issues with $\mathcal{PT}$-symmetric quantum theory in section 2.6.

2.2 The Hamiltonian and Time Evolution in Quantum Mechanics

While there are multiple ways of writing the postulates of quantum mechanics, usually differing by levels of mathematical rigour (although may also vary by the number of postulates, such

---

[1] after a discussion with D. Bessis

as [25] and [26]), they generally agree on the fundamental principles. As the focus of Parity-Time ($\mathcal{PT}$)-symmetry is generally on the Hamiltonian and time evolution of the system being studied, we here look at the postulates relating to the Hamiltonian and time evolution of a quantum system in more detail.

Most lists of the postulates start with a statement about how the state of a quantum system is described by a wavefunction in a Hilbert space $\mathcal{H}$. Relevant here is that the wavefunction is normalised. For a discrete system, the wavefunction can be described by a weighted sum of orthonormal basis states, here denoted by

$$|\psi\rangle = \sum_j a_j |e_j\rangle \quad \text{and} \quad |\phi\rangle = \sum_j b_j |e_j\rangle . \tag{2.1}$$

This normalisation is typically described using the inner product (here referred to as the 'Dirac inner product'), often written as

$$(|\phi\rangle, |\psi\rangle) = \langle\phi|\psi\rangle = \sum_j b_j^* a_j \tag{2.2}$$

for a discrete system, where $\langle\phi| = (|\phi\rangle)^\dagger$ and

$$(|\phi(\mathbf{x},t)\rangle, |\psi(\mathbf{x},t)\rangle) = \int_{-\infty}^{\infty} \phi^*(\mathbf{x},t)\,\psi(\mathbf{x},t)\,d\mathbf{x} \tag{2.3}$$

for a continuous system. However, as discussed in section 2.3, this is already a simplification of the more general mathematical definition of an inner product. From this, the normalisation is typically given by

$$(|\psi\rangle, |\psi\rangle) = 1 \quad \text{or} \quad (|\phi(\mathbf{x},t)\rangle, |\psi(\mathbf{x},t)\rangle) = 1. \tag{2.4}$$

Importantly, this normalisation is time-independent. That is, evolving the state for some time or letting it undergo some transformation does not change the normalisation of the state (assuming a closed system).

The remaining postulates tend to follow from various logical ideas applied to the above. From the assumption that the expectation value

$$\langle A\rangle = \langle\psi|A|\psi\rangle \quad \text{or} \quad \langle A\rangle = \int_{-\infty}^{\infty} \psi^*(\mathbf{x},t)\,A\psi(\mathbf{x},t)\,d\mathbf{x} \tag{2.5}$$

of an observable A must be real, it is then assumed that any operator corresponding to an observable must be Hermitian. By itself, this statement is not strictly true in that a real expectation value does not necessarily imply a Hermitian operator [27], although further context and constraints apply which makes it valid for practical applications (again, of a closed system). This will also be discussed in section 2.3.

A measurement is often described by saying that the state after a measurement outcome (that is, an eigenvalue of an observable) is the sum of eigenvectors corresponding to that eigenvalue. As this is generally outside the scope of this thesis, we comment no further except to mention that this is more accurately and easily described using the language of Projection Valued Measures (PVMs), Positive Operator Valued Measures (POVMs) and Krauss Operators, describing quantum channels, looked at in more detail in e.g. [25].

The evolution of a closed quantum system is then described in one of two equivalent ways: By the time evolution of the state being described by the Schrödinger equation; or by the state at some later time t being an operator applied to the state at an earlier time t_0. That is, the Schrödinger equation is given by

$$i\hbar\frac{d}{dt}\left|\psi\right\rangle = H\left|\psi\right\rangle. \tag{2.6}$$

If the Hamiltonian H is time-independent, the transformation is then given by the matrix exponential

$$U\left(t,t_0\right) = e^{-iH(t-t_o)}. \tag{2.7}$$

If H is instead time-dependent, U can potentially be described by a Dyson series or Magnus expansion. However, we can still describe this for small δt by

$$U\left(t_0+\delta t,t_0\right) = e^{-\frac{i}{\hbar}H\delta t} = I - \frac{i}{\hbar}H\delta t + \mathcal{O}\left(\delta t^2\right), \tag{2.8}$$

valid when δt is much less than the relevant time parameter given by the fastest term in the Hamiltonian. Comparing with classical physics, H is then the Hamiltonian describing the energy of a system. As such, as energy is an observable, H is then usually assumed to be Hermitian, or $H = H^\dagger$. As H is Hermitian, U must then be unitary. However, this is again a simplistic treatment of this idea and will be expanded on in more detail in section 2.3.

While the above applies to dynamics of closed systems, an open system dynamics are best described by using density matrices. That is, for a system with a state vector basis $|e_j\rangle$, an arbitrary density matrix can be written as

$$\rho = \sum_{jk} c_{jk}\left|e_j\right\rangle\!\left\langle e_k\right|. \tag{2.9}$$

We can calculate the time evolution of a density matrix in a closed system:

$$\begin{aligned}\dot{\rho} &= \sum_{jk} c_{jk}\left[\frac{d}{dt}\left(\left|e_j\right\rangle\right)\left\langle e_k\right| + \left|e_j\right\rangle\frac{d}{dt}\left(\left\langle e_k\right|\right)\right] && (2.10)\\ &= -\frac{i}{\hbar}\sum_{jk} c_{jk}\left(H\left|e_j\right\rangle\!\left\langle e_k\right| - \left|e_j\right\rangle\!\left\langle e_k\right|H\right) && (2.11)\\ &= -\frac{i}{\hbar}\left[H,\rho\right]. && (2.12)\end{aligned}$$

This can be further extended to time evolution in an open system by considering a system $\mathcal{H}_S$ coupled to an environment $\mathcal{H}_E$ to give the overall Hilbert space $\mathcal{H}_S \otimes \mathcal{H}_E$. This Hilbert space is assumed to be closed so that the overall evolution is unitary. Then, the environment modes are traced over to get a quantum channel. The equation of motion that gives this evolution is often given by the Lindblad (Master) equation [28]:

$$\mathcal{L}\left(\rho\right) = \dot{\rho} = -i\left[H,\rho\right] + \frac{1}{2}\sum_{l}\kappa_l\left(2F_l\rho F_l^{\dagger} - F_l^{\dagger}F_l\rho - \rho F_l^{\dagger}F_l\right), \tag{2.13}$$

which is Markovian (the environment 'forgets' the previous state/interaction of the system much faster than the time-scale used) for $\kappa_l > 0\,\forall\, l, t$. While physical quantum systems tend to evolve using non-Markovian open dynamics, the amount of non-Markovianity gets less pronounced as the environment gets larger.

2.3 Pseudo-Hermitian and Parity-Time-symmetric Hamiltonians

While the above is generally accepted as a valid description of quantum physics, in recent years and decades, some of the assumptions intrinsic to the postulates as originally written have begun to be questioned. One such question arises from the realisation that having real eigenvalues does not necessarily imply that an operator has to be Hermitian, which led to the discovery of Parity-Time-symmetric ($\mathcal{PT}$-symmetric) Hamiltonians [1], discussed in section 2.3.1. Further study of $\mathcal{PT}$-symmetric Hamiltonians then led to considering the more general case of pseudo-Hermitian Hamiltonians [2–4], discussed in section 2.3.3.

2.3.1 Parity-Time-Symmetric Hamiltonians

As mentioned, enforcing that observables must have real eigenvalues does not actually imply that the observable must be Hermitian. This was first realised by Carl Bender [1] for continuous systems where he gave the prototypical example of a $\mathcal{PT}$-symmetric Hamiltonian:

$$H = p^2 + m^2x^2 - \left(ix\right)^N, \tag{2.14}$$

which is equivalent to the Hamiltonian

$$H = p^2 + x^2\left(ix\right)^{\epsilon} \tag{2.15}$$

for $N = 2 + \epsilon$. For $\epsilon \geq 0$, this has a real and positive spectrum despite being non-Hermitian for $\epsilon \neq 2N$ for $N \in \mathbb{N}$. This was shown by approximating the energy levels for $m = 0$ using the WKB method to get

$$E_n \approx \left[\frac{\Gamma\left(\frac{3}{2}+\frac{1}{N}\right)\sqrt{\pi}\left(n+\frac{1}{2}\right)}{\sin\left(\frac{\pi}{N}\right)\Gamma\left(1+\frac{1}{N}\right)}\right]^{\frac{2N}{N+2}}. \tag{2.16}$$

A reproduction of the graph showing the first 10 energy levels is given in figure 2.1 for $N \geq 2$.

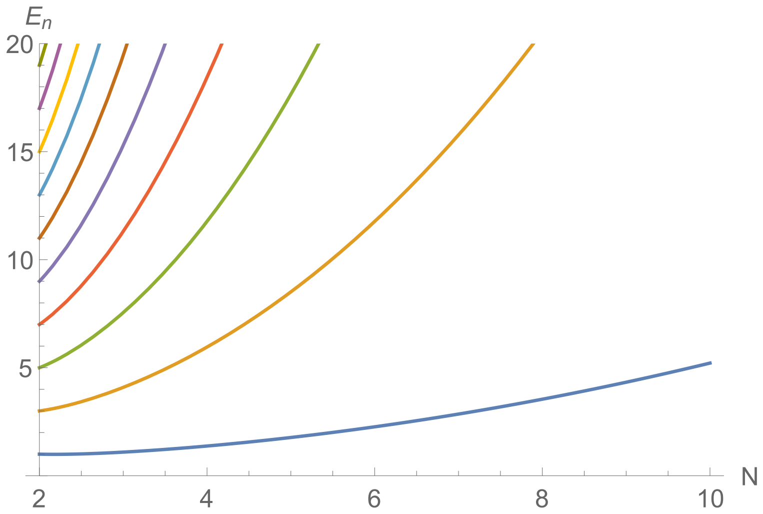

Figure 2.1: Reproduction of figure 1 in [1] showing the first 10 energy levels of the continuous $\mathcal{PT}$-symmetric Hamiltonian given by equation 2.14 for $m = 0$ and $N \geq 2$ calculated using the WKB method to give the approximate solutions in equation 2.16.

Bender showed that this Hamiltonian has real energies by considering the (linear) Parity and (anti-linear) Time reversal operators $\mathcal{P}$ and $\mathcal{T}$. Here, these are defined by

$$\mathcal{P} : p \mapsto -p, x \mapsto -x \tag{2.17}$$

$$\mathcal{T} : p \mapsto -p, x \mapsto x, i \mapsto -i \tag{2.18}$$

and an operator $\mathcal{O}$ is defined as being $\mathcal{PT}$-symmetric when it commutes with the $\mathcal{PT}$ operator:

$$[\mathcal{O}, \mathcal{PT}] = 0. \tag{2.19}$$

For a linear operator, if it commutes with another (linear) operator $\mathcal{O}$, then an eigenstate of $\mathcal{O}$ is simultaneously an eigenstate of that operator. However, the $\mathcal{PT}$ operator is anti-linear, so this does not necessarily always apply. When this does apply, $\mathcal{O}$ is considered to have unbroken $\mathcal{PT}$-symmetry (alternatively, in the $\mathcal{PT}$-unbroken phase or $\mathcal{PT}$-unbroken regime) and the eigenvalues are real. When this does not apply but the Hamiltonian is still $\mathcal{PT}$-symmetric, it is either in the broken regime, where eigenvalues are complex-conjugate pairs, or at the Exceptional Point (EP), discussed further in section 2.4.

This idea can also be applied to discrete Hamiltonians. The prototypical examples a discrete $\mathcal{PT}$-symmetric Hamiltonian is given by[2] [29]

$$H_2' = \begin{pmatrix} re^{i\theta} & s \\ s & re^{-i\theta} \end{pmatrix}, \tag{2.20}$$

---

[2] We refer to this as H_2' due to using H_2 and H_3 in chapter 4 which differ only by relabelling $r = \gamma$ and setting $s = 1$ and $\theta = \pi/2$

where the Parity and Time reversal operators are now given by

$$\mathcal{P} = \begin{pmatrix} 0 & 1 \\ 1 & 0 \end{pmatrix} \tag{2.21}$$

$$\mathcal{T} : i \mapsto -i \tag{2.22}$$

H_2' has eigenvalues

$$\lambda_\pm' = r\cos\theta \pm \sqrt{s^2 - r^2\sin^2\theta} \tag{2.23}$$

which are plotted in figure 2.2. This shows the $\mathcal{PT}$-unbroken regime for $s^2 > r^2\sin^2\theta$ where the eigenvalues are real and the broken regime for $s^2 < r^2\sin^2\theta$ where the eigenvalues are instead complex. At $s^2 = r^2\sin^2\theta$, we have that $\lambda_+' = \lambda_-'$, showing the eigenvalues are degenerate. However, as discussed in section 2.4, the eigenvectors also become degenerate at this point, known as the Exceptional Point (EP).

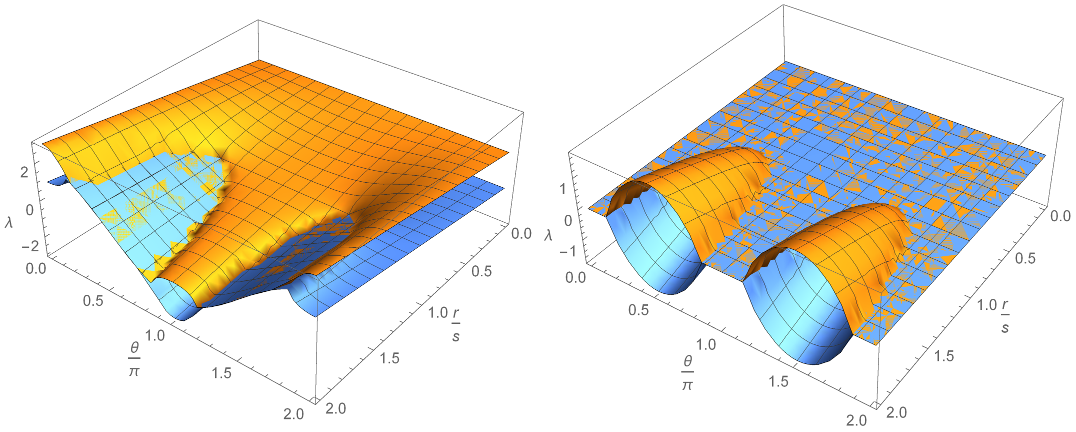

Figure 2.2: Real (left) and imaginary (right) parts of the eigenvalues (equation 2.23) of the 2-dimesnional $\mathcal{PT}$-symmetric Hamiltonian given by equation 2.20. When $s^2 > r^2\sin^2\theta$, the system is in the unbroken regime. When $s^2 < r^2\sin^2\theta$, the system is in the broken regime. The point where $s^2 = r^2\sin^2\theta$ has degenerate eigenvalues and is known as the Exceptional Point (EP). The EP will be discussed in more detail in section 2.4.

2.3.2 Introducing the Charge Operator

While $\mathcal{PT}$-symmetric Hamiltonians demonstrate that requiring an operator to have real eigenvalues does not necessarily mean that the operator has to be Hermitian, this is not the only constraint of quantum systems. Taking $\theta = \pi/2$ and calculating the time evolution of a state evolving under the Hamiltonian H_2' gives

$$|\psi(t)\rangle = e^{-iH_2't}|\psi(0)\rangle \tag{2.24}$$

$$= \begin{pmatrix} \cos\left(\sqrt{s^2-r^2}t\right) + \frac{r\sin\left(\sqrt{s^2-r^2}t\right)}{\sqrt{s^2-r^2}} & -i\frac{s\sin\left(\sqrt{s^2-r^2}t\right)}{\sqrt{s^2-r^2}} \\ -i\frac{s\sin\left(\sqrt{s^2-r^2}t\right)}{\sqrt{s^2-r^2}} & \cos\left(\sqrt{s^2-r^2}t\right) - \frac{r\sin\left(\sqrt{s^2-r^2}t\right)}{\sqrt{s^2-r^2}} \end{pmatrix} |\psi(0)\rangle\,. \tag{2.25}$$

Calculating the norm of this time evolved state then gives that the norm (hence, probability) is not conserved with time: for a state starting in

$$\left|\psi\left(0\right)\right\rangle = \left|0\right\rangle , \tag{2.26}$$

at some later time t, this state is now

$$\left|\psi\left(t\right)\right\rangle = \left[\cos\left(\sqrt{s^2-r^2}t\right) + \frac{r\sin\left(\sqrt{s^2-r^2}t\right)}{\sqrt{s^2-r^2}}\right]\left|0\right\rangle - i\frac{s\sin\left(\sqrt{s^2-r^2}t\right)}{\sqrt{s^2-r^2}}\left|1\right\rangle , \tag{2.27}$$

which has a (Dirac) norm

$$\begin{aligned}\left\langle\psi\left(t\right)|\psi\left(t\right)\right\rangle &= \left|\cos\left(\sqrt{s^2-r^2}t\right) + \frac{r\sin\left(\sqrt{s^2-r^2}t\right)}{\sqrt{s^2-r^2}}\right|^2 + \left|\frac{s\sin\left(\sqrt{s^2-r^2}t\right)}{\sqrt{s^2-r^2}}\right|^2 && (2.28)\\ &= \cos^2\left(\sqrt{s^2-r^2}t\right) + \frac{\left(s^2+r^2\right)\sin^2\left(\sqrt{s^2-r^2}t\right)}{s^2-r^2} + \frac{r\sin\left(2\sqrt{s^2-r^2}t\right)}{\sqrt{s^2-r^2}} && (2.29)\\ &\neq 1, && (2.30)\end{aligned}$$

as shown in figure 2.3.

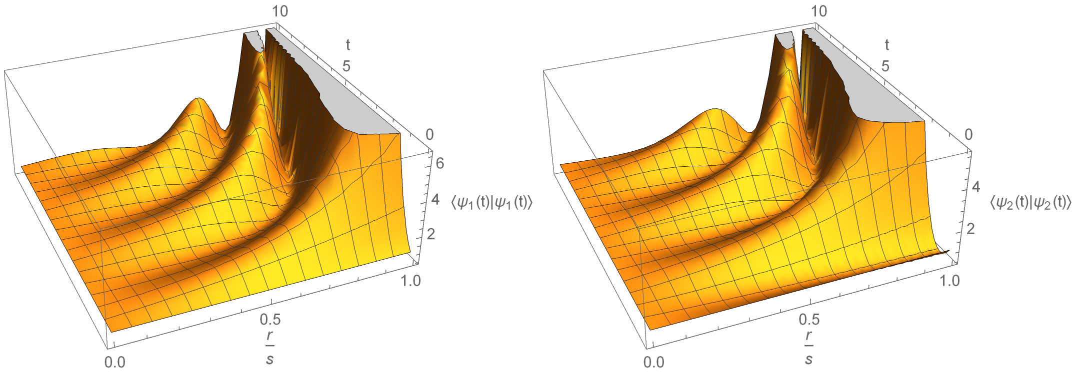

Figure 2.3: Inner product norm of a state starting in (left) $\left|0\right\rangle$ and (right) $\left|1\right\rangle$ evolving under the $\mathcal{PT}$-symmetric Hamiltonian $H_2'\left(\theta=\pi/2\right)$. This shows that the norm oscillates with time in the unbroken $\mathcal{PT}$-symmetry region and increases above 1 with increasing parameter r.

A typical idea might be to enforce that the evolution is manually normalised, to get

$$\left|\psi'\left(t\right)\right\rangle = \frac{1}{\left\langle\psi\left(t\right)|\psi\left(t\right)\right\rangle}\left|\psi\left(t\right)\right\rangle . \tag{2.31}$$

However, an alternative approach can be found be reconsidering the definition of the inner product. That is, outside of convention and simplicity, there is no a priori reason that the inner product has to be defined as it is in equations 2.2 and 2.3. In general, an inner product is instead determined by a metric. For a $\mathcal{PT}$-symmetric system in the $\mathcal{PT}$-unbroken regime, this can be done with the addition of a charge operator $\mathcal{C}$ and redefining the inner product to be $\langle\phi|\psi\rangle^{\mathcal{CPT}} = (\mathcal{CPT}\phi)\cdot\psi$. This is done by defining

$$\langle\psi|_{\mathcal{CPT}} = \left(\mathcal{CPT}\left|\psi\right\rangle\right)^T. \tag{2.32}$$

The charge operator is defined by first realising that the $\mathcal{PT}$-norm is constant but not always positive. For H_2' given by equation 2.20, the eigenvectors are given by

$$|\varepsilon_+\rangle = \frac{1}{\sqrt{2\cos\alpha}}\begin{pmatrix} e^{i\alpha/2} \\ e^{-i\alpha/2} \end{pmatrix} \quad \text{and} \quad |\varepsilon_-\rangle = \frac{i}{\sqrt{2\cos\alpha}}\begin{pmatrix} e^{-i\alpha/2} \\ -e^{i\alpha/2} \end{pmatrix}, \tag{2.33}$$

where $s\sin\alpha = r\sin\theta$. The $\mathcal{PT}$-inner product gives

$$\langle\varepsilon_\pm|\varepsilon_\pm\rangle_{\mathcal{PT}} = \pm 1 \tag{2.34}$$

$$\langle\varepsilon_\pm|\varepsilon_\mp\rangle_{\mathcal{PT}} = 0, \tag{2.35}$$

demonstrating orthogonality although not positivity. To make these inner products positive, $\mathcal{C}$ is introduced as

$$\mathcal{C} = |\varepsilon_+\rangle\langle\varepsilon_+|_{\mathcal{CPT}} - |\varepsilon_-\rangle\langle\varepsilon_-|_{\mathcal{CPT}} = \frac{1}{\cos\alpha}\begin{pmatrix} i\sin\alpha & 1 \\ 1 & -i\sin\alpha \end{pmatrix} \tag{2.36}$$

and now the inner products are orthonormal:

$$\langle\varepsilon_\pm|\varepsilon_\pm\rangle_{\mathcal{CPT}} = 1 \tag{2.37}$$

$$\langle\varepsilon_\pm|\varepsilon_\mp\rangle_{\mathcal{CPT}} = 0. \tag{2.38}$$

This holds for other $\mathcal{PT}$-symmetric systems in the unbroken regime, where the charge operator required to make the inner product positive is defined in terms of the eigenvectors of the system.

2.3.3 Pseudo-Hermitian Hamiltonian formalism

Alternatively, the concept of $\mathcal{PT}$-symmetric Hamiltonians can be extended to include pseudo-Hermitian Hamiltonians [2–4]. This is defined by using the metric operator η to redefine the inner product

$$\langle\phi|\psi\rangle_\eta = \left\langle\phi\right|\eta\left|\psi\right\rangle. \tag{2.39}$$

The property that H is η-pseudo-Hermitian is then defined by

$$H^\dagger = \eta H\eta^{-1}. \tag{2.40}$$

Using the inner product to get the expectation value of H now gives

$$\left\langle\phi\right|\eta\left|H\psi\right\rangle = \left\langle H\phi\right|\eta\left|\psi\right\rangle, \tag{2.41}$$

equivalent to being Hermitian in this new inner-product space. For a $\mathcal{CPT}$-symmetric Hamiltonian, this gives $\eta = \mathcal{PC}$ by definition. This can also be done by considering a similarity transform $\varrho = \varrho^\dagger = +\sqrt{\eta}$ such that the pseudo-Hermitian (equivalently, quasi-Hermitian) Hamiltonian H is related to a Hermitian Hamiltonian h by [3]

$$H = \varrho^{-1} h \varrho. \tag{2.42}$$

This in turn defines the properties of H and its inner product. The expectation value of h is given by the Dirac inner product, which relates to the pseudo-Hermitian inner product by

$$\langle \phi | H | \psi \rangle_\eta = \langle \phi | \varrho^2 H \psi \rangle = \langle \phi | \varrho h \varrho \psi \rangle = \langle \varrho \phi | h | \varrho \psi \rangle . \tag{2.43}$$

This can further be made time dependent [30] and is useful in simulating $\mathcal{PT}$-symmetric, pseudo-Hermitian and other non-Hermitian Hamiltonians, as looked at in section 2.6.

2.4 Eigenvectors and Exceptional Points

2.4.1 Left and Right Eigenvectors

As a result of being non-Hermitian, the eigenvectors of pseudo-Hermitian and $\mathcal{PT}$-symmetric operators are different to those of Hermitian operators. For a Hermitian operator $\mathcal{O}$, the eigenvectors are defined by $\mathcal{O}|v_j\rangle = \lambda_j |v_j\rangle$, with $\langle v_j| = (|v_j\rangle)^\dagger$. However, for a Hermitian system, this no longer holds, so the 'right' eigenvectors are different to the 'left' eigenvectors. Continuing with the example of H_2', we have that

$$|\varepsilon_+\rangle \propto \begin{pmatrix} -e^{-i\alpha} \\ 1 \end{pmatrix} \quad \text{and} \quad |\varepsilon_-\rangle \propto \begin{pmatrix} e^{i\alpha} \\ 1 \end{pmatrix}, \tag{2.44}$$

which comes from $H_2'|v_j\rangle = \lambda_j |v_1\rangle$ where

$$\lambda_{1/2} = \frac{r}{s}\cos\theta \mp \cos\alpha. \tag{2.45}$$

The left eigenvectors are then then transpose of the (right) eigenvectors of the transpose of the operator, or

$$\langle u_j | \mathcal{O} = \sigma_j \mathcal{O} \implies \mathcal{O}^\dagger |u_j\rangle = \mathcal{O}^\dagger \sigma_j^\dagger. \tag{2.46}$$

In this case, as H_2' is transpose-symmetric, the left eigenvectors are the transpose of the right eigenvectors, as opposed to the conjugate-transpose in the Hermitian case.

2.4.2 Exceptional Points

There are various regions of $\mathcal{PT}$-symmetric Hamiltonians. Aside from the real-valued, symmetric (and therefore Hermitian) point ($r = 0$ in H_2'), these are split into the regions of unbroken symmetry, broken symmetry and Exceptional Point (EP).

---

[3] Technically, this equation only defines quasi-Hermitianity. However, if it is quasi-Hermitian, it must also be pseudo-Hermitian, so we ignore this distinction here.

Dynamics

As mentioned in section 2.3.1, the unbroken symmetry region has real eigenvalues and the broken region has complex eigenvalues, which gives different dynamics. While in the unbroken region, the dynamics are oscillatory, the dynamics in the broken region either increase or decay exponentially with time. However, at the transition between these two regions is the EP. Here, both the eigenvalues and the eigenvectors become degenerate (known as coalescence) and the behaviour of the dynamics is polynomial with time. The number of eigenvectors that coalesce to a single vector is the order of the EP, which determines the exact behaviour of the system.

As an example, we again take the eigenvectors of H_2'. These become equal at

$$-e^{-i\alpha} = e^{i\alpha} \implies e^{-2i\alpha} = -1 \implies \alpha = \pi\left(\frac{1}{2} + n\right). \tag{2.47}$$

This gives that the EP occurs at $s = r\sin\theta$ or,

$$H'_{2,EP} = r\begin{pmatrix} e^{i\theta} & \sin\theta \\ \sin\theta & e^{-i\theta} \end{pmatrix}. \tag{2.48}$$

This can be simplified by further taking $\theta = \pi/2$ to get

$$H'_{2,EP} = r\begin{pmatrix} i & 1 \\ 1 & -i \end{pmatrix}. \tag{2.49}$$

Squaring this gives $H'^2_{2,EP} = 0$, which demonstrates the polynomial behaviour typical of an EP: The evolution of a system being acted on by this Hamiltonian is

$$e^{-iH_2't} = I - iH_2't = \begin{pmatrix} 1+rt & r \\ r & 1-rt \end{pmatrix}. \tag{2.50}$$

In general, an N^{th} order EP (EPN) gives polynomial evolution of degree $N-1$.

Jordan Decomposition

Aside from the evolution of a system at the EP being polynomial, the EPs of a system have a number of properties. The first of these is that the matrix of the system at the EP can be transformed into Jordan normal form[4] via a similarity transform [31], such as

$$V^{-1}HV = \begin{pmatrix} \lambda_1 & 0 & 0 & 0 \\ 0 & \lambda_1 & 1 & 0 \\ 0 & 0 & \lambda_1 & 0 \\ 0 & 0 & 0 & \lambda_2 \end{pmatrix}. \tag{2.51}$$

---

[4] The Jordan normal form is where, instead of a matrix diagonalising into its eigenvalue decomposition, the eigenvalues are in the main diagonal, with 1s in the superdiagonal

Where a matrix has a degenerate eigenvalue λ (in this example, λ_1), this first requires making a distinction between degenerate values, where the eigenvectors are different and EPs, where both eigenvectors and eigenvalues coalesce. The order of the EP is then given by the size of the largest Jordan block. In this specific example, while there is a triple degeneracy in λ_1, the largest Jordan block is 2-dimensional, so this forms an EP2.

Behaviour near the EP

Near the EP, the behaviour of the system is also affected by the presence of the EP [5]. This can be expressed by the difference between eigenvalues surrounding the EPN. Parameterising the Hamiltonian by γ so that the EPN occurs at γ_c and moving away from the EPN by a small $\delta\gamma = \gamma - \gamma_c$ gives that the eigenvalues become

$$\lambda = \lambda_c + \sum_{j=1}^{\infty} C_j \left(\delta\gamma\right)^{\frac{j}{N}} \tag{2.52}$$

and the eigenvectors become

$$\left|v\right\rangle = \left|v_{EP}\right\rangle + \sum_{j=1}^{\infty} \left(\delta\gamma\right)^{\frac{j}{N}} \left|\phi_j\right\rangle, \tag{2.53}$$

where the different possible values of the N^{th} root of $\delta\gamma$ give the different eigenvalues and eigenvectors. Near the EP $\left(\delta\gamma^{1/N} \ll 1\right)$, this then becomes

$$\lambda = \lambda_c + C_1 \left(\delta\gamma\right)^{\frac{1}{N}} + \mathcal{O}\left(\delta\gamma^{\frac{2}{N}}\right) \tag{2.54}$$

$$\left|v\right\rangle = \left|v_{EP}\right\rangle + \left(\delta\gamma\right)^{\frac{1}{N}} \left|\phi_1\right\rangle + \mathcal{O}\left(\delta\gamma^{\frac{2}{N}}\right). \tag{2.55}$$

For H_2' with $\theta = \pi/2$, $s = r_c = 1$ and $r = r_c + \delta r = 1 + \delta r$, the eigenvalues are given by

$$\lambda_{\pm} = \pm\sqrt{2i\delta r}\sqrt{1 + \frac{\delta r}{2i}}, \tag{2.56}$$

which can be expanded as a binomial expansion to be of the same form as equation 2.52 with $\lambda_c = 0$. Similarly, the eigenvectors are given by

$$\left|v\right\rangle \propto \begin{pmatrix} i \\ 1 \end{pmatrix} + \left(\delta r + \lambda_{\pm}\right)\begin{pmatrix} 1 \\ 0 \end{pmatrix}, \tag{2.57}$$

which can similarly be expanded. Near the EP ($\delta r \ll 1$), these are

$$\lambda_{\pm} = \pm\sqrt{2i\delta r} + \mathcal{O}\left(\delta r\right) \tag{2.58}$$

$$\left|v\right\rangle \propto \begin{pmatrix} i \\ 1 \end{pmatrix} \pm \sqrt{2i\delta r}\begin{pmatrix} 1 \\ 0 \end{pmatrix} + \mathcal{O}\left(\delta r\right). \tag{2.59}$$

Topology and Riemann surfaces

The presence of an EP can also be shown by considering the topology of a system near an EP. The Riemann surface (displaying the real and imaginary parts of each eigenvalue with the real and imaginary parts of some parameter) shows the main features of the system, such as the coalesence at the EP as well as the sheets and branch cut(s) that show their behaviour. Due to the behaviour of the eigenvalues near the EPN that scales with $\delta\gamma^{1/N}$, encircling the EP by adding a phase to the parameter to get $\delta\gamma e^{i\varphi}$ generates a topological Berry phase and changes the eigenvector, which can also be shown in the Riemann surface [32]. This is characterised by the winding number, which gives the number of times the EP needs to be encircled before returning to the starting point. In the above example, using H_2', we have that encircling the EP once gives a phase of 2π to δr, so that

$$\lambda_{\pm}\left(\varphi=2\pi\right) \approx \mp\sqrt{2i\delta r} \quad \text{and} \left|v\left(\varphi=2\pi\right)\right\rangle \propto \begin{pmatrix} i \\ 1 \end{pmatrix} \mp \sqrt{2i\delta r}\begin{pmatrix} 1 \\ 0 \end{pmatrix}, \tag{2.60}$$

so the point that started in one eigenvector is now on the other eigenvector. For more complex systems with a larger winding number, the direction of travel also matters. The Riemann surface of H_2' is shown in figure 2.4 and graphically shows the above properties.

2.5 Previous/Current Simulation Methods

A number of classical methods of creating and simulating $\mathcal{PT}$ symmetric systems exist, such as coupled lasers, optical simulation and electric circuits. However, while small systems can be simulated classically, bigger systems require more efficient simulation methods. As there is a computational limit to how quickly large $N\times N$ or $2^N\times 2^N$ systems can be simulated classically, quantum simulation methods might potentially be able to offer a time advantage. However, this often runs into potential issues as the time evolution of a $\mathcal{PT}$-symmetric Hamiltonian, as shown in figure 2.5, does not have a constant normalisation. As such, simulations of $\mathcal{PT}$-symmetric Hamiltonians need to be postselected, which is an inefficient process. Despite this, a variety of simulations have been performed or simulation methods created, often falling into the category of adding extra loss (or using a purely lossy Hamiltonian) or using the ideas of pseudo-Hermitian Hamiltonians to create a method of simulation known as dilation.

2.5.1 Using loss transformations

Most often used in optical systems, this generally involves taking a $\mathcal{PT}$-symmetric Hamiltonian with both gain and loss terms along the diagonal of the Hamiltonian and subtracting the highest gain term. In particular, for a Hamiltonian $H = H_{\text{Herm}} + H_{\text{diag}}$ where H_{Herm} is Hermitian and H_{diag} is a diagonal matrix containing terms $i\gamma_{jj}$ (for real γ), the first step in this process is to transform to the matrix $H' = H - iI\max_j\gamma_{jj}$ so that all the non-Hermitian terms in the

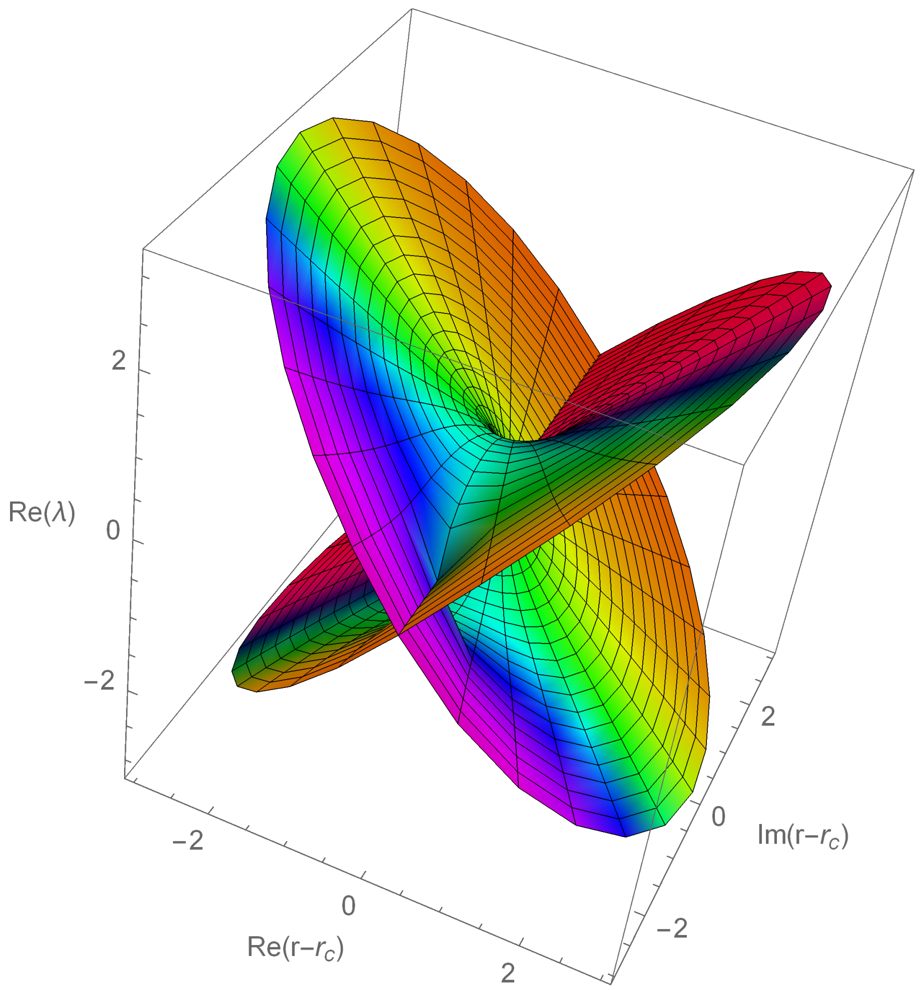

Figure 2.4: Riemann surface of the eigenvalues of $H_2'\left(\theta=\pi/2, s=1\right)$ near the EP at $r=r_c=1$. This demonstrates a number of properties typical of EPs. Picking a point close enough to the EP and encircling the EP once causes both a phase change and switches the eigenvectors and eigenvalues. Encircling the EP a second time brings us back to the starting point, showing this has a winding number of 2.

Hamiltonian are now loss terms. As the identity commutes with any operator, this gives that the evolution is given by

$$U'\left(t\right)=e^{-\max_j \gamma_{jj}}U\left(t\right), \tag{2.61}$$

where $U\left(t\right)$ is the evolution of H which contains both loss and gain terms. As such, if the transformation $U'\left(t\right)$ can be created, postselecting on a successful evolution will give the same dynamics as the full Hamiltonian with gain and loss.

Two particular examples where this idea has been used (although in different ways) are in $\mathcal{PT}$-symmetric quantum interference [33] where loss was made in a continuous way and for a $\mathcal{PT}$-symmetric quantum random walk [21] where the loss happened at discrete places. The quantum interference experiment consisted of two photons in two waveguides L and R, with

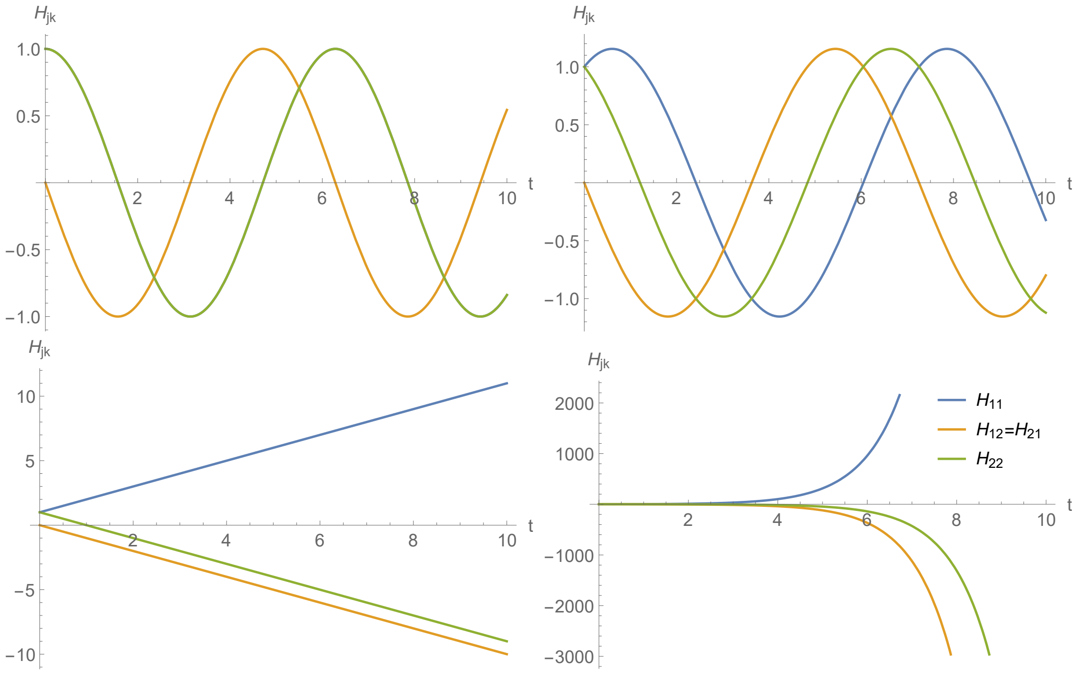

Figure 2.5: Evolution of H_2' for (top left) the Hermitian region with $\gamma = 0$, (top right) unbroken region with $\gamma = 0.5$, (bottom left) EP with $\gamma = 1$ and (bottom right) broken region with $\gamma = 1.5$. This demonstrates the typical regions of $\mathcal{PT}$-symmetric systems where there are oscillations in the unbroken region, polynomial (here linear) growth at the EP and exponential growth in the broken region.

one of the waveguides (here L) being lossier than the other, with this extra loss created by bending the waveguide, which causes continuous loss by interacting with the environment. This can be modelled using the Lindblad equation (equation 2.13) with a single loss term (giving $l = 1$) $\kappa = \gamma$ and corresponding loss operator $F = a_L$. When postselected (by detecting the same number of photons as were input), this was used to model both $\mathcal{PT}$-symmetric evolution of a single photon and $\mathcal{PT}$-symmetric Hong-Ou-Mandel (HOM) interference.

Alternatively, loss can also be made more discrete, such as in [21]. Here, in creating a quantum walk, the system consists of a discrete position space (here, physical modes) coupled to a qubit (such as polarisation of the light used here). The operators used consist of a translation operator S, coin operator C and loss operators L and L', where

$$S = \sum_x \left(|x\rangle\langle x+1| \otimes |0\rangle\langle 0| + |x\rangle\langle x-1| \otimes |1\rangle\langle 1|\right) \tag{2.62}$$

$$C\left(\theta\left(x\right)\right) = I_x \otimes \begin{pmatrix} \cos\theta\left(x\right) & \sin\theta\left(x\right) \\ \sin\theta\left(x\right) & -\cos\theta\left(x\right) \end{pmatrix} \tag{2.63}$$

$$L = I_x \otimes \begin{pmatrix} l_1 & 0 \\ 0 & l_2 \end{pmatrix} \tag{2.64}$$

$$L' = I_x \otimes \begin{pmatrix} l_2 & 0 \\ 0 & l_1 \end{pmatrix}, \tag{2.65}$$

with $0 \leq l_1, l_2 \leq 1$. This was then used to define a Floquet operator (due to the alternating loss terms l_1 and l_2)

$$U = LSC\left(\theta_2\left(x\right)\right)L'SC\left(\theta_1\left(x\right)\right). \tag{2.66}$$

The loss terms are then implemented by coupling that mode to another mode with a vacuum state input by a beamsplitter such that l_1 or l_2 of the input light gets transmitted. This particular experiment was used to create Floquet topological phases with topological edge states.

2.5.2 Hamiltonian Dilation

The general approach to simulating the dynamics of a non-Hermitian system using dilation is to embed the system to be simulated $\mathcal{H}_{\text{sys}}$ using an ancilla system (usually a single qubit) $\mathcal{H}_{\text{anc}}$ to get the overall Hermitian Hilbert space $\mathcal{H} = \mathcal{H}_{\text{sys}} \otimes \mathcal{H}_{\text{anc}}$. The aim is then to simulate the evolution of

$$|\Psi\rangle = \mu\,|\psi\rangle\,|a\rangle + \nu\,|\chi\rangle\,|b\rangle\,, \tag{2.67}$$

where $|a\rangle$ and $|b\rangle$ are orthogonal, μ and ν are normalisation parameters, $|\psi\rangle$ is the state evolving under the (normalised) non-Hermitian Hamiltonian and $|\chi\rangle$ is in general unknown, although can be defined for pseudo-Hermitian Hamiltonians using the metric operator η as $|\chi\rangle = \eta\,|\psi\rangle$.

This has been done with the pseudo-Hermitian Hamiltonian [8]

$$H = E_0 I + s \begin{pmatrix} i\sin\alpha & 1 \\ 1 & -i\sin\alpha \end{pmatrix}, \tag{2.68}$$

which has the metric

$$\eta = e^{\beta\sigma_y} = \frac{1}{\cos\alpha} \begin{pmatrix} 1 & -i\sin\alpha \\ i\sin\alpha & 1 \end{pmatrix}, \tag{2.69}$$

where β is defined by $\tanh\beta = \sin\alpha$. This gives the initial state

$$|\boldsymbol{\Psi}\rangle = |\psi\rangle\,|0\rangle + \eta\,|\psi\rangle\,|1\rangle\,. \tag{2.70}$$

With a normalisation factor

$$f = \sqrt{\frac{\cos\alpha}{2}}, \tag{2.71}$$

the overall (Hermitian) Hamiltonian is then

$$\mathbf{H} = f^2 \left[\left(H\eta^{-1} + \eta H \right) \otimes I_2 + \left(H - \eta H^\dagger \eta^{-1} \right) \otimes i\sigma_y \right], \tag{2.72}$$

which gives the evolution of this state as

$$\mathbf{U} = f^2 \left[\left(U\eta^{-1} + \eta U \right) \otimes I_2 + \left(U - \eta U \eta^{-1} \right) \otimes i\sigma_y \right] = F \otimes I_2 + G \otimes i\sigma_y. \tag{2.73}$$

Postselecting on

$$P_0 = I_2 \otimes |0\rangle\langle 0| \tag{2.74}$$

then gives $\mathcal{PT}$-symmetric evolution with a final output state

$$P_0 \left| \mathbf{\Psi}(t) \right\rangle = \left| \psi(t) \right\rangle |0\rangle . \tag{2.75}$$

This idea was later extended to include time-dependent broken-$\mathcal{PT}$-symmetric systems [7,9] using a time-dependent metric operator

$$\eta(t) = \sqrt{\left(1 + \eta_0^2\right) e^{-iHt} e^{iHt} - I} \tag{2.76}$$

with $\eta_0 > 0$ arbitrarily chosen so that $\eta^\dagger(t)\,\eta(t)$ is positive over the entire simulation time.

2.6 Creating $\mathcal{PT}$-symmetric Quantum Systems

There are various methods of creating classical $\mathcal{PT}$-symmetric systems, such as coupled lasers, non-Hermitian electrical circuits and optomechanics. These can have various applications, such as unidirectional optical transmission, creating a negative refractive index and improved light absorption. Due to $\mathcal{PT}$-symmetric systems being generally easier to create in classical systems than quantum systems without having to rely on postselection, there are fewer experimental applications of $\mathcal{PT}$-symmetric quantum systems than there are of classical systems. Creating a quantum $\mathcal{PT}$-symmetric system without some form of loss or postselection is considered extremely difficult if not fundamentally impossible. However, open and passive $\mathcal{PT}$-symmetric systems can and have been created in quantum systems and whether quantum analogues of classical applications can occur can at least be looked at theoretically. As there are a wide variety of classical $\mathcal{PT}$-symmetric systems and potential applications, here we look at a small subset of these that are relevant to optics and quantum information processing.

Optical systems

Two common methods of creating $\mathcal{PT}$-symmetric systems in classical optics are in waveguides (or optical fibres) and microring resonators (which are also used in optomechanical systems). Lossy systems can be created by having different losses in different waveguides, which also applies in creating lossy quantum systems, such as in [33]. In a waveguide, the (classical) refractive index is equivalent to the (quantum) potential. As such, being $\mathcal{PT}$-symmetric is equivalent to the condition that the refractive index $n(\mathbf{r}) = n^*(-\mathbf{r})$. As the imaginary component of the refractive index gives the loss present in the system, this condition requires the amount of gain to match the amount of loss. This is often achieved using Optical Parametric Amplification (OPA). As OPA is a classical effect, this cannot be directly used to create a quantum $\mathcal{PT}$-symmetric system. However, OPA is similar to the quantum effect of squeezing (discussed in chapter 3), which we use throughout chapters 5 and 6 to create quantum $\mathcal{PT}$-symmetric systems. Semiconductor Optical Amplifiers have also been used in microring resonators to create single mode $\mathcal{PT}$-symmetric miroring lasers. Operating such systems near the EP improves sensitivity and create unusual lasers, such as orbital angular momentum microlasers.

If there is an equivalence between classical and quantum $\mathcal{PT}$-symmetry, this potentially suggests that an EP of a quantum optical system may have applications in sensing or photon creation.

Slowing down of decoherence

This is a specific potential application of $\mathcal{PT}$-symmetric systems that can occur when a $\mathcal{PT}$-symmetric system is coupled to an environment (here assumed to be Markovian) that causes decoherence [6]. Similar to previous examples used in this chapter, this can be shown by considering the 2D $\mathcal{PT}$-symmetric Hamiltonian H_2' with $\theta = \pi/2$ and $s = 1$ in the $\mathcal{PT}$-unbroken regime. For an environment with spectral density $J(\omega) = J_0 \omega e^{-\omega/\omega_c}$ and $\omega_c \gg k_B T$, the decoherence functions behaves as

$$D(t) \sim e^{-\pi J_0 \left(1-r^2\right) k_B T t} \tag{2.77}$$

and so, increasing the strength of the $\mathcal{PT}$-parameter r decreases the speed of the decoherence, which vanishes completely at the EP.

Alternatively, the $\mathcal{PT}$-symmetric system can also be considered as being embedded in (as opposed to coupled to) a larger, overall Hermitian (closed) system such as in equation 2.67 except with an arbitrarily large ancilla system as opposed to a qubit. In this case, the trace distance between two arbitrary states evolving under this Hamiltonian is then

$$D(t) = \left[1 + \left(\frac{2r \sin^2\left(\sqrt{1-r^2}t\right)}{1-r^2}\right)^2\right]^{-\frac{1}{2}}. \tag{2.78}$$

As there are times when $\dot{D} > 0$, this means that the system is retrieving information from the environment, which is therefore non-Markovian behaviour.

‘Local $\mathcal{PT}$ symmetry violates the no-signaling principle’

However, aside from pseudo-Hermitian Hamiltonians being equivalent to Hermitian Hamiltonians, whether or not $\mathcal{PT}$-symmetric quantum mechanics as typically considered is a valid theory of quantum mechanics is still an open question. One result that shows this is [34]. Starting with the assumptions that $\mathcal{PT}$-symmetric systems are tomographically local (i.e. measurements occur locally) that can co-exist with a Hermitian system and that measurement probabilities are calculated using normalisation conventional in quantum physics, they consider the entangled state

$$|\psi\rangle = \frac{1}{\sqrt{2}} \left(|+\rangle_A |+\rangle_B + |-\rangle_A |-\rangle_A \right), \tag{2.79}$$

shared between the parties A and B, where $\sqrt{2} \, |\pm\rangle = |0\rangle \pm |1\rangle$. If A then applies either I or σ_x before evolving under the evolution given by H_2' at the EP, B obtains the state

$$|\pm i\rangle = \frac{1}{\sqrt{2}} \left(|0\rangle \pm i \, |1\rangle \right), \tag{2.80}$$

depending on the operation A performed, with probability 1. As this is instananeous, this occurs even when A and B are spacelike separated, which is superluminal signalling. The authors propose 3 solutions to this problem:

1. The first assumption is wrong and $\mathcal{PT}$-symmetric systems are not tomographically local. As this is generally considered a requirement of real systems, this is saying that $\mathcal{PT}$-symmetry is not a valid theory.
2. The second assumption is wrong and the rules of a $\mathcal{PT}$-symmetric system are different to that of a Hermitian quantum system. One possible solution to this could be related to the similarity transform between pseudo-Hermitian and Hermitian systems, although this potentially reduces to that of regular Hermitian quantum mechanics.
3. Superluminal signalling is possible. As this is directly violating a fundamental law of physics, this is considered to be extremely unlikely.

‘$\mathcal{PT}$-symmetric photonic quantum systems with gain and loss do not exist’

The question of whether $\mathcal{PT}$-symmetric quantum systems can exist has also been directly applied to photonics [35]. While classical electromagnetic waves can have gain and loss, the creation and annihilation operators a and $a^\dagger$ of a quantum photonic systems have to fulfil the commutation relation $\left[a, a^\dagger\right] = 0$, so creating loss in such a system requires the use of Langevin noise operators f so that

$$\dot{a} = \left(-i\omega - \Gamma\right) a + f, \tag{2.81}$$

where Γ is the loss rate. As such, the noise is related to the loss and so, nonzero noise is impossible with nonzero loss. It follows that creating a system with gain would satisfy the equation

$$\dot{a} = \left(-i\omega + \Gamma\right) a + f^{\dagger}. \tag{2.82}$$

As a result, inputting a coherent state into a system, such as a waveguide, with loss and gain causes thermal broadening, which is used to make the claim that '$\mathcal{PT}$-symmetric photonic quantum systems with gain and loss do not exist' unless postselection is used.

However, this approach only considers a linear medium, so that different frequency modes cannot interact. As discussed in chapter 3, this is not generally true of optical systems. As such, chapters 5 and 6 are dedicated to nonlinear optical systems, which can potentially be used to create $\mathcal{PT}$-symmetric photonic quantum systems.

Chapter 3

Nonlinear Quantum Optics

This is a background chapter that summarises already existing results.

3.1 Introduction

Classical optics is a relatively common method for simulating and creating classical $\mathcal{PT}$-symmetric systems [10–20]. Similarly, quantum optics is a common method for simulating passive, quantum $\mathcal{PT}$-symmetric systems, as well more general simulations [7, 21–23]. Here, we review the features of quantum optics that we will use later to simulate $\mathcal{PT}$-symmetric systems and create single photon states.

After deriving the photonic creation and annihilation operators from the electromagnetic field in section 3.2, this consists at looking at the input/output formalism that considers interactions with a medium as transformations of the creation and annihilation operators in the Heisenberg picture in section 3.3. When these transformations are quadratic/Gaussian in the operator terms, this gives two different types of transformations. The first, looked at in section 3.4 are here referred to as linear transformations, as they are transformations that arise from interacting with a linearly responding medium and leads to unitary transformations on the operators. The second, looked at in section 3.5 are referred to as nonlinear transformations as they arise from interactions in a nonlinearly responding medium and gives symplectic transformations on the operators. These transformations can be used to create approximate single photon states. However, this can be enhanced by using microring resonators to create better states. As such, we then look at microring resonators in the linearly responding regime in section 3.6.

3.2 Creation/annihilation operators

The electromagnetic field can be quantised by first starting with Maxwell's equations [36]:

$$\nabla \cdot \mathbf{E} = \rho \tag{3.1}$$

$$\nabla \times \mathbf{B} - \dot{\mathbf{E}} = \mathbf{J} \tag{3.2}$$

$$\nabla \times \mathbf{E} + \dot{\mathbf{B}} = 0 \tag{3.3}$$

$$\nabla \cdot \mathbf{B} = 0, \tag{3.4}$$

in Heavyside-Lorentz units ($\epsilon_0 = 1$ and $\mu_0 = 1$) with $c = 1$ (and later setting $\hbar = 1$), where $\mathbf{E}$ is the electric field, $\mathbf{B}$ is the magnetic field, ρ is the charge density and $\mathbf{J}$ is the current density. The electric and magnetic fields can then be written in terms of a scalar and vector potential φ and $\mathbf{A}$:

$$\mathbf{E} = -\nabla\varphi - \dot{\mathbf{A}} \tag{3.5}$$

$$\mathbf{B} = \nabla \times \mathbf{A}. \tag{3.6}$$

This can be made relativistic by defining (using Einstein notation) the four-vector potential A^μ, charge-current density J^μ and field strength $F^{\mu\nu}$

$$A^\mu = (\varphi, \mathbf{A}) \tag{3.7}$$

$$J^\mu = (\rho, J) \tag{3.8}$$

$$F^{\mu\nu} = \partial^\mu A^\nu - \partial^\nu A^\mu. \tag{3.9}$$

This gives that the electric and magnetic fields are

$$F^{0j} = E^j \tag{3.10}$$

$$F^{jk} = \varepsilon^{jkl} B_l, \tag{3.11}$$

which allows us to rewrite Maxwell's equations as

$$\partial_\nu F^{\mu\nu} = J^\mu \tag{3.12}$$

$$\varepsilon_{\mu\nu\rho\sigma} \partial^\rho F^{\mu\nu} = 0 \tag{3.13}$$

and define the Lagrangian density as

$$\mathcal{L} = -\frac{1}{4} F^{\mu\nu} F_{\mu\nu} + J^\mu A_\mu, \tag{3.14}$$

as this gives the Lorentz, gauge, time-reversal and parity-reversal invariant action $S = \int \mathcal{L}\, d^4x$ that generates Maxwell's equations. The coulomb gauge ($\nabla \cdot A = 0$) can then be enforced by taking

$$A_j\left(x\right) \to \left(\delta_{jk} - \frac{\nabla_j \nabla_k}{\nabla^2}\right) A_k\left(x\right) \tag{3.15}$$

by using the Fourier Transform

$$\tilde{A}_j(k) \to \left(\delta_{jk} - \frac{k_j k_k}{\mathbf{k}^2}\right) A_k(k). \tag{3.16}$$

In a free field (when the charge-current density, $J^\mu = 0$), requiring that S is stationary and varying φ and A gives that

$$\mathcal{L} = \frac{1}{2}\dot{A}_j\dot{A}_j - \frac{1}{2}\nabla_k A_j \nabla_k A_j \implies \partial^2 A_j(x) = 0. \tag{3.17}$$

This has the general solution

$$\mathbf{A}(x) = \frac{1}{(2\pi)^3 2\omega} \sum_{\lambda=\pm} \int v_\lambda^*(\mathbf{k})\, a_\lambda(\mathbf{k})\, e^{ikx} + v_\lambda(\mathbf{k})\, a_\lambda^\dagger(\mathbf{k})\, e^{-ikx}\, d^3k, \tag{3.18}$$

where v_λ are polarisation vectors that are orthogonal to $\mathbf{k}$. The conjugate momentum operator is then

$$\Pi_j = \frac{\partial \mathcal{L}}{\partial \dot{A}_j} = \dot{A}_j \tag{3.19}$$

and the Hamiltonian density is

$$\mathcal{H} = \Pi_j \dot{A}_j - \mathcal{L} = \frac{1}{2}\Pi_j\Pi_j + \frac{1}{2}\nabla_k A_j \nabla_k A_j. \tag{3.20}$$

This gives annihilation and creation operators

$$a_\lambda(\mathbf{k}) = i v_\lambda(\mathbf{k}) \cdot \int e^{-ikx}\partial_0 \mathbf{A}(x) - \left(\partial_0 e^{-ikx}\right)\mathbf{A}(x)\ d^3x \tag{3.21}$$

$$a_\lambda^\dagger(\mathbf{k}) = -i v_\lambda^*(\mathbf{k}) \cdot \int e^{ikx}\partial_0 \mathbf{A}(x) - \left(\partial_0 e^{ikx}\right)\mathbf{A}(x)\ d^3x, \tag{3.22}$$

with commutation relations

$$\left[a_\lambda(\mathbf{k}), a_{\lambda'}(\mathbf{k}')\right] = 0 \tag{3.23}$$

$$\left[a_\lambda^\dagger(\mathbf{k}), a_{\lambda'}^\dagger(\mathbf{k}')\right] = 0 \tag{3.24}$$

$$\left[a_\lambda(\mathbf{k}), a_{\lambda'}^\dagger(\mathbf{k}')\right] = (2\pi)^3 2\omega \delta^3(\mathbf{k}' - \mathbf{k})\,\delta_{\lambda\lambda'}. \tag{3.25}$$

The Hamiltonian can be rewritten as

$$H = \frac{1}{2(2\pi)^3} \sum_{\lambda=\pm} \int a_\lambda^\dagger(\mathbf{k})\, a_\lambda(\mathbf{k})\ d^3k + \frac{\omega}{(2\pi)^3} \int d^3k V. \tag{3.26}$$

Redefining the creation and annihilation operators such that

$$\left[a_\lambda(\mathbf{k}), a_{\lambda'}^\dagger(\mathbf{k}')\right] = \delta^3(\mathbf{k}' - \mathbf{k})\,\delta_{\lambda\lambda'}, \tag{3.27}$$

the Hamiltonian density becomes

$$\mathcal{H} = \omega\left(a_\lambda^\dagger a_\lambda + \frac{1}{2}\right), \tag{3.28}$$

where the dependence on **k** is now implicit. This is the Hamiltonian of a single mode of a free electromagnetic field, defining the number (of photons) operator as $n = a^\dagger a$. This has eigenvalues and eigenstates

$$\hat{n}\,|n\rangle = n\,|n\rangle\,. \tag{3.29}$$

While not used here, the quadrature operators X and P can also be defined as [37]

$$X \propto \frac{1}{\sqrt{2}}\left(a + a^\dagger\right) \tag{3.30}$$

$$P \propto \frac{i}{\sqrt{2}}\left(a - a^\dagger\right). \tag{3.31}$$

3.3 Input/Output formalism/operators

This can then be extended to include interactions in a material that can cause transformations on the photons in the system. For a system with discrete values of allowed frequency/wavenumber and multiple modes m, giving a Hamiltonian

$$H = \sum_m \sum_k \sum_{\lambda=\pm} \left(a^\dagger_{mk\lambda} a_{mk\lambda} + \frac{1}{2}\right)\omega + H_{\text{int}}, \tag{3.32}$$

which then acts on the state of the system. This gives photon number (Fock) states

$$\bigotimes_{mk\lambda} |n_{p,mk\lambda}\rangle \tag{3.33}$$

Alternatively, this can be looked at in the Heisenberg picture to calculate the evolution of the creation and anihilation operators. The expectation value of $\mathcal{O} = a_{mk\lambda},\ a^\dagger_{mk\lambda}$ is then

$$\left\langle \psi \left| U^\dagger\left(t, t_0\right) \mathcal{O}\left(t_0\right) U\left(t, t_0\right) \right| \psi \right\rangle, \tag{3.34}$$

where $U\left(t, t_0\right) = e^{-iH(t-t_0)}$ for time-independent H. As there is no explicit time dependence in $a_{mk\lambda}$ and $a^\dagger_{mk\lambda}$, this gives

$$\frac{d}{dt}\mathcal{O}\left(t\right) = i\left[H, \mathcal{O}\left(t\right)\right]. \tag{3.35}$$

From the commutation relations, this gives

$$\left(\frac{d}{dt} + i\omega\right) a_{mk\lambda} = i\left[H_{\text{int}}, a_{mk\lambda}\right] \tag{3.36}$$

$$\left(\frac{d}{dt} - i\omega\right) a^\dagger_{mk\lambda} = i\left[H_{\text{int}}, a^\dagger_{mk\lambda}\right], \tag{3.37}$$

which can be simplified by defining

$$\bar{a}_{mk\lambda} = a e^{i\omega t} \tag{3.38}$$

$$\bar{a}^\dagger_{mk\lambda} = a^\dagger e^{-i\omega t} \tag{3.39}$$

to get

$$\frac{d}{dt}\bar{\mathcal{O}}\left(t\right) = i\left[H_{\text{int}}, \bar{\mathcal{O}}\left(t\right)\right]. \tag{3.40}$$

When H_{int} is no more than quadratic in the creation and annihilation operators, this can be written as a matrix equation

$$\frac{d}{dt}\bar{\mathbf{a}}\left(t\right) = H_{\text{eff}}\bar{\mathbf{a}}\left(t\right), \tag{3.41}$$

where the vector of operators $\bar{\mathbf{a}}$ includes the creation and annihilation operators, potentially with other operators, such as the identity or the noise operators in section 2.6; H_{eff} is a matrix acting on the operator space of the system $\mathcal{S} \subset \mathcal{B}\left(\mathcal{H}\right)$ and which exponentiates to give the transformation

$$\begin{aligned}\bar{\mathbf{a}}\left(t\right) &= M\left(t,t_0\right)\bar{\mathbf{a}}\left(t_0\right) &(3.42)\\ &= e^{-iH_{\text{eff}}(t-t_0)}\bar{\mathbf{a}}\left(t_0\right) &(3.43)\\ &= U_{\text{int}}^{\dagger}\left(t,t_0\right)\bar{\mathbf{a}}\left(t_0\right)U_{\text{int}}\left(t,t_0\right). &(3.44)\end{aligned}$$

This can be considered as being output operators $\bar{\mathbf{a}}\left(t\right) = \bar{\mathbf{a}}_{\text{out}}$ in terms of input operators $\bar{\mathbf{a}}\left(t_0\right) = \bar{\mathbf{a}}_{\text{in}}$ and a transformation or scattering matrix $M\left(t,t_0\right) = e^{-iH_{\text{eff}}(t-t_0)}$.

3.3.1 Symplectic transformations

In the case when $\bar{\mathbf{a}}$ consists only of the creation and annihilation operators $\bar{a}_{mk\lambda}$ and $\bar{a}_{mk\lambda}^{\dagger}$ (here ordered so that all the annihilation operators are written before the creation operators so that $\bar{\mathbf{a}}_j$ are annihilation operators for $1 < j \leq N$ and creation operators for $N < j \leq 2N$), we can write the transformation matrix M as

$$M = \begin{pmatrix} A & B \\ C & D \end{pmatrix}, \tag{3.45}$$

giving

$$\bar{\mathbf{a}}_{\text{out},j} = \begin{cases} \sum_{k=1}^{N}\left(A_{jk}\bar{\mathbf{a}}_{\text{in},k} + B_{jk}\bar{\mathbf{a}}_{\text{in},k+N}\right) & \text{for} \quad 1 < j \leq N \\ \sum_{k=1}^{N}\left(C_{j-N,k}\bar{\mathbf{a}}_{\text{in},k} + D_{j-N,k}\bar{\mathbf{a}}_{\text{in},k+N}\right) & \text{for} \quad N < j \leq 2N \end{cases}. \tag{3.46}$$

As the commutation relations must remain valid and as $\bar{\mathbf{a}}_{j+N} = \bar{\mathbf{a}}_j^{\dagger}$, this simplifies to a symplectic transformation matrix

$$M = \begin{pmatrix} A & B \\ B^* & A^* \end{pmatrix}, \tag{3.47}$$

with a determinant of 1. Defining

$$\Omega = \begin{pmatrix} 0 & I \\ -I & 0 \end{pmatrix} \tag{3.48}$$

gives that this can also be considered as a matrix satisfying the equation

$$M^T\Omega M = \Omega. \tag{3.49}$$

3.4 Linear/passive transformations

A symplectic transformation is here considered linear[1] when $B = 0$. From equation 3.49, this gives that $A^\dagger A = I$, so that A is unitary. From this, we consider two different types of transformations - those that are formed of a single evolution under a single Hamiltonian that we consider as a 'basic transformation' that can be used to form a block element in a larger transformation, such as a unitary interferometer that can simulate arbitrary unitary transformations on N modes.

3.4.1 Basic transformations

Rotation/Phase Shift

This is defined by the Hamiltonian

$$H_{\text{int, phase}} = \phi_{mk\lambda} a^\dagger_{mk\lambda} a_{mk\lambda} \tag{3.50}$$

that can act on a single mode. On that mode, this gives

$$A_{\text{phase}} = e^{-i\phi_{mk\lambda}t} = e^{-i\phi'_{mk\lambda}}, \tag{3.51}$$

causing a phase shift of the input photon.

Beamsplitter

A standard beamsplitter has the Hamiltonian

$$H_{\text{int, BS}} = i\theta a^\dagger_{mk\lambda} a_{m'k\lambda} - i\theta^* a_{mk\lambda} a^\dagger_{m'k\lambda}, \tag{3.52}$$

which gives the transformation

$$A_{\text{BS}} = \begin{pmatrix} \cos|\theta|\,t & \frac{\theta^*}{|\theta|}\sin|\theta|\,t \\ -\frac{\theta}{|\theta|}\sin|\theta|\,t & \cos|\theta|\,t \end{pmatrix} = \begin{pmatrix} \cos|\theta'| & \frac{\theta'^*}{|\theta'|}\sin|\theta'| \\ -\frac{\theta'}{|\theta'|}\sin|\theta'| & \cos|\theta'| \end{pmatrix} \tag{3.53}$$

between modes m and m'. At $\theta = 0$, this performs the identity operation while at $\theta' = \pm\pi/2$ or $\theta' = \pm i\pi/2$, this performs a swap operation with differing phases. Alternatively, at $\theta' = \pm\pi/4$ or $\theta' = \pm i\pi/4$, this is a balanced (i.e. '50:50') beamsplitter, such as

$$A_{\text{BS, }\theta=\pi/4} = \frac{1}{\sqrt{2}}\begin{pmatrix} 1 & 1 \\ -1 & 1 \end{pmatrix}, \tag{3.54}$$

---

[1] As there is an ambiguity over the term 'linear', we here use it to mean 'optics in a linearly responding medium', as opposed to the alternative 'transformations acting on the creation and annihilation operators that are linear and can be described using matrices'. In the former terminology (used here), the latter can either be linear or nonlinear, so as it is more useful here to have a distinction between the two, we use the former definition.

acting as a Hadamard matrix. This gives the Hong-Ou-Mandel (HOM) effect when a single photon state is input into each mode and a two photon state is output from one mode, with a zero photon (vacuum) state in the other mode.

A different variant of a beamsplitter is a polarising beamsplitter. This is a polarisation-dependent beamsplitter such as

$$H_{\text{int, PBS}} = i\theta a^{\dagger}_{mkV} a_{m'kV} - i\theta^{*} a_{mkV} a^{\dagger}_{m'kV}, \tag{3.55}$$

where $\lambda = V$ is arbitrarily chosen as a PBS acting on vertically polarised photons, while acting as an identity transformation on horizontally polarised photons.

Displacement/Coherent states

Acting on a specific mode, the displacement operator is

$$H_{\text{int, D}} = i\alpha a^{\dagger}_{mk\lambda} - i\alpha^{*} a_{mk\lambda}, \tag{3.56}$$

which gives

$$M : \begin{pmatrix} a_{mk\lambda} \\ a^{\dagger}_{mk\lambda} \end{pmatrix} \mapsto \begin{pmatrix} 1 & 0 & \alpha \\ 0 & 1 & \alpha^{*} \end{pmatrix} \begin{pmatrix} a_{mk\lambda} \\ a^{\dagger}_{mk\lambda} \\ I \end{pmatrix}. \tag{3.57}$$

Acting with the displacement operator on the vacuum state (or more generally, a coherent state) then gives a coherent state

$$|\alpha_{mk\lambda}\rangle = e^{-\frac{|\alpha|^2}{2}} \sum_{n=0}^{\infty} \frac{\alpha^2}{\sqrt{n!}} |n_{mk\lambda}\rangle, \tag{3.58}$$

as a result of the property that

$$e^{\alpha a^{\dagger} - \alpha^{*} a} = e^{-\frac{|\alpha|^2}{2}} e^{\alpha a^{\dagger}} e^{-\alpha^{*} a}. \tag{3.59}$$

3.4.2 Unitary interferometers

It is possible to build up a series of beamsplitters and phase shifters with multiple inputs and outputs that create a larger unitary transformation on photons input into a given number of input modes.

Mach-Zender Interferometer

A variant of a Mach-Zender interferometer, consisting of a phase-shifter, followed by a 50:50 beamsplitter, phase-shifter and another 50:50 beamsplitter can then be used to create a variable beamsplitter, as shown in figure 3.1.

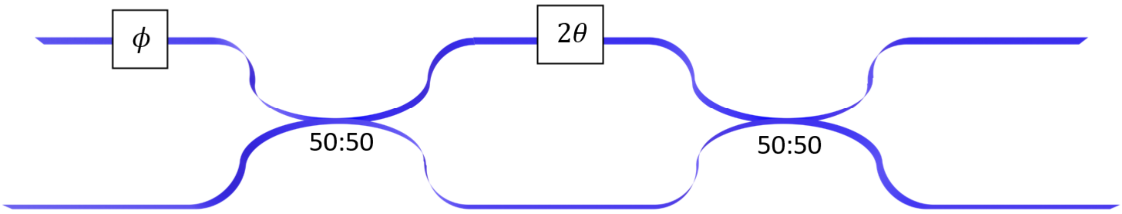

Figure 3.1: Mach-Zender interferometer consisting of 2 phase shifts with 2 50:50 beamsplitters, which is equivalent to a single variable beamsplitter described by equation 3.60. In future diagrams, the phases and beamsplitter notation will be omitted.

This gives the transformation

$$A_{\text{VBS}}\left(\theta,\phi\right)=A_{\text{BS}}\left(\frac{\pi}{4}\right)A_{\text{phase}}\left(2\theta\right)A_{\text{BS}}\left(\frac{\pi}{4}\right)A_{\text{phase}}\left(\phi\right)=\begin{pmatrix}e^{-i\phi}\cos\theta & -\sin\theta\\ e^{-i\phi}\sin\theta & \cos\theta\end{pmatrix}, \tag{3.60}$$

which is used as a building block in larger interferometers shown in the rest of this section.

Reck scheme

An N-mode interferometer was first considered by Reck et. al. [38] who showed that a triangular lattice of variable beamsplitters, such as in figure 3.2, can be used to create an arbitrary unitary transformation. This works by recursively transforming into a basis where the elements of the N^{th} row and column of an $N \times N$ unitary to be implemented U_N become 0, except for a phase on element $N \times N$, leaving an $N-1 \times N-1$ unitary. That is, the rotation matrix consisting of variable beamsplitters acting on each mode

$$R_N = A_{\text{VBS};N,N-1}\cdots A_{\text{VBS};N,1} \tag{3.61}$$

can rotate between an arbitrary row vector and a 'computational' basis state:

$$\begin{pmatrix}0 & \dots & 1\end{pmatrix}\cdot R_N^{-1}=\begin{pmatrix}e^{-i\phi_1}\cos\theta_1 & \dots & \sin\theta_{N-1}\cdots\sin\theta_1\end{pmatrix}. \tag{3.62}$$

In this basis U_N becomes

$$U_N\cdot R_N = U_{N-1}\oplus e^{i\alpha}, \tag{3.63}$$

at which point another rotation is applied on the $N-1\times N-1$ unitary. This gives that an arbitrary unitary U_N can be described by the rotations

$$U_N = R_N^{-1}\cdots R_2^{-1}D, \tag{3.64}$$

where D is a diagonal matrix of phases. As these phases are not measured when detecting output photons, they do not need to be included on a physical implementation of a Reck scheme.

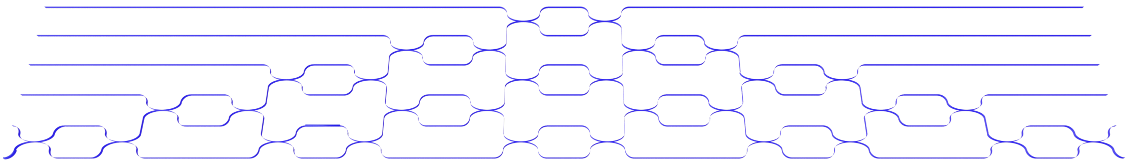

Figure 3.2: Diagram of a 6-mode Reck scheme consisting of a triangular lattice of variable beamsplitters. An N-mode Reck scheme requires $N\left(N-1\right)/2$ such beamsplitters. This works by recursively rotating the $N \times N$ target unitary into a basis where it becomes an $N-1 \times N-1$ unitary with a phase on the remaining mode.

Clements scheme

The Reck scheme was later improved by Clements et. al. [39], who designed a shorter interferometer using a square lattice, shown in figure 3.3 for 8 modes. While this uses the same number of beamsplitters as the Reck scheme, as it is shorter, it is less lossy. In addition, as each mode or waveguide contains the same number of beamsplitters, the loss across each mode is more uniform than the Reck scheme. Similar to the Reck scheme, the Clements scheme takes a unitary and applies recursive transformations to rotate it into a diagonal basis by rotating the outermost diagonal first, where the Reck scheme rotated rows and columns. Unlike the Reck scheme, this is done by applying transformations to alternate sides of the unitary to rotate into a basis where the unitary consists only of diagonal elements. The final transformation then consists of variable beamsplitters acting on alternate rows, as shown in figure 3.3.

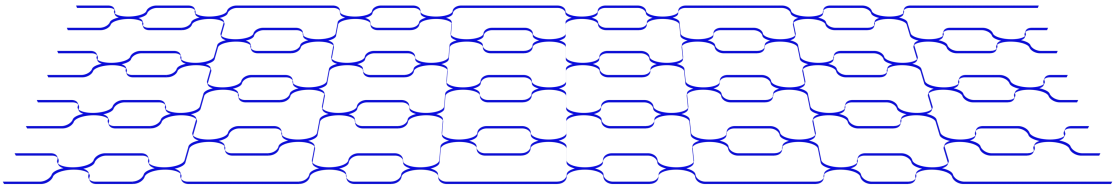

Figure 3.3: Diagram of an 8-mode Clements scheme consisting of a square/rectangular lattice of variable beamsplitters. An N-mode Clements scheme requires $N\left(N-1\right)/2$ such beamsplitters, as with the Reck scheme. This works by recursively rotating the $N \times N$ target unitary into a basis where the outermost diagonal elements are 0 until the main diagonal is the only non-zero diagonal and consists only of phases.

3.5 Nonlinear/active transformations

When $B \neq 0$, the transformations are no longer photon-number preserving and can often include interactions between photons of different frequencies, unlike the linear and passive transformations of section 3.4. While other transformations that cannot be described using matrix transformations are possible, here, we only look at squeezing and its various forms, as well as Self-phase modulation (SPM) and cross-phase modulation (XPM) that arise from Four Wave Mixing (FWM).

3.5.1 Squeezing

Generally, squeezing happens in a single physical mode and can cause interactions between different frequency or polarisation spaces, known as two mode squeezing. However, there is a special case of this when the interactions happen on the same space, known as single mode squeezing.

Single mode squeezing

This is described by the Hamiltonian

$$H_{\text{int, S1}} = \frac{i}{2}\left(z^* a_{mk\lambda} a_{mk\lambda} - z a^\dagger_{mk\lambda} a^\dagger_{mk\lambda}\right) \tag{3.65}$$

and gives the transformation, for $zt = re^{i\theta}$,

$$M = \begin{pmatrix} \cosh r & -e^{i\theta}\sinh r \\ -e^{-i\theta}\sinh r & \cosh r \end{pmatrix}. \tag{3.66}$$

This also defines a single mode squeezed vacuum state as

$$|S_1\rangle = e^{-iHt}|vac\rangle = \frac{1}{\sqrt{\cosh r}} \sum_{n=0}^{\infty} \frac{\sqrt{(2n)!}}{2^n n!} \left(-e^{i\phi}\tanh r\right)^n |2n\rangle\,, \tag{3.67}$$

which 'squeezes' the vacuum state so that the standard deviation in one variable (such as one of the quadratures) is below $1/\sqrt{2}$, while the uncertainty in the conjugate variable is correspondingly larger, as shown in figure 3.4.

Two mode squeezing

This is a more general form of squeezing, that acts on two physical or (more commonly) frequency modes, potentially with different polarisations. The Hamiltonian is of the form

$$H_{\text{int, S2}} = i\left(z^* a_{mk\lambda} a_{m'k'\lambda'} - z a^\dagger_{mk\lambda} a^\dagger_{m'k'\lambda'}\right), \tag{3.68}$$

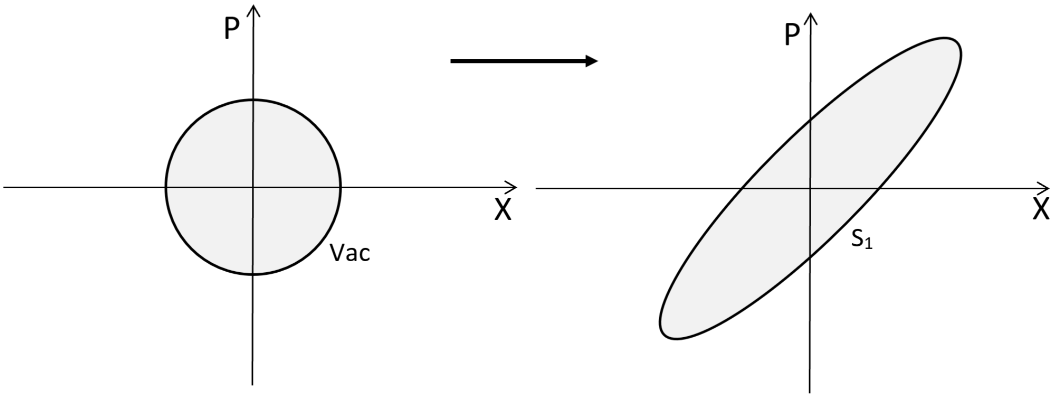

Figure 3.4: Phase diagram in quadrature space of (left) a vacuum state and (right) a squeezed vacuum state. Squeezing causes the variance in one variable to decrease while increasing it in the other such that (for an ideal squeezer) the area is preserved. Physical implementation of squeezers are generally noisy, so the corresponding area under a physical (noisy) implementation of squeezing is likely to be larger.

where at least one of m', k' and λ' must be different to m, k and λ respectively. This then generates the transformation

$$M\begin{pmatrix} a_{mk\lambda} \\ a_{m'k'\lambda'} \\ a^\dagger_{mk\lambda} \\ a^\dagger_{m'k'\lambda'} \end{pmatrix} = \begin{pmatrix} \cosh r & 0 & 0 & -e^{i\theta}\sinh r \\ 0 & \cosh r & -e^{i\theta}\sinh r & 0 \\ 0 & -e^{-i\theta}\sinh r & \cosh r & 0 \\ -e^{-i\theta}\sinh r & 0 & 0 & \cosh r \end{pmatrix} \begin{pmatrix} a_{mk\lambda} \\ a_{m'k'\lambda'} \\ a^\dagger_{mk\lambda} \\ a^\dagger_{m'k'\lambda'} \end{pmatrix}, \tag{3.69}$$

which gives a two-mode squeezed vacuum state as

$$|S_2\rangle = \frac{1}{\cosh r}\sum_{n=0}^{\infty}\left(-e^{i\phi}\tanh r\right)^n |n\rangle_{mk\lambda}|n\rangle_{m'k'\lambda'}\,. \tag{3.70}$$

In particular, for a low squeezing parameter $r \ll 1$, this can be approximated as (arbitrarily setting $\phi = 0$)

$$\begin{aligned} |S_2\rangle &= \frac{1}{\cosh r}\left[-\tanh r\,|1\rangle_{mk\lambda}|1\rangle_{m'k'\lambda'} + \tanh^2 r\,|2\rangle_{mk\lambda}|2\rangle_{m'k'\lambda'} + \mathcal{O}\left(r^3\right)\right] && (3.71)\\ &= -\left(r + \mathcal{O}\left(r^3\right)\right)|1\rangle_{mk\lambda}|1\rangle_{m'k'\lambda'} + \left(r^2 + \mathcal{O}\left(r^4\right)\right)|2\rangle_{mk\lambda}|2\rangle_{m'k'\lambda'} + \mathcal{O}\left(r^3\right) && (3.72)\\ &= -r\,|1\rangle_{mk\lambda}|1\rangle_{m'k'\lambda'} + \mathcal{O}\left(r^2\right), && (3.73)\end{aligned}$$

approximating an entangled single photon state. Heralding on one of the modes then gives an approximate heralded single photon state in the other mode. However, due to the requirement that the squeezing parameter $r \ll 1$, this can only occur with the low probability $\sim r^2$.

3.5.2 Generating squeezing

Squeezing is usually physically creating by inputting a coherent (laser) state into a nonlinear medium, where the order of the nonlinearity determines the interactions that occur [40]. The two most commonly considered nonlinearities are the second order $\chi^{(2)}$ generating Spontaneous Parametric Down Conversion (SPDC) and the third order $\chi^{(3)}$ generating Four Wave Mixing (FWM), as well as Self Phase Modulation (SPM) and Cross Phase Modulation (XPM).

Spontaneous Parametric Down Conversion (SPDC)

SPDC is a second order process characterised by a single pump photon annihilating to create two lower frequency signal and idler photons. This can be degenerate, where the created photons are the same frequency; or non-degenerate, where the created photons are at different frequencies. The Hamiltonian describing this process is typically given by

$$H_{\text{int, SPDC}} = \Lambda a_{m_P k_P \lambda_P} a^{\dagger}_{m_S k_S \lambda_S} a^{\dagger}_{m_I k_I \lambda_I} + \Lambda^* a^{\dagger}_{m_P k_P \lambda_P} a_{m_S k_S \lambda_S} a_{m_I k_I \lambda_I}, \tag{3.74}$$

where $\Lambda \propto \chi^{(2)}$ is dependent on a variety of factors, such as the system SPDC is occuring in (such as a waveguide spiral, microring resonator, or nonlinear crystal). This can be split into 3 types of SPDC, depending on the polarisation of the pump, signal and idler photons:

- Type 0: $\lambda_P = \lambda_S = \lambda_I$
- Type I: $\lambda_P \neq \lambda_S = \lambda_I$
- Type II: $\lambda_S \neq \lambda_I$.

SPDC calculations are generally made analytically and numerically tractable by either inputting a pulsed laser for the pump or a CW laser which can be approximated as a lossless coherent state under the undepleted pump approximation so that[2]

$$a_{m_P k_P \lambda_P} \to \langle a_{m_P k_P \lambda_P} \rangle = \alpha_{m_P k_P \lambda_P}, \tag{3.75}$$

allowing the SPDC Hamiltonian to be approximated as a squeezing Hamiltonian.

Four Wave Mixing (FWM)

FWM is a third order process characterised by two pump photons annihilating to create two signal and idler photons. As two pump photons are involved, these can come from a single pump input, in which case the created photons are nondegenerate. Two input pumps can also be used, in which case, it can be possible to tune the system so that the process can be degenerate,

---

[2] As the creation and annihilation operators are still operators, this is more technically accurately done by first calculating the relevant equations of motion of the various operators before approximating the pump operators by their expectation values

creating signal and idler photons of the same frequency. As there are four photons in total involved in this process, FWM also allows other effects, Self- and Cross- Phase Modulation (SPM and XPM). As such, the FWM Hamiltonian can typically be described by

$$\begin{aligned}H_{\text{int, FWM}} = {} & \Lambda a_{m_P k_P \lambda_P} a_{m_P k_P \lambda_P} a^{\dagger}_{m_S k_S \lambda_S} a^{\dagger}_{m_I k_I \lambda_I} + \Lambda^* a^{\dagger}_{m_P k_P \lambda_P} a^{\dagger}_{m_P k_P \lambda_P} a_{m_S k_S \lambda_S} a_{m_I k_I \lambda_I} \\ & + \eta a^{\dagger}_{m_P k_P \lambda_P} a^{\dagger}_{m_P k_P \lambda_P} a_{m_P k_P \lambda_P} a_{m_P k_P \lambda_P} \\ & + \zeta a^{\dagger}_{m_S k_S \lambda_S} a^{\dagger}_{m_P k_P \lambda_P} a_{m_S k_S \lambda_S} a_{m_P k_P \lambda_P} + \zeta a^{\dagger}_{m_I k_I \lambda_I} a^{\dagger}_{m_P k_P \lambda_P} a_{m_I k_I \lambda_I} a_{m_P k_P \lambda_P},\end{aligned} \tag{3.76}$$

where the Λ terms give FWM, the η term gives SPM and the ζ terms give XPM. As with SPDC, this can be simplified by making the undepleted pump approximation and taking the pump to be either pulsed or a CW coherent state to get the approximated Hamiltonian (for a single input pump)

$$\begin{aligned}H'_{\text{int, FWM}} = {} & \Lambda \alpha^2 a^{\dagger}_{m_S k_S \lambda_S} a^{\dagger}_{m_I k_I \lambda_I} + \Lambda^* \alpha^{*2} a_{m_S k_S \lambda_S} a_{m_I k_I \lambda_I} + \eta \left|\alpha\right|^4 \\ & + \zeta \left|\alpha\right|^2 a^{\dagger}_{m_S k_S \lambda_S} a_{m_S k_S \lambda_S} + \zeta \left|\alpha\right|^2 a^{\dagger}_{m_I k_I \lambda_I} a_{m_I k_I \lambda_I}.\end{aligned} \tag{3.77}$$

The nondegenerate FWM term then gives two mode squeezing, the SPM term has the effect of shifting the refractive index and the XPM term causes the input pump to shift the phase of the output signal and idler photons.

3.6 Microring resonators

Generally, a microring (ring) resonator is a structure that allows for interference at the input and output by coupling to one or more waveguides and allows any input resonant light to make multiple trips around the ring. While the resonator depicted in figure 3.5 is a circle, other shapes, such as racetracks, squares and rectangles are also possible and can often be less lossy than circular resonators due to the continuous bend required for a circular ring.

For light confined in a waveguide or ring, the creation and annihilation operators in a ring can be parametised by the angle in the ring, such that the distance travelled over an angle θ is $l = r\theta$. This gives that the ring annihilation operator $b\left(\theta = 0\right) = b\left(\theta = 2\pi\right)$. As this is a periodic boundary condition, the allowed wavenumbers are discretised to give

$$k_n = \frac{2\pi n}{L} = \frac{n}{r}. \tag{3.78}$$

Introducing waveguide modes $\psi_{J,n}$ for frequency (and potentially polarisation) mode J in waveguide n, with a coupling rate $\gamma_{J,n}$ (which can be frequency dependent) allows for coupling light into and out of the waveguide, as in figure 3.5. Loss can similarly be modelled by similarly using a ‘phantom’ waveguide with modes ϕ_J and coupling rates μ_J. As multiple phantom waveguides are equivalent to a single phantom waveguide with $\mu_J = \sum_n \mu_{J,n}$, we

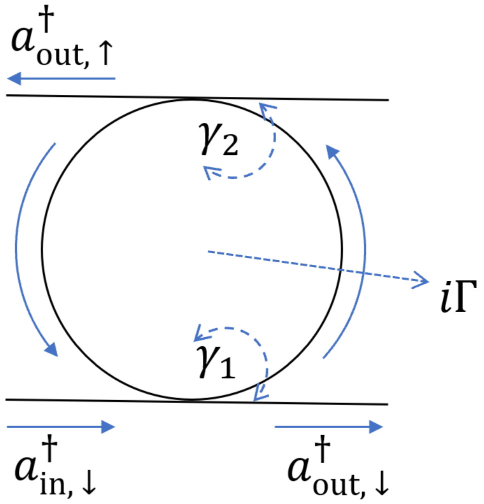

Figure 3.5: Diagram of a microring resonator coupled to two waveguides with an input mode coupled through the lower waveguide and output through both the lower and upper waveguides. Each waveguide has a corresponding coupling rate which, when combined with the loss intrinsic to the waveguide (through e.g. a rough surface), contributes to an overall loss rate.

consider only a single phantom waveguide. With these modes input to the waveguide, this gives the linear Hamiltonian

$$H_L = H_{\text{waveguides}} + H_{\text{ring},L} + H_{\text{coupling, rw}} \tag{3.79}$$

$$\begin{aligned} &= \sum_{J,n} \left[\omega_J \int \psi^\dagger_{J,n}(x)\,\psi_{J,n}(x)\; dx + \frac{1}{2} i v_J \int \frac{d\psi^\dagger_{J,n}(x)}{dx} \psi_{J,n}(x) - \psi^\dagger_{J,n}(x) \frac{d\psi_{J,n}(x)}{dx}\; dx \right] \\ &\quad + \sum_{J} \left[\omega_J \int \phi^\dagger_{J}(x)\,\phi_{J}(x)\; dx + \frac{1}{2} i v_J \int \frac{d\phi^\dagger_{J}(x)}{dx} \phi_{J}(x) - \phi^\dagger_{J}(x) \frac{d\phi_{J}(x)}{dx}\; dx \right] \\ &\quad + \sum_{J} \left[\omega_J b^\dagger_J b_J + \mu_J b^\dagger_J \phi_J(0) + \mu^*_J b_J \phi^\dagger_J(0) \right] + \sum_{J,n} \left[\gamma_{J,n} b^\dagger_J \psi_{J,n}(0) + \gamma^*_{J,n} b_J \psi^\dagger_{J,n}(0) \right]. \end{aligned} \tag{3.80}$$

splitting the waveguide operators into 'input' and 'output' operators

$$\psi_{J1}(x,t) = \begin{cases} \psi_{J1<}(x,t) & \text{for } x<0 \\ \psi_{J1>}(x,t) & \text{for } x>0 \end{cases}, \qquad \psi_{J2}(x,t) = \begin{cases} \psi_{J2<}(x,t) & \text{for } x>0 \\ \psi_{J2>}(x,t) & \text{for } x<0 \end{cases} \tag{3.81}$$

$$\phi_{Jn}(x,t) = \begin{cases} \phi_{Jn<}(x,t) & \text{for } x<0 \\ \phi_{Jn>}(x,t) & \text{for } x>0, \end{cases}, \tag{3.82}$$

where the ring is taken to couple to the waveguides at $x = 0$, the ring operators are taken to travel anti-clockwise, with input into waveguide 1 (coupled below the ring as in figure

3.5) travelling left-to-right and the input to waveguide 2 (coupled above the ring) travelling right-to-left, with

$$\psi_{Jn}(0,t) = \frac{1}{2}\left(\psi_{Jn<}(0,t) + \psi_{Jn>}(0,t)\right), \tag{3.83}$$

gives the Heisenberg equation of motion

$$\left(\frac{d}{dt} + \bar{\Gamma}_J\right)\bar{b}_J(t) = -i\sum_n \gamma^*_{Jn}\bar{\psi}_{Jn<}(0,t) - i\mu^*_J\bar{\phi}_{J<}(0,t), \tag{3.84}$$

where the total loss rate is defined by

$$\bar{\Gamma}_J = \sum_n \Gamma_{Jn} + M_J = \sum_n \frac{|\gamma_{Jn}|^2}{2v} + \frac{|\mu_J|^2}{2u}. \tag{3.85}$$

Typically, such as in chapter 6, a coherent CW or pulsed state α is input into waveguide 1 (assumed to be lossless for simplicity) with vacuum input into both waveguide 2 and the phantom waveguide (although a thermal state input may be more realistic). Taking the expectation value of the operators in equation 3.84 gives the classical equation of motion

$$\left(\frac{d}{dt} + \bar{\Gamma}_J\right)\bar{\beta}_J(t) = -i\gamma^*_{J1}\alpha(0,t). \tag{3.86}$$

For a CW input, the steady state solution can be calculated to be

$$\bar{\beta}_J = -i\frac{\gamma^*_{J1}}{\bar{\Gamma}_J}\alpha, \tag{3.87}$$

while for a pulsed input, the Fourier transform can be taken to give

$$\bar{\beta}_J(k) = -i\frac{\gamma^*_{J1}}{-ikv + \bar{\Gamma}_J}\alpha(k). \tag{3.88}$$

A similar process can be used to calculate the steady state and Fourier transformed solutions of the ring operators for pump, signal and idler modes of a nonlinear process such as FWM or SPDC, which in turn gives the output mode operators used to calculate correlation functions giving various photon statistics.

Chapter 4

Simulation Methods by Embedding into a Larger System

Section 4.1 is an introductory/background section and contains a summary of this chapter. Sections 4.2.1 and 4.3.1 are background sections and summarise pre-existing work. The rest of this chapter is my own work. Experimental data in sections 4.3 and 4.4 was taken by Nicola Maraviglia and Patrick Yard and can be found in [41–43]. Also related, although not directly referenced here is [44].

4.1 Introduction

A number of methods of simulating $\mathcal{PT}$-symmetric and non-Hermitian systems have been considered or experimentally implemented. Generally, these consist of some method of embedding the non-Hermitian Hamiltonian into a larger system. There are two main classes of methods of achieving this. One such method involves making Hamiltonians that are non-Hermitian because of gain and loss terms purely lossy. This can be done by 'shifting' the Hamiltonian by the value of the largest gain term and embedding this into a larger system, such as in [22, 23, 45]. Equivalently, this can also be achieved by adding in loss terms to the transformation in the form of beamsplitters in a photonic system, as in [21]. Alternatively, the non-Hermitian Hamiltonian can be 'dilated' into a larger Hermitian Hamiltonian, which could be done using an ancilla qubit, relying on the metric operator. While this method works for arbitrary non-Hermitian Hamiltonians [8], in the case of $\mathcal{PT}$-symmetric Hamiltonians in the unbroken regime, this is considerably simplified due to the simpler definition of the metric operator [7].

In this chapter, we consider possible ways of adapting the first two methods, first using open systems in section 4.2. Then, in section 4.3, in comparison with the ideas of [21], we use Halmos 'Unitary' dilation to consider two coupled $\mathcal{PT}$-symmetric systems evolving such that the overall combined system is unitary. Applications of such a combined system or simulation method are then considered in section 4.4. Unitary dilation has a number of potential applications, both within and outside $\mathcal{PT}$-symmetry. Varying the distinguishability of the input photons allows for tuning the strength of the off-diagonal blocks of the dilated unitary, as in section 4.4.1. As the system is comprised of non-Hermitian systems coupled in such a way that makes the overall system Hermitian, this allows for simulating exotic particles and systems, as in section 4.4.2.

Throughout this chapter, we consider the 2- and 3- dimensional $\mathcal{PT}$-symmetric Hamiltonians

$$H_2 = \begin{pmatrix} i\gamma & 1 \\ 1 & -i\gamma \end{pmatrix} \qquad \text{and} \qquad H_3 = \begin{pmatrix} i\gamma & 1 & 0 \\ 1 & 0 & 1 \\ 0 & 1 & -i\gamma \end{pmatrix}. \tag{4.1}$$

Defining $\epsilon_2 = \sqrt{1-\gamma^2}$ and $\epsilon_3 = \sqrt{2-\gamma^2}$, H_2 has eigenvalues ϵ_2 and $-\epsilon_2$ and H_3 has eigenvalues ϵ_3, 0 and $-\epsilon_3$. We also define the time evolution matrix of these Hamiltonians by $G_N = e^{-iH_N t}$, giving, for $N = 2, 3$,

$$G_N = I - i\frac{1}{\epsilon_N} H_N \sin \epsilon_N t - \frac{1}{\epsilon_N^2} H_N^2 \left(1 - \cos \epsilon_N t\right). \tag{4.2}$$

At the EP, this becomes

$$G_2\left(\gamma = 1\right) = \begin{pmatrix} 1+t & -it \\ -it & 1-t \end{pmatrix} \tag{4.3}$$

$$G_3\left(\gamma = 1\right) = \begin{pmatrix} 1+\sqrt{2}t+\frac{1}{2}t^2 & -i\left(t+\frac{1}{\sqrt{2}}t^2\right) & -\frac{1}{2}t^2 \\ -i\left(t+\frac{1}{\sqrt{2}}t^2\right) & 1-t^2 & -i\left(t-\frac{1}{\sqrt{2}}t^2\right) \\ -\frac{1}{2}t^2 & -i\left(t-\frac{1}{\sqrt{2}}t^2\right) & 1-\sqrt{2}t+\frac{1}{2}t^2 \end{pmatrix} \tag{4.4}$$

We also assume that inputs are single photon states, or other Fock states, as opposed to more general quantum states of light, such as squeezed states. While this is discussed in chapter 3 and more specifically in chapter 6, we assume that a single photon input is created by inputting a pulsed laser into a source using Spontaneous Parametric Down Conversion (SPDC) or Four Wave Mixing (FWM) to create pairs of photons, with one of these photons heralded separately to the experiment or interferometer. It is also assumed that the squeezing parameter is low enough that higher-order photon terms are small enough to be ignored. This scheme is shown in figure 4.1, a more detailed experimental description of which can be found in [41]. However, a different interferometric setup is given in chapter 5 which considers the photon source as part of the simulation set-up.

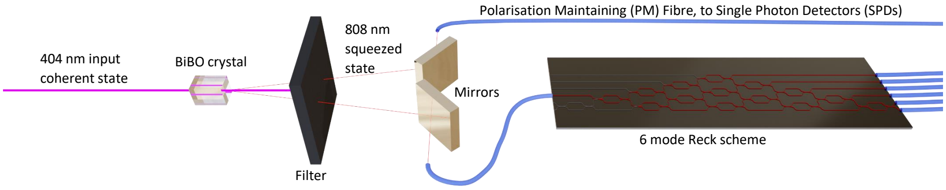

Figure 4.1: Diagram depicting the setup of a squeezed state, heralded to give a single photon input into mode 4 of a 6-mode Reck scheme [38]. A 404 nm coherent state is input into a BiBO crystal to undergo Spontaneous Parametric Down Conversion (SPDC), which creates a squeezed state (with 1 frequency mode and 2 spatial modes) with a low squeezing parameter. This is then heralded to approximately create a single photon input to the Reck scheme, which implements an arbitrary unitary transformation on that single photon.

4.2 Embedding as an open subsystem

4.2.1 Passive systems using Markovian Dynamics

The evolution of a Markovian, open system can be described by the Lindblad master equation [28]

$$\mathcal{L}\left(\rho\right) = \dot{\rho} = -i\left[H,\rho\right] + \frac{1}{2}\sum_{l}\kappa_l\left(2F_l\rho F_l^{\dagger} - F_l^{\dagger}F_l\rho - \rho F_l^{\dagger}F_l\right), \tag{4.5}$$

for $\kappa_l > 0\,\forall\, l, t$. Comparing with Hermitian evolution of a closed system,

$$\mathcal{L}_H\left(\rho\right) = \dot{\rho} = -i\left[H,\rho\right], \tag{4.6}$$

gives that we can desrcibe the evolution of the open system as the evolution of a non-Hermitian effective Hamiltonian

$$H_{\text{eff}} = H - \frac{i}{2}\sum_{l}\kappa_l F_l^{\dagger}F_l, \tag{4.7}$$

with an additional ‘jump’ term given by $\mathcal{L}_J = \sum_l \kappa_l F_l \rho F_l^{\dagger}$ to give the overall evolution as

$$\mathcal{L}\left(\rho\right) = \dot{\rho} = -i\left[H_{\text{eff}},\rho\right]^{\#} + \sum_{l}\kappa_l F_l\rho F_l^{\dagger} = \left(\mathcal{L}_H + \mathcal{L}_J\right)\left(\rho\right), \tag{4.8}$$

where the redefined commutator $[H_{\text{eff}},\rho]^{\#} = H_{\text{eff}}\rho - \rho H_{\text{eff}}^{\dagger}$, as in [46]. In the postselected regime, the evolution is then described by the non-Hermitian Hamiltonian H_{eff}.

To give an explicit example of such a system, we look at the 2-dimensional Hamiltonian

$$H_{\text{eff}} = \begin{pmatrix} 0 & 1 \\ 1 & -2i\gamma \end{pmatrix} = H_2 - i\gamma I, \tag{4.9}$$

which can be embedded into a 3-dimensional system, split into a Decoherence-Free Subsystem (DFS) [46] and decohering subsystem using the Feshbach partitioning formalism [47], where the effective Hamiltonian is embedded. That is, we define the Hamiltonian

$$H_{M3} = \begin{pmatrix} 0 & 0 & 0 \\ 0 & 0 & 1 \\ 0 & 1 & 0 \end{pmatrix}, \tag{4.10}$$

along with Lindblad operator

$$F_{M3} = \begin{pmatrix} 0 & 0 & 1 \\ 0 & 0 & 0 \\ 0 & 0 & 0 \end{pmatrix}, \tag{4.11}$$

where the bottom-right 2×2 block describes a subsystem where the effective, passive $\mathcal{PT}$-symmetric Hamiltonian acts,

$$H_{\text{eff},M3} = \begin{pmatrix} 0 & 0 & 0 \\ 0 & 0 & 1 \\ 0 & 1 & -\frac{i}{2}\kappa \end{pmatrix}, \tag{4.12}$$

with the jump term connecting this to the (upper-left) element ρ_{00} of the density matrix describing a DFS

$$\mathcal{L}_{J,M3}\left(\rho\right) = \begin{pmatrix} \kappa\rho_{33} & 0 & 0 \\ 0 & 0 & 0 \\ 0 & 0 & 0 \end{pmatrix}. \tag{4.13}$$

Postselecting on the bottom-right 2×2 block gives passive $\mathcal{PT}$-symmetric behaviour at the cost of successful postselection decaying exponentially with time, as shown in figure 4.3.

4.2.2 Active systems using non-Markovian Dynamics

In principle, this can be adapted to embed an active $\mathcal{PT}$-symmetric Hamiltonian into a 2×2 subspace of a 4×4 non-Markovian system. This relies on the property that if $\kappa_l\left(t\right) < 0$ for some t and $\int_{t_0}^{t} \kappa_l\left(t'\right) dt' > 0 \, \forall t$, evolution is a (completely positive) non-Markovian channel [48, 49]. Defining the Hamiltonian

$$H_{NM4} = \begin{pmatrix} 0 & 0 & 0 & 0 \\ 0 & 0 & 0 & 0 \\ 0 & 0 & 0 & 1 \\ 0 & 0 & 1 & 0 \end{pmatrix} \tag{4.14}$$

as well as the Lindblad operators

$$F_{1,NM4} = \begin{pmatrix} 0 & 0 & 1 & 0 \\ 0 & 0 & 0 & 0 \\ 0 & 0 & 0 & 0 \\ 0 & 0 & 0 & 0 \end{pmatrix} \quad \text{and} \quad F_{2,NM4} = \begin{pmatrix} 0 & 0 & 0 & 0 \\ 0 & 0 & 0 & 1 \\ 0 & 0 & 0 & 0 \\ 0 & 0 & 0 & 0 \end{pmatrix}, \tag{4.15}$$

defines an effective Hamiltonian

$$H_{\text{eff},NM4} = \begin{pmatrix} 0 & 0 & 0 & 0 \\ 0 & 0 & 0 & 0 \\ 0 & 0 & -\frac{i}{2}\kappa_1 & 1 \\ 0 & 0 & 1 & -\frac{i}{2}\kappa_2 \end{pmatrix} \tag{4.16}$$

with jump terms given by

$$\mathcal{L}_{J,NM4}\left(\rho\right) = \begin{pmatrix} \kappa_1\rho_{33} & 0 & 0 & 0 \\ 0 & \kappa_2\rho_{44} & 0 & 0 \\ 0 & 0 & 0 & 0 \\ 0 & 0 & 0 & 0 \end{pmatrix}. \tag{4.17}$$

To give an example of how this could be used to create $\mathcal{PT}$-symmetric evolution, for a total simulation time T, we can define

$$\kappa_1 = 2\gamma\,, \quad \kappa_2 = \begin{cases} 2\gamma & \text{for } 0 \leq t \leq \frac{T}{2} \\ -2\gamma & \text{for } \frac{T}{2} < t \leq T \end{cases}, \tag{4.18}$$

which, when postselected in the bottom-right subsystem, gives purely lossy evolution for $t \leq T/2$ followed by $\mathcal{PT}$-symmetric evolution for $T/2 < t < T$. This is displayed in figure 4.2.

However, while this method can in principle be used to simulate non-Hermitian Hamiltonians with gain terms as well as loss, the success probability of measuring the system to be in the subsystem described by the $\mathcal{PT}$-symmetric Hamiltonian decays exponentially with simulation time, although the final postselection probability is generally higher than the equivalent Markovian version given in section 4.2.1, shown in figure 4.3.

4.3 Halmos Unitary Dilation

4.3.1 Definition of Unitary Dilation

Originally described in [50] and recently used in [51], (Halmos') unitary dilation can be considered as a normalised variant of a Singular Value Decomposition (SVD). Starting with the SVD of an arbitrary $N \times N$ matrix $M = U\overrightarrow{\sigma}V^\dagger$ for U, V unitary matrices and $\overrightarrow{\sigma}$ a diagonal matrix of the singular values, unitary dilation consists of performing the SVD of M and normalising the singular values. This normalised SVD is then considered as a subsystem of a larger unitary system, which allows it to be implemented by a unitary process, such as a Clements or Reck scheme interferometer.

For a SVD of matrix M giving $M = U\overrightarrow{\sigma}V^\dagger$, denoting the singular values as σ_j to give the $(j,k)^{th}$ element of $\overrightarrow{\sigma}$ as $\overrightarrow{\sigma}_{jk} = \delta_{jk}\sigma_j$ and normalising by the maximum singular value

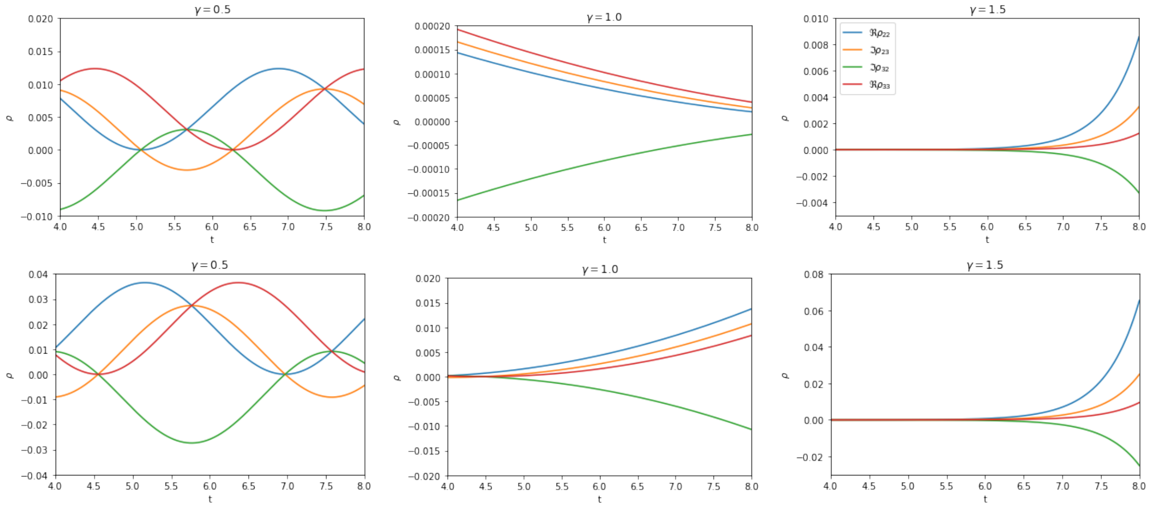

Figure 4.2: Evolution described by equations 4.16 and 4.18. Plots show the real parts of ρ_{33}, ρ_{44} and the imaginary parts of ρ_{34} and ρ_{43}, with $\mathrm{Im}\,(\rho_{33}) = \mathrm{Im}\,(\rho_{44}) = \mathrm{Re}\,(\rho_{34}) = \mathrm{Re}\,(\rho_{43}) = 0$. Total evolution time is taken to be $T = 8$ arbitrary units, the second half of which is shown, being the evolution of an active $\mathcal{PT}$-symmetric Hamiltonian with both gain and loss, created using non-Markovian Lindbladian dynamics. Top row starts with $\rho_{33} = 1$ and all other elements being 0 and bottom row has $\rho_{44} = 1$, with all other elements being 0. Left is the unbroken regime with $\gamma = 0.5$, middle is the Exceptional Point (EP) with $\gamma = 1$ and right is the broken regime with $\gamma = 1.5$. This displays the usual behaviour of $\mathcal{PT}$-symmetric Hamiltonians with oscillatory behaviour in the unbroken regime, pollynomal decay/growth at the EP and exponential decay/growth in the broken regime.

$\sigma_M = \max_j \sigma_j$ allows us to write

$$\frac{1}{\sigma_M} M = \tilde{M} = U \left(\frac{1}{\sigma_M} D \right) V^\dagger = U \tilde{D} V^\dagger. \tag{4.19}$$

As all the normalised singular values are $0 \leq \sigma_j / \sigma_M \leq 1$, we can write these as

$$\cos\theta_j = \frac{\sigma_j}{\sigma_M}, \tag{4.20}$$

so we can now write the elements of $\tilde{\sigma}$ as $\tilde{\sigma}_{jk} = \delta_{jk} \cos\theta_j$, which we denote by writing $\tilde{\sigma} = \cos\overrightarrow{\theta}$. This can now be embedded into a larger unitary system by a beamsplitter-type transformation to get

$$U_M = \begin{pmatrix} U & 0 \\ 0 & A \end{pmatrix} \begin{pmatrix} cos\,\overrightarrow{\theta} & i\sin\overrightarrow{\theta} \\ i\sin\overrightarrow{\theta} & \cos\overrightarrow{\theta} \end{pmatrix} \begin{pmatrix} V^\dagger & 0 \\ 0 & B \end{pmatrix}, \tag{4.21}$$

for any $A, B \in \mathrm{U}\,(N)$. Throughout the rest of this chapter, we take $A = V$ and $B = U^\dagger$. This

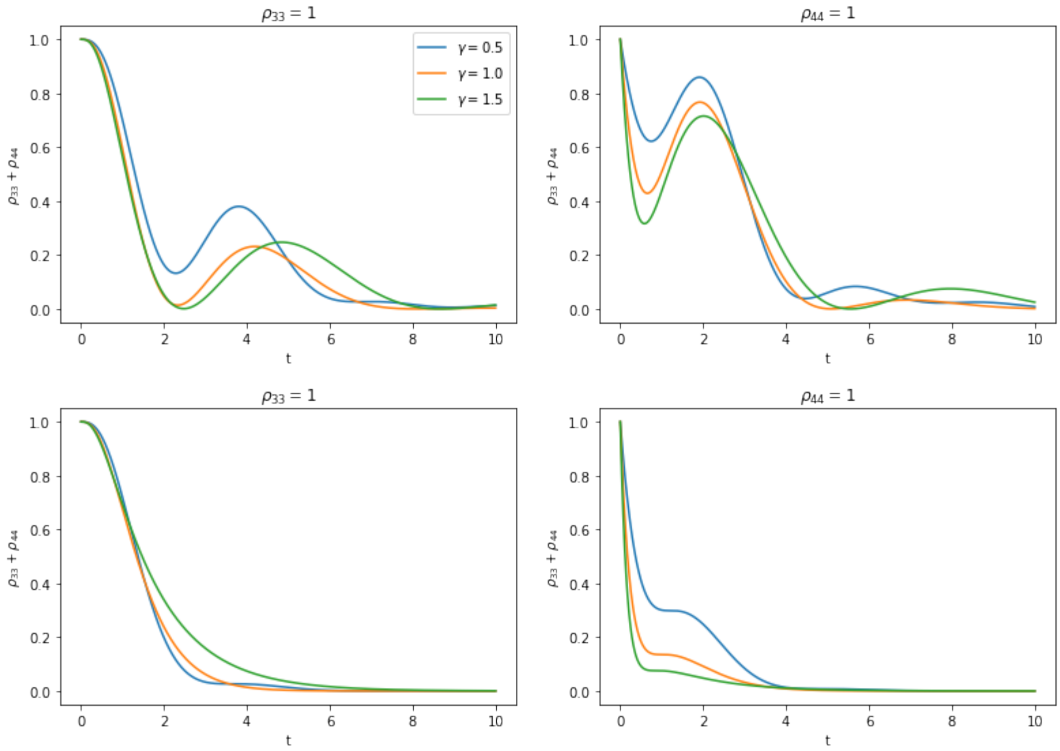

Figure 4.3: Comparison of the final postselection probability for Markovian (bottom) and non-Markovian (top) cases with time, for $\gamma = 0.5, 1.0, 1.5$. Left is for an input state $\rho_{33} = 1$ with all other elements of the density matrix $= 0$, right is for an input state $\rho_{44} = 1$, with all other elements $= 0$. The Markovian version has a monotonically decreasing (most often with an exponential decay) success probability, unlike the non-Markovian case. While this follows an envelope of (often exponential) decay with time, there are γ-dependent oscillations within this envelope.

gives

$$U_M = \begin{pmatrix} U \cos \overrightarrow{\theta} V^\dagger & iU\sqrt{I - \cos^2 \overrightarrow{\theta}}\, U^\dagger \\ iV\sqrt{I - \cos^2 \overrightarrow{\theta}}\, V^\dagger & V \cos \overrightarrow{\theta} U^\dagger \end{pmatrix} \tag{4.22}$$

$$= \begin{pmatrix} \tilde{M} & i\sqrt{I - \tilde{M}\tilde{M}^\dagger} \\ i\sqrt{I - \tilde{M}^\dagger \tilde{M}} & \tilde{M}^\dagger \end{pmatrix}, \tag{4.23}$$

using the property that $\sqrt{WCW^{-1}} = W\sqrt{C}W^{-1}$. We also have that, when $M = M^{\mathrm{T}}$,

$$\left(MM^\dagger\right)^* = M^\dagger M \implies U^* = V \tag{4.24}$$

$$\implies \left(\sqrt{I - \tilde{M}^\dagger \tilde{M}}\right)^* = \sqrt{I - \tilde{M}\tilde{M}^\dagger} \tag{4.25}$$

and so, defining $D = \sqrt{I - \tilde{M}\tilde{M}^\dagger}$ gives

$$U_M = \begin{pmatrix} \tilde{M} & iD \\ iD^* & \tilde{M}^\dagger \end{pmatrix} . \tag{4.26}$$

In order to simulate an N-dimensional system using spatial modes on a photonic chip with this dilation method, we therefore require $2N$-modes. To keep the mapping between photon number and computational spaces simple, we initially assume the $2N$-mode system is constrained to the one-photon subspace, so we can decompose the Fock space into particle number subspaces as $\mathcal{F} = \mathcal{H}_1$, where the subscript gives the total particle number. Modes 1 to N are denoted as the forward/top (sub)system and $N+1$ to $2N$ as the reverse/bottom (sub)system. This gives the basis states as

$$\left\{ |k\rangle = |0_p\rangle^{\otimes(k-1)} |1_p\rangle |0_p\rangle^{\otimes(2N-k)} = a_k^\dagger |0_p\rangle^{\otimes 2N} \right\}_{k=1}^{2N} \tag{4.27}$$

where $|0_p\rangle$ is the vacuum state. To make the transformation the dilated unitary gives between different subspaces of the system explicit, this gives, for $1 \le j \le N$ and as shown in figure 4.4,

$$U_M |j\rangle = \sum_{k=1}^{N} \left(\tilde{M}_{kj} |k\rangle + iD^*_{kj} |k+N\rangle \right) \tag{4.28}$$

$$U_M |j+N\rangle = \sum_{k=1}^{N} \left(\tilde{M}^\dagger_{kj} |k+N\rangle + iD_{kj} |k\rangle \right) . \tag{4.29}$$

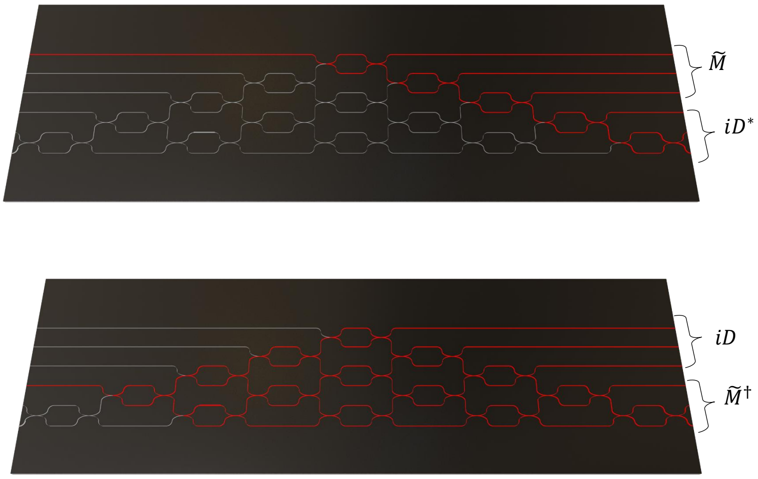

Figure 4.4: Inputting a single photon into the top N modes gives that the photon has undergone the transformation given by $\tilde{M}$ if detected in the top N modes or iD^* if detected in the bottom N modes. Similarly, a photon input into the bottom N modes undergoes the transformation given by $\tilde{M}^\dagger$ if detected in one of the bottom N modes and iD if detected in the top N modes.

4.3.2 Normalisation

Splitting the $2N \times 2N$ matrix into subspaces allows for considering both of these subspaces separately, meaning we can write a different (normalised) density matrix for each subspace, with an additional 'vacuum' mode representing 0 photons in that subspace. The density matrix at time t can be written as

$$\rho\left(t\right) = U_M \rho\left(0\right) U_M^\dagger = \begin{pmatrix} \rho_{FF} & \rho_{FR} \\ \rho_{RF} & \rho_{RR} \end{pmatrix}. \tag{4.30}$$

For a system initially in the state $\rho = \sum_{k,l}^{2N} p_{kl} \left|k\right\rangle\!\left\langle l\right|$, performing the partial trace over the reverse subsystem gives

$$\begin{aligned}
\rho_F = \mathrm{tr}_R \rho &= \mathrm{tr}_R \sum_{k,l=1}^{2N} p_{kl} \left|k\right\rangle\!\left\langle l\right| \\
&= \mathrm{tr}_R \sum_{k,l=1}^{2N} p_{kl} \left|0_p\right\rangle^{\otimes(k-1)} \left|1_p\right\rangle \left|0_p\right\rangle^{\otimes(2N-k)} \left\langle 0_p\right|^{\otimes(l-1)} \left\langle 1_p\right| \left\langle 0_p\right|^{\otimes(2N-l)} \\
&= \mathrm{tr}_R \Bigg(\sum_{k,l=1}^{N} p_{kl} \left|0_p\right\rangle^{\otimes(k-1)} \left|1_p\right\rangle \left|0_p\right\rangle^{\otimes(2N-k)} \left\langle 0_p\right|^{\otimes(l-1)} \left\langle 1_p\right| \left\langle 0_p\right|^{\otimes(2N-l)} \\
&\qquad + \sum_{k,l=N+1}^{2N} p_{kl} \left|0_p\right\rangle^{\otimes(k-1)} \left|1_p\right\rangle \left|0_p\right\rangle^{\otimes(2N-k)} \left\langle 0_p\right|^{\otimes(l-1)} \left\langle 1_p\right| \left\langle 0_p\right|^{\otimes(2N-l)} \\
&\qquad + \sum_{k=1}^{N} \sum_{l=N+1}^{2N} p_{kl} \left|0_p\right\rangle^{\otimes(k-1)} \left|1_p\right\rangle \left|0_p\right\rangle^{\otimes(2N-k)} \left\langle 0_p\right|^{\otimes(l-1)} \left\langle 1_p\right| \left\langle 0_p\right|^{\otimes(2N-l)} \\
&\qquad + \sum_{k=N+1}^{2N} \sum_{l=1}^{N} p_{kl} \left|0_p\right\rangle^{\otimes(k-1)} \left|1_p\right\rangle \left|0_p\right\rangle^{\otimes(2N-k)} \left\langle 0_p\right|^{\otimes(l-1)} \left\langle 1_p\right| \left\langle 0_p\right|^{\otimes(2N-l)} \Bigg) \\
&= \sum_{k,l=1}^{N} p_{kl} \left|0_p\right\rangle^{\otimes(k-1)} \left|1_p\right\rangle \left|0_p\right\rangle^{\otimes(N-k)} \left\langle 0_p\right|^{\otimes(l-1)} \left\langle 1_p\right| \left\langle 0_p\right|^{\otimes(N-l)} \\
&\qquad + \sum_{k,l=N+1}^{2N} p_{kl} \left|0_p\right\rangle^{\otimes n} \left\langle 0_p\right|^{\otimes n} \delta_{k,l} \\
&= \sum_{k,l=1}^{N} p_{kl} \left|k\right\rangle\!\left\langle l\right| + \sum_{k=N+1}^{2N} p_{kk} \left|\mathrm{vac}\right\rangle\!\left\langle \mathrm{vac}\right|,
\end{aligned}$$

with equivalent results when the partial trace is performed over the forward system, showing the partial trace operation over the reverse (forward) system sums the diagonal elements of the bottom (top) N modes and places this value in the vacuum state of the forward (reverse) system, as well as performing the decoherence map between the photon number subspaces, as per the photon number superselection rule [52, 53]. This also shows the basis states of the forward or reverse subsystem are $\left\{ \left|k\right\rangle^{(F/R)} = \left|0_p\right\rangle^{\otimes(k-1)} \left|1_p\right\rangle \left|0_p\right\rangle^{\otimes(N-k)} \right\}_{k=1}^{N}$ and an additional basis state in each subsystem of $|0_p\rangle^{\otimes N} = |\mathrm{vac}\rangle$. That is, this causes the Fock space of the subsystems to be decomposed into particle number subspaces as $\mathcal{F}^{(F/R)} = \mathcal{H}_0^{(F/R)} \oplus \mathcal{H}_1^{(F/R)}$, with no coherence between the single-particle subspace and the vacuum possible.

An ideal tomography measurement of this will then project on to the single photon subspace and normalise to give

$$\tilde{\rho}_F = \frac{\sum_{k,l=1}^{N} p_{kl} |k\rangle\langle l|}{\sum_{k=1}^{N} p_{kk}}$$

for the forward subsystem and

$$\tilde{\rho}_R = \frac{\sum_{k,l=N+1}^{2N} p_{kl} |k\rangle\langle l|}{\sum_{k=N+1}^{2N} p_{kk}}$$

for the reverse subsystem. As both systems can be measured simultaneously, the diagonal elements of one subsystem can then be used to calculate the elements of the 'un-normalised' density matrix of the other subsystem.

For $M = G_N(t)$, there are different possible methods of matrix normalisation, which give different dilated unitaries. One of these considers the maximum norm over the entire evolution time, the other considers the norm at each instant of evolution time. Denoting the maximum singular value of $G(t)$ by $\|G_N(t)\|_2 = \sigma_{\max}(G_N(t))$, these different normalisations give

$$\tilde{G}_N(t) = \frac{G_N(t)}{\|G_N(t)\|_2} = \frac{G_N(t)}{\sigma_{\max}(G_N(t))} \quad \text{or} \quad \tilde{G}_N(t) = \frac{G_N(t)}{\|G_N\|_2} = \frac{G_N(t)}{\max_t[\sigma_{\max}(G_N(t))]}. \tag{4.31}$$

The type of normalisation used then determines the evolution of the system, with each having its own advantages and disadvantages and giving different simulation results, as shown in figures 4.5, 4.6 and 4.7. Here, we use $\sigma_1(t)$ as the time-dependent maximum singular value, giving the first normalisation method and σ_M to be the time-independent maximum singular value, giving the second normalisation method.

In a $\mathcal{PT}$-symmetric system in the unbroken regime, as the eigenvalues are real, the various amplitudes oscillate with time, so the maximum singular value over the entire simulation time is the maximum singular value over a single oscillation period. For general non-Hermitian system, or a $\mathcal{PT}$-symmetric system at the EP or in the broken regime, this is not the case. The maximum singular value over all simulation time can often be at the start of the evolution, such as in the case of systems with only loss terms. They can also be at the end of the simulation time, such as in broken $\mathcal{PT}$-symmetric systems with exponential growth as with H_2. Starting with equation 4.2, we can write

$$G_2 = \begin{pmatrix} \cos\epsilon_2 t + \frac{\gamma}{\epsilon_2}\sin\epsilon_2 t & i\frac{1}{\epsilon_2}\sin\epsilon_2 t \\ i\frac{1}{\epsilon_2}\sin\epsilon_2 t & \cos\epsilon_2 t - \frac{\gamma}{\epsilon_2}\sin\epsilon_2 t \end{pmatrix}, \tag{4.32}$$

so we can calculate the singular values of G_2 as the square roots of the eigenvalues of

$$G_2 G_2^\dagger = \begin{pmatrix} \frac{1}{\epsilon_2^2} - \frac{\gamma^2}{\epsilon_2^2}\cos 2\epsilon_2 t + \frac{\gamma}{\epsilon_2}\sin 2\epsilon_2 t & -\frac{2i\gamma}{\epsilon_2^2}\sin^2\epsilon_2 t \\ \frac{2i\gamma}{\epsilon_2^2}\sin^2\epsilon_2 t & \frac{1}{\epsilon_2^2} - \frac{\gamma^2}{\epsilon_2^2}\cos 2\epsilon_2 t - \frac{\gamma}{\epsilon_2}\sin 2\epsilon_2 t \end{pmatrix}, \tag{4.33}$$

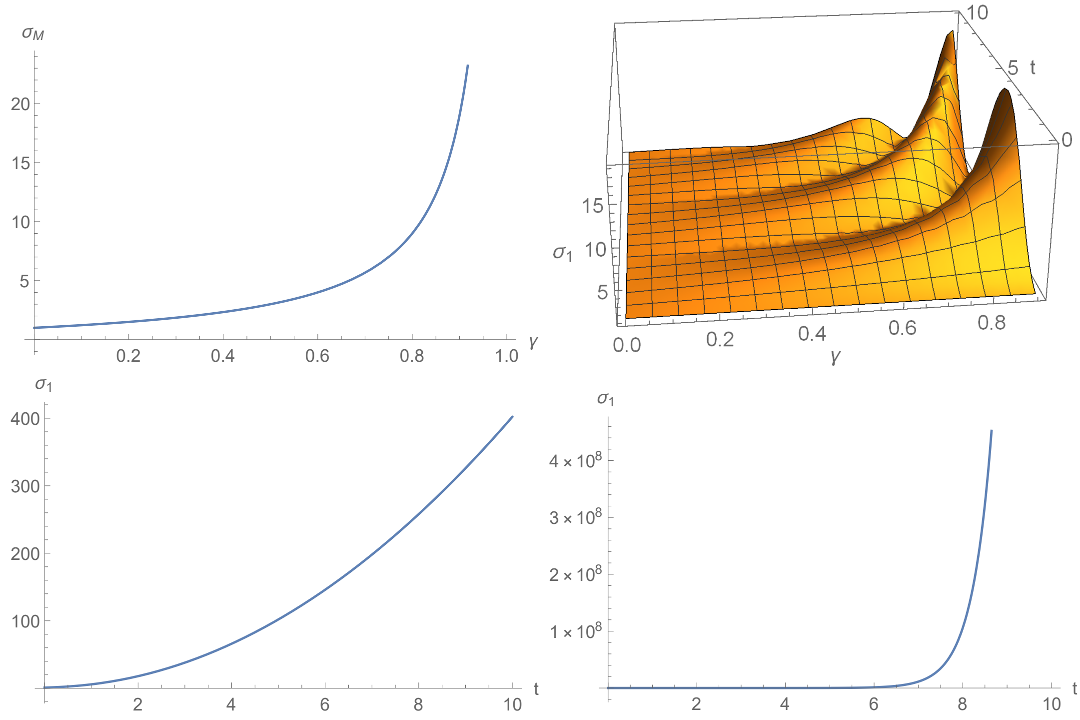

Figure 4.5: Maximum Singular Values for G_2. Upper-left plot shows the maximum singular value over the entire simulation time σ_M in the $\mathcal{PT}$-unbroken regime, varying with γ. Upper-right shows the time-dependent maximum singular value σ_1 as a function of time and γ. This shows both the increase in σ as the EP is approached as well as the increase in period. Bottom-left and bottom-right graphs show the maximum singular value σ_1, varying with time, at the EP and in the broken regime ($\gamma = 1.5$) respectively, showing polynomial growth with time at the EP and exponential growth in the broken regime.

which gives the square of singular values of G_2 as

$$\sigma_{1/2}^2\left(t\right) = \frac{1}{\epsilon_2^2}\left[1 - \gamma^2 \cos 2\epsilon_2 t \pm \gamma\sqrt{\left(1 - \cos 2\epsilon_2 t\right)\left(2 - \gamma^2 - \gamma^2 \cos 2\epsilon_2 t\right)}\right], \tag{4.34}$$

with the maximum time dependent singular value being defined as $\sigma_1\left(t\right)$. In the unbroken regime, shown in figure 4.5, this has a maximum value (over time) of

$$\sigma_M^2 = \frac{1 - \gamma^4 + 2\gamma\epsilon_2^2}{\epsilon_2^4} \qquad \text{at} \qquad t = \frac{\pi + 2\pi n}{2\epsilon_2}, \tag{4.35}$$

for $n \in \mathbb{Z}$. In the broken regime, the maximum singular value monotonically increases, so a maximum singular value over time cannot be defined, so this is instead taken to be the largest singular value (σ_1) at the final simulation time T.

We can also repeat this process at the EP, which gives

$$G_2\left(\gamma = 1\right) G_2^\dagger\left(\gamma = 1\right) = \begin{pmatrix} 1 + 2t + 2t^2 & 2it^2 \\ -2it^2 & 1 - 2t + 2t^2 \end{pmatrix}, \tag{4.36}$$

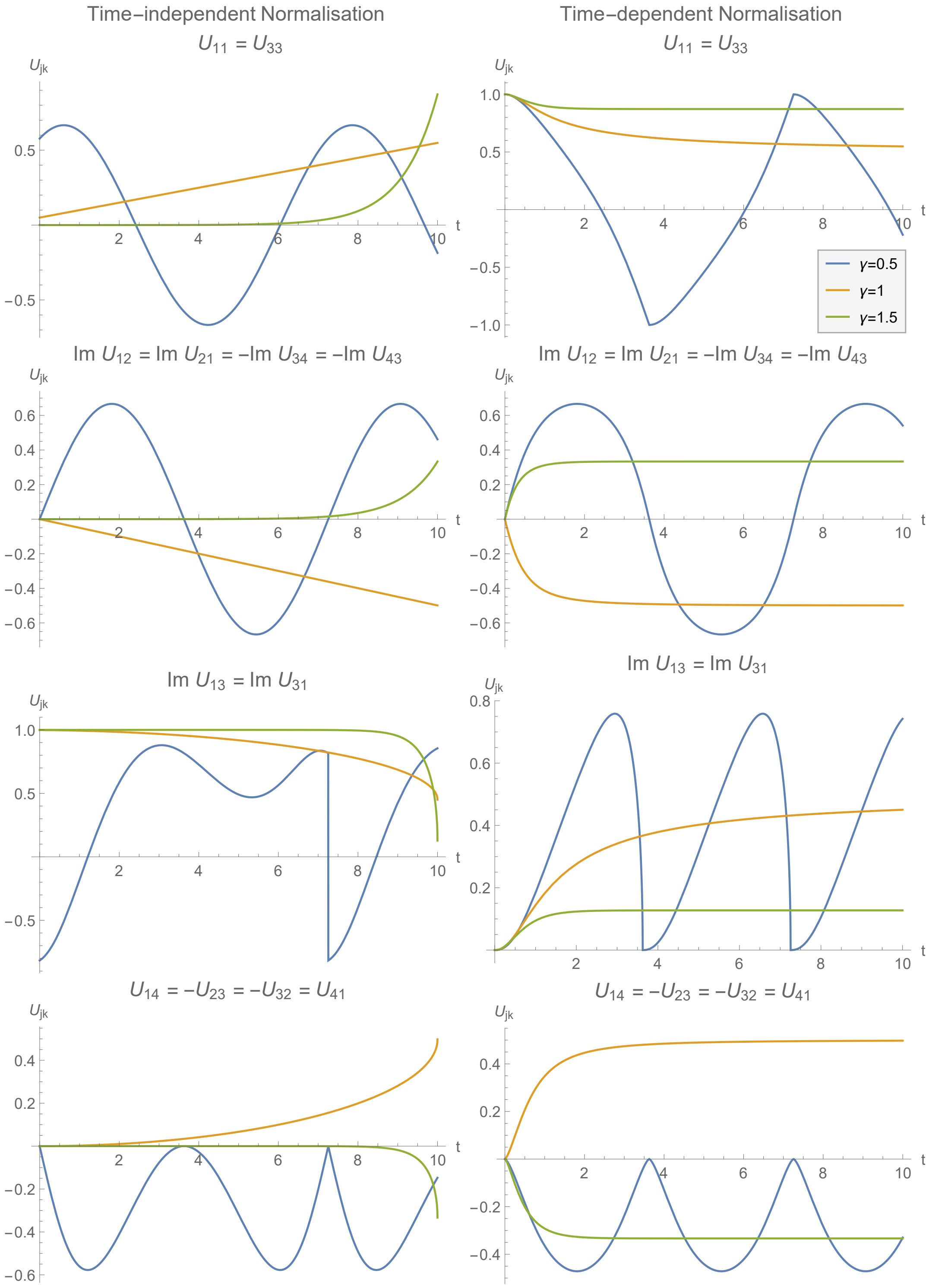

Figure 4.6: Elements of the Dilated Unitary, continued in figure 4.7

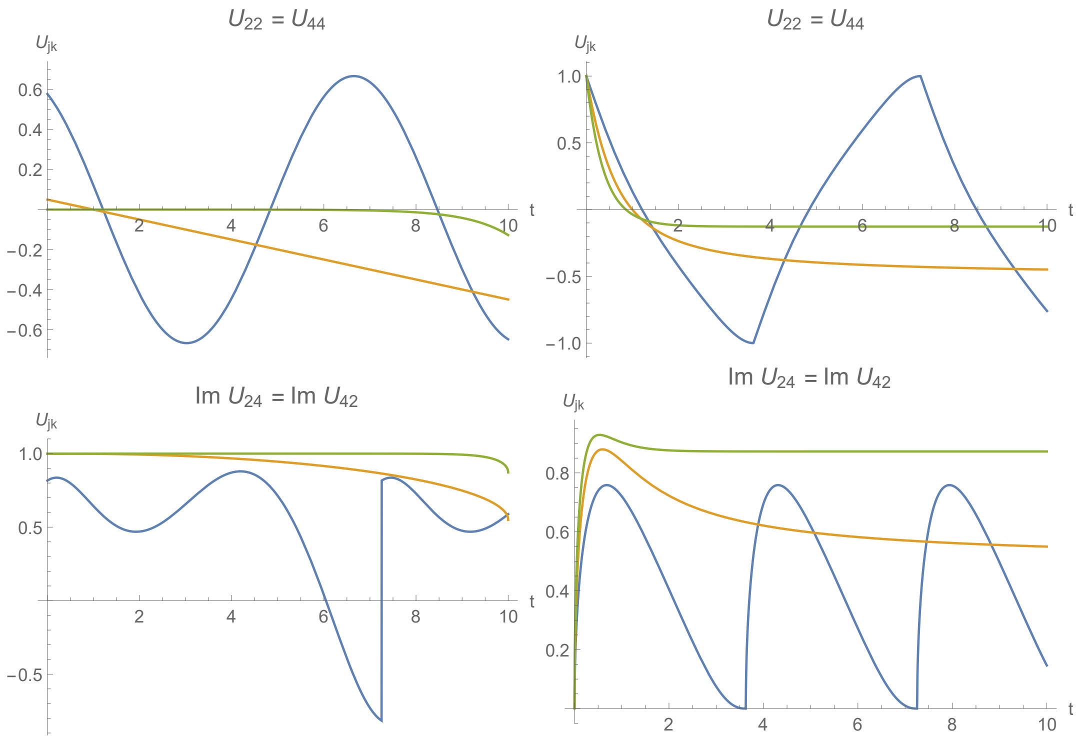

Figure 4.7: Elements of the Dilated unitary, for time-independent normalisation, σ_M (left) and time-dependent normalisation, $\sigma_1(t)$ (right). These different normalisation methods give qualitatively different results, with time-independent normalisation giving smooth values for $\tilde{G}_2$, although discontinuous values for D in the unbroken regime, while time-dependent normalisation gives neither $\tilde{G}_2$ or D as being necessarily smooth, but both being continuous. At the EP and in the broken regime, the time-dependent normalisation method gives evolution towards a stable point, while using the time-independent normalisation method gives typical $\mathcal{PT}$-symmetric behaviour with poynomial growth in $\tilde{G}_2$ at the EP and exponential growth in the broken regime.

which gives the singular values of G_2 as

$$\sigma^2_{1/2}(\gamma = 1) = 1 + 2t^2 \pm 2t\sqrt{1 + t^2}, \tag{4.37}$$

again meaning that a maximum singular value over time cannot be defined, so we again use $\sigma_M = \sigma_1(T)$.

Taking the normalisation to be the maximum singular value over entire simulation time (‘time-independent scaling’, using σ_M for normalisation) gives that the entire transformation matrix M gets scaled by this constant value and so, calculating the full un-normalised transformation from the normalised transformation can be done by multiplying by this scale factor. However, this has the disadvantage that when a different simulation time is used, this scaling factor may need to be recalculated and so, will be different for each simulation.

Instead taking the normalisation to be the time dependent maximum singular value (‘time-dependent scaling’, using $\sigma_1(t)$ for normalisation) has the disadvantage that M is no longer scaled by a constant, rather a time-dependent value, so calculating the un-normalised transformation requires both full knowledge of the time-dependent scaling and additional calculations. The corresponding advantage of this is that because the scaling factor is a time-dependent variable, it does not depend on the total simulation time.

As in figures 4.6 and 4.7, these two simulation methods give qualitatively different results, especially noticeable in the broken $\mathcal{PT}$-symmetric regime and EP. Time-independent scaling gives that the elements of the state or density matrix increase/decrease polynomially (at the EP) or exponentially (in the broken phase) with time, as typical for $\mathcal{PT}$-symmetric systems. However, taking a time-dependent scaling instead gives evolution towards fixed stable points. This contrasts with the unbroken regime, where both methods of normalisation cause the system to oscillate with time, with time-dependent normalisation causing this oscillation to be skewed.

4.3.3 Effective Hamiltonian

For either method of normalisation, we can then define an effective (Hermitian) Hamiltonian H_{eff} by $U = e^{-iH_{\text{eff}}t}$. Differentiating with respect to time and post-multiplying by $U^\dagger$ gives

$$\frac{dU}{dt}U^\dagger = -iH_{\text{eff}}UU^\dagger = -iH_{\text{eff}} \tag{4.38}$$

While this can be numerically approximated, here we analytically calculate the off-diagonal blocks D and D^* for both normalisations of H_2. We can do this by using the property that, for a 2×2 matrix M_2, a square root of M_2 can be calculated using[1]

$$\sqrt{M_2} = \frac{1}{\sqrt{TrM_2 + 2\sqrt{detM_2}}}\left(M_2 + \sqrt{detM_2}I_2\right). \tag{4.39}$$

Starting with time-independent scaling, we can then apply this to the matrix $\sigma_M D_M = \sqrt{\sigma_M^2 I_2 - G_2 G_2^\dagger}$ to get

$$\epsilon_2^2\sigma_M^2 D_M^2 = \begin{pmatrix} \gamma^2 + 2\gamma + \gamma^2\cos 2\epsilon_2 t - \gamma\epsilon_2\sin 2\epsilon_2 t & 2i\gamma\sin^2\epsilon_2 t \\ -2i\gamma\sin^2\epsilon_2 t & \gamma^2 + 2\gamma + \gamma^2\cos 2\epsilon_2 t + \gamma\epsilon_2\sin 2\epsilon_2 t \end{pmatrix} \tag{4.40}$$

$$Tr\left(\sigma_M^2 D_M^2\right) = \frac{2}{\epsilon_2^2}\left(\gamma^2 + 2\gamma + \gamma^2\cos 2\epsilon_2 t\right) \tag{4.41}$$

$$det\left(\sigma_M^2 D_M^2\right) = \left[\frac{2\gamma\cos\epsilon_2 t}{1-\gamma}\right]^2. \tag{4.42}$$

---

[1] This can be shown by using this to calculate $\sqrt{M_2}^2$

Similarly, for the time-dependent scaling, for $\sigma_t D_t = \sqrt{\sigma_t^2 I_2 - G_2 G_2^\dagger}$, we get

$$\begin{align}
\sigma_1^2 D_t^2 &= \frac{1}{\epsilon_2^2} \begin{pmatrix} \frac{\epsilon_2^2}{2} Tr\left(\sigma_1^2 D_t^2\right) - \gamma\epsilon_2 \sin 2\epsilon t & 2i\gamma \sin^2 \epsilon t \\ -2i\gamma \sin^2 \epsilon_2 t & \frac{\epsilon_2^2}{2} Tr\left(\sigma_1^2 D_t^2\right) + \gamma\epsilon_2 \sin 2\epsilon t \end{pmatrix} \tag{4.43} \\
Tr\left(\sigma_1^2 D_t^2\right) &= \frac{2}{\epsilon_2^2} \gamma \sqrt{\left(1 - \cos 2\epsilon_2 t\right)\left(2 - \gamma^2 - \gamma^2 \cos 2\epsilon t\right)} \tag{4.44} \\
det\left(\sigma_1^2 D_t^2\right) &= 0. \tag{4.45}
\end{align}$$

This gives the elements of D, in turn giving the evolution of the state in figures 4.6 and 4.7.

We then use equation 4.38 to numerically calculate the elements of the effective Hamiltonian, shown in figure 4.8. This also shows a qualitative difference between the two normalisation methods, with time-independent normalisation giving discontinuities in the effective Hamiltonian in the unbroken regime, similar to the discontinuities in the dilated unitary. The effective Hamiltonian also shows the difference at the EP and in the broken regime, with the time-dependent normalisation reaching a fixed point and time-independent normalisation showing (normalised) exponential growth in the broken regime.

4.4 Applications of Unitary Dilation

4.4.1 Varying Distinguishability

While this dilated unitary can be used to simulate unitary evolution of coupled $\mathcal{PT}$-symmetric systems, it can also be used to simulate a single $\mathcal{PT}$-symmetric system with non-unitary evolution, using postselection. That is, for a N-mode system dilated into a $2N$-mode unitary, with a photon input into any of the top N modes (or a superposition of the top N modes), postselecting the photon to be output from the top N modes simulates (normalised) evolution of a $\mathcal{PT}$-symmetric system. Using this same process for the bottom N modes would instead simulate a time-reversed $\mathcal{PT}$-symmetric system.

However, with M photons input, while inputting these photons into some combination of the top N modes and postselecting on the same would allow for sampling from the nonunitary transformation $G_N^{\otimes M}$, being able to input photons of varying distinguishability between the top and bottom N modes allows for different transformations to be created, using postselection.

To demonstrate this, we first consider 2 photons input into a $2N$ mode system and use the system-label notation of [54,55]. That is, as well as assigning a 'system' mode number to a creation (annihilation) operator $a_s^\dagger$ (a_s) representing the physical waveguide the operator acts on, we additionally assign a 'label' mode l, here written as $\leftarrow$ or $\rightarrow$ that represents an orthogonal non-spatial mode, such as frequency or temporal delay that determines the distinguishability of the input photons. This gives creation (annihilation) operators $a_{sl}^\dagger$ (a_{sl}). Where the system modes of a state are given by column-elements in a ket, the label modes are instead given by

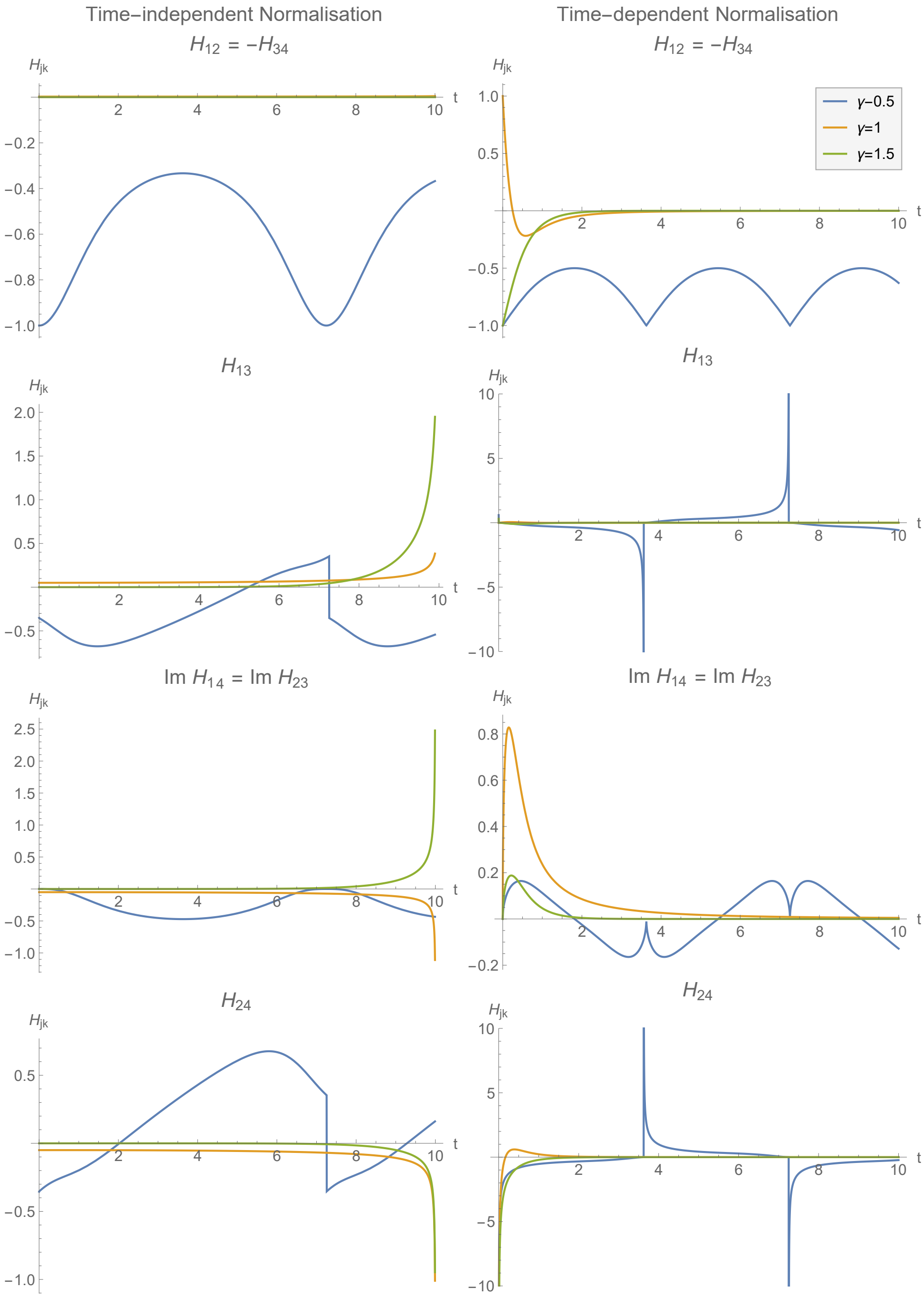

Figure 4.8: Non-zero elements of the effective Hamiltonian of the dilated unitary, defined by equation 4.38. In the unbroken regime, the elements of the effective Hamiltonian are periodic, although discontinuous when time-independent normalisation is used. This discontinuity vanishes at the EP and in the broken regime. In these regimes, the two different normalisation methods again give qualitatively different results, with time-independent normalisation (left) having a spike in the effective Hamiltonian at the end of the simulation time, while time-dependent normalisation (right) has the elements of the effective Hamiltonian starting at a non-zero value and decaying to zero as the transformation reaches a steady state.

row-elements. For a 4-mode system ($N = 2$) with 2 label modes with one photon entering mode 1 and and another entering mode 3, we can write this as a distinguishable/indistinguishable state in the Hilbert space $\mathcal{H} = \mathcal{H}_s \otimes \mathcal{H}_i \otimes \mathcal{H}_s \otimes \mathcal{H}_i$ by, for example,

$$|\psi_d\rangle = a^\dagger_{1\leftarrow} a^\dagger_{3\rightarrow} = \left|\begin{matrix} 1 & 0 \\ 0 & 0 \\ 0 & 1 \\ 0 & 0 \end{matrix}\right\rangle = \text{Sym}\left[|1\leftarrow\rangle\,|3\rightarrow\rangle\right] = \frac{1}{\sqrt{2}}\left[|1\leftarrow\rangle\,|3\rightarrow\rangle + |3\rightarrow\rangle\,|1\leftarrow\rangle\right] \tag{4.46}$$

$$|\psi_i\rangle = a^\dagger_{1\leftarrow} a^\dagger_{3\leftarrow} = \left|\begin{matrix} 1 & 0 \\ 0 & 0 \\ 1 & 0 \\ 0 & 0 \end{matrix}\right\rangle = \text{Sym}\left[|1\leftarrow\rangle\,|3\leftarrow\rangle\right] = \frac{1}{\sqrt{2}}\left[|1\leftarrow\rangle\,|3\leftarrow\rangle + |3\leftarrow\rangle\,|1\leftarrow\rangle\right], \tag{4.47}$$

where the symmetrisation occurs due to boson statistics. Measuring the label mode determines which photon is in which mode in the distinguishable case. Generally, in most optics experiments, such as boson sampling, distinguishability is considered a 'bad' effect, allowing for easier classical simulation [56], however here, we consider it a 'neutral' quantum phenomenon that can potentially even have useful consequences. Transformations, such as the interferometer giving the transformation corresponding to a dilated unitary in the this section, are assumed to act on the system modes without acting on the label modes to give the transformation

$$\mathcal{U} : a^\dagger_{jl} \mapsto \sum_k U_{kj} a^\dagger_{kl}, \tag{4.48}$$

giving the transformation $U \otimes I_2$ on a single photon. For two photons input, the transformation given by $\mathcal{U}$ is then $(U \otimes I_2) \otimes (U \otimes I_2)$. Relabling the modes to the Hilbert space $\mathcal{H}_s \otimes \mathcal{H}_s \otimes \mathcal{H}_i \otimes \mathcal{H}_i$ gives the transformation as $U \otimes U \otimes I_4$, which is then symmetrised. For U_{G_N}, this is

$$U_{G_N} \otimes U_{G_N} = \begin{pmatrix} G_N \otimes G_N & iG_N \otimes D_N & iD_N \otimes G_N & -D_N \otimes D_N \\ iG_N \otimes D_N^* & G_N \otimes G_N^\dagger & -D_N \otimes D_N^* & iD_N \otimes G_N^\dagger \\ iD_N^* \otimes G_N & -D_N^* \otimes D_N & G_N^\dagger \otimes G_N & iG_N^\dagger \otimes D_N \\ -D_N^* \otimes D_N^* & iD_N^* \otimes G_N^\dagger & iG_N^\dagger \otimes D_N^* & G_N^\dagger \otimes G_N^\dagger \end{pmatrix}. \tag{4.49}$$

However, we now impose the 'pre-selection' restriction that one photon is input into the top N modes and one photon is input into the bottom N modes and similarly postselect on one photon being output from the top N modes and one from the bottom N modes. This gives both the input and ouptut states as being within the subspace defined by the states

$$\left\{\text{Sym}\left[|jl\rangle\left|(k+N)\,l'\right\rangle\right] = a^\dagger_{jl} a^\dagger_{(k+N)l'}\,|0_p\rangle^{\otimes 2N}\right\}_{j,k=1;l,l'\in\{\leftarrow,\rightarrow\}}^{j,k=N}. \tag{4.50}$$

Within this pre- and post- selected subspace, the unitary transformation can be written as

$$U_{G_N} \otimes U_{G_N} = \begin{pmatrix} * & * & * & * \\ * & G_N \otimes G_N^\dagger & -D_N \otimes D_N^* & * \\ * & -D_N^* \otimes D_N & G_N^\dagger \otimes G_N & * \\ * & * & * & * \end{pmatrix}, \tag{4.51}$$

where $*$ represents elements outside the subspace of input and measured outcomes.

Inputting a state $\mathrm{Sym}\left[\left|jl\right\rangle\left|(k+N)\,l'\right\rangle\right] = \left(\left|jl\right\rangle\left|(k+N)\,l'\right\rangle + \left|(k+N)\,l'\right\rangle\left|jl\right\rangle\right)/\sqrt{2}$ means we can write the output state as

$$U\otimes U\left|\psi\right\rangle = \frac{1}{\sqrt{2}}\begin{pmatrix} * \\ G_N\otimes G_N^{\dagger}\left|jl\right\rangle\left|(k+N)\,l'\right\rangle - D_N\otimes D_N^{*}\left|(k+N)\,l'\right\rangle\left|jl\right\rangle \\ -D_N^{*}\otimes D_N\left|jl\right\rangle\left|(k+N)\,l'\right\rangle + G_N^{\dagger}\otimes G_N\left|(k+N)\,l'\right\rangle\left|jl\right\rangle \\ * \end{pmatrix} \tag{4.52}$$

$$= \mathrm{Sym}\left[G_N\otimes G_N^{\dagger}\left|jl\right\rangle\left|(k+N)\,l'\right\rangle - D_N\otimes D_N^{*}\left|(k+N)\,l'\right\rangle\left|jl\right\rangle\right]. \tag{4.53}$$

We can then project/postselect onto the same system subspace and label state as was input. This can be done using the symmetrised form of the projector

$$\mathbb{P}_{\uparrow,l,\downarrow,l'} = \mathrm{Sym}\left[(I_N\oplus 0_N)\otimes\left|l\right\rangle\!\left\langle l\right|\otimes(0_N\oplus I_N)\otimes\left|l'\right\rangle\!\left\langle l'\right|\right], \tag{4.54}$$

which postselects on the photon in label mode l being in the top subspace and the photon in label mode l' being in the bottom subspace. Represented in figure 4.9, this gives, for distinguishable states ($l\neq l'$),

$$\mathbb{P}_{\uparrow,l,\downarrow,l'}U\otimes U\left|\psi_d\right\rangle = \mathrm{Sym}\left[G_N\otimes G_N^{\dagger}\left|jl\right\rangle\left|(k+N)\,l'\right\rangle\right] \tag{4.55}$$

and for indistinguishable states ($l = l'$),

$$\mathbb{P}_{\uparrow,l,\downarrow,l}U\otimes U\left|\psi_i\right\rangle = \mathrm{Sym}\left[G_N\otimes G_N^{\dagger}\left|jl\right\rangle\left|(k+N)\,l\right\rangle - D_N\otimes D_N^{*}\left|(k+N)\,l\right\rangle\left|jl\right\rangle\right]. \tag{4.56}$$

This form of postselection therefore allows for using distinguishable states to simulate uncoupled $\mathcal{PT}$-symmetric systems, with one of these systems being the time reverse of the other, while if the input state were instead indistinguishable, the overall combined system would instead be coupled. We can however, make the system partially indistinguishable, such as by time-delaying one of the input photons with a small enough delay that the two photon wavepackets have a nonzero temporal overlap. We can write this as a superposition of distinguishable and indistinguishable states,

$$\left|\psi_{\mathrm{in}}\right\rangle = \alpha\left|\psi_i'\right\rangle + \beta\left|\psi_d'\right\rangle = \mathrm{Sym}\left[\sum_{jk} a_{jk}\left(\alpha\left|j\leftarrow\right\rangle\left|(k+N)\leftarrow\right\rangle + \beta\left|j\leftarrow\right\rangle\left|(k+N)\rightarrow\right\rangle\right)\right], \tag{4.57}$$

which, after the transformation given by the dilated unitary, becomes

$$\begin{aligned} U\otimes U\left|\psi\right\rangle =& \mathrm{Sym}\left[\sum_{jk} a_{jk}G_N\otimes G_N^{\dagger}\left(\alpha\left|j\leftarrow\right\rangle\left|(k+N)\leftarrow\right\rangle + \beta\left|j\leftarrow\right\rangle\left|(k+N)\rightarrow\right\rangle\right)\right] \\ &- \mathrm{Sym}\left[\sum_{jk} a_{jk}D_N\otimes D_N^{*}\left(\alpha\left|j\leftarrow\right\rangle\left|(k+N)\leftarrow\right\rangle + \beta\left|j\leftarrow\right\rangle\left|(k+N)\rightarrow\right\rangle\right)\right]. \end{aligned} \tag{4.58}$$

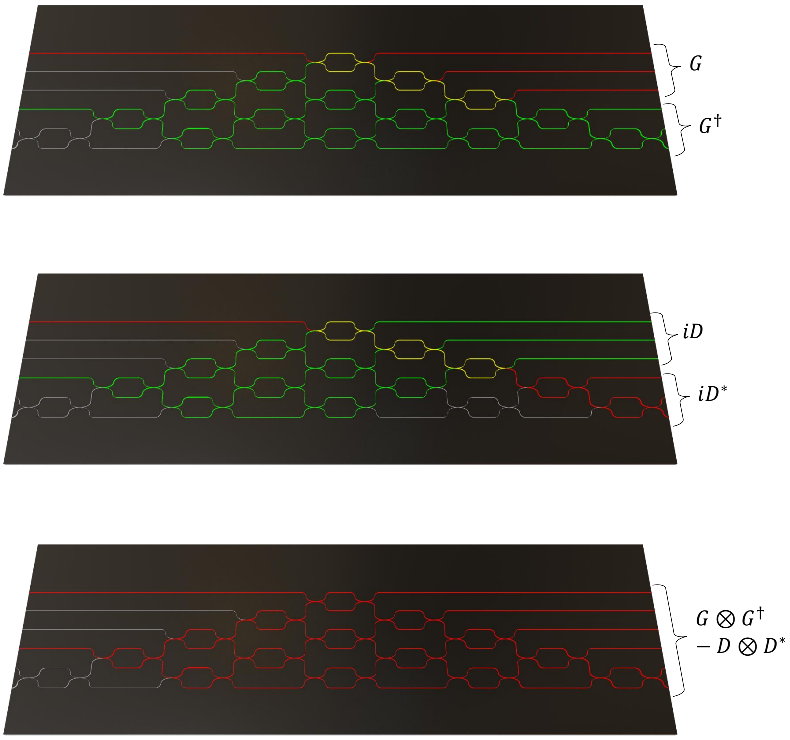

Figure 4.9: Inputting a single photon into the top N modes (here, $N = 3$) and another indistinguishable photon (using a different 'label' mode, represented here by a different colour/frequency) into the bottom N modes and postselecting on one photon out the top N modes and the other out the bottom N modes gives that we can additionally postselect on which label comes out of the top/bottom modes. This is represented by the top diagram, where the output top/bottom label mode is the same as the input top/bottom label mode, giving the transformation $G\otimes G^\dagger$, as well as the middle diagram where the output top/bottom label mode is instead the input bottom/top label mode, which instead gives the transformation $-D\otimes D^*$. By contrast, inputting indistinguishable photons, represented by the bottom diagram, gives that the cases represented by the top and middle diagrams are indistinguishable, so both of these events cannot be distinguished between and the overall transformation is instead $G\otimes G^\dagger - D\otimes D^*$.

We now project using the symmetrised form of the projection operator

$$\mathbb{P}_{\uparrow,l,\downarrow} = \mathrm{Sym}\left[(I_N\oplus 0_N)\otimes |l\rangle\langle l|\otimes(0_N\oplus I_N)\otimes I_2\right], \tag{4.59}$$

similar to equation 4.54, except without projecting onto the second label mode. When the label modes are the same (the photons are indistinguishable), the state is already in the subspace spanned by the projection operator. When the label modes are different (the photons are distinguishable), projecting one photon into one label mode automatically enforces that the other photon is in the other label mode. This gives the output state

$$\begin{aligned}
|\psi_{\text{out}}\rangle &= \mathbb{P}_{\uparrow,l,\downarrow} U \otimes U\,|\psi\rangle && (4.60)\\
&= \alpha\,\mathrm{Sym}\left[\left(G_N \otimes G_N^{\dagger} - D_N \otimes D_N^{*}\right)\sum_{jk} a_{jk}\,|j \leftarrow\rangle\,|(k+N)\leftarrow\rangle\right] && (4.61)\\
&\quad + \beta\,\mathrm{Sym}\left[G_N \otimes G_N^{\dagger}\sum_{jk} a_{jk}\,|j \leftarrow\rangle\,|(k+N)\rightarrow\rangle\right] && (4.62)\\
&= G_N \otimes G_N^{\dagger}\,|\psi_{\text{in}}\rangle - \alpha\,D_N \otimes D_N^{*}\,|\psi_i'\rangle\,. && (4.63)
\end{aligned}$$

That is, within this postselected space, the transformation is that of two coupled $\mathcal{PT}$-symmetric systems, one the time-reverse of the other, with a tunable coupling given by the strength of the indistinguishability of the input photons. This is shown in figure 4.10 for H_2.

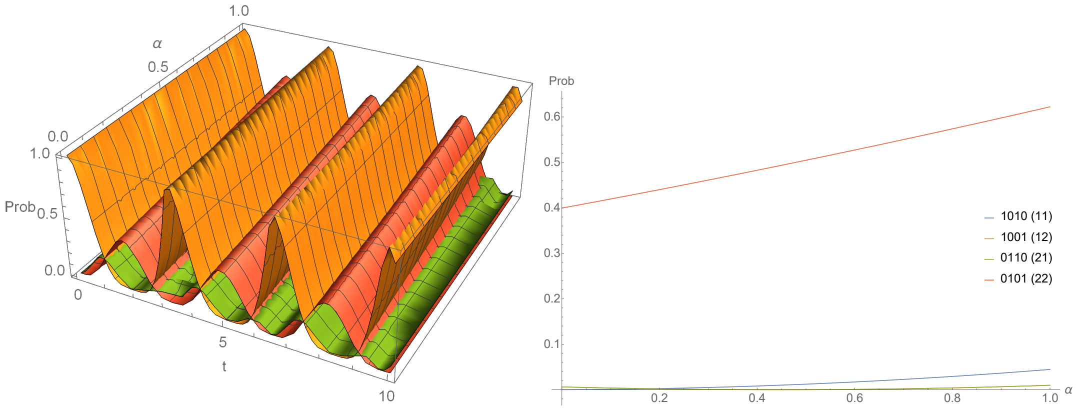

Figure 4.10: Evolution of a partially distinguishable 2-photon state given by equation 4.63 with $\gamma = 0.25$ with (left) both time and distinguishability parameter α and (right) cross-section of the same evolution at $t = 5$. Graphs show that varying the input distinguishability can have a large effect on the output photon statistics due to how the parameter α changes the strength of the off-diagonal blocks that cause the interaction between forward and reverse systems.

This could be considered as a $\mathcal{PT}$-symmetric extension of the HOM effect [24], which involves a single mode system with $G = \cos\theta$. As such, this could be further extended to higher numbers of photons, such as in [57, 58].

4.4.2 Particle Physics simulations

There are two main applications of using unitary dilation in particle physics. One of these applications is to explore exotic non-Hermitian particles and theories, such as the 8- and 12-mode $\mathcal{PT}$-symmetric Dirac equations in [59]. Another is to look at the evolution of decaying particles, which, while not necessarily $\mathcal{PT}$-symmetric, could be non-Hermitian, similar to the Lindblad evolution of section 4.2. This can be done by defining a Hamiltonian $H = M - i\Gamma$, where both M (mass matrix) and Γ (loss matrix) are Hermitian, causing the overal Hamiltonian to be non-Hermitian [60].

Here, we consider neutral B mesons, B^0 and $\bar{B}^0$, comprising of down and bottom (anti-)quarks, $B^0 = d\bar{b}$ and $\bar{B}^0 = \bar{d}b$. For the purposes of showing that basic models of non-Hermitian particle physics can be simulated with current systems, similar to [61], we take a simplistic approach and ignore strong force interactions. This allows us to write a single quark q in the computational basis as

$$\mathcal{Q} = \begin{pmatrix} Q \\ \bar{Q}^\dagger \end{pmatrix} = \begin{pmatrix} q\uparrow \\ q\downarrow \\ \bar{q}^\dagger\uparrow \\ \bar{q}^\dagger\downarrow \end{pmatrix} = \begin{pmatrix} 00 \\ 01 \\ 10 \\ 11 \end{pmatrix}, \tag{4.64}$$

where q ($\bar{q}$) is the quark (antiquark) state and ↑ (↓) is the up (down) spin state. This naturally extends to the basis states for particles consisting of pairs of quarks, such as B mesons. For such particles, consisting of down (d) and bottom (b) quarks, we can write these basis states as

$$\begin{pmatrix} 000 \\ 001 \\ 010 \\ 011 \\ 100 \\ 101 \\ 110 \\ 111 \end{pmatrix} = \begin{pmatrix} d\uparrow \\ d\downarrow \\ b\uparrow \\ b\downarrow \\ \bar{d}^\dagger\uparrow \\ \bar{d}^\dagger\downarrow \\ \bar{b}^\dagger\uparrow \\ \bar{b}^\dagger\downarrow \end{pmatrix} = \begin{pmatrix} D \\ B \\ \bar{D}^\dagger \\ \bar{B}^\dagger \end{pmatrix}. \tag{4.65}$$

In the regime of Hermitian physics, this could be considered to be two quarks evolving under 2 separate Dirac equations, which are then coupled together by various interactions. That is, for

$$\gamma^0 = \begin{pmatrix} 0 & I \\ I & 0 \end{pmatrix}, \quad \gamma^j = \begin{pmatrix} 0 & \sigma^j \\ -\sigma^j & 0 \end{pmatrix}, \tag{4.66}$$

where $j \in \{1, 2, 3\}$ and σ^j are the Pauli matrices, the Dirac equation is [36]

$$\left(-i\gamma^\mu \partial_\mu + m\right)\Psi = 0, \tag{4.67}$$

where Ψ is a Dirac field, $\mathcal{B}$ or $\mathcal{D}$. While a $\mathcal{PT}$-symmetric version of the 4-mode Dirac equation is the same as the Hermitian version, the 8-mode $\mathcal{PT}$-symmetric Dirac equation, unlike the Hermitian version, does not uncouple into separate Dirac equations. We can write this $\mathcal{PT}$-symmetric 'model-8' Dirac equation in Hamiltonian form as [59]

$$\begin{pmatrix} p_j\sigma^j & 0 & (m_0+m_3)I & (m_1-im_2)I \\ 0 & p_j\sigma^j & (m_1+im_2)I & (m_0-m_3)I \\ (m_0+m_3)I & (m_1+im_2)I & -p_j\sigma^j & 0 \\ (m_1-im_2)I & (m_0-m_3)I & 0 & -p_j\sigma^j \end{pmatrix}\psi = E\psi = H\psi. \tag{4.68}$$

This describes a $\mathcal{PT}$-symmetric particle of mass $m_{\text{eff}}^2 = m_0^2 - m_2^2$. This could be combined as in section 4.4.1, such as by simulating the evolution of the state Sym $\left[D \otimes \bar{B} + B \otimes \bar{D}\right]$, which would describe a simplified $\mathcal{PT}$-symmetric variation of $B - \bar{B}$ oscillations.

4.5 Discussion and Conclusion

In this chapter, we have shown that there are different ways of embedding a non-Hermitian or non-unitary system into a larger system. We have shown this by considering an open system, which can be Markovian, allowing for passive $\mathcal{PT}$-symmetry, or non-Markovian, which allows for a form of active $\mathcal{PT}$-symmetric systems. However, using open systems to simulate $\mathcal{PT}$-symmetric systems causes additional loss that causes the elements of the density matrix of the system to decay with an exponential envelope, although this could potentially be avoided by using Floquet dynamics.

An alternative way of embedding a non-Hermitian (here, $\mathcal{PT}$-symmetric) system into a unitary is to use unitary dilation, which could be considered as taking two non-Hermitian systems and coupling them with a time-dependent, potentially discontinuous coupling. In order to do this, the system has to be normalised by its maximum singular value, which allows for two different normalisation methods. The first is a time-independent normalisation, which retains all the features of a $\mathcal{PT}$-symmetric system, at the cost of discontinuities in both the dilated unitary and effective Hamiltonian that descibes the dilated unitary. The alternative is a time-independent normalisation which instead skews the typical unbroken $\mathcal{PT}$-symmetry behaviour, turning the oscilations of the $\mathcal{PT}$-symmetric systems into more of a ‘sawtooth’ wave. At the EP and in the broken regime, it instead causes the system to converge towards a fixed stationary point. However, for the system simulated here, no discontinuities were created in the dilated unitary.

By considering inputting two photons into the interferometer giving the unitary transformation, unitary dilation can also be considered as an extension of the HOM effect, where inputting photons of varying distinguishability and postselecting on the outcome allows for this variability in the distinguishability to translate to variability in coupling strength. This can lead to other applications, such as simulating composite particles. This method could be further extended to larger system sizes and more photons.

Chapter 5

Design of a Nonunitary Interferometer

Section 5.1 is an introductory/background section and contains a summary of this chapter. This chapter is based on [62] and is my own work.

5.1 Introduction

One of the defining features of simulation method used in the previous chapter is that the transformation created by the $\mathcal{PT}$-symmetric Hamiltonian needs to be normalised. It is generally true with other current methods of simulating $\mathcal{PT}$-symmetric systems that some form of normalisation needs to be used such as removing gain terms, using a metric operator or re-scaling the transformation matrix. This is fundamentally due to the transformation arising from a non-Hermitian Hamiltonian being non-unitary. As a result, while the eigenvalues of the system may be real, the norm is not necessarily constant, which is necessary for a quantum system to conserve probability or particle number in a closed system.

However, particle number is not always a conserved quantity in quantum systems. In particular, in a given frequency mode, nonlinear optical transformations can create photons from a vaccuum state, which suggests that nonlinear optics could be a potential method of simulating $\mathcal{PT}$-symmetric Hamiltonians. In this chapter, this is done by considering the transformations on the mode operator space of a nonlinear optical system in section 5.2, which describes an 'effective Hamiltonian' of this space. In section 5.3, these transformations are then shown to be exactly $\mathcal{PT}$-symmetric transformations with a determinant of 1, making the set of allowed effective Hamiltonians a subset of possible $\mathcal{PT}$-antisymmetric Hamiltonians. From this, the idea of a linear optical interferometer implementing a unitary transformation is extended to a nonunitary optical interferometer implementing a nonunitary transformation in section 5.4. It is further shown in section 5.5 that this can be Trotterised similar to the Trotterisation process in (Hermitian) Hamiltonian simulation.

A 2D $\mathcal{PT}$-symmetric lattice is considered in section 5.6 and its ground state is numerically calculated using a standard tensor network, for an infinite lattice. This shows the different phases of the system, which is then used in section 5.7 to emulate the nonunitary interferometer simulating a small lattice of this system accross the different feromagnetic and paramagnetic phases in the $\mathcal{PT}$-broken and -unbroken phases.

This shows that nonlinear optical transformations can be considered as a subset of $\mathcal{PT}$-symmetric transformations and as such, nonlinear optics can be used as a method to simulate nonunitary transformations similar to how linear optics can be used to simulate unitary transformations.

5.2 Effective Hamiltonians

While (unitary) transformations in quantum physics are typically considered to arise from the exponential of some Hamiltonian, section 4.3 shows that this is not necessarily always the simplest method of creating unitary transformations. However, section 4.3.3 shows that even when this happens, an effective Hamiltonian (which may be time-dependent) that generates the unitary evolution can still be defined. Here, this concept is extended to consider an 'effective Hamiltonian' as the matrix generating the symplectic transformation of operators of (optical) modes of a system, or more generally, the transformation of any operator in the Heisenberg picture.

That is, measuring some operator O on the Hilbert space $\mathcal{H}$ of a system being acted on by a (for the purposes of simplicity) time independent Hamiltonian H, this can alternatively be described using the Heisenberg picture by considering the Heisenberg evolution of operator

$$O\left(t\right)=U^{\dagger}\left(t\right)OU\left(t\right)=e^{iHt}Oe^{-iHt}=e^{-iAd_{H}t}O=M_{U}O. \tag{5.1}$$

As discussed in chapter 3, this arises from the existence of what could be considered as an effective Hamiltonian acting on the operator space of the system $\mathcal{S}\subset\mathcal{B}\left(\mathcal{H}\right)$,

$$H_{\text{eff}}=Ad_{H}=\left[H,\cdot\right], \tag{5.2}$$

which further allows for defining $M_U=e^{-iH_{\text{eff}}t}$, or equivalently, defining $-iH_{\text{eff}}t$ as the matrix logarithm of M_U if and only if M_U is invertible. As we can simply apply the inverse of the original applied Hamiltonian, $-H$, to obtain the transformation M_U^{-1}, this inverse must exist. To give explicit examples of this, we consider the optical transformations of: a phase shift; beamsplitter; single mode squeezing; and two-mode squeezing. These are described by their respective Hamiltonians

$$\begin{aligned}
H_{\text{phase};j}&=\phi_{j}a_{j}^{\dagger}a_{j} && (5.3)\\
H_{\text{BS};jk}&=i\theta a_{j}^{\dagger}a_{k}-i\theta^{*}a_{k}^{\dagger}a_{j} && (5.4)\\
H_{S;j}&=\frac{1}{2}i\left(z^{*}a_{j}a_{j}-za_{j}^{\dagger}a_{j}^{\dagger}\right) && (5.5)\\
H_{S;jk}&=i\zeta^{*}a_{j}a_{k}-i\zeta a_{j}^{\dagger}a_{k}^{\dagger}, && (5.6)
\end{aligned}$$

where the subscripts j and k refer to the modes the operation is being performed on. Calculating the effective Hamiltonians acting on $a_j^\dagger, a_k^\dagger, a_j$ and a_k, written as elements of a vector, this allows the effective Hamiltonians acting on these operators to be written in matrix form as

$$H_{\text{eff, phase};j}\begin{pmatrix}a_j^\dagger\\ a_j\end{pmatrix}=\begin{pmatrix}\phi_j & 0\\ 0 & -\phi_j\end{pmatrix}\begin{pmatrix}a_j^\dagger\\ a_j\end{pmatrix} \tag{5.7}$$

$$H_{\text{eff, BS};jk}\begin{pmatrix}a_j^\dagger\\ a_k^\dagger\\ a_j\\ a_k\end{pmatrix}=i\begin{pmatrix}0 & \theta & 0 & 0\\ -\theta^* & 0 & 0 & 0\\ 0 & 0 & 0 & \theta^*\\ 0 & 0 & -\theta & 0\end{pmatrix}\begin{pmatrix}a_j^\dagger\\ a_k^\dagger\\ a_j\\ a_k\end{pmatrix} \tag{5.8}$$

$$H_{\text{eff, S};j}\begin{pmatrix}a_j^\dagger\\ a_j\end{pmatrix}=i\begin{pmatrix}0 & z^*\\ z & 0\end{pmatrix}\begin{pmatrix}a_j^\dagger\\ a_j\end{pmatrix} \tag{5.9}$$

$$H_{\text{eff, S};jk}\begin{pmatrix}a_j^\dagger\\ a_k^\dagger\\ a_j\\ a_k\end{pmatrix}=i\begin{pmatrix}0 & 0 & 0 & \zeta^*\\ 0 & 0 & \zeta^* & 0\\ 0 & \zeta & 0 & 0\\ \zeta & 0 & 0 & 0\end{pmatrix}\begin{pmatrix}a_j^\dagger\\ a_k^\dagger\\ a_j\\ a_k\end{pmatrix}. \tag{5.10}$$

However, there is a difference in taking the expectation value of (or equivalently, measuring) an operator O when using this as an 'effective Hamiltonian' on the operator space and using the actual Hamiltonian that acts on the Hilbert space. As an example, for the start state $|\psi\rangle$ and projection operator $P = |\phi\rangle\langle\phi|$, the system is measured to be in state $|\phi\rangle$ with probability $|\langle\phi|U|\psi\rangle|^2 = \langle\psi|M_U|\phi\rangle\langle\phi|\psi\rangle$. As this is conceptually different to how measurements and expectation values are typically considered, H_{eff} is not a 'true' effective Hamiltonian, although this terminology will be useful later in sections 5.3 (which shows that the properties of H_{eff} are still relevant) and 5.4 (which addresses this issue at a more fundamental level).

5.3 Symplectic Transformations as PT-symmetric Transformations

As shown by equations 5.9 and 5.10, for nonlinear transformations (such as squeezing), the effective Hamiltonian is not Hermitian. The specific example of combining a beamsplitter with squeezing of one direction in one mode and the opposite direction in the second mode can be shown to be $\mathcal{PT}$-anti-symmetric (arbitrarily taking θ and z to be real):

$$
\begin{aligned}
H &= H_{BS;12} + H_{S;1} + H_{-S;2} && (5.11)\\
&= i\theta a_1^\dagger a_2 - i\theta a_2^\dagger a_1 + \frac{1}{2} i \left(z a_1 a_1 - z a_1^\dagger a_1^\dagger \right) - \frac{1}{2} i \left(z a_2 a_2 - z a_2^\dagger a_2^\dagger \right) && (5.12)
\end{aligned}
$$

$$
\implies H_{\text{eff};12} \begin{pmatrix} a_j^\dagger \\ a_k^\dagger \\ a_j \\ a_k \end{pmatrix} = i \begin{pmatrix} 0 & \theta & z & 0 \\ -\theta & 0 & 0 & -z \\ z & 0 & 0 & \theta \\ 0 & -z & -\theta & 0 \end{pmatrix} \begin{pmatrix} a_j^\dagger \\ a_k^\dagger \\ a_j \\ a_k \end{pmatrix}. \tag{5.13}
$$

The eigenvalues of H_{eff} are then

$$
\lambda_\pm = \pm i \sqrt{z^2 - \theta^2}, \tag{5.14}
$$

which has the usual typical features of eigenvalues of a $\mathcal{PT}$-symmetric system. Shown by calculating the eigenvectors, this has the unusual property that the system contains a degenerate EP2 at $z^2 = \theta^2$:

$$
v_{1,\pm} = \frac{1}{z} \begin{pmatrix} -\theta \\ \pm\sqrt{z^2 - \theta^2} \\ 0 \\ z \end{pmatrix}, \qquad v_{2,\pm} = \frac{1}{z} \begin{pmatrix} \mp\sqrt{z^2 - \theta^2} \\ -\theta \\ z \\ 0 \end{pmatrix}. \tag{5.15}
$$

Calculating $M_U = e^{-iH_{\text{eff}}}$ further gives

$$
\begin{aligned}
M_U &= \begin{pmatrix} \cosh\sqrt{z^2-\theta^2} & \theta\frac{\sinh\sqrt{z^2-\theta^2}}{\sqrt{z^2-\theta^2}} & z\frac{\sinh\sqrt{z^2-\theta^2}}{\sqrt{z^2-\theta^2}} & 0 \\ -\theta\frac{\sinh\sqrt{z^2-\theta^2}}{\sqrt{z^2-\theta^2}} & \cosh\sqrt{z^2-\theta^2} & 0 & -z\frac{\sinh\sqrt{z^2-\theta^2}}{\sqrt{z^2-\theta^2}} \\ z\frac{\sinh\sqrt{z^2-\theta^2}}{\sqrt{z^2-\theta^2}} & 0 & \cosh\sqrt{z^2-\theta^2} & \theta\frac{\sinh\sqrt{z^2-\theta^2}}{\sqrt{z^2-\theta^2}} \\ 0 & -z\frac{\sinh\sqrt{z^2-\theta^2}}{\sqrt{z^2-\theta^2}} & -\theta\frac{\sinh\sqrt{z^2-\theta^2}}{\sqrt{z^2-\theta^2}} & \cosh\sqrt{z^2-\theta^2} \end{pmatrix} && (5.16)\\
&= I_4 \cosh\sqrt{z^2-\theta^2} + I_2 \otimes iY \frac{\theta \sinh\sqrt{z^2-\theta^2}}{\sqrt{z^2-\theta^2}} + X \otimes Z \frac{z \sinh\sqrt{z^2-\theta^2}}{\sqrt{z^2-\theta^2}}, && (5.17)
\end{aligned}
$$

which at the EP, simplifies to

$$
M_U = \begin{pmatrix} 1 & \theta & \theta & 0 \\ -\theta & 1 & 0 & -\theta \\ \theta & 0 & 1 & \theta \\ 0 & -\theta & -\theta & 1 \end{pmatrix} = I_4 - iH_{\text{eff}}. \tag{5.18}
$$

This indicates a qualitative difference between the 3 regimes, depending on whether $|z| < |\theta|$, $|z| > |\theta|$ or $|z| = |\theta|$. When $|z| < |\theta|$, the eigenvalues of the system are real and the system acts most like a squeezed beamsplitter, having oscillations of a nonzero photon number. In contrast, when $|z| > |\theta|$, the eigenvalues are imaginary and the system acts purely like a squeezer. However, at the EP $|z| = |\theta|$, the behaviour of the system is linear with $z = \pm\theta$, which is a transformation not typically considered in optics. Calculating the mean and variance of the number and quadrature operators gives

$$\begin{aligned}\langle 0| M_U a_1^\dagger M_U a_1 |0\rangle &= \langle 0| \left[\cosh\sqrt{z^2-\theta^2}a_1^\dagger - \theta\frac{\sinh\sqrt{z^2-\theta^2}}{\sqrt{z^2-\theta^2}}a_2^\dagger + z\frac{\sinh\sqrt{z^2-\theta^2}}{\sqrt{z^2-\theta^2}}a_1\right]\cdot \\ &\quad \left[z\frac{\sinh\sqrt{z^2-\theta^2}}{\sqrt{z^2-\theta^2}}a_1^\dagger + \cosh\sqrt{z^2-\theta^2}a_1 - \theta\frac{\sinh\sqrt{z^2-\theta^2}}{\sqrt{z^2-\theta^2}}a_2\right]|0\rangle \quad (5.19)\\ &= z^2\frac{\sinh^2\sqrt{z^2-\theta^2}}{z^2-\theta^2} \quad (5.20)\\ \langle 0| M_U a_2^\dagger M_U a_2 |0\rangle &= \langle 0| \left[\cosh\sqrt{z^2-\theta^2}a_2^\dagger + \theta\frac{\sinh\sqrt{z^2-\theta^2}}{\sqrt{z^2-\theta^2}}a_1^\dagger - z\frac{\sinh\sqrt{z^2-\theta^2}}{\sqrt{z^2-\theta^2}}a_2\right]\cdot \\ &\quad \left[-z\frac{\sinh\sqrt{z^2-\theta^2}}{\sqrt{z^2-\theta^2}}a_2^\dagger + \cosh\sqrt{z^2-\theta^2}a_2 + \theta\frac{\sinh\sqrt{z^2-\theta^2}}{\sqrt{z^2-\theta^2}}a_1\right]|0\rangle \\ &\quad (5.21)\\ &= z^2\frac{\sinh^2\sqrt{z^2-\theta^2}}{z^2-\theta^2} \quad (5.22)\end{aligned}$$

for the number operator expectations $\langle N_1\rangle$ and $\langle N_2\rangle$,

$$(\Delta N_1)^2 = (\Delta N_2)^2 = z^2\frac{\sinh^2\sqrt{z^2-\theta^2}}{z^2-\theta^2}\left[\theta^2\frac{\sinh^2\sqrt{z^2-\theta^2}}{z^2-\theta^2} + 2\cosh^2\sqrt{z^2-\theta^2}\right] \quad (5.23)$$

for their variances,

$$\langle x_1\rangle = \langle x_2\rangle = \langle p_1\rangle = \langle p_2\rangle = 0 \quad (5.24)$$

for the quadrature operator expectations and

$$\begin{aligned}(\Delta x_1)^2 &= z\frac{\sinh\sqrt{z^2-\theta^2}\cosh\sqrt{z^2-\theta^2}}{\sqrt{z^2-\theta^2}} + \left(z^2+\theta^2\right)\frac{\sinh^2\sqrt{z^2-\theta^2}}{2\left(z^2-\theta^2\right)} + \frac{1}{2}\cosh^2\sqrt{z^2-\theta^2} \\ &\quad (5.25)\\ (\Delta x_2)^2 &= -z\frac{\sinh\sqrt{z^2-\theta^2}\cosh\sqrt{z^2-\theta^2}}{\sqrt{z^2-\theta^2}} + \left(z^2+\theta^2\right)\frac{\sinh^2\sqrt{z^2-\theta^2}}{2\left(z^2-\theta^2\right)} + \frac{1}{2}\cosh^2\sqrt{z^2-\theta^2}, \\ &\quad (5.26)\end{aligned}$$

where $(\Delta x_1)^2 = (\Delta p_2)^2$ and $(\Delta x_2)^2 = (\Delta p_1)^2$. At the EP, this becomes

$$\begin{aligned}\langle N_1\rangle = \langle N_2\rangle &= z^2 \quad (5.27)\\ (\Delta N_1)^2 = (\Delta N_2)^2 &= 2z^2 + z^4 \quad (5.28)\\ (\Delta x_1)^2 = (\Delta p_2)^2 &= \frac{1}{2} + z + z^2 \quad (5.29)\\ (\Delta x_2)^2 = (\Delta p_1)^2 &= \frac{1}{2} - z + z^2. \quad (5.30)\end{aligned}$$

Overall, this shows the qualitatively different behaviour in the different regimes.

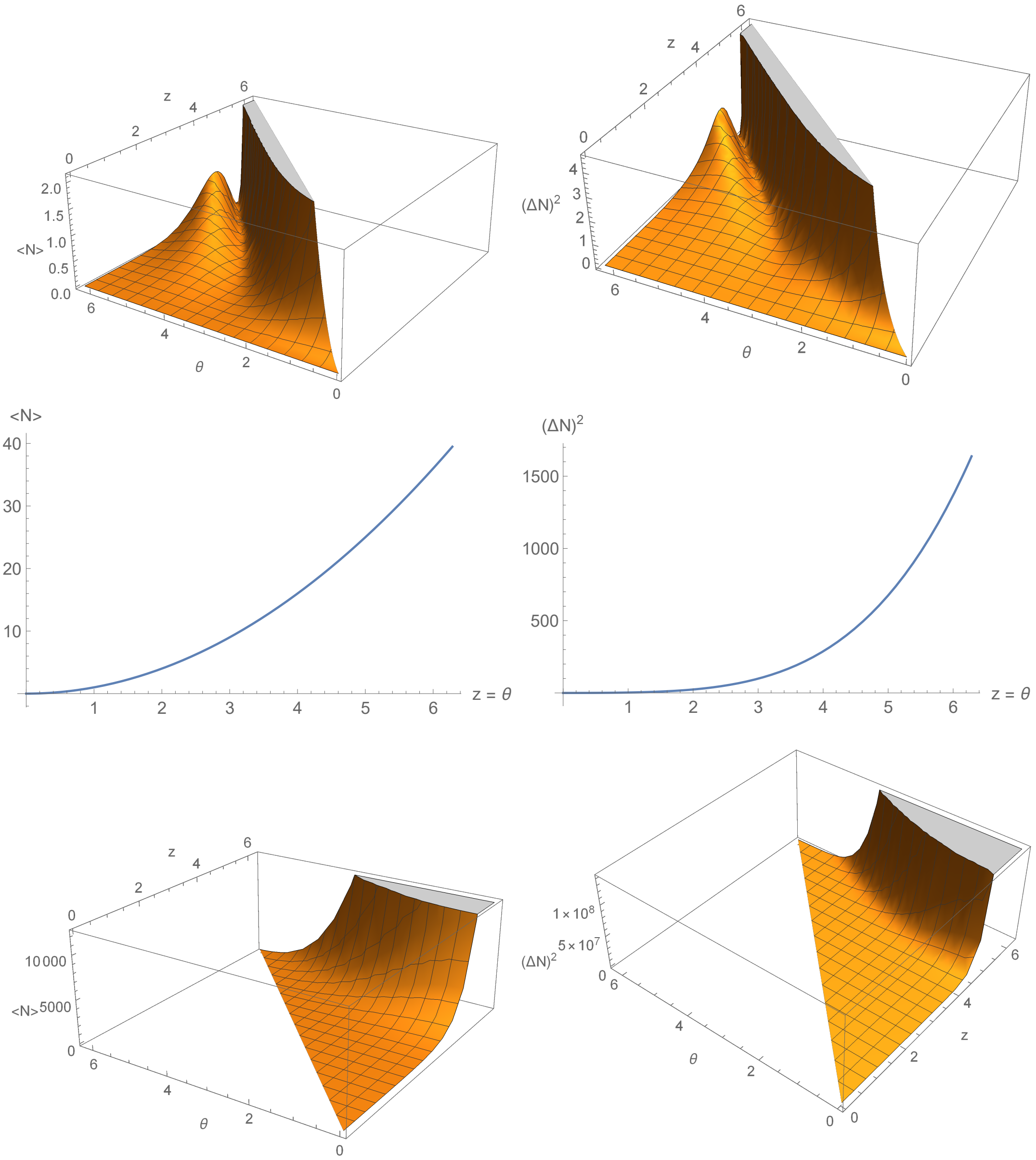

Figure 5.1: Graphs showing the average photon number (left) and variation (right) of the combined squeezing and beamsplitter Hamiltonian of equation 5.12, where the expectation value is taken with respect to the vacuum state. Top graphs show the $\mathcal{PT}$-symmetric regime where $|z| < |\theta|$, which shows that the system acts as expected with both squeezing and a beamsplitter as the photon number is nonzero (with no photons input) and oscillates with z and θ. Middle graphs show the EP $|z| = |\theta|$, where the photon number and variance increases polynomially with z. Bottom graphs show the broken regime where the system acts purely like a squeezer with an exponentially increasing average photon number, although in a realistic situation (such as Four Wave Mixing), this would eventually reach a saturation point.

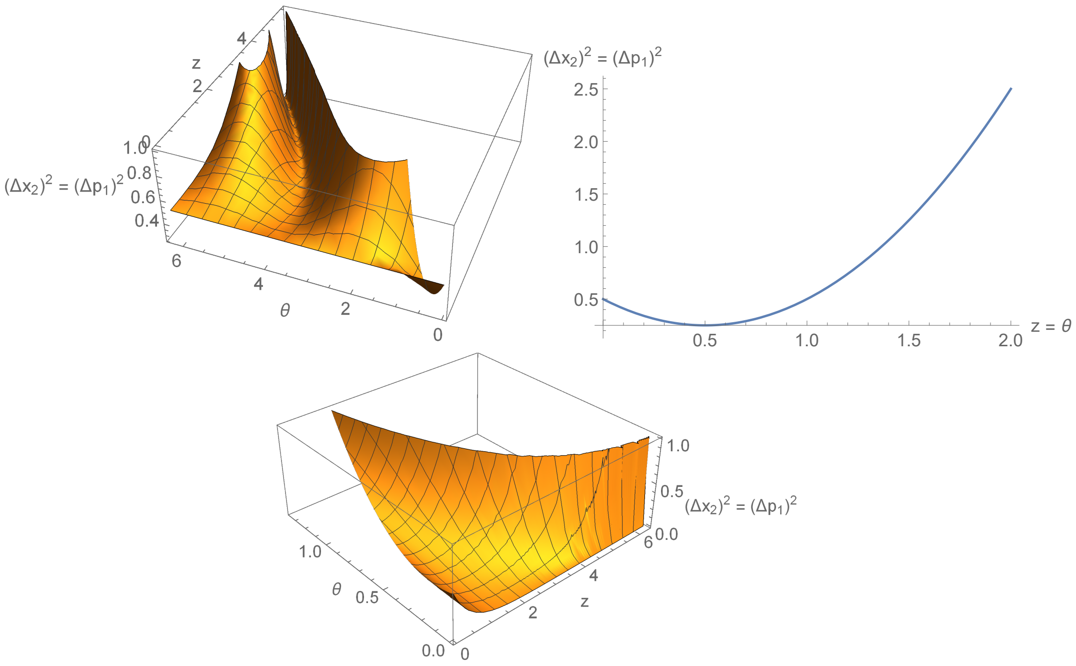

Figure 5.2: Graphs showing the quadrature operator variances $(\Delta x_2)^2 = (\Delta p_1)^2$ of the combined squeezing and beamsplitter Hamiltonian of equation 5.12, where the expectation value is taken with respect to the vacuum state. Squeezing occurs when $(\Delta x_2)^2 = (\Delta p_1)^2 < 1/2$. In the unbroken regime (top left), this occurs at various points as the variance oscillates with z and θ. At the EP (top right), the variance is polynomial and below $1/2$ for $z < 1$, with a minimum value at $z = 1/2$. The broken regime (bottom) shows the difference between a typical squeezer (where the variance decreases exponentially) and this system where even a small increase in θ increases the variance to above $1/2$ and as z gets larger, the value of θ required to do this decreases.

This concept can be further extended to arbitrarily large D-dimensional systems. For $D = 2n$, defining

$$\mathcal{P}_X = \begin{pmatrix} 0 & I_n \\ I_n & 0 \end{pmatrix}, \quad \mathcal{P}_Z = \begin{pmatrix} I_n & 0 \\ 0 & -I_n \end{pmatrix} \quad \text{and} \quad M = \begin{pmatrix} A & B \\ C & D \end{pmatrix}, \tag{5.31}$$

for A, B, C and D $n \times n$ matrices. Taking M to be $\mathcal{P}_X\mathcal{T}$ symmetric gives

$$\begin{pmatrix} 0 & I \\ I & 0 \end{pmatrix} \begin{pmatrix} A^* & B^* \\ C^* & D^* \end{pmatrix} \begin{pmatrix} 0 & I \\ I & 0 \end{pmatrix} = \begin{pmatrix} A & B \\ C & D \end{pmatrix}, \tag{5.32}$$

giving

$$D^* = A \quad \text{and} \quad C^* = B. \tag{5.33}$$

Writing

$$M = \begin{pmatrix} A & B \\ B^* & A^* \end{pmatrix} \tag{5.34}$$

immediately gives that enforcing M to be $\mathcal{P}_X\mathcal{T}$ symmetric with a determinant of 1 makes M a Bogoliubov transformation. That is, we can describe any Bogoliubov transformation as a $\mathcal{P}_X\mathcal{T}$ symmetric transformation with determinant 1. Alternatively, we can take

$$\begin{aligned} I_{2n} &= M_S \mathcal{P}_Z \mathcal{T} M_S^T \left(\mathcal{P}_Z\mathcal{T}\right)^{-1} && (5.35)\\ &= \begin{pmatrix} A & B \\ C & D \end{pmatrix} \begin{pmatrix} I & 0 \\ 0 & -I \end{pmatrix} \begin{pmatrix} A^* & C^* \\ B^* & D^* \end{pmatrix} \begin{pmatrix} I & 0 \\ 0 & -I \end{pmatrix} && (5.36)\\ &= \begin{pmatrix} A & B \\ C & D \end{pmatrix} \begin{pmatrix} A^* & -C^* \\ -B^* & D^* \end{pmatrix} && (5.37)\\ &= \begin{pmatrix} AA^* - BB^* & -AC^* + BD^* \\ CA^* - DB^* & -CC^* + DD^* \end{pmatrix}, && (5.38) \end{aligned}$$

which gives the same constraints as the property $M_S \Omega M_S^T = \Omega$.

5.4 Design of a Nonunitary Interferometer

In order to design an interferometer that can be used to implement nonunitary transformations, we first look at a typical unitary interferometer (such as that used in chapter 4) implementing the unitary channel $\mathcal{U}_U$ created using linear transformations, that is, phase shifters and beamsplitters. On the vaccuum state, the interferometer has no effect as it consists of only linear components:

$$\mathcal{U}_U : |\text{vac}\rangle \mapsto U |\text{vac}\rangle = |\text{vac}\rangle . \tag{5.39}$$

Inputting a single photon before the interferometer then gives the desired unitary transformation:

$$\mathcal{U}_U : a_j^\dagger |\text{vac}\rangle \mapsto U a_j^\dagger U^\dagger U |\text{vac}\rangle = \sum_j U_{kj} a_j^\dagger |\text{vac}\rangle . \tag{5.40}$$

This then helps define how a nonunitary interferometer should work. The aim is to create the transformation matrix M such that the final output state is given by

$$|\psi\rangle = \sum_j M_{kj} a_j^\dagger |\text{vac}\rangle . \tag{5.41}$$

However, simply applying a nonlinear transformation may not give the correct output. This can be shown by considering how the photons input into the typical interferometer are most often created. While there are different methods of doing this, here we consider Four Wave Mixing (FWM), equivalent to 2-mode squeezing (under the undepleted pump approximation)[1] given by equation 5.6. After performing FWM/squeezing, the state is then given by (denoting

---

[1] This is discussed in more detail in chapter 6

the modes used here by subscripts a and b to distinguish them from the numerical modes in the interferometer)

$$\begin{aligned} U_{FWM}\left|0\right\rangle &= e^{-iH_{FWM}}\left|0\right\rangle \\ &= \left(1+\mathcal{O}\left(\zeta^2\right)\right)\left|0\right\rangle_a\left|0\right\rangle_b - \left(\zeta+\mathcal{O}\left(\zeta^3\right)\right)\left|1\right\rangle_a\left|1\right\rangle_b + \mathcal{O}\left(\zeta^2\right)\left|2\right\rangle_a\left|2\right\rangle_b + \dots \end{aligned} \tag{5.42}$$

and heralding on mode b with (as an example) an ideal non-number-resolving single photon detector, the state input to the interferometer (before normalisation) could be described as

$$\rho = -\left(\zeta+\mathcal{O}\left(\zeta^3\right)\right)\left|1\right\rangle\!\left\langle 1\right|_a + \mathcal{O}\left(\zeta^2\right)\left|2\right\rangle\!\left\langle 2\right|_a, \tag{5.43}$$

which, for a low squeezing parameter $\zeta \ll 1$, approximates a single photon state. Applying the transformation $\mathcal{U}_M$ to this gives the transformation after heralding as

$$\mathcal{U}_M : \rho \mapsto -M\left(\zeta+\mathcal{O}\left(\zeta^3\right)\right)a^\dagger U_M\left|0\right\rangle\!\left\langle 0\right|_a U_M^\dagger + \mathcal{O}\left(\zeta^2 M^2\right)a^\dagger a^\dagger U_M\left|0\right\rangle\!\left\langle 0\right|_a U_M^\dagger, \tag{5.44}$$

which may or may not be a good approximation of the transformation M depending on the effect U_M has on the vacuum state. Instead, to achieve a better transformation, we first apply the transformation $U_M^\dagger$ before creating the single photon state. This has the effect of sandwiching the single photon creation between 2 unitary transformations, causing it to act as if calculations are done in the Heisenberg picture while remaining in the Schrödinger picture. That is, for the channel $\mathcal{U}_M$ acting only on the 'a' modes of the system,

$$\left|\psi\right\rangle = U_a U_{FWM} U_a^\dagger\left|0\right\rangle = e^{\zeta^* U_a a_j U_a^\dagger b - \zeta U_a a_j^\dagger U_a^\dagger b^\dagger}\left|0\right\rangle, \tag{5.45}$$

which when expanded out to first order in ζ as above, gives

$$\begin{aligned} \left|\psi\right\rangle = &\left(1+\mathcal{O}\left(\zeta^2\left\|M\right\|^2\right)\right)\left|0\right\rangle_a\left|0\right\rangle_b - \left(\zeta\sum_j M_{kj}a_j^\dagger + \mathcal{O}\left(\zeta^3\left\|M\right\|^3\right)\right)\left|0\right\rangle_{a_j}\left|1\right\rangle_b \\ &+ \mathcal{O}\left(\zeta^2\left\|M\right\|^2\right)\left|2\right\rangle_a\left|2\right\rangle_b, \end{aligned} \tag{5.46}$$

which can be further heralded as above. To turn this into a reconfigurable interferometer, similar to a Reck [38] or Clements [39] scheme built from basic components (here, phase shifters, beamsplitters and squeezers), in comparison with chapter 4, similar to [63], we start with the singular value decomposition (SVD) to get

$$M = M_U M_D M_{V^\dagger} \tag{5.47}$$

where M_U and M_V are unitary matrices and M_D is a diagonal matrix consisting of the singular values of M. Acting with M on the system modes can then be split into steps of implementing M_U, implementing the transformation given by the singular values and implementing $M_{V^\dagger}$.

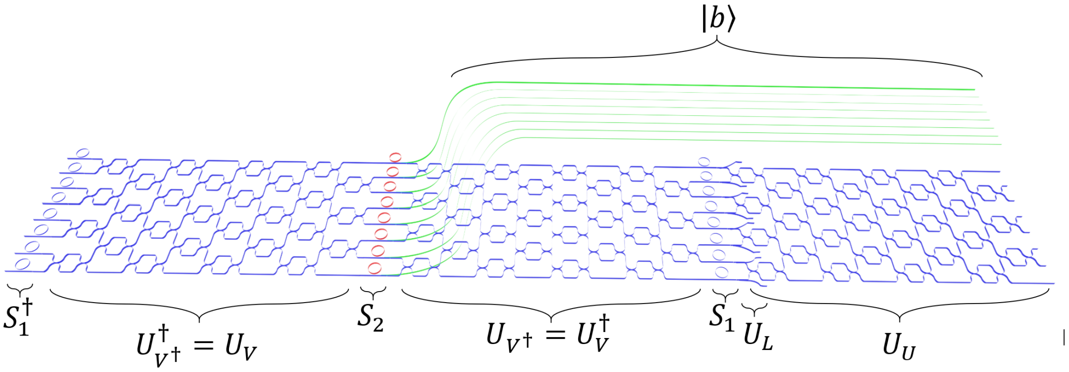

Figure 5.3: Diagram of optical circuit representing the transformation given in equation 5.50. $|b\rangle$ represents heralding modes, S_2 is two-mode squeezing generating pairs of photons and S_1 and $S_1^\dagger$ being single-mode squeezing, with $S_1 U_L = U_D$. U_V and U_U are transformations given by other unitary interferometers, here a Clements scheme [39].

That is, the overall transformation, shown in figure 5.3, is given by

$$\begin{aligned} MA\,|\text{vac}\rangle &= M_U M_D M_{V^\dagger} A\,|\text{vac}\rangle && (5.48)\\ &= U_U U_D U_{V^\dagger} A U_{V^\dagger}^\dagger U_D^\dagger U_U^\dagger\,|\text{vac}\rangle && (5.49)\\ &= U_U U_D U_{V^\dagger} A U_{V^\dagger}^\dagger U_D^\dagger\,|\text{vac}\rangle\,. && (5.50)\end{aligned}$$

where U_U, $U_{V^\dagger}$ and $U_{V^\dagger}^\dagger$ are unitary transformations that can be created with a Reck or Clements interferometer and A is the vector representing the creation and annihilation operators

$$A = \begin{pmatrix} a_1^\dagger & \dots & a_N^\dagger & a_1 & \dots & a_N \end{pmatrix}^T. \tag{5.51}$$

As the singular values M_D are real and positive numbers, we can now write these as

$$M_{D,jj} = \begin{cases} \cosh r_j & \text{if } M_{D,JJ} > 1, \\ 1 & \text{if } M_{D,jj} = 1, \\ \cos\theta_j & \text{if } M_{D,jj} < 1. \end{cases} \tag{5.52}$$

Coupling the system to an ancilla system C allows for additional beamsplitters to act as 'loss modes' for singular values less than 1 and single-mode squeezers to act as 'gain modes' for singular values greater than 1. As there is no requirement for M_D to have a constant norm, there is no requirement for the non-Hermitian evolution to be norm preserving. Instead, non-norm-preserving operations may indicate that a non-constant number of bosons or particles may be present in the system being simulated.

5.5 Trotterisation

Similar to creating unitary interferometers, when a single photon is input into a single mode, given a nonunitary transformation matrix, calculating the various parameters required to create the interferometer requires more computing than simply reading off the matrix elements corresponding to the given input mode. While this method no longer works for multiple input photons, calculating the SVD and further breaking the unitary transformations into smaller components can still be made more efficient using e.g. methods from Hamiltonian simulation at the cost of requiring more components and a physically longer interferometer. To give an example of this, we start with the Hamiltonian to be simulated $H = \sum_j H_j$ and define $\mu = \max_j \left(\|H_{\text{eff},j}\|\right)$ for

$$U_{a,j} A U_{a,j}^\dagger = e^{-iH_{\text{eff},j}t} A, \tag{5.53}$$

which gives

$$\begin{aligned}
U_{a,k}U_{a,j}U_{FWM}U_{a,j}^\dagger U_{a,k}^\dagger &= U_{a,k} e^{\zeta^* U_{a,j} a_k U_{a,j}^\dagger b - \zeta U_{a,j} a_k^\dagger U_{a,j}^\dagger b^\dagger} U_{a,k}^\dagger && (5.54)\\
&= U_{a,k} \exp\left[e^{-iH_{\text{eff},j}t}\left(\zeta^* a_k b - \zeta a_k^\dagger b^\dagger\right)\right] U_{a,k}^\dagger && (5.55)\\
&= \exp\left[e^{-iH_{\text{eff},k}t} e^{-iH_{\text{eff},j}t}\left(\zeta^* a_k b - \zeta a_k^\dagger b^\dagger\right)\right] && (5.56)\\
&= \exp\left[\left(e^{-i\left(H_{\text{eff},k}+H_{\text{eff},j}\right)t} + \frac{1}{2}\left[H_{\text{eff},k}, H_{\text{eff},j}\right]t^2 + \mathcal{O}\left(\mu^3 t^3\right)\right)\left(\zeta^* a_k b - \zeta a_k^\dagger b^\dagger\right)\right]. && (5.57)
\end{aligned}$$

This process can be repeated for $H = \sum_j^n H_j$ to give

$$\begin{aligned}
\prod_j^n e^{-iH_{\text{eff},j}\delta t} &= e^{-i\sum_j^n H_{\text{eff},j}\delta t} + \delta t^2 \sum_{j=2}^n \left[H_{\text{eff},j}, \sum_{k=1}^{j-1} H_{\text{eff},k}\right] + \mathcal{O}\left(\mu^3 \delta t^3\right) && (5.58)\\
&= e^{-i\sum_j^n H_{\text{eff},j}\delta t} + \mathcal{O}\left(n^2 \mu^2 \delta t^2\right). && (5.59)
\end{aligned}$$

Applying this operator to the vacuum state and expanding further gives

$$\begin{aligned}
\mathcal{U} : U_{FWM}\left|0\right\rangle \mapsto \prod_j U_{a,j} U_{FWM} U_{a,j}^\dagger \left|0\right\rangle && (5.60)\\
= \exp\left[M_a\left(\zeta^* a_k b - \zeta a_k^\dagger b^\dagger\right)\right]\left|0\right\rangle && (5.61)\\
= \left[1 + M_a\left(\zeta^* a_k b - \zeta a_k^\dagger b^\dagger\right) + \frac{1}{2}\left(M_a\left(\zeta^* a_k b - \zeta a_k^\dagger b^\dagger\right)\right)^2 + \mathcal{O}\left(\|M_a\|^3 \zeta^3\right)\right]\left|0\right\rangle, && (5.62)
\end{aligned}$$

where

$$\begin{aligned}
M_a &= e^{-i\sum_j H_{\text{eff},j}\delta t} + \delta t^2 \sum_{j=2}^n \left[H_{\text{eff},j}, \sum_{k=1}^{j-1} H_{\text{eff},k}\right] + \mathcal{O}\left(\mu^3 \delta t^3\right) && (5.63)\\
&= \begin{pmatrix} F_a & G_a \\ G_a^* & F_a^* \end{pmatrix}. && (5.64)
\end{aligned}$$

This gives

$$\begin{aligned}\mathcal{U}: U_{FWM}\left|0\right\rangle \mapsto &\left|0\right\rangle_a \left|0\right\rangle_b - F_a\zeta \left|1_k\right\rangle_a \left|1\right\rangle_b - \frac{1}{2}M_a\left(\zeta^* a_k b - \zeta a_k^\dagger b^\dagger\right) F_a\zeta\left|1_k\right\rangle_a\left|1\right\rangle_b \\ &+\mathcal{O}\left(\|M_a\|^3\zeta^3\right)\left|0\right\rangle \qquad (5.65)\\ =& \left|0\right\rangle_a\left|0\right\rangle_b - F_a\zeta\left|1_k\right\rangle_a\left|1\right\rangle_b - \frac{1}{2}|\zeta|^2\sum_{lm} F^*_{a;mk}F_{a;lk}a_m a_l^\dagger\left|0\right\rangle_a\left|0\right\rangle_b \\ &- \frac{1}{2}|\zeta|^2\sum_{lm} G^*_{a;mk}F_{a;lk}a_m^\dagger a_l^\dagger\left|0\right\rangle_a\left|0\right\rangle_b - \frac{1}{\sqrt{2}}\zeta^2\sum_{lm}F_{a;mk}F_{a;lk}a_m^\dagger a_l^\dagger\left|0\right\rangle_a\left|2\right\rangle_b \\ &- \frac{1}{\sqrt{2}}\zeta^2\sum_{lm}G_{a;mk}F_{a;lk}a_m a_l^\dagger\left|0\right\rangle_a\left|2\right\rangle_b + \mathcal{O}\left(\|M_a\|^3\zeta^3\right) \qquad (5.66)\\ =& \left[1-\frac{1}{2}|\zeta|^2\left(F_a^\dagger F_a\right)_{kk}\right]\left|0\right\rangle_a\left|0\right\rangle_b - F_a\zeta\left|1_k\right\rangle_a\left|1\right\rangle_b \\ &- \frac{1}{2}|\zeta|^2\sum_{lm} G^*_{a;mk}F_{a;lk}a_m^\dagger a_l^\dagger\left|0\right\rangle_a\left|0\right\rangle_b - \frac{1}{\sqrt{2}}\zeta^2\sum_{lm}F_{a;mk}F_{a;lk}a_m^\dagger a_l^\dagger\left|0\right\rangle_a\left|2\right\rangle_b \\ &- \frac{1}{\sqrt{2}}\zeta^2\left(G_a^T F_a\right)_{kk}\left|0\right\rangle_a\left|2\right\rangle_b + \mathcal{O}\left(\|M_a\|^3\zeta^3\right), \qquad (5.67)\end{aligned}$$

valid for $\|M_a\|\zeta < 1$. As $\zeta \ll 1$ is generally assumed and can easily be decreased in experiment if large numbers of photons are measured, this will not be considered to be an issue. The maximum singular value of M_a can additionally be bounded by $e^{n\mu\delta t} = 1 + n\mu\delta t + \mathcal{O}\left(n^2\mu^2\delta t^2\right)$ [64], which can be used to find an initial maximum allowed value for ζ. Heralding with an ideal non-number resolving photon detector in mode b gives

$$\begin{aligned}U_{FWM}\left|0\right\rangle &\mapsto \rho \\ &\propto F_a\zeta\left|1_k\right\rangle\left\langle 1_k\right|_a + \frac{1}{\sqrt{2}}\zeta^2\sum_{lm}F_{a;mk}F_{a;lk}a_m^\dagger a_l^\dagger\left|0\right\rangle\left\langle 0\right|_a \\ &\quad + \frac{1}{\sqrt{2}}\zeta^2\left(G_a^T F_a\right)_{kk}\left|0\right\rangle\left\langle 0\right|_a + \mathcal{O}\left(\zeta^3\right). \qquad (5.68)\end{aligned}$$

The third term in the above contributes to the vacuum state in the a modes and so does not contribute to any error. The second term, by contrast, is a two-photon term, which will either contribute to an error, if a single photon is detected ($m = l$), or can be ignored, if two photons get detected ($m \neq l$). This can be described by rewriting ρ (after heralding with a perfect detector) as

$$\begin{aligned}\rho \propto& F_a\left|1_k\right\rangle\left\langle 1_k\right|_a + \zeta\sum_l F^2_{a;lk}\left|2_k\right\rangle\left\langle 2_k\right|_a + \frac{1}{\sqrt{2}}\zeta\sum_{l,m\neq l}F_{a;mk}F_{a;lk}\left|1_l 1_m\right\rangle\left\langle 1_l 1_m\right|_a \\ &+ \frac{1}{\sqrt{2}}\zeta\left(G_a^T F_a\right)_{kk}\left|0\right\rangle\left\langle 0\right|_a + \mathcal{O}\left(\zeta^3\right). \qquad (5.69)\end{aligned}$$

At time δt this gives an overall error

$$\delta t^2\sum_{j=2}^{n}\left[H_{\text{eff},j}, \sum_{k=1}^{j-1}H_{\text{eff},k}\right] + \zeta F_a^T F_a + \mathcal{O}\left(\mu^3\delta t^3 + \zeta^3\right) = \mathcal{O}\left(n^2\mu^2\delta t^2 + \zeta\|M\|\right). \qquad (5.70)$$

As $e^{-i\sum_j H_{\mathrm{eff},j}\delta t}$ commutes with itself, the overall error for a state at time $t = p\delta t$ only increases linearly with p, or

$$\left(e^{-i\sum_j H_{\mathrm{eff},j}t/p} + \mathcal{O}\left(n^2\mu^2\frac{t^2}{p^2}\right)\right)^p + \mathcal{O}\left(\zeta\|M\left(t\right)\|\right) = e^{-i\sum_j H_{\mathrm{eff},j}t} + \mathcal{O}\left(n^2\mu^2\frac{t^2}{p} + \zeta\|M\left(t\right)\|\right), \tag{5.71}$$

giving the final error as

$$\epsilon = \mathcal{O}\left(n^2\mu^2\frac{t^2}{p} + \zeta\|M\left(t\right)\|\right). \tag{5.72}$$

Simulating H to within error ϵ can therefore be achieved in a time complexity

$$\mathcal{O}\left(\frac{n^3\mu^2t^2}{\epsilon - \zeta\|M\|}\right). \tag{5.73}$$

5.6 Model of a 2D Parity-Time Symmetric Hamiltonian

Having designed an interferometer that can simulate $\mathcal{PT}$-symmetric (and other non-Hermitian) systems with an arbitrary number of dimensions similar to a unitary interferometer, we now consider an example system to be simulated. Here, this will be a staggered transverse field in a Heisenberg spin lattice.

Moving from a one-dimensional to a two-dimensional lattice of size (N, M), the Parity $\mathcal{P}$ reversal operator is now defined as $\mathcal{P}\sigma_{j,k}\mathcal{P}^{-1} = \sigma_{N+1-j,M+1-k}$ and the time reversal operator remains defined as $\mathcal{T}i\mathcal{T}^{-1} = -i$. As with a 1D lattice, an operator $\mathcal{O}$ is $\mathcal{PT}$-symmetric when $[\mathcal{PT}, \mathcal{O}] = 0$.

This staggered transverse field in a Heisenberg spin lattice can be considered as a 2D extension to [65] combined with [66]. Starting with a single spin with a Hamiltonian

$$H_A = \begin{pmatrix} 0 & h+\gamma \\ h-\gamma & 0 \end{pmatrix}, \tag{5.74}$$

which has an EP at $|\gamma| = |h|$, this is $\mathcal{PT}$-symmetric for $|\gamma| < |h|$ and $\mathcal{PT}$-broken for $|\gamma| > |h|$. Unlike typically considered $\mathcal{PT}$-symmetric Hamiltonians, where the Hamiltonian is neither $\mathcal{T}$-symmetric or $\mathcal{P}$-symmetric, here, when $h, \gamma \in \Re$ the Hamiltonian is both Parity-symmetric and Time-symmetric as there is no dependence on i. This can be built up into a larger Hamiltonian by considering an arbitrary number of spins on an A-B lattice, with

$$H_{nn;jk} = \sum_{l,m\in nn(j,k)} \sigma^z_{j,k}\sigma^z_{l,m} \tag{5.75}$$

$$H_{A;jk} = h\sigma^x_{j,k} + i\gamma\sigma^y_{j,k} \tag{5.76}$$

$$H_{B;jk} = h\sigma^x_{j,k} - i\gamma\sigma^y_{j,k}, \tag{5.77}$$

where $\sigma^q_{j,k}$ for $q \in \{x, y, z\}$ is the Pauli matrix acting on qubit j. This gives the overall Hamiltonian

$$H = \frac{J}{2}\sum_{j,k} H_{nn;jk} + \sum_{j=k \bmod 2} H_{A;jk} + \sum_{j\neq k \bmod 2} H_{B;jk} \tag{5.78}$$

$$= J\left(\sum_{k=1}^{N_2}\sum_{j=1}^{N_1-1}\sigma^z_{j,k}\sigma^z_{j+1,k} + \sum_{k=1}^{N_2-1}\sum_{j=1}^{N_1}\sigma^z_{j,k}\sigma^z_{j,k+1}\right) + \sum_{k=1}^{N_2}\sum_{j=1}^{N_1}\left(h\sigma^x_{j,k} + (-1)^{j+k}\, i\gamma\sigma^y_{j,k}\right). \tag{5.79}$$

Numerical calculations of the eigenvalues suggest that the unbroken regime of this system remains the same independent of the size of the system, unlike the D-dimensional Hamiltonian H_D with diagonal gain-loss terms and nearest neighbour interactions,

$$H_D = \sum_{d=1}^{D} (-1)^d\, i\gamma\, |d\rangle\langle d| + \sum_{d=1}^{D-1} J\left(|d\rangle\langle d+1| + |d+1\rangle\langle d|\right), \tag{5.80}$$

where the size of the $\mathcal{PT}$-symmetric region shrinks with increasing D as shown in figure 5.4.

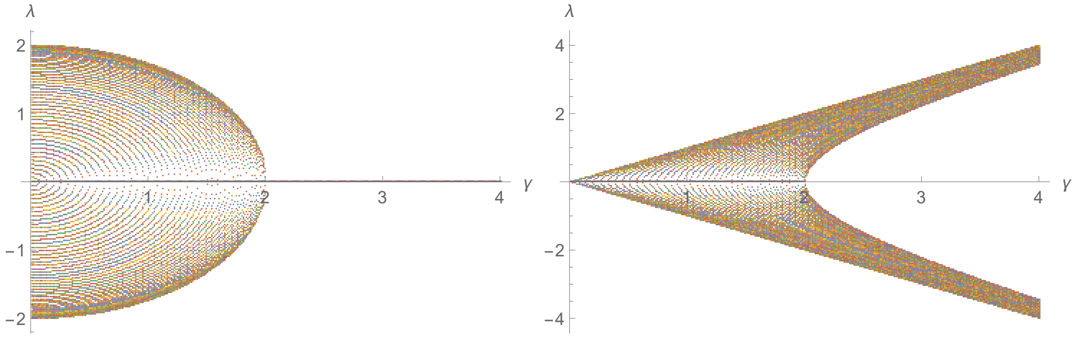

Figure 5.4: Real part (left) and imaginary part (right) eigenvalues of 5.80 with $D = 100$, demonstrating that, as the system gets larger, the EPs start to occur at values closer to $\gamma = 0$. This means that the range of the $\mathcal{PT}$-symmetric region gets smaller with increasing dimension.

5.6.1 Tensor network simulation of ground state of an infinite lattice

To numerically calculate the properties of the ground state of equation 5.78 for an infinite lattice, we use the Time Evolving Block Decimation (TEBD) algorithm [67] described and written by Glen Evenbly [68] to optimise an infinite Projected Entangled Pair States (iPEPS) [69] tensor network. This is first done for a typical example of the Hermitian system (where $\gamma = 0$) in figure 5.6 which numerically calculates the critical point at $h \approx 0.75$. In order to demonstrate that this process works in the unbroken $\mathcal{PT}$-symmetric region, a typical example of the convergence and energy density calculation at a single point (here $h = 1.06$ and $\gamma = 0.11$) is given in figure 5.5, although the convergence at each point can vary considerably, with some numerical issues changing the amount of convergence possible at around $h \approx 0.65$. While this affect the quantitative results, the resulting outputs below and above this point are qualitatively similar. These ground state solutions are given in figure 5.7 and the ground state density matrix giving these solutions in 5.8.

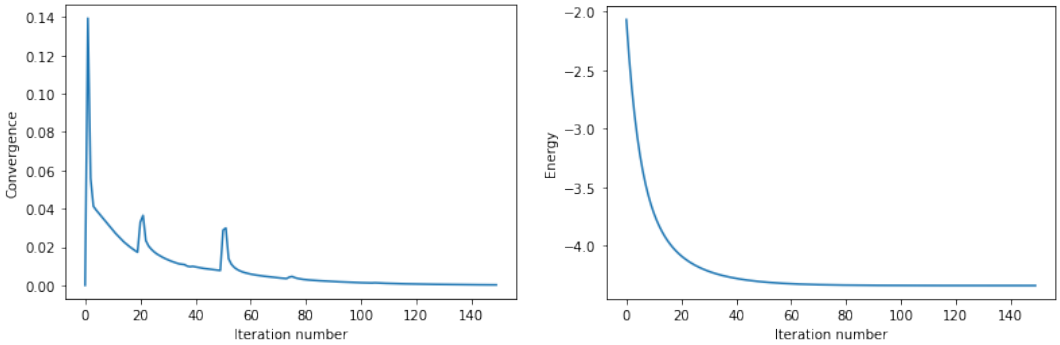

Figure 5.5: Typical example of calculating the ground state of equation 5.78 at $h = 1.06$ and $\gamma = 0.11$ using the Time Evolving Block Decimation (TEBD) algorithm. After tens of iterations, the state has approximately converged to the ground state, although letting the program run for longer further improves the convergence.

Overall, this demonstrates that, due to the real eigenvalues in the $\mathcal{PT}$-unbroken regime, tensor networks are a viable option for finding ground phases of $\mathcal{PT}$-symmetric systems as well as $\mathcal{PT}$-symmetric systems beyond one dimension with a non-vanishingly small unbroken region can exist and can have additional phases that do not exist in the equivalent Hermitian system, which could be of interest when simulating larger $\mathcal{PT}$-symmetric systems. This also shows the critical point of the Hermitian system, here numerically calculated at approximately $h = 0.83$, which can be encircled by varying γ. The contour lines of the spontaneous magnetisation suggest the possibility of a scaling with the parameter $\beta = \sqrt{h^2 - \gamma^2}$, similar to [66] below $\sqrt{h^2 - \gamma^2} \approx 0.83$ for the spontaneous magnetisation, although the scaling of the energy density with this parameter continues beyond this line. While the critical point only appears in the Hermitian regime where $\gamma = 0$, this may nonetheless suggest some kind of transitional behaviour where the system behaves differently far below and far above this line.

5.7 Example Simulation

Having looked at classical methods of calculating properties of the ground state of an infinite lattice, we now turn to using the nonunitary interferometer of section 5.4 to simulate the time evolution of a finite, small lattice with 4 spins in one direction and 2 in the other. This was done with code shown in Appendix A using Strawberry Fields [70, 71].

Starting in the paramagnetic ground state $|+\rangle_{2,4} = \sum_{k=1}^{4} \sum_{j=1}^{2} |+\rangle_{j,k}$ and the ferromagnetic ground state $|0\rangle_{2,4} = \sum_{k=1}^{4} \sum_{j=1}^{2} |0\rangle_{j,k}$, we simulate the evolution of this Heisenberg

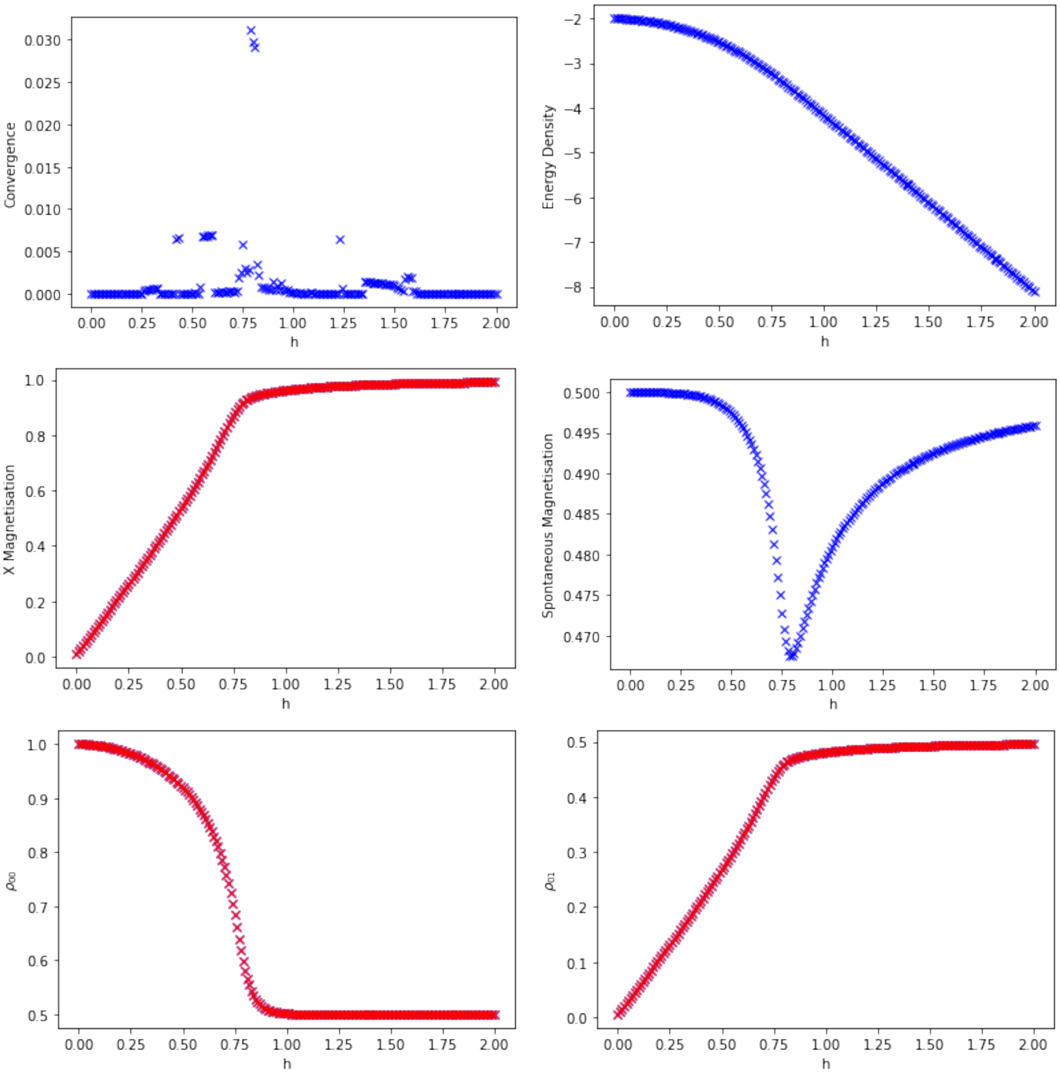

Figure 5.6: Graphs showing the calculated ground state of the Hermitian ($\gamma = 0$) Transverse Field Ising model with bond dimension 4 and timestep = 0.01, after 200 iterations. Shown in the top left graph, this generally converges well, although is slower to converge around the critical point at $h \approx 0.75$. The energy density (top middle) continually decreases with applied h. The magnetisation (top right) in the σ^x-direction continually increases from 0 until saturation at the critical point with a value of 1 and is the same for both A and B sites. The total (spontaneous) magnetisation (bottom left) is smallest at the critical point, although remains relatively constant for all values of h. The density matrix elements ρ_{00} (bottom middle) and ρ_{01} (bottom right) display the transition from spins being aligned in the σ^z-direction at $h = 0$ to spins being aligned in the σ^x-direction past the critical point, for $h \gtrapprox 0.75$.

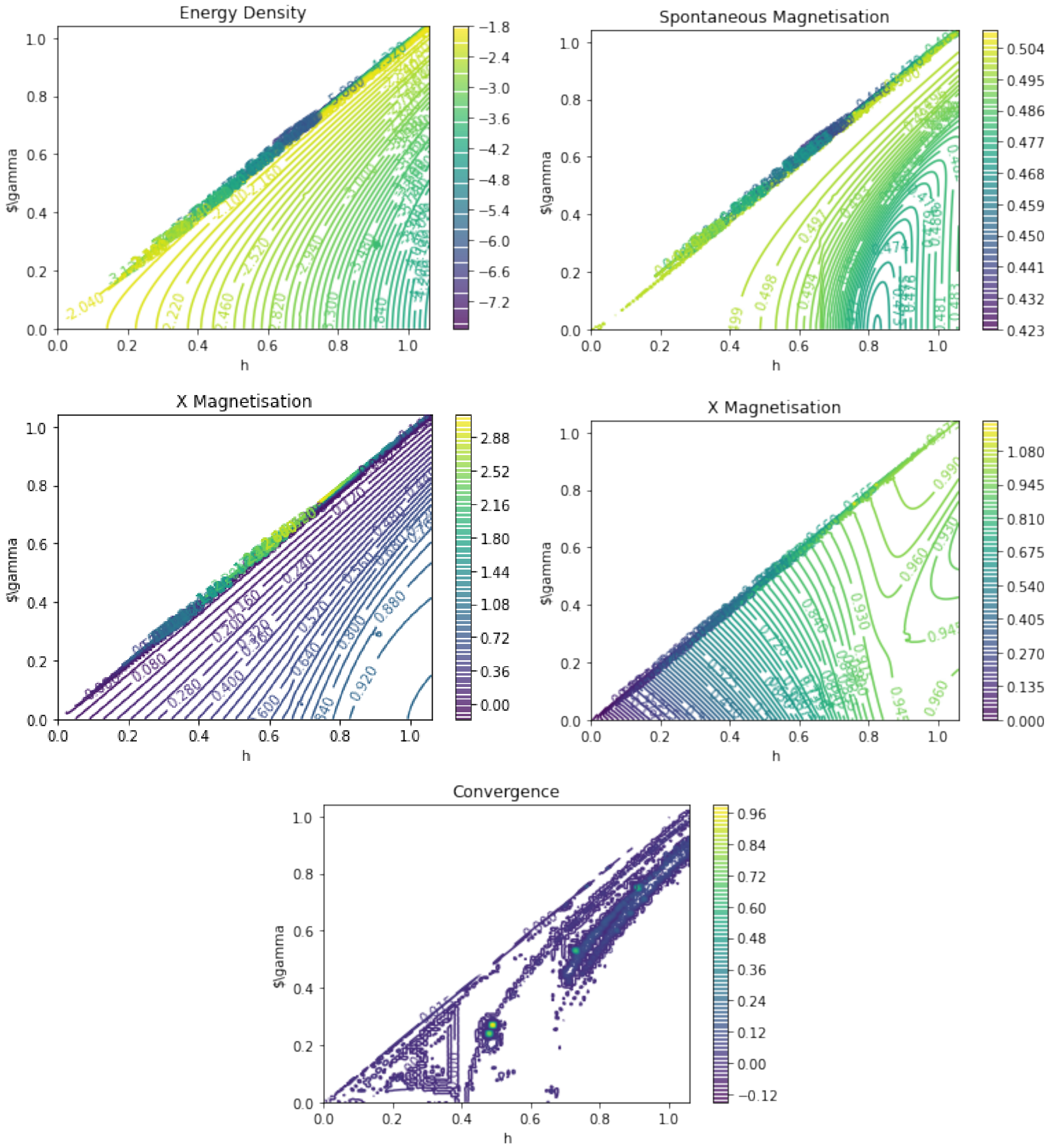

Figure 5.7: Graphs show calculations of the ground state energy density (top left), spontaneous magnetisation (top right), X magnetisation (‘A’ Lattice sites, middle left; ‘B’ lattice sites, middle right) and convergence (bottom) of the lattice given by the Hamiltonian in equation 5.78. This shows that the energy density decreases with increasing h and increases with increasing γ. The spontaneous magnetisation gives a critical point around $h = 0.83$, $\gamma = 0$ (which can now be encircled, unlike the Hermitian version of the lattice). The contours of the spontaneous magnetisation appear to follow lines corresponding to $\beta = \sqrt{h^2 - \gamma^2}$ (at least approximately), suggesting a non-Hermitian extension to the ferromagnetic phase for approximately $\beta < 0.83$ in the unbroken $\mathcal{PT}$-symmetric phase. Similar to the energy density, the X magnetisation of the A lattice has no stationary points, although the B lattice has a saddle point around $h = 0.9$ and $\gamma = 0.3$. Apart from an anomalous point around $h = 0.5$ and near the EP past the critical point, this generally converges well.

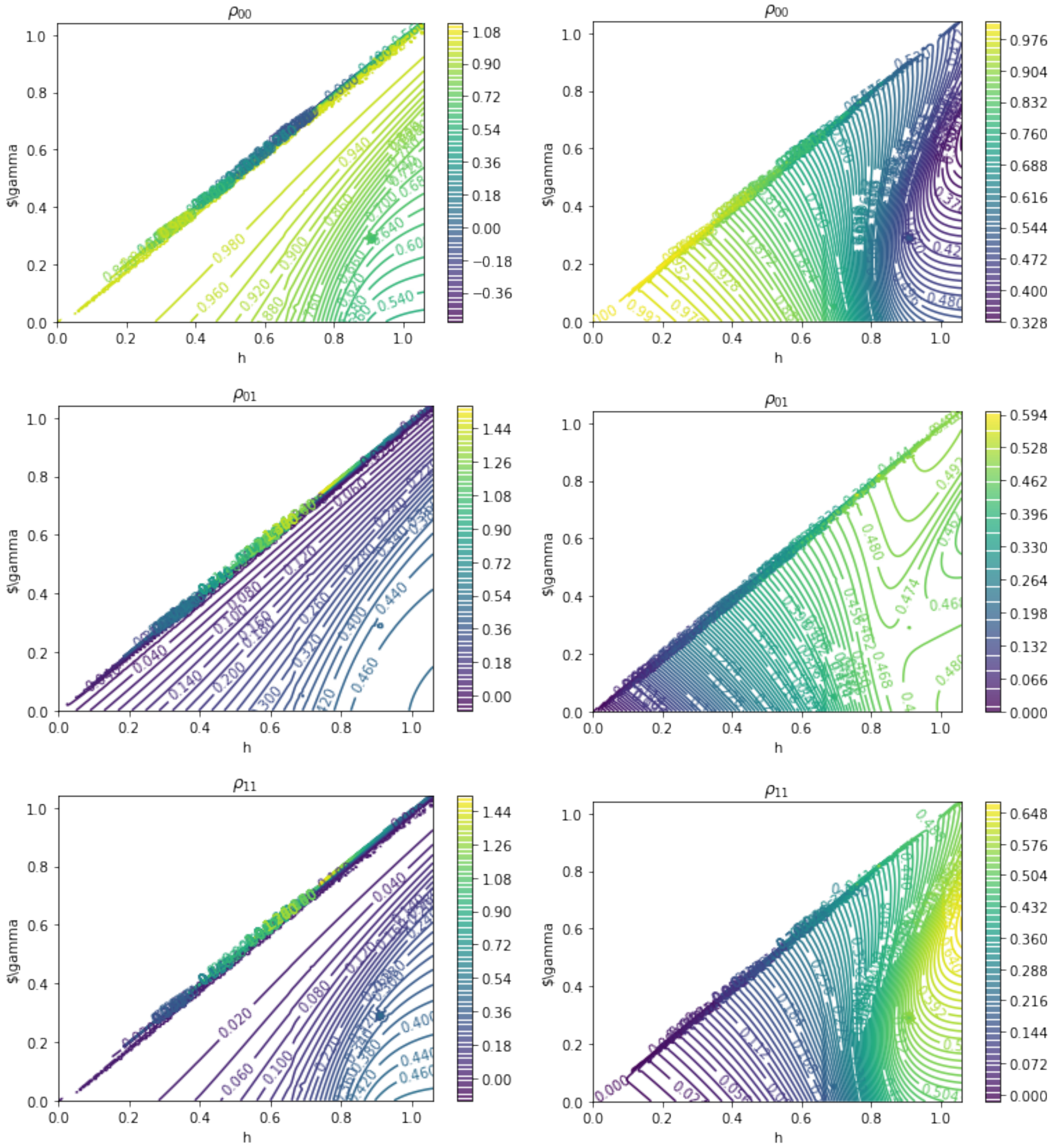

Figure 5.8: Graphs showing the calculated ground state of the Hamiltonian given by equation 5.78. Top shows ρ_{00}, middle shows $\rho_{01} = \rho_{10}$ and bottom shows ρ_{11}. Left shows the ground state of the ‘A’ lattice sites and right shows the ‘B’ lattice sites. The A lattice sites show similar behaviour at all calculated values, where increasing h increases (decreases) the value of that element of the density matrix and increasing γ decreases (increases) the value of that element. This is demonstrated by the contour lines having no stationary points. This contrasts with the B lattice sites which appear to show a saddle point around $h = 0.9$ and $\gamma = 0.3$.

lattice for a variety of parameters in figure 5.9, dividing by ζ to account for the (undetected) vacuum output to obtain the un-normalised evolution. We also plot the average (first order) correlation between spins separated by a distance (n, m)

$$\left\langle \sigma^z_{J,K} \sigma^z_{J+n,K+m} \right\rangle = \frac{1}{2\left(N_1 - n\right)\left(N_2 - m\right)} \sum_{j=1}^{N_1-n} \sum_{k=1}^{N_2-m} \left(\left\langle \sigma^z_{j,k} \sigma^z_{j+n,k+m} \right\rangle + \left\langle \sigma^z_{j,k} \sigma^z_{j+n,k-m} \right\rangle \right), \tag{5.81}$$

demonstrating that this system still evolves in the paramagnetic and ferromagnetic phases in the unbroken $\mathcal{PT}$-symmetric regime.

These dynamics depend on the parameter $\beta = \sqrt{h^2 - \gamma^2}$. When $\beta \in \mathbb{R}$, the evolution can either be oscillatory, or if $h \gg \gamma$, can be paramagnetic as in figure 5.9.

To demonstrate the different phases of this system, we also plot the average normalised correlation,

$$\left\langle \sigma^z_{J,K} \sigma^z_{J+n,K+m} \right\rangle_{\text{norm}} = \frac{1}{P} \left\langle \sigma^z_{J,K} \sigma^z_{J+n,K+m} \right\rangle, \tag{5.82}$$

in figure 5.10 for the Hermitian and unbroken phase and figure 5.11 for the EP and broken phase. These demonstrate the different correlations that arise from crossing the EP and the Critical Points (CPs) where $|h| = |j|$ and $\gamma = 0$. These CPs separate the ferromagnetic phase from the paramgnetic phase. In the $\mathcal{PT}$-unbroken phase, away from the CPs, in the ferromagnetic phase, the system is always correlated, oscillating between a highly correlated and less correlated system. In the paramagnetic phase, these oscillations can cause different parts of the state to become anti-correlated in the σ^z direction. Breaking the $\mathcal{PT}$ symmetry then causes the system to evolve towards a fixed point of low correlations. At the EP, the system similarly evolves towards a fixed point, except here, it is a completely correlated/anti-correlated one, depending on correlation distance.

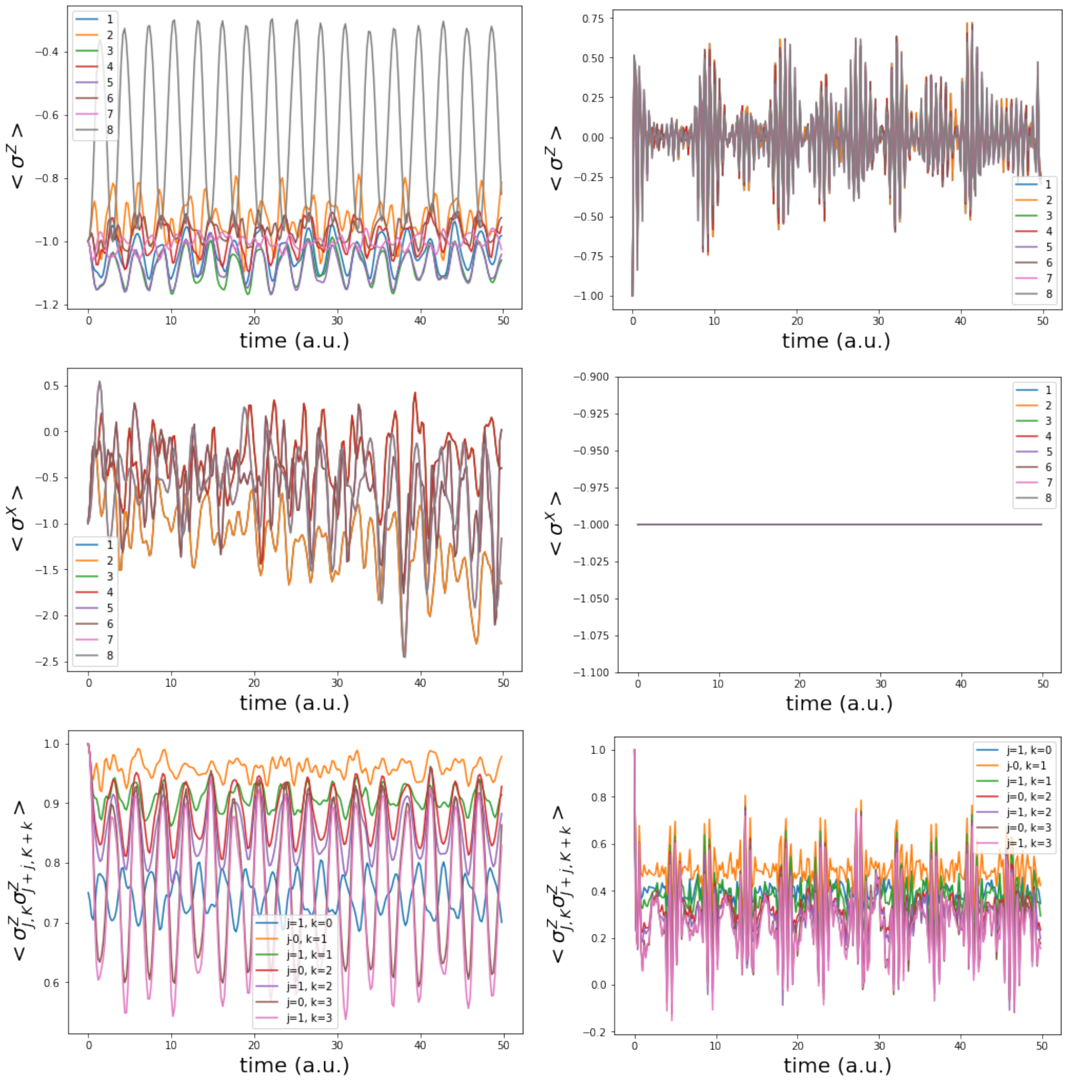

Figure 5.9: Evolution of the $\mathcal{PT}$-symmetric Heisenberg spin lattice Hamiltonian given by equation 5.78, setting $J = 1$, with qubit-qubit coupling in the z-direction, applied magnetic field in the x-direction and $\mathcal{PT}$-symmetry parameter γ in the y-direction. Top: Average spin in the z-direction, $\langle \sigma^z \rangle$, starting from the state $|0\rangle_{2,4}$ Middle: Average spin in the x-direction, $\langle \sigma^x \rangle$, starting from the state $|+\rangle_{2,4}$. Bottom: Average Correlation, equation 5.81, starting from the state $|0\rangle_{2,4}$. Left: $h = 0.5$, $\gamma = 0.2$. Right: $h = 1000$, $\gamma = 1$. While for $\gamma < h \leq J = 1$, the evolution of $\langle \sigma^x \rangle$ is seemingly random, if oscillatory, when $h > J$ and $h \gg \gamma$, the spin chain is paramagnetic, with $\langle \sigma^x \rangle \approx 1$. In contrast, the evolution of $\langle \sigma^z \rangle$ is highly oscillatory regardless of whether the system is in a paramagnetic or ferromagnetic phase, as long as it is in the unbroken $\mathcal{PT}$-symmetry phase.

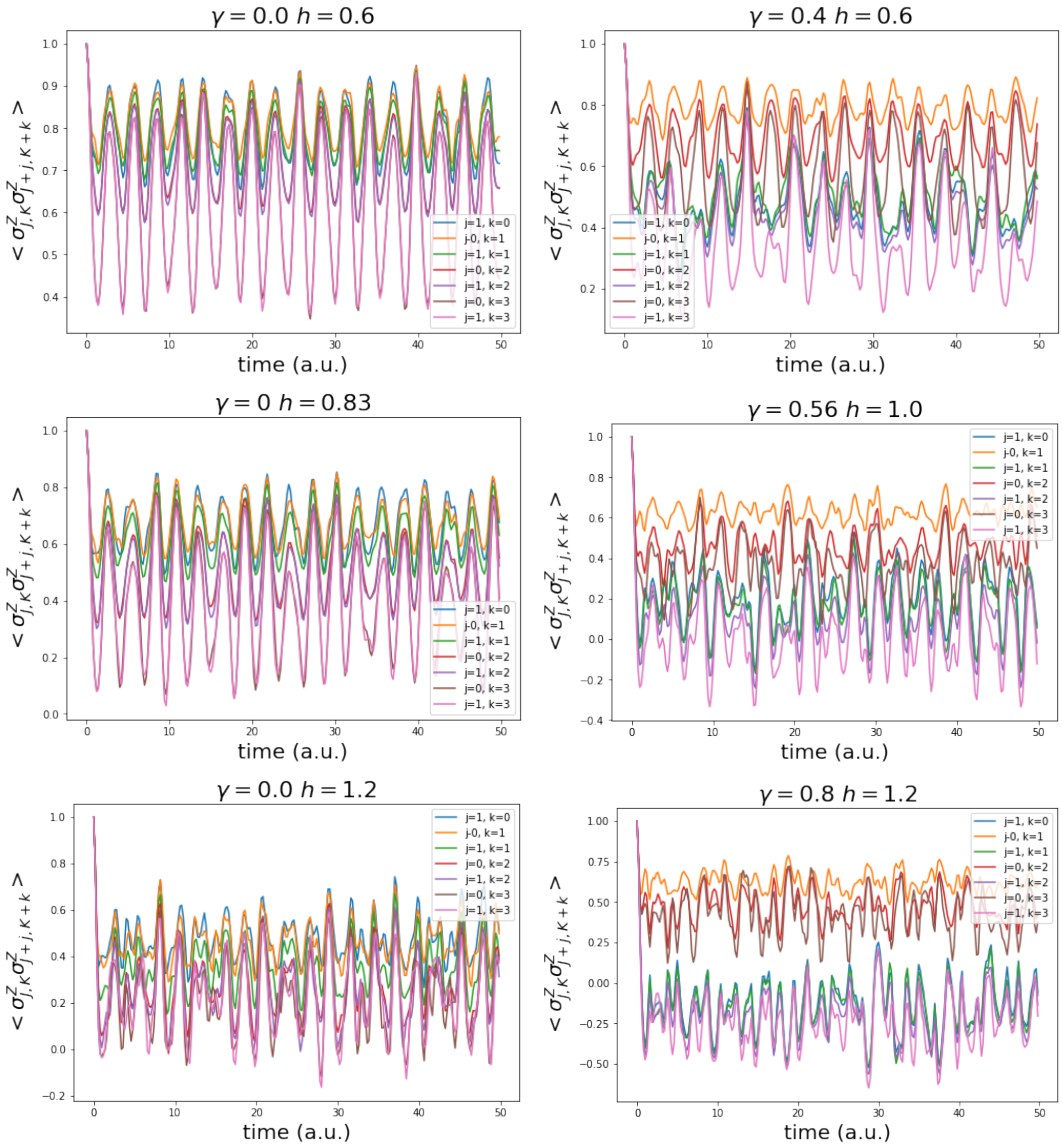

Figure 5.10: Evolution of the $\mathcal{PT}$-symmetric Heisenberg spin lattice Hamiltonian given by equation 5.78, setting $J = 1$, with qubit-qubit coupling in the z-direction, applied magnetic field in the x-direction and $\mathcal{PT}$-symmetry parameter γ in the y-direction. Left: Hermitian phase, where $\gamma = 0$; right: non-Hermitian $\mathcal{PT}$-unbroken phase, where $0 < \gamma^2 < h^2$. Top: Extension of ferromagnetic phase, with $\beta < 0.83$; middle: (approximate) Critical Point, $h \approx 0.83$ extended to values $\beta \approx 0.83$; bottom: Paramagnetic phase, $\beta > 0.83$. This demonstrates that in the Hermitian and $\mathcal{PT}$-symmetric regime, increasing the value of h lowers both the maximum and minimum value of the normalised correlation, with a small anticorrelation as the Critical Point is approached. Increasing the value of γ tends to increase the correlation (anticorrelation) of the spins with the same (different) j position, due to the alternating sign of γ in the Hamiltonian.

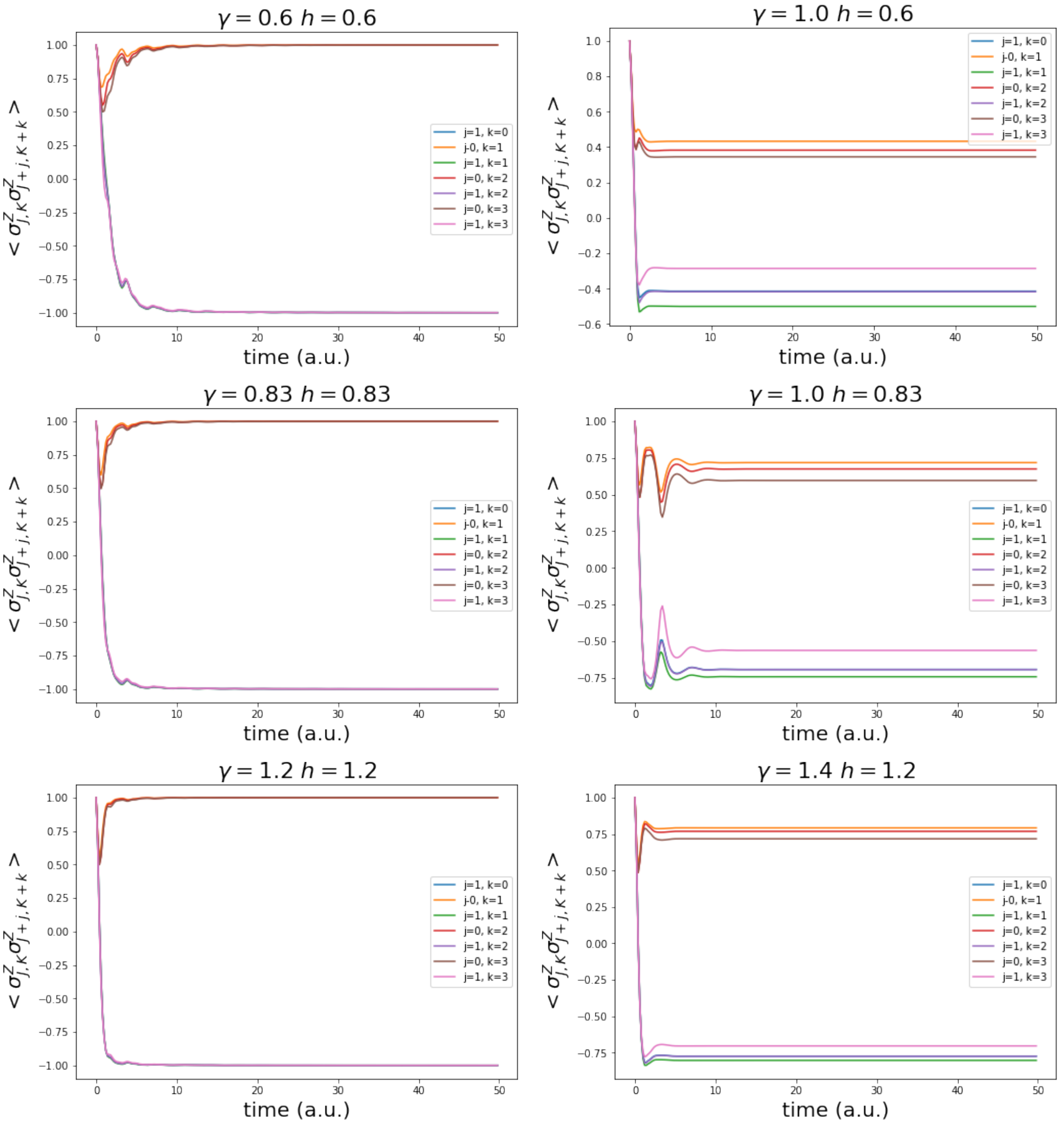

Figure 5.11: Evolution of the $\mathcal{PT}$-symmetric Heisenberg spin lattice Hamiltonian given by equation 5.78, setting $J = 1$, with qubit-qubit coupling in the z-direction, applied magnetic field in the x-direction and $\mathcal{PT}$-symmetry parameter γ in the y-direction. Left: Exceptional Point (EP), $\gamma^2 = h^2$ and $\beta = 0$; Right: $\mathcal{PT}$-broken phase, $\gamma^2 > h^2$. Top: $h = 0.6 < 0.83$; middle: $h = 0.83 \approx 0.83$; right: $h = 1.2 > 0.83$. This demonstrates that, at the Exceptional Point, the system is maximally (anti-)correlated, where the normalised correlation between any 2 points becomes ± 1, depending on the $j-$distance between the two points. In the broken phase, the system then becomes less (anti-)correlated.

5.8 Discussion and Conclusion

In this chapter, we have shown a link between symplectic transformations in nonlinear optical systems and $\mathcal{PT}$-(anti-)symmetry. We used this to create a design of a nonlinear optical interferometer implementing a nonunitary transformation on the optical modes. This could be considered as an extension to a typical linear interferometer, such as a Reck or Clements scheme, which implements unitary transformations. As with these interferometers, there are two sources of inefficiency in this nonunitary interferometer when used as a method of simulating Hamiltonians. One is unavoidable when creating transformations on modes in that, comparing with qubits, a linear number of qubits (typically considered when calculating computational complexity) is equivalent to an exponential number of modes. In this, an interferometer with only a single photon input cannot be considered as an efficient method of quantum simulation, which is also true of the nonunitary interferometer considered in this chapter. However, the other source of inefficiency, arising from exponentiating the Hamiltonian, can in principle be removed. As with Hermitian Hamiltonians, this is done by the process of Trotterisation. This allows us to simulate a Hamiltonian to within a given error in a polynomial (here quadratic) time, with the difference between typical (Hermitian) Trotterisation processes and the process used here being that the norm (maximum singular value) of the nonunitary matrix being simulated multiplied by the probability of obtaining a single photon adds to the simulation error. However, as the norm of a matrix can be efficiently upper bounded, the process remains efficient for non-zero error.

We then created a model for a 2D $\mathcal{PT}$-symmetric staggered transverse field Heisenberg spin lattice and used a typical tensor network (with no additions) to numerically calculate the ground state of an infinite lattice in the $\mathcal{PT}$-unbroken phase. This showed a critical point in the Hermitian phase that can be encircled in the $\mathcal{PT}$-unbroken phase. This also showed that the ferromagnetic and parramagnetic phases that appear in the Hermitian phase can be extended into the $\mathcal{PT}$-unbroken phase. We then emulated the nonunitary interferometer simulating this Hamiltonian for a small lattice over the various different phases that exist. While the largest differences occur between the Hermitian/unbroken (where the correlations are oscillatory) and EP/broken phases (where the correlations tend towards a stationary fixed point), increasing the value of the $\mathcal{PT}$-symmetry parameter increases the amount of splitting that occurs in the (anti-)correlation present in the lattice, where spins increasingly tend to align in one direction or the other. This effect is maximised at the EP, after which (in the broken phase), while the system still tends towards a fixed steady state, this state is less (anti-)correlated than at the EP.

Chapter 6

Parity-Time Symmetric Coupled Microring Resonators

> *Forwards and backwards crossovers in a figure of 8*
>
> — British Ice Skating, *Learn to Skate*

Section 6.1 is an introductory/background section and contains a summary of this chapter. The rest of this chapter is my own work The definitions and calculations in section 6.2 are largely relatively trivial extensions of pre-existing work and are included for both completeness and a lack of these definitions and calculations existing for coupled rings. This chapter is based on [72].

6.1 Introduction

Many of the typical methods of creating $\mathcal{PT}$-symmetric systems involve using systems with both gain and loss. A typical small system would be two modes, such as waveguides, coupled together, one with gain and the other with the same amount of loss as the first has gain, such as [73]. Such a system is often described by a Hamiltonian with gain and loss terms on the diagonal of the matrix, such as

$$H_2 = \begin{pmatrix} i\gamma & 1 \\ 1 & -i\gamma \end{pmatrix}, \tag{6.1}$$

as considered in chapter 4. Much of the theoretical work of quantum $\mathcal{PT}$-symmetry has also been with such Hamiltonians featuring multiple modes with loss and gain. Similarly, simulations of quantum $\mathcal{PT}$-symmetric systems, whether quantum or classical simulations, are also often focused on systems with loss and gain on the diagonal elements of the Hamiltonian, such as [74]. This is true even of non-$\mathcal{PT}$-symmetric systems with loss and gain, such as [75].

However, it was recently found that such '$\mathcal{PT}$symmetric photonic quantum systems with gain and loss do not exist' [35]. As such, different forms of $\mathcal{PT}$-symmetric Hamiltonians than diagonal terms giving gain and loss are considered in this chapter. However, we still look

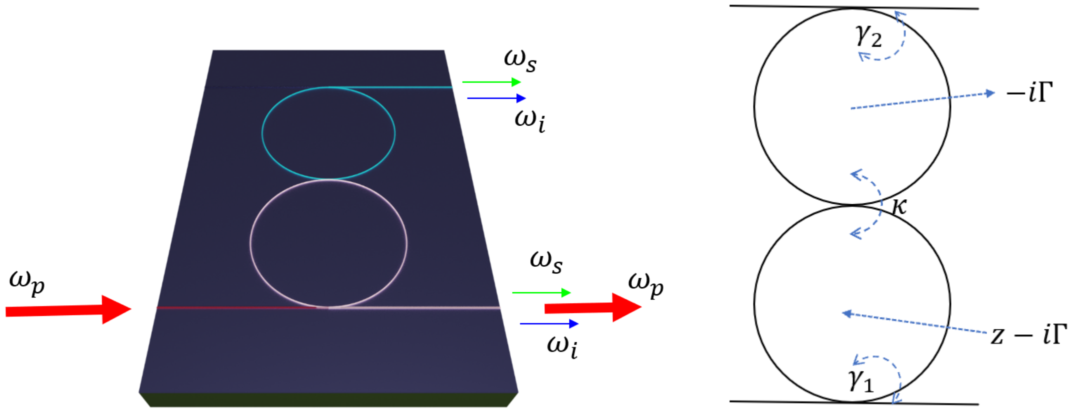

Figure 6.1: Diagram of the coupled rings modelled in this chapter. A pump (pulsed or continuous wave) is input into a waveguide, which couples into a microring resonantor. In this ring, Four Wave Mixing (FWM) or Spontanteous Paramtric Down Converesion (SPDC) may occur, creating a 2 mode squeezed state in signal and idler photon modes. The pump is therefore considered as a 'gain' on these two modes in this first/lower ring. The created signal and idler photons then couple into a second (top) ring and potentially out a second waveguide. Both rings have an 'intrinsic' loss that is unavoidable due to e.g. surface roughness. Coupling into the waveguide gives an additional (albeit coherent) loss term. This gives tunable gain, coupling and loss, although the corresponding non-Hermitian matrix (describing the transformation on the created photon modes) has a more complicated structure than most typically considered or simulated $\mathcal{PT}$-symmetric Hamiltonians.

at systems that could be considered to have gain and loss in a different format. To do this, we look at nonlinear optical systems which give symplectic, nonunitary transformations on the creation/annihilation operators. We consider squeezing as a 'gain' operation, which can be balanced with any intrinsic loss of the system to create a $\mathcal{PT}$-symmetric quantum system. Such a system could be coupled waveguides, or as in this chapter, coupled microring resonators, as shown in figure 6.1.

To do this, we follow the notation of Vernon and Sipe [76, 77], which we extend to coupled rings. In doing this, we show that $\mathcal{PT}$-symmetric quantum systems can exist. This also gives that different methods of creating the system give different results. This is shown by comparing the results of a pulsed input to that of a continuous wave (CW) input. While both of these are $\mathcal{PT}$-symmetric, using the pulsed input, the Excpetionl Point of the system can only be found numerically and appears independently of the input power. However, for a CW input, there are multiple EPs and the quantum to classical threshold can be easily shown and depends on the input power.

In section 6.2, we start by taking the Hamiltonian of the system, consisting of a linear and a nonlinear term in the Hamiltonian and use this to calculate the transformation of the creation and annihilation operators, which can then be used to write a matrix equation, which we descibe as an effective (non-Hermitian) Hamiltonian. The nonlinear term depends on the order of the electric susceptibility $\chi^{(n)}$ of the material. Typically considered materials are either second order, allowing for effects such as Spontaneous Parametric Down Conversion (SPDC, where each pump photon annihilated creates a signal and idler photon); or third order, allowing for effects such as Four Wave Mixing (FWM, 2 pump photons creating a signal and idler photon) and Cross- and Self- Phase Modulation (XPM and SPM, where the optical Kerr effect causes changes in phases of the pump, signal and idler photons). In order to linearise the equations of motion and write them as a matrix equation, non-degenerate processes will be assumed, where the signal and idler photons have different frequencies so that they can be treated separately. The eigenvalues and eigenvectors of the effective Hamiltonian created in section 6.2 are then found in section 6.3 and used to find the Exceptional Points (EPs) of the system. For a CW pump, this gives a variety of types of EPs, which can be defined by whether they occur on a lossy background, neutral background, or a background with gain. However, the transition from a lossy background to one with gain is the transition from quantum to classical behaviour, so the background of gain gives (the classical effect of) Optical Parametric Oscillation and cannot be described by the method used here due to the above method of linearising, which ignores terms important in OPO. However, for a pulsed pump, the EPs are found in reverse, by finding the results that demonstrate a typical EP-type enhancement in section 6.6 from the Joint Spectral Intensity (JSI) defined in section 6.4, which shows a noticeable difference between being at the EP and not, which also shows the effects of an EP with a CW pump. To calculate these results, the equations of motions are solved in section 6.5.

However, an EP of the system does not necessarily mean that the system is better than the non-$\mathcal{PT}$-symmetric version. While an increase in the number of photons output from a $\mathcal{PT}$-symmetric photon source could be expected compared with the non-$\mathcal{PT}$-symmetric equivalent, we find that this does not always happen here. Rather, for a pulsed input, the best results (being an enhancement in output photon number of orders of magnitude for the given input pump strength and simultaneously single photon purities well above 99%) come from matching the coupling with the difference between the losses in the rings to find an EP (i.e. the input pump strength is independent of the EP enhancement) and if the difference in losses are too small, there may be no EP enhancement found. This is opposed to the more typically considered idea where gain, coupling and loss are matched. There may be other potential advantages to having coupled rings not considered here, such as a potential reduction in thermal noise due to parasitic nonlinear effects [78], as well as differences between the theoretical model and experimental implementation that any such predictions need to be compared in experiment.

6.2 Transformation of operators in coupled rings

We start with the Linear part of the Hamiltonian of [76, 77], extending it to include multiple rings and adding additional terms that describe point coupling between the rings. That is, we take $H = H_L + H_{NL}$, where the linear term is given by

$$
\begin{aligned}
H_L ={}& H_{\text{waveguides}} + H_{\text{ring},L} + H_{\text{coupling, rr}} + H_{\text{coupling, rw}} \qquad (6.2)\\
={}& \hbar \sum_{J,n} \left[\omega_J \int \psi^{\dagger}_{J,n}(x)\, \psi_{J,n}(x)\, dx + \frac{1}{2} i v_J \int \frac{d\psi^{\dagger}_{J,n}(x)}{dx} \psi_{J,n}(x) - \psi^{\dagger}_{J,n}(x) \frac{d\psi_{J,n}(x)}{dx}\, dx \right] \\
&+ \hbar \sum_{J,n} \left[\omega_J \int \phi^{\dagger}_{J,n}(x)\, \phi_{J,n}(x)\, dx + \frac{1}{2} i v_J \int \frac{d\phi^{\dagger}_{J,n}(x)}{dx} \phi_{J,n}(x) - \phi^{\dagger}_{J,n}(x) \frac{d\phi_{J,n}(x)}{dx}\, dx \right] \\
&+ \hbar \sum_{J,n} \left[\omega_J b^{\dagger}_{J,n} b_{J,n} \right] + \hbar \sum_{J} \left[\kappa_J b^{\dagger}_{J1} b_{J2} + \kappa^{*}_J b^{\dagger}_{J2} b_{J1} \right] \\
&+ \hbar \sum_{J,n} \left[\gamma_{J,n} b^{\dagger}_{J,n} \psi_{J,n}(0) + \gamma^{*}_{J,n} b_{J,n} \psi^{\dagger}_{J,n}(0) + \mu_{J,n} b^{\dagger}_{J,n} \phi_{J,n}(0) + \mu^{*}_{J,n} b_{J,n} \phi^{\dagger}_{J,n}(0) \right], \qquad (6.3)
\end{aligned}
$$

where the subscript J represents the frequency mode (pump P, signal S and idler I) and subscript n, the ring mode (rings 1 and 2 for 2 coupled rings). ω is the frequency of mode J, γ is the coupling rate between ring and waveguide and κ is the coupling rate between rings. The creation and annihilation operators of the photons in the waveguides are given by $\psi^{\dagger}$ and ψ respectively and similarly, the creation and annihilation operators of the photons in the rings are given by $b^{\dagger}$ and b. Additional creation and annihilation operators, denoted by $\phi^{\dagger}$ and ϕ are also used to represent 'phantom' waveguides used to model additional intrinsic loss of the system. The nonlinear term depends on the order of the electric susceptibility. For second order $\chi^{(2)}$ processes, there is only a single nonlinear term involving 3 frequency modes that conserves energy, which gives the nonlinear part of the SPDC Hamiltonian

$$
H_{NL2} = \hbar \sum_{n} \left[\Lambda b_{Pn} b^{\dagger}_{Sn} b^{\dagger}_{In} + \Lambda^{*} b^{\dagger}_{Pn} b_{Sn} b_{In} \right], \qquad (6.4)
$$

where Λ is here given by [77, 79]

$$
\Lambda \approx \frac{\sqrt{\hbar \omega_P^3}\, \chi^{(2)}}{4 \epsilon_0 n^4 V_{\text{ring}}}. \qquad (6.5)
$$

This describes the SPDC process where pump photons get down converted into signal and idler photons. For third order $\chi^{(3)}$ processes, there are multiple allowed terms for 3 modes, so the nonlinear part of the FWM Hamiltonian is

$$
\begin{aligned}
H_{NL3} ={}& \hbar \sum_{n} \Big[\Lambda b_{Pn} b_{Pn} b^{\dagger}_{Sn} b^{\dagger}_{In} + \Lambda^{*} b^{\dagger}_{Pn} b^{\dagger}_{Pn} b_{Sn} b_{In} \\
&+ \eta b^{\dagger}_{Pn} b^{\dagger}_{Pn} b_{Pn} b_{Pn} + \zeta b^{\dagger}_{Sn} b^{\dagger}_{Pn} b_{Sn} b_{Pn} + \zeta b^{\dagger}_{In} b^{\dagger}_{Pn} b_{In} b_{Pn} \Big], \qquad (6.6)
\end{aligned}
$$

where we now have [77, 79]

$$\Lambda = 2\eta = \frac{\zeta}{2} \approx \frac{\hbar\omega_P^2\chi^{(3)}}{4\epsilon_0 n^4 V_{\text{ring}}} = \frac{\hbar\omega_P^2 c n_2}{n^2 V_{\text{ring}}}. \tag{6.7}$$

Λ is the rate of FWM, where pairs of pump photons are converted into signal and idler photons, η is the rate of SPM and ζ XPM, which cause the pump and signal idler photons to gain additional phases. For the pump operator in ring 1, the Heisenberg equations of motion can be written for SPDC as

$$\left(\frac{d}{dt} + i\omega_P\right) b_{P1}(t) = -i\gamma_{P1}^*\psi_{P1}(0,t) - i\mu_{P1}^*\phi_{P1}(0,t) - i\Lambda^* b_{S1}(t)\, b_{I1}(t) - i\kappa b_{P2}(t), \tag{6.8}$$

and for FWM as

$$\begin{aligned}\left(\frac{d}{dt} + i\omega_P + 2i\eta b_{P1}^\dagger(t)\, b_{P1}(t)\right) b_{P1}(t) = -i\gamma_{P1}^*\psi_{P1}(0,t) - i\mu_{P1}^*\phi_{P1}(0,t)\\ - 2i\Lambda^* b_{P1}^\dagger(t)\, b_{S1}(t)\, b_{I1}(t) - i\kappa b_{P2}(t)\end{aligned} \tag{6.9}$$

with equivalent equations for the other modes and ring. Defining $\bar{A}_{J,n} = e^{i\omega_J t}A_{J,n}$, $\Delta = \omega_S + \omega_I - 2\omega_P$ and splitting the waveguide operators into 'input' and 'output' operators

$$\psi_{Jn}(x,t) = \begin{cases} \psi_{Jn<}(x,t) & \text{for } x<0 \\ \psi_{Jn>}(x,t) & \text{for } x>0 \end{cases}, \qquad \phi_{Jn}(x,t) = \begin{cases} \phi_{Jn<}(x,t) & \text{for } x<0 \\ \phi_{Jn>}(x,t) & \text{for } x>0, \end{cases} \tag{6.10}$$

with

$$\psi_{Jn}(0,t) = \frac{1}{2}\left(\psi_{Jn<}(0,t) + \psi_{Jn>}(0,t)\right), \tag{6.11}$$

allows us to calculate the Heisenberg Equations of Motion in the rotating frame, used throughout this chapter. Given in full in appendix B, for the pump operators in ring 1, these are

$$\left(\frac{d}{dt} + \bar{\Gamma}_{P1}\right)\bar{b}_{P1}(t) = -i\gamma_{P1}^*\bar{\psi}_{P1<}(0,t) - i\mu_{P1}^*\bar{\phi}_{P1<}(0,t) - i\Lambda^*\bar{b}_{S1}(t)\,\bar{b}_{I1}(t)\, e^{-i\Delta t} - i\kappa\bar{b}_{P2}(t) \tag{6.12}$$

for SPDC and

$$\begin{aligned}\left(\frac{d}{dt} + \bar{\Gamma}_{P1} + 2i\eta\bar{b}_{P1}^\dagger(t)\,\bar{b}_{P1}(t)\right)\bar{b}_{P1}(t) = -i\gamma_{P1}^*\bar{\psi}_{P1<}(0,t) - i\mu_{P1}^*\bar{\phi}_{P1<}(0,t)\\ - 2i\Lambda^*\bar{b}_{P1}^\dagger(t)\,\bar{b}_{S1}(t)\,\bar{b}_{I1}(t)\, e^{-i\Delta t} - i\kappa\bar{b}_{P2}(t)\end{aligned} \tag{6.13}$$

for FWM, where the loss rate of mode J in ring n is defined (independently of SPDC or FWM processes) as

$$\bar{\Gamma}_{Jn} = \sum_m \Gamma_{Jm} + M_{Jn} = \sum_m \frac{|\gamma_m|^2}{2v} + \frac{|\mu_n|^2}{2u}, \tag{6.14}$$

where the sum over m accounts for the waveguides m that couple into ring n[1]. Taking the undepleted pump approximation, making the $\Lambda^*\bar{b}^\dagger_{Pn}(t)\,\bar{b}_{Sn}(t)\,\bar{b}_{In}(t)\,e^{-i\Delta t}$ terms in the pump equations negligible allows for a semi-classical solution. This is done by replacing the pump operators by their expectation values:

$$\langle\phi_{P1<}\rangle = \langle\phi_{P2<}\rangle = 0, \qquad b_{P1} \to \langle b_{P1}\rangle = \beta_{P1}, \qquad b_{P2} \to \langle b_{P2}\rangle = \beta_{P2}. \tag{6.15}$$

The equations of motion can now be written as the matrix equation

$$i\frac{d}{dt}\begin{pmatrix}\bar{b}_{S1}(t)\\ \bar{b}^\dagger_{I1}(t)\\ \bar{b}_{S2}(t)\\ \bar{b}^\dagger_{I2}(t)\end{pmatrix} = \bar{H}_{\text{eff}}\begin{pmatrix}\bar{b}_{S1}(t)\\ \bar{b}^\dagger_{I1}(t)\\ \bar{b}_{S2}(t)\\ \bar{b}^\dagger_{I2}(t)\end{pmatrix} + \bar{D}, \tag{6.16}$$

where

$$\bar{D} = \begin{pmatrix}\left[\gamma^*_{S1}\bar{\psi}_{S1<}(0,t) + \mu^*_{S1}\bar{\phi}_{S1<}(0,t)\right]\\ -\left[\gamma_{I1}\bar{\psi}^\dagger_{I1<}(0,t) + \mu_{I1}\bar{\phi}^\dagger_{I1<}(0,t)\right]\\ \left[\gamma^*_{S2}\bar{\psi}_{S2<}(0,t) + \mu^*_{S2}\bar{\phi}_{S2<}(0,t)\right]\\ -\left[\gamma_{I2}\bar{\psi}^\dagger_{I2<}(0,t) + \mu_{I2}\bar{\phi}^\dagger_{I2<}(0,t)\right]\end{pmatrix} \tag{6.17}$$

is the driving term, consisting of the input waveguide operators, with elements labelled $\bar{D}_{Kn}$, and

$$\bar{H}_{\text{SPDC, eff}} = \begin{pmatrix}-i\bar{\Gamma}_{S1} & \Lambda\bar{\beta}_{P1}(t) & \kappa & 0\\ -\Lambda^*\bar{\beta}^*_{P1}(t) & -i\bar{\Gamma}_{I1} & 0 & -\kappa^*\\ \kappa^* & 0 & -i\bar{\Gamma}_{S2} & \Lambda\bar{\beta}_{P2}(t)\\ 0 & -\kappa & -\Lambda^*\bar{\beta}^*_{P2}(t) & -i\bar{\Gamma}_{I2}\end{pmatrix}, \tag{6.18}$$

$$\bar{H}_{\text{FWM, eff}} = \begin{pmatrix}-i\bar{\Gamma}_{S1} + \zeta|\bar{\beta}_{P1}(t)|^2 & \Lambda\bar{\beta}^2_{P1}(t) & \kappa & 0\\ -\Lambda^*\bar{\beta}^{*2}_{P1}(t) & -i\bar{\Gamma}_{I1} - \zeta|\bar{\beta}_{P1}(t)|^2 & 0 & -\kappa^*\\ \kappa^* & 0 & -i\bar{\Gamma}_{S2} + \zeta|\bar{\beta}_{P2}(t)|^2 & \Lambda\bar{\beta}^2_{P2}(t)\\ 0 & -\kappa & -\Lambda^*\bar{\beta}^{*2}_{P2}(t) & -i\bar{\Gamma}_{I2} - \zeta|\bar{\beta}_{P2}(t)|^2\end{pmatrix} \tag{6.19}$$

are the effective Hamiltonians for SPDC and FWM determining the evolution of mode operators. This gives the state of the ring operators at time t as

$$\begin{pmatrix}\bar{b}_{S1}(t)\\ \bar{b}^\dagger_{I1}(t)\\ \bar{b}_{S2}(t)\\ \bar{b}^\dagger_{I2}(t)\end{pmatrix} = -i\int_{-\infty}^{t}\Theta\left(t-t'\right)G\left(t-t'\right)\bar{D}\left(t'\right)\,dt', \tag{6.20}$$

---

[1] For ring-waveguide couplings more complicated than the one-to-one coupling used here, a matrix containing elements γ_{nm} could instead be used

for $G(t-t') = e^{-i\tilde{H}_{\text{eff}}(t-t')}$, with elements G_{JmKn} relating input Kn to output Jm. That is, $\tilde{b}_{Jm} = -i\sum_{Kn}\int_{-\infty}^{t}\Theta(t-t')\,G_{JmKn}(t-t')\,\bar{D}_{Kn}(t')$, which allows for calculating the output operators

$$\bar{\psi}_{Jm>}(0,t) = \bar{\psi}_{Jm<}(0,t) - \frac{i\gamma_{Jm}}{v_J}\bar{b}_{Jm}(t) \tag{6.21}$$

$$\begin{aligned}\bar{\psi}_{Jm>}(0,t) = \int\sum_{n}\big[&q_{JmJn}(t-t')\,\bar{\psi}_{Jn<}(0,t') + p_{JmJn}(t-t')\,\bar{\phi}_{Jn<}(0,t')\\ &+ q_{JmKn}(t-t')\,\bar{\psi}^{\dagger}_{Kn<}(0,t') + p_{JmKn}(t-t')\,\bar{\phi}^{\dagger}_{Kn<}(0,t')\,\big]dt',\end{aligned} \tag{6.22}$$

where for $J = S(I)$, $K = I(S)$ and the terms that describe the transformation from input (real and phantom) waveguide operators to output waveguide operators are, for $J = S$,

$$q_{JmKn}(t-t') = \delta_{JK}\delta_{mn}\delta(t-t') \pm \frac{\gamma_{Jm}\gamma^{*}_{Kn}}{v_{Jm}}e^{-i\Delta_p(t\pm t')}G_{JmKn}(t-t'), \tag{6.23}$$

$$p_{JmKn}(t-t') = \pm\frac{\gamma_{Jm}\mu^{*}_{Kn}}{v_{Jm}}e^{-i\Delta_p(t\pm t')}G_{JmKn}(t-t') \tag{6.24}$$

and for $J = I$,

$$q_{JmKn}(t-t') = \delta_{JK}\delta_{mn}\delta(t-t') \pm \frac{\gamma_{Jm}\gamma^{*}_{Kn}}{v_{Jm}}e^{-i\Delta_p(t\pm t')}G^{*}_{JmKn}(t-t'), \tag{6.25}$$

$$p_{JmKn}(t-t') = \pm\frac{\gamma_{Jm}\mu^{*}_{Kn}}{v_{Jm}}e^{-i\Delta_p(t\pm t')}G^{*}_{JmKn}(t-t') \tag{6.26}$$

where $+$ is used for $J \neq K$ and $-$ for $J = K$. These can then be used to calculate the correlation functions in section 6.4.

6.2.1 Stability of the steady state pump solution

When the pump is a CW pump, in the steady state, semi-classical approximation, we can calculate the expectation value of the pump by putting the equations of motion for the pump (equations 6.12 and B.4 for SPDC and 6.13 and B.10 for FWM) into matrix form. For SPDC, this gives

$$\frac{d}{dt}\begin{pmatrix}\bar{\beta}_{P1}(t)\\ \bar{\beta}_{P2}(t)\end{pmatrix} = -i\begin{pmatrix}-i\bar{\Gamma}_{P1} & \kappa\\ \kappa^{*} & -i\bar{\Gamma}_{P2}\end{pmatrix}\begin{pmatrix}\bar{\beta}_{P1}(t)\\ \bar{\beta}_{P2}(t)\end{pmatrix} - i\begin{pmatrix}\gamma^{*}_{P1}\bar{\alpha}_{P1}e^{-i\Delta_{P1}t}\\ \gamma^{*}_{P2}\bar{\alpha}_{P2}e^{-i\Delta_{P2}t}\end{pmatrix}, \tag{6.27}$$

where the input to each ring has been assumed to be a CW input with a constant dephasing Δ_{Pn} such that

$$\left\langle\bar{\psi}_{Pn<}(0,t)\right\rangle = \bar{\alpha}_{Pn}e^{-i\Delta_{Pn}}, \qquad \left\langle\bar{\phi}_{Pn<}(0,t)\right\rangle = 0. \tag{6.28}$$

We then define $\tilde{\beta}_{Pn} = \bar{\beta}_{Pn}e^{-i\Delta_{Pn}t}$, which is constant in a steady state solution: $\dot{\tilde{\beta}}_{Pn}(t) = 0$, simplifying equation 6.27 into

$$\begin{pmatrix}-i\bar{\Gamma}_{P1} - \Delta_{P1} & \kappa e^{i(\Delta_{P2}-\Delta_{P1})t}\\ \kappa^{*}e^{-i(\Delta_{P2}-\Delta_{P1})t} & -i\bar{\Gamma}_{P2} - \Delta_{P2}\end{pmatrix}\begin{pmatrix}\tilde{\beta}_{P1}(t)\\ \tilde{\beta}_{P2}(t)\end{pmatrix} = -\begin{pmatrix}\gamma^{*}_{P1}\bar{\alpha}_{P1}\\ \gamma^{*}_{P2}\bar{\alpha}_{P2}\end{pmatrix}. \tag{6.29}$$

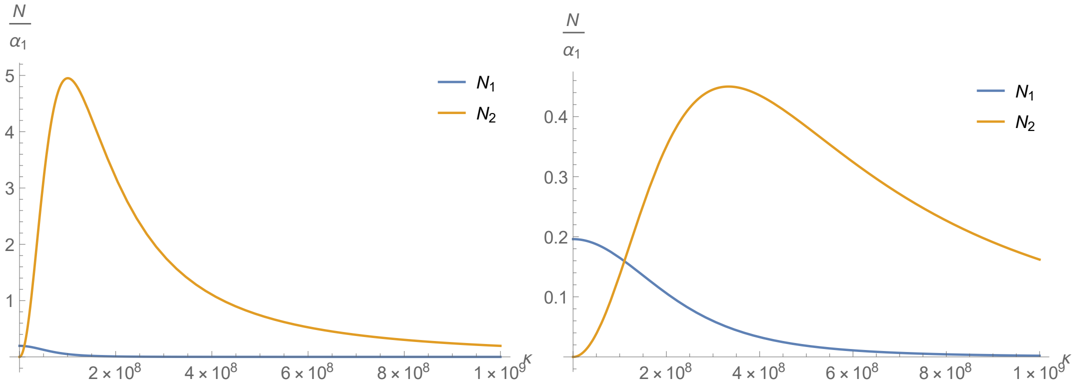

Figure 6.2: Graph of the photon number $N = |\beta|^2$ in the coupled ring system of a $\chi^{(2)}$ material, with no detuning. Left is when there is only a single waveguide coupled to the system (via the first ring) here giving $\bar{\Gamma}_1 \sim 10^9$ and $\bar{\Gamma}_2 \sim 10^7$ and the light gets 'stored' in the second ring. However, very little of the light stored is able to get coupled out again, so the system has a very low efficiency. Right graph is turning the second waveguide coupling on (although still with only one pump input, into the first waveguide), now giving $\bar{\Gamma}_2 \sim 10^8$. This waveguide now means that the light can no longer be stored and it instead coupled out via the top waveguide. However, as the light that was in the second ring can now be easily output, a higher proportion of the input light is coupled to the output, as opposed to incoherently lost as is the case with the left graph.

This gives the solution

$$\begin{pmatrix} \tilde{\beta}_{P1}(t) \\ \tilde{\beta}_{P2}(t) \end{pmatrix} = \frac{1}{\left(i\bar{\Gamma}_{P1} + \Delta_{P1}\right)\left(i\bar{\Gamma}_{P2} + \Delta_{P2}\right) - |\kappa|^2} \begin{pmatrix} i\bar{\Gamma}_{P2} + \Delta_{P2} & \kappa e^{i(\Delta_{P2}-\Delta_{P1})t} \\ \kappa^* e^{-i(\Delta_{P2}-\Delta_{P1})t} & i\bar{\Gamma}_{P1} + \Delta_{P1} \end{pmatrix} \begin{pmatrix} \gamma_{P1}^* \bar{\alpha}_{P1} \\ \gamma_{P2}^* \bar{\alpha}_{P2} \end{pmatrix}. \tag{6.30}$$

Particularly interesting is the case where the pump only couples in and out through one waveguide. Here, shown in figure 6.2, the second ring acts as a 'storage' in the steady state, having more light in a given instant than is coupled into the system at that instant (although overall this system is very inefficient). In the case where only one ring is resonant with the pump frequency (setting $\kappa = 0$ and $\alpha_{P2} = 0$; taken to be ring 1 without loss of generality), shown in figure 6.3 this further gives

$$\tilde{\beta}_P = \frac{\gamma_P^* \bar{\alpha}_P}{i\bar{\Gamma}_P + \Delta_P} \implies N_P = |\beta_P|^2 = \frac{|\gamma_P|^2 |\alpha_P|^2}{\bar{\Gamma}_P^2 + \Delta_P^2}. \tag{6.31}$$

Following [80] and adding a perturbation $\tilde{\beta}_{Pn}(t) = \tilde{\beta}_{Pn}^{(0)} + \delta\tilde{\beta}_{Pn}(t)$ gives

$$\frac{d}{dt}\begin{pmatrix} \delta\bar{\beta}_{P1}(t) \\ \delta\bar{\beta}_{P2}(t) \end{pmatrix} = -i \begin{pmatrix} -i\bar{\Gamma}_{P1} - \Delta_{P1} & \kappa e^{i(\Delta_{P2}-\Delta_{P1})t} \\ \kappa^* e^{-i(\Delta_{P2}-\Delta_{P1})t} & -i\bar{\Gamma}_{P2} - \Delta_{P2} \end{pmatrix} \begin{pmatrix} \delta\bar{\beta}_{P1}(t) \\ \delta\bar{\beta}_{P2}(t) \end{pmatrix}, \tag{6.32}$$

which is stable when the real part of both eigenvalues are negative [80]. These eigenvalues, shown in figure 6.4 for the pump only coupling into and out of a single ring (although being

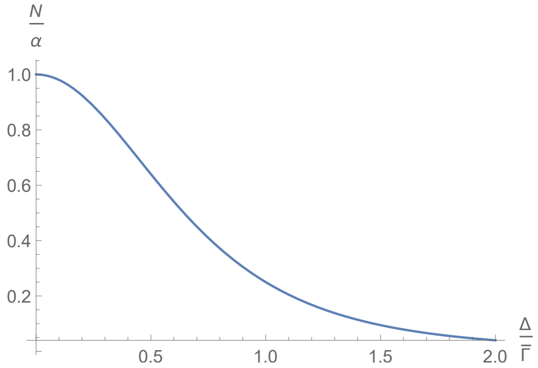

Figure 6.3: Graph of the photon number $N = |\beta|^2$ in a single ring system of a $\chi^{(2)}$ material, varying detuning Δ, with $\bar{\Gamma} \sim 10^9$. Increasing the detuning causes less of the input light to couple into the ring system as the frequency of the input light goes further off-resonance with the ring.

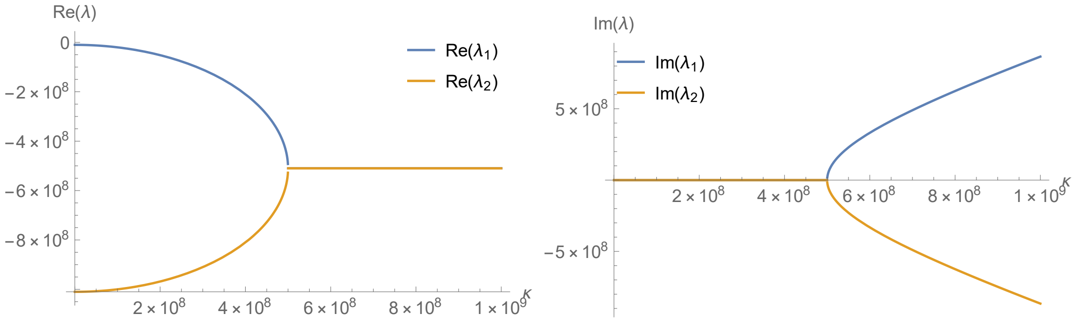

Figure 6.4: Graph of the eigenvalues of the coupled ring system of a $\chi^{(2)}$ material, with no detuning, varying with coupling between the rings. Left (right) graph shows the real (imaginary) parts of the eigenvalues of the system, showing a lossy-$\mathcal{PT}$-symmetric-like system with a second-order EP at $\kappa = \left(\bar{\Gamma}_1 - \bar{\Gamma}_2\right)/2$, independent of the input pump power. However, this appears to make no difference to the system and the peak value of the pump occurs at a different value of coupling.

resonant with both), are given by

$$\frac{1}{2}\left[-\bar{\Gamma}_{P1} - \bar{\Gamma}_{P2} + i\left(\Delta_{P1} + \Delta_{P2}\right) \pm \sqrt{\left(\bar{\Gamma}_{P1} - \bar{\Gamma}_{P2} - i\left(\Delta_{P1} - \Delta_{P2}\right)\right)^2 - 4|\kappa|^2}\right]. \tag{6.33}$$

The real parts of these eigenvalues are always negative for $\bar{\Gamma}_{P1} = \bar{\Gamma}_{P2}$ or $\Delta_{P1} = \Delta_{P2}$.

However, for FWM, the solution is complicated by having SPM terms in the pump equations of motion. Taking the same steady state, semi-classical approximation for FWM gives

$$\left(\bar{\Gamma}_{P1} + 2i\eta|\tilde{\beta}_{P1}|^2 - i\Delta_{P1}\right)\tilde{\beta}_{P1}(t) = -i\gamma_{P1}^*\bar{\alpha}_{P1<} - i\kappa\tilde{\beta}_{P2}(t)\, e^{i(\Delta_{P2}-\Delta_{P1})t} \tag{6.34}$$

$$\left(\bar{\Gamma}_{P2} + 2i\eta|\tilde{\beta}_{P2}|^2 - i\Delta_{P2}\right)\tilde{\beta}_{P2}(t) = -i\gamma_{P2}^*\bar{\alpha}_{P2<} - i\kappa^*\tilde{\beta}_{P1}(t)\, e^{-i(\Delta_{P2}-\Delta_{P1})t}. \tag{6.35}$$

The absolute value squared gives

$$\left(\bar{\Gamma}_{P1}^2 + \left(2\eta|\tilde{\beta}_{P1}|^2 - \Delta_{P1}\right)^2\right) N_{P1} = |\gamma_{P1}|^2|\bar{\alpha}_{P1<}|^2 + |\kappa|^2 N_{P2} + 2\Re\left[\gamma_{P1}\kappa^*\bar{\alpha}_{P1<}\tilde{\beta}_{P2}^*\left(t\right)e^{-i(\Delta_{P2}-\Delta_{P1})t}\right] \tag{6.36}$$

$$\left(\bar{\Gamma}_{P2}^2 + \left(2\eta|\tilde{\beta}_{P2}|^2 - \Delta_{P2}\right)^2\right) N_{P2} = |\gamma_{P2}|^2|\bar{\alpha}_{P2<}|^2 + |\kappa|^2 N_{P1} + 2\Re\left[\gamma_{P2}\kappa^*\bar{\alpha}_{P2<}\tilde{\beta}_{P1}^*\left(t\right)e^{i(\Delta_{P2}-\Delta_{P1})t}\right], \tag{6.37}$$

which can be solved by either taking $\Delta_{P1} = 2\eta|\tilde{\beta}|_{P1}^2$ and $\Delta_{P2} = 2\eta|\tilde{\beta}|_{P2}^2$, or again having only a single ring resonant with the pump frequency. In the first case, we get

$$\begin{pmatrix} \bar{\Gamma}_{P1} & i\kappa e^{i(\Delta_{P2}-\Delta_{P1})t} \\ i\kappa^* e^{-i(\Delta_{P2}-\Delta_{P1})t} & \bar{\Gamma}_{P2} \end{pmatrix} \begin{pmatrix} \tilde{\beta}_{P1}\left(t\right) \\ \tilde{\beta}_{P2}\left(t\right) \end{pmatrix} = -i \begin{pmatrix} \gamma_{P1}\bar{\alpha}_{P1<} \\ \gamma_{P2}\bar{\alpha}_{P2<} \end{pmatrix}, \tag{6.38}$$

which gives a similar solution to the SPDC case in equation 6.30,

$$\begin{pmatrix} \tilde{\beta}_{P1}\left(t\right) \\ \tilde{\beta}_{P2}\left(t\right) \end{pmatrix} = -\frac{1}{\bar{\Gamma}_{P1}\bar{\Gamma}_{P2} + |\kappa|^2} \begin{pmatrix} i\bar{\Gamma}_{P2} & \kappa e^{i(\Delta_{P2}-\Delta_{P1})t} \\ \kappa^* e^{-i(\Delta_{P2}-\Delta_{P1})t} & i\bar{\Gamma}_{P1} \end{pmatrix} \begin{pmatrix} \gamma_{P1}\bar{\alpha}_{P1<} \\ \gamma_{P2}\bar{\alpha}_{P2<} \end{pmatrix}. \tag{6.39}$$

when there is only an input in the first waveguide, this gives that

$$\Delta_{P1} = 2\eta|\tilde{\beta}_{P1}|^2 = \frac{2\eta\bar{\Gamma}_{P2}^2|\gamma_{P1}|^2\bar{\alpha}_{P1}^2}{\left(\bar{\Gamma}_{P1}\bar{\Gamma}_{P2} + |\kappa|^2\right)^2} \tag{6.40}$$

although the number of photons stored in each ring matches that of the SPDC case with the solution given by equation 6.30 and shown in figure 6.2, although it varies by a constantly varying phase. The other analytical solution here is when $\alpha_{P1} = \alpha_{P2}$ and so, by symmetry, $\Delta_{P1} = \Delta_{P2}$, again the same as the SPDC case with zero detuning. Alternatively, when the pump is resonant only with the first ring, we have that N_P is a solution to the equation

$$4\eta N_P^3 - 4\eta\Delta_P N_P^2 + \left(\bar{\Gamma}_{P1}^2 + \Delta_P^2\right) N_P - |\gamma_P|^2|\alpha_P|^2 = 0. \tag{6.41}$$

From [80], we have that the solution is stable for $|\Delta_P| < \sqrt{3}\bar{\Gamma}$ and bistable for $|\Delta_P| > \sqrt{3}\bar{\Gamma}$. In the bistable regime, the solution is unstable when $N_- < N_P < N_+$, where

$$N_\pm = \frac{1}{3\Lambda}\left(2\Delta_P \pm \sqrt{\Delta_P^2 - 3\bar{\Gamma}^2}\right), \tag{6.42}$$

which happen to be the stationary points of equation 6.41. This is exactly the single-ring solution calculated in [77], which contains various plots of the stability of this solution.

6.3 Eigenvalues, Eigenvectors and Exceptional Points

To calculate the eigenvalues of the SPDC case, we start with the Hamiltonian of equation 6.18 and use the detuned basis with $\tilde{a}_{Jn} = \bar{a}_{Jn}e^{-i\Delta_{Pn}t}$. We also assume that the detuning of each pump from the ring resonance is the same so that $\Delta_{P1} = \Delta_{P2} = \Delta_P$ (in order to remove oscillations, allowing the system to reach a steady state), assume that the loss of the signal modes are equal to the loss of the idler modes, so that $\bar{\Gamma}_{S1} = \bar{\Gamma}_{I1} = \bar{\Gamma}_1$ and $\bar{\Gamma}_{S2} = \bar{\Gamma}_{I2} = \bar{\Gamma}_2$, denote $\Lambda\bar{\beta}_{P1} = z_1$, $\Lambda\bar{\beta}_{P2} = z_2$ and make the simplifying assumption that all the parameters are real. This gives

$$\tilde{H}_{SPDC,\text{eff}} = \begin{pmatrix} -i\bar{\Gamma}_1 - \Delta_P & z_1 & \kappa & 0 \\ -z_1 & -i\bar{\Gamma}_1 + \Delta_P & 0 & -\kappa \\ \kappa & 0 & -i\bar{\Gamma}_2 - \Delta_P & z_2 \\ 0 & -\kappa & -z_2 & -i\bar{\Gamma}_2 + \Delta_P \end{pmatrix}. \tag{6.43}$$

When $\bar{\Gamma}_1 = \bar{\Gamma}_2 = \bar{\Gamma}$, defining

$$\tilde{\sigma}_{\pm,SPDC} = \sqrt{\Delta_P^2 - \frac{1}{2}\left(z_1^2 + z_2^2\right) + \kappa^2 \pm \sqrt{\frac{1}{4}\left(z_1^2 - z_2^2\right)^2 - \kappa^2\left(\left(z_1 - z_2\right)^2 - 4\Delta_P^2\right)}}, \tag{6.44}$$

as shown in figure 6.5 for $\Delta_P = z_2 = 0$, this has eigenvalues

$$-i\bar{\Gamma} \pm \sigma_{+,SPDC} \quad \text{and} \quad -i\bar{\Gamma} \pm \sigma_{-,SPDC}. \tag{6.45}$$

First, we look at the case where $\left(z_1 - z_2\right)^2 = 4\Delta_P^2$. This gives

$$\tilde{\sigma}_{\pm,SPDC} = \sqrt{\frac{1}{4}\left(z_1 - z_2\right)^2 - \frac{1}{2}\left(z_1^2 + z_2^2\right) + \kappa^2 \pm \frac{1}{2}\left(z_1^2 - z_2^2\right)} \tag{6.46}$$

$$\implies \begin{cases} \sigma_+ &= \sqrt{\frac{1}{4}\left(z_1 - z_2\right)^2 - z_2^2 + \kappa^2} \\ \sigma_- &= \sqrt{\frac{1}{4}\left(z_1 - z_2\right)^2 - z_1^2 + \kappa^2} \end{cases}, \tag{6.47}$$

also shown in figure 6.5.

For $|z_1 - z_2| > 2\Delta_P$, setting

$$\kappa = \pm\frac{z_1^2 - z_2^2}{2\sqrt{\left(z_1 - z_2\right)^2 - 4\Delta_P^2}} \tag{6.48}$$

gives

$$\tilde{\sigma}_{\pm,SPDC} = \frac{1}{2}\sqrt{\frac{4\left(z_1 + z_2\right)^2\Delta_P^2 - \left(\left(z_1 - z_2\right)^2 - 4\Delta_P^2\right)^2}{\left(z_1 - z_2\right)^2 - 4\Delta_P^2}}, \tag{6.49}$$

describing 2 second order EP surfaces that can be tuned to either be on a lossy background where the eigenvalues have a $-i\bar{\Gamma}$ term, to a 'neutral' background with no imaginary terms in the eigenvalues, or a background with gain, where the eigenvalues instead have a term equivalent to $+i\bar{\Gamma}$. This transition from a lossy EP to one with gain can be shown by e.g. setting $\Delta_P = 0$ and defining $z' = \left(z_1 - z_2\right)/2$, which gives the eigenvalues as $-i\left(\bar{\Gamma} \pm z'\right)$ which

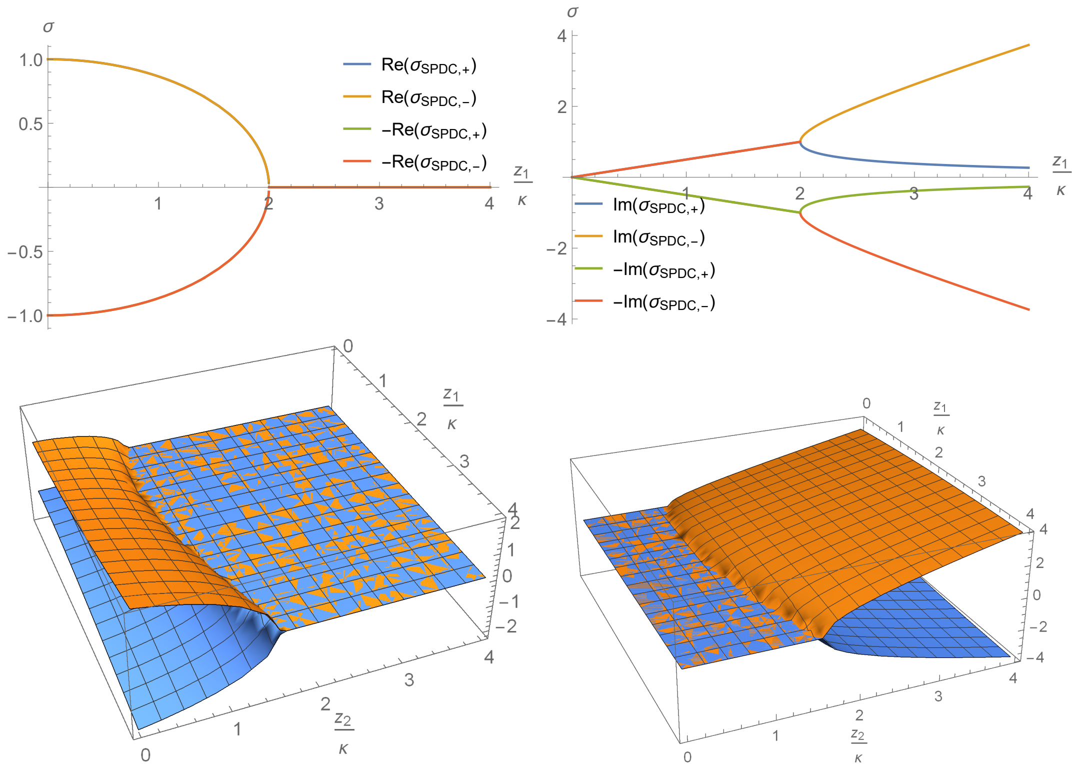

Figure 6.5: Graph of $\sigma_{\pm,SPDC}$, with (top) no detuning and $z_2 = 0$, (bottom) $|z_1 - z_2| = 2|\Delta_P|$, varying with pump strength. Left (right) graph shows the real (imaginary) parts. Top graphs show a $\mathcal{PT}$-symmetric-like system with coupled second-order EPs at $z_1 = 2\kappa$. Bottom graphs show a lossy EP2 line using σ_+, which is symmetric under exchange of $\sigma_+ \leftrightarrow \sigma_-$ and $z_1 \leftrightarrow z_2$.

gives a lossy background for $z < \bar{\Gamma}$, a neutral background at $z = \bar{\Gamma}$ and a background with gain for $z > \bar{\Gamma}$. For $\Delta_P \neq 0$, shown in figure 6.6, setting

$$\Delta_P^2 = \frac{1}{2}\left(z_1^2 + z_2^2\right) - \kappa^2 = \frac{1}{2}\left(z_1^2 + z_2^2\right) - \frac{\left(z_1^2 - z_2^2\right)^2}{4\left(\left(z_1 - z_2\right)^2 - 4\Delta_P^2\right)} \tag{6.50}$$

gives a fourth order lossy EP surface with eigenvalue $-i\bar{\Gamma}$ at

$$\Delta_P = \frac{1}{4}\left[z_1 + z_2 \pm \sqrt{5z_1^2 - 6z_1z_2 + 5z_2^2}\right] \quad \text{or} \quad \Delta_P = -\frac{1}{4}\left[z_1 + z_2 \pm \sqrt{5z_1^2 - 6z_1z_2 + 5z_2^2}\right]. \tag{6.51}$$

While these solutions are not always valid, at $z_2 = 0$, an EP4 line parametrised by z_1 is given by the solution $\Delta_P = z_1\left(\sqrt{5} - 1\right)/4$. Alternatively, when $\bar{\Gamma}_1 \neq \bar{\Gamma}_2$, the eigenvalues are the solutions to the equation

$$\begin{aligned}\lambda^4 + 2i\lambda^3\left(\bar{\Gamma}_1 + \bar{\Gamma}_2\right) + \lambda^2\left[z_1^2 + z_2^2 - \left(\bar{\Gamma}_1 + \bar{\Gamma}_2\right)^2 - 2\left(\bar{\Gamma}_2\bar{\Gamma}_2 + \Delta_P^2 + \kappa^2\right)\right]& \\ +2i\lambda\left[-\left(\bar{\Gamma}_1 + \bar{\Gamma}_2\right)\left(\bar{\Gamma}_1\bar{\Gamma}_2 + \Delta^2 + \kappa^2\right) + \bar{\Gamma}_2 z_1^2 + \bar{\Gamma}_1 z_2^2\right]& \\ +\kappa^4 + \left(\bar{\Gamma}_1^2 + \Delta_P^2 - z_1^2\right)\left(\bar{\Gamma}_2^2 + \Delta_P^2 - z_2^2\right) - 2\kappa^2\left(-\bar{\Gamma}_1\bar{\Gamma}_2 + \Delta_P^2 + z_1z_2\right) = 0.&\end{aligned} \tag{6.52}$$

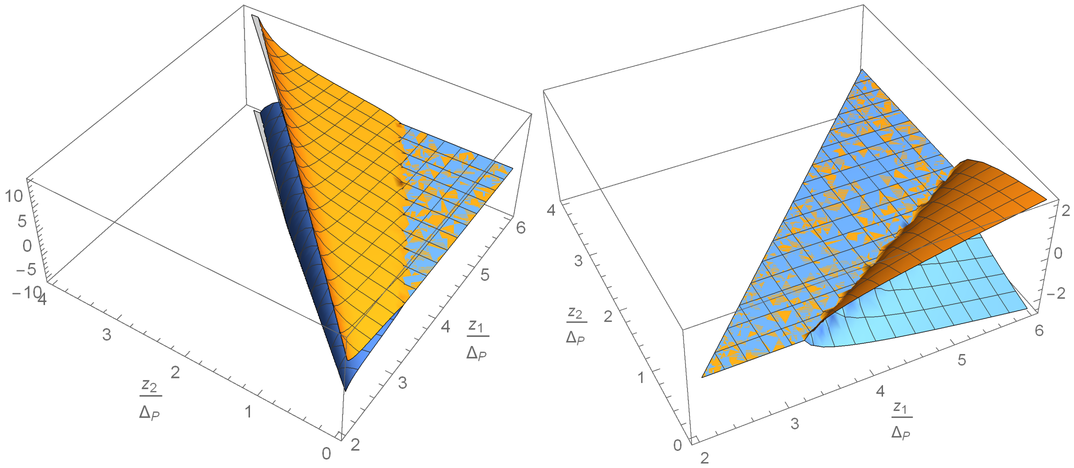

Figure 6.6: Graph of $\sigma_{EP2,SPDC}$, showing the (lossy) EP2 surface described by equation 6.48 with an EP4 line with the value of Δ_P given in equation 6.51, varying with pump strength for $|z_1 - z_2| > 2|\Delta_P|$. Left (right) graph shows the real (imaginary) part.

This can be simplified by taking the pump as resonant only in the first ring (so that $z_2 = 0$) and no waveguide coupling to the second ring, with both rings having the same intrinsic loss μ, allowing us to write this Hamiltonian as

$$\tilde{H}'_{SPDC,\text{eff}} = -iMI + \begin{pmatrix} -i\Gamma_1 - \Delta_P & z_1 & \kappa & 0 \\ -z_1 & -i\Gamma_1 + \Delta_P & 0 & -\kappa \\ \kappa & 0 & -\Delta_P & 0 \\ 0 & -\kappa & 0 & \Delta_P \end{pmatrix}, \tag{6.53}$$

which has eigenvalues as $-iM + \sigma'_{SPDC}$, where σ'_{SPDC} are now the solutions to the equation

$$\begin{aligned} \lambda^4 + 2i\lambda^3\Gamma_1 + \lambda^2\left[z_1^2 - \Gamma_1^2 - 2\left(\Delta_P^2 + \kappa^2\right)\right] - 2i\lambda\Gamma_1\left(\Delta_P^2 + \kappa^2\right) & \\ + \left(\kappa^2 - \Delta_P^2\right)^2 + \Delta_P^2\left(\Gamma_1^2 - z_1^2\right) = 0. & \end{aligned} \tag{6.54}$$

At $\Delta_P = 0$, shown in figure 6.7, this now gives

$$\sigma'_{1\pm,SPDC} = -\frac{i}{2}\left(z_1 + \Gamma_1\right) \pm \frac{1}{2}\sqrt{4\kappa^2 - \left(z_1 + \Gamma_1\right)^2} \tag{6.55}$$

$$\sigma'_{2\pm,SPDC} = \frac{i}{2}\left(z_1 - \Gamma_1\right) \pm \frac{1}{2}\sqrt{4\kappa^2 - \left(z_1 - \Gamma_1\right)^2}. \tag{6.56}$$

Further setting $2\kappa = z_1 - \Gamma_1 = 2M$ now gives an EP2, with respective eigenvalue 0. Overall, this shows a rich multi-dimensional structure with multiple EPs in multiple regimes.

For FWM, defining $z = \Lambda\bar{\beta}^2$, again taken to be real and only coupling into a single (the

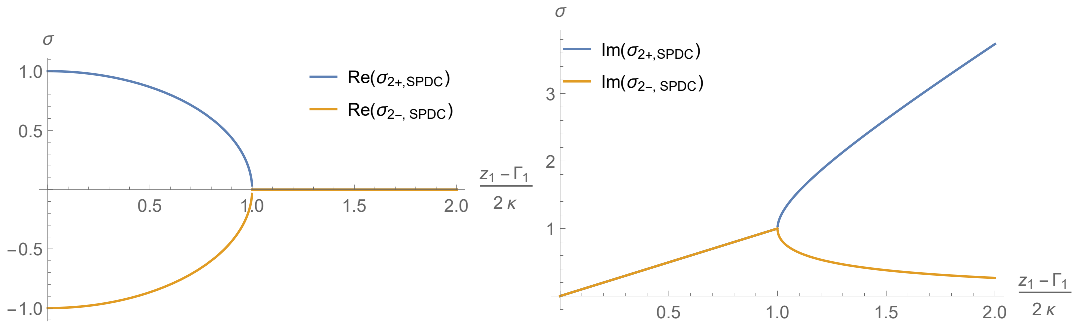

Figure 6.7: Graph of $\sigma_{2,SPDC}$, described by equation 6.56 with an EP2 at $z_1 - \Gamma_1 = 2\kappa$. Left (right) graph shows the real (imaginary) part. This EP can be tuned to be on a lossy background (for $\kappa < M$; the imaginary term in the eigenvalue is negative), a background with gain ($\kappa > M$; imaginary term is positive), or a 'neutral' background that typifies an ideal $\mathcal{PT}$-symmetric system ($\kappa = M$ with the coalescing eigenvalues equal to 0).

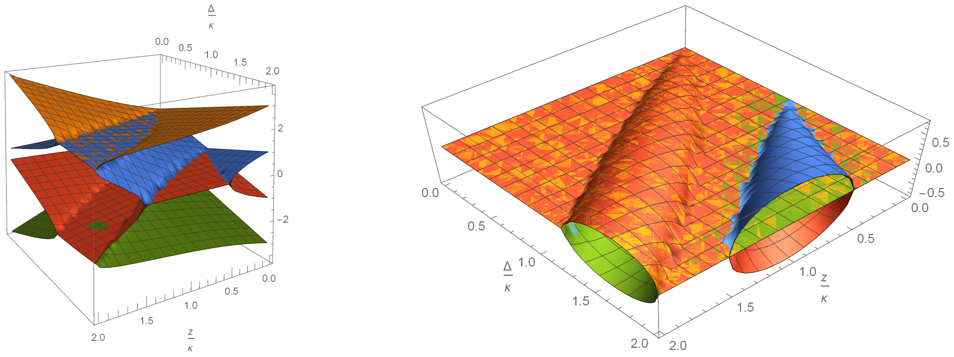

Figure 6.8: Graph of $\sigma_{\pm,FWM}$, described by equation 6.59 with multiple EPs, with different eigenvectors coalescing at different points. Left (right) graph shows the real (imaginary) part. As with figure 6.7, this EP can be tuned to be on a lossy background, a background with gain, or a 'neutral' background.

first) ring, we instead have

$$\tilde{H}_{FWM,\text{eff}} = \begin{pmatrix} -i\bar{\Gamma} - \Delta_P + 2z & z & \kappa & 0 \\ -z & -i\bar{\Gamma} + \Delta_P - 2z & 0 & -\kappa \\ \kappa & 0 & -i\bar{\Gamma} - \Delta_P & 0 \\ 0 & -\kappa & 0 & -i\bar{\Gamma} + \Delta_P \end{pmatrix}, \tag{6.57}$$

which has eigenvalues

$$-i\bar{\Gamma} \pm \sigma_{+,FWM} \quad \text{and} \quad -i\bar{\Gamma} \pm \sigma_{-,FWM}, \tag{6.58}$$

where, shown in figure 6.8,

$$\sigma_{\pm,FWM} = \sqrt{\frac{3}{2}z^2 - 2z\Delta_P + \Delta_P^2 + \kappa^2 \pm \frac{1}{2}\sqrt{z^2\left(3z - 4\Delta_P\right)^2 + 4\left(z - 2\Delta_P\right)\left(3z - 2\Delta_P\right)\kappa^2}}. \tag{6.59}$$

Setting

$$\kappa = \pm \frac{z\left(3z-4\Delta_P\right)}{\sqrt{4\left(2\Delta_P-z\right)\left(3z-2\Delta_P\right)}} \tag{6.60}$$

for $2\Delta_P/3 < z < 2\Delta_P$ gives 2 second order EP surfaces as before, shown in figure 6.9. However, solving to give a higher order EP, while enforcing that Δ_P is real gives the solution

$$\Delta_P = \frac{z\left(5\pm\sqrt{13}\right)}{4} \approx 2.2 \quad \text{or} \quad 0.35, \tag{6.61}$$

which are invalid solutions.

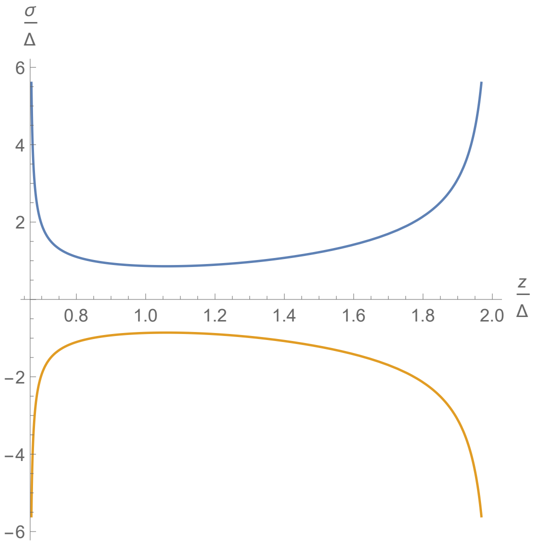

Figure 6.9: Graph of $\sigma_{EP,FWM}$, described by equation 6.59, reaching an EP by setting the coupling as in 6.60 within the allowed parameter range that allows for a physically valid κ. However, in this regime, σ is here real and never 0 within the valid parameter range. As such, there is no higher order EP within this parameter range and these EPs occur on a lossy background.

As such, while SPDC has fourth order EPs, FWM only has second order EPs. As with SPDC, we can alternatively set $\Gamma_2 = 0$, so that the rings have different loss rates, given the eigenvalues as $-iM + \sigma'_{FWM}$, where σ'_{FWM} are the solutions to the equation

$$\begin{aligned}\lambda^4 + 2i\lambda^3\Gamma_1 + \lambda^2\left[4z\Delta_P - 3z^2 - \Gamma_1^2 - 2\left(\Delta_P^2+\kappa^2\right)\right] - 2i\lambda\Gamma_1\left(\Delta_P^2+\kappa^2\right)& \\ +\Delta^2\left(3z^2+\Gamma_1^2-4z\Delta_P\right) + \left(\Delta_P^2-\kappa^2\right)^2 + 4z\Delta_P\kappa^2 = 0.&\end{aligned} \tag{6.62}$$

This has a quartic equation, which has multiple roots when

$$-9z^4 + 24z^3\Delta_P + 2z^2\left(3\Gamma_1^2 - 8\Delta_P^2 - 6\kappa^2\right) - 8z\Delta_P\left(\Gamma_1^2-4\kappa^2\right) + 4\Delta_P^2\left(\Gamma_1^2-4\kappa^2\right) = 0 \tag{6.63}$$

Excluding the trivial solution $z = \Delta_P = 0$, this occurs at the values

$$\Gamma_1 = \pm\frac{z}{\sqrt{3}}, \qquad \Delta_P = \frac{z}{2}; \tag{6.64}$$

$$\Gamma_1 = \pm\sqrt{3}z, \qquad \Delta_P = \frac{3z}{2}; \tag{6.65}$$

$$\kappa = \pm\frac{\sqrt{2\Gamma_1^2\left(3z^2 - 4z\Delta_P + 2\Delta_P^2\right) - z^2\left(3z - 4\Delta_P\right)^2}}{2\sqrt{\left(3z - 2\Delta_P\right)\left(z - 2\Delta_P\right)}}. \tag{6.66}$$

While whether equation 6.66 does or does not define an EP2 is considerably harder to verify, this can still be compared with equation 6.60 in that the coupling value giving multiple roots is parameterised in terms of z and Δ_P and is valid within a given parameter range.

6.4 Definitions of Correlation Functions

A number of correlation functions are used to examine the behaviour of photon sources, which we look at here. The initial definitions of these (temporal) correlation functions are taken from [81]. While these correlation functions are later considered in frequency space, as per [77], the assumption of an infinitely narrow pump in a CW solution can cause squares of delta functions to appear, so definitions need to be adjusted to include the resolution of the photon detectors, which has the result of smoothing the δ function. This will be implicitly applied in later sections. Here, these definitions are rewritten in terms of the unnormalised and unheralded first order correlation functions which are referred to here as $G_m^{(1)}\left(t_l, t_p\right)$ and $A_m\left(t_l, t_p\right)$ and hold for an arbitrary number of coupled rings. The correlation functions defined here can be heralded or unheralded and normalised or unnormalised. They are also taken to be symmetric under $S \leftrightarrow I$ exchange. We assume that $\Gamma_{Jn} = \Gamma_{Kn} = \Gamma_n$ and $M_{Jn} = M_{Kn} = M_n$ for all J, K throughout. A more extensive list is given in appendix C.

6.4.1 First order Correlation Functions

un-normalised cross-correlation

Due to the symmetry of the system, where $\psi_{Sn<}$ transforms into terms involving $\psi_{Sm>}$, $\psi_{Im>}^{\dagger}$, $\phi_{Sm>}$ and $\phi_{Im>}^{\dagger}$; and $\psi_{In<}$ transforms into terms involving $\psi_{Sm>}$, $\psi_{Im>}^{\dagger}$, $\phi_{Sm>}$ and $\phi_{Im>}^{\dagger}$. This means that $\psi_{Sn>}$ and $\psi_{In>}^{\dagger}$ commute, so the cross-correlation function is 0.

$$v\left\langle \bar{\psi}_{Im>}^{\dagger}\left(t_l\right)\bar{\psi}_{Sm>}\left(t_2\right)\right\rangle = 0 \tag{6.67}$$

un-normalised, unheralded

These are the 'fundamental' correlation functions that other correlation functions can be written in terms of. For the output being measured in mode m,

$$\begin{aligned} G_m^{(1)}(t_l,t_p) = \left[G_m^{(1)}(t_p,t_l)\right]^* &= v\left\langle \bar{\psi}^\dagger_{Sm>}(t_l)\,\bar{\psi}_{Sm>}(t_p)\right\rangle && (6.68)\\ &= \int\sum_n \left[q^*_{SmIn}(t_l,t')\,q_{SmIn}(t_p,t') + p^*_{SmIn}(t_l,t')\,p_{SmIn}(t_p,t')\right]dt' && (6.69)\\ &= \int\sum_n \frac{\bar{\Gamma}_n}{\Gamma_n} q^*_{SmIn}(t_l,t')\,q_{SmIn}(t_p,t')\;dt' && (6.70)\\ &= 4\Gamma_m e^{-i\Delta_p(t_l-t_p)}\int\sum_n \bar{\Gamma}_n G^*_{SmIn}(t_l-t')\,G_{SmIn}(t_p-t')\;dt'. && (6.71)\end{aligned}$$

At $t_l = t_p$ this defines both a normalisation and the number of output photons,

$$J_m = G_m^{(1)}(t,t) = 4\Gamma_m\int\sum_n \bar{\Gamma}_n|G_{SmIn}(t-t')|^2\,dt'. \tag{6.72}$$

in some given time-bin. This can also be simplistically considered in frequency space by first considering $t_l = t_S$ and $t_p = t_S + \tau_S$. As seen in later sections, the only time dependence in this correlation function is from the parameter $t_l - t_p = \tau_S$. As a result, this correlation function can simplistically (albeit naively and inaccurately; for full details see e.g. [77]) be considered in frequency space by taking the Fourier Transform with respect to τ_S to give $G_m^{(1)}(\omega'_S)$, where ω'_S is the difference in frequency from the signal frequency ω_S. Although not directly measured when measuring a single photon, we also define

$$\begin{aligned} A_m(t_l,t_p) = A^*_m(t_p,t_l) &= v\left\langle\bar{\psi}_{Sm>}(t_l)\,\bar{\psi}_{Im>}(t_p)\right\rangle && (6.73)\\ &= \int\sum_n q_{SmSn}(t_l-t')\,q_{ImSn}(t_p-t') + p_{SmSn}(t_l-t')\,p_{ImSn}(t_p-t')\,dt' && (6.74)\\ &= 2\Gamma_m e^{-i\Delta(t_p+t_l)}\Big[G_{SmIm}(t_p-t_l)\\ &\qquad -2\int\sum_n\bar{\Gamma}_n G_{SmSn}(t_l-t')\,G_{SmIn}(t_p-t')\;dt'\Big]. && (6.75)\end{aligned}$$

6.4.2 Second order Correlation Functions

Similar to the first order correlation functions, these can be heralded or unheralded and normalised or unnormalised.

un-normalised, unheralded

$$\begin{aligned} G_m^{(2)}(t_1,t_2,t_3,t_4) &= v^2\left\langle\bar{\psi}^\dagger_{Sm>}(t_1)\,\bar{\psi}^\dagger_{Sm>}(t_2)\,\bar{\psi}_{Sm>}(t_3)\,\bar{\psi}_{Sm>}(t_4)\right\rangle && (6.76)\\ &= G_m^{(1)}(t_2,t_3)\,G_m^{(1)}(t_1,t_4) + G_m^{(1)}(t_1,t_3)\,G_m^{(1)}(t_2,t_4). && (6.77)\end{aligned}$$

At $t_1 = t_4 = t$ and $t_2 = t_3 = t'$, this becomes

$$G_m^{(2)}\left(t,t'\right) = J_m^2 + |G_m^{(1)}\left(t,t'\right)|^2. \tag{6.78}$$

normalised, unheralded

$$\begin{aligned} g_m^{(2)}\left(t_1,t_2,t_3,t_4;t_{s_1},t_{s_2}\right) &= \frac{\left\langle \bar{\psi}_{Sm>}^{\dagger}\left(t_1\right)\bar{\psi}_{Sm>}^{\dagger}\left(t_2\right)\bar{\psi}_{Sm>}\left(t_3\right)\bar{\psi}_{Sm>}\left(t_4\right)\right\rangle}{\left\langle \bar{\psi}_{Sm>}^{\dagger}\left(t_{s_1}\right)\bar{\psi}_{Sm>}\left(t_{s_1}\right)\right\rangle \left\langle \bar{\psi}_{Sm>}^{\dagger}\left(t_{s_2}\right)\bar{\psi}_{Sm>}\left(t_{s_2}\right)\right\rangle} \qquad (6.79) \\ &= \frac{G_m^{(1)}\left(t_2,t_3\right)G_m^{(1)}\left(t_1,t_4\right) + G_m^{(1)}\left(t_1,t_3\right)G_m^{(1)}\left(t_2,t_4\right)}{J_m^2} \qquad (6.80) \end{aligned}$$

When $t_1 = t_2 = t_3 = t_4 = t$, this gives $g^{(2)}\left(t\right) = 2$ as expected. Alternatively, setting $t_1 = t_4 = t$ and $t_2 = t_3 = t'$ gives

$$g_m^{(2)}\left(t,t'\right) = 1 + |g_m^{(1)}\left(t,t'\right)|^2 \implies 1 \le g_m^{(2)}\left(t,t'\right) \le 2, \tag{6.81}$$

showing that unheralded single photons from such a source cannot be used as a good source of single photons as they are equivalent to a thermal state in this correlation function.

normalised, heralded

$$\begin{aligned} g_{m,h}^{(2)}\left(t_1,t_2,t_3,t_4;t_{s_1},t_{s_2}\right) &= \frac{\left\langle \bar{\psi}_{Sm>}^{\dagger}\left(t_1\right)\bar{\psi}_{Sm>}^{\dagger}\left(t_2\right)\bar{\psi}_{Sm>}\left(t_3\right)\bar{\psi}_{Sm>}\left(t_4\right)\right\rangle_h}{\left\langle \bar{\psi}_{Sm>}^{\dagger}\left(t_{s_1}\right)\bar{\psi}_{Sm>}\left(t_{s_1}\right)\right\rangle_h \left\langle \bar{\psi}_{Sm>}^{\dagger}\left(t_{s_2}\right)\bar{\psi}_{Sm>}\left(t_{s_2}\right)\right\rangle_h} \\ &= \frac{\left\langle \bar{\psi}_{Im>}^{\dagger}\left(t_i\right)\bar{\psi}_{Sm>}^{\dagger}\left(t_1\right)\bar{\psi}_{Sm>}^{\dagger}\left(t_2\right)\bar{\psi}_{Sm>}\left(t_3\right)\bar{\psi}_{Sm>}\left(t_4\right)\bar{\psi}_{Im>}\left(t_i\right)\right\rangle \left\langle \bar{\psi}_{Im>}^{\dagger}\left(t_i\right)\bar{\psi}_{Im>}\left(t_i\right)\right\rangle}{\left\langle \bar{\psi}_{Im>}^{\dagger}\left(t_i\right)\bar{\psi}_{Sm>}^{\dagger}\left(t_{s_1}\right)\bar{\psi}_{Sm>}\left(t_{s_1}\right)\bar{\psi}_{Im>}\left(t_i\right)\right\rangle \left\langle \bar{\psi}_{Im>}^{\dagger}\left(t_i\right)\bar{\psi}_{Sm>}^{\dagger}\left(t_{s_2}\right)\bar{\psi}_{Sm>}\left(t_{s_2}\right)\bar{\psi}_{Im>}\left(t_i\right)\right\rangle}. \end{aligned}$$

Using

$$\begin{aligned} \left\langle \bar{\psi}_{Im>}^{\dagger}\left(t_i\right)\bar{\psi}_{Sm>}^{\dagger}\left(t_s\right)\bar{\psi}_{Sm>}\left(t_s\right)\bar{\psi}_{Im>}\left(t_i\right)\right\rangle &= A_m^*\left(t_s,t_i\right)A_m\left(t_s,t_i\right) + G_m^{(1)}\left(t_i,t_i\right)G_m^{(1)}\left(t_s,t_s\right) \qquad (6.82) \\ &= |A_m\left(t_s,t_i\right)|^2 + J_m^2 \qquad (6.83) \end{aligned}$$

and setting $t_2 = t_3 = t'$ and $t_1 = t_4 = t$ gives

$$\begin{aligned} g_{m,h}^{(2)}\left(t,t';t_{s_1},t_{s_2}\right) &= \frac{2J_m\Re\left[A_m^*\left(t',t_i\right)A_m\left(t,t_i\right)G_m^{(1)}\left(t,t'\right)\right]}{\left(|A_m\left(t_{s_1},t_i\right)|^2 + J_m^2\right)\left(|A_m\left(t_{s_2},t_i\right)|^2 + J_m^2\right)} \qquad (6.84) \\ &+ \frac{J_m^2\left[|A_m\left(t',t_i\right)|^2 + |A_m\left(t,t_i\right)|^2 + J_m^2 + |G_m^{(1)}\left(t,t'\right)|^2\right]}{\left(|A_m\left(t_{s_1},t_i\right)|^2 + J_m^2\right)\left(|A_m\left(t_{s_2},t_i\right)|^2 + J_m^2\right)}. \qquad (6.85) \end{aligned}$$

At $t = t_{s_1} = t_{s_2} = t'$, this simplifies to

$$g^{(2)}_{m,h}\left(t, t; t_{s_1}, t_{s_2}\right) = 2J^2_m \frac{2|A_m\left(t, t_i\right)|^2 + J^2_m}{\left(|A_m\left(t, t_i\right)|^2 + J^2_m\right)^2}. \tag{6.86}$$

In the case of an ideal pure single photon source, this would be 0, so the aim is often to get this value to be as close to 0 as possible.

un-normalised Joint Temporal Intensity

$$G^{(2)}_{si,m}\left(t_1, t_2, t_3, t_4\right) = v^2 \left\langle \bar{\psi}^{\dagger}_{Im>}\left(t_1\right) \bar{\psi}^{\dagger}_{Sm>}\left(t_2\right) \bar{\psi}_{Sm>}\left(t_3\right) \bar{\psi}_{Im>}\left(t_4\right) \right\rangle \tag{6.87}$$

$$= A^*_m\left(t_2, t_1\right) A_m\left(t_3, t_4\right) + G^{(1)}_m\left(t_1, t_4\right) G^{(1)}_m\left(t_2, t_3\right). \tag{6.88}$$

As with the heralded $G^{(1)}_m$, setting $t_1 = t_4 = t_i$ and $t_2 = t_3 = t_s$ gives

$$G^{(2)}_{si,m}\left(t_i, t_s\right) = |A_m\left(t_s, t_i\right)|^2 + J^2_m. \tag{6.89}$$

However, the normalisation of the JTI is different to the other correlation functions and it is also not usually heralded.

6.5 Solving the Equations of Motion

6.5.1 Continuous Wave solutions

To solve the equations of motion in the CW case, we start by calculating the elements of the time evolution of the effective Hamiltonian, $G\left(t\right) = e^{-iH_{\text{eff}}t}$, which are then used in equation 6.20 to calculate the transformation of the input waveguide operators into the ring operators at time t. $G\left(t\right)$ can be written as

$$G\left(t\right) = \begin{pmatrix} G_{S_1S_1} & G_{S_1I_1} & G_{S_1S_2} & G_{S_1I_2} \\ G_{I_1S_1} & G_{I_1I_1} & G_{I_1S_2} & G_{I_1I_2} \\ G_{S_2S_1} & G_{S_2I_1} & G_{S_2S_2} & G_{S_2I_2} \\ G_{I_2S_1} & G_{I_2I_1} & G_{I_2S_2} & G_{I_2I_2} \end{pmatrix} = \frac{2e^{-\Gamma t}}{\sigma^2_+ - \sigma^2_-} \begin{pmatrix} G_{11} & G_{12} & G_{13} & G_{14} \\ G^*_{12} & G^*_{11} & G^*_{14} & G^*_{13} \\ G_{13} & -G^*_{14} & G_{33} & G_{34} \\ -G_{14} & G^*_{13} & G^*_{34} & G^*_{33} \end{pmatrix}. \tag{6.90}$$

In general, these matrix elements are lengthy and involve many terms. However, when the total loss in each ring is equal (which is likely not ideal for a $\mathcal{PT}$-symmetric system) these terms are considerably simplified. As an example, for FWM, these matrix elements are, defining

$\sigma_{\pm} = \sqrt{a \pm b}$,

$$\begin{aligned} G_{11} = \frac{e^{-\bar{\Gamma}t}}{2b} \Bigg[& \left(b + 3z^2 - 4z\Delta\right)\cos\sigma_+ t + \left(b - 3z^2 + 4z\Delta\right)\cos\sigma_- t \\ & + i\left(-6z^3 + \Delta\left(4\kappa^2 + b\right) + 11\Delta z^2 - 2z\left(2\Delta^2 + 2\kappa^2 + b\right)\right)\frac{1}{\sigma_+}\sin\sigma_+ t \\ & + i\left(6z^3 + \Delta\left(-4\kappa^2 + b\right) - 11\Delta z^2 + 2z\left(2\Delta^2 + 2\kappa^2 - b\right)\right)\frac{1}{\sigma_-}\sin\sigma_- t\Bigg] \end{aligned} \tag{6.91}$$

$$G_{12} = iz\frac{e^{-\bar{\Gamma}t}}{b}\left[\frac{1}{\sigma_-}\left(\sigma_-^2 - \Delta^2\right)\sin\sigma_- t - \frac{1}{\sigma_+}\left(\sigma_+^2 - \Delta^2\right)\sin\sigma_+ t\right] \tag{6.92}$$

$$\begin{aligned} G_{13} = \kappa\frac{e^{-\bar{\Gamma}t}}{2b} \Bigg[& 2\left(z - \Delta\right)\cos\sigma_+ t - 2\left(z - \Delta\right)\cos\sigma_- t \\ & + i\left(-3z^2 + 8z\Delta - 4\Delta^2 - b\right)\frac{1}{\sigma_+}\sin\sigma_+ t + i\left(3z^2 - 8z\Delta + 4\Delta^2 - b\right)\frac{1}{\sigma_-}\sin\sigma_- t\Bigg] \end{aligned} \tag{6.93}$$

$$G_{14} = \frac{e^{-\bar{\Gamma}t}}{b}z\kappa\left[-\cos\sigma_+ t + \cos\sigma_- t + i\Delta\frac{1}{\sigma_+}\sin\sigma_+ t - i\Delta\frac{1}{\sigma_-}\sin\sigma_- t\right] \tag{6.94}$$

$$\begin{aligned} G_{33} = \frac{e^{-\bar{\Gamma}t}}{2b} \Bigg[& \left(4z\Delta + b - 3z^2\right)\cos\sigma_+ t + \left(-4z\Delta + b + 3z^2\right)\cos\sigma_- t \\ & + i\left(4z\Delta^2 - 4z\kappa^2 + 4\Delta\kappa^2 + \Delta b - 3z^2\Delta\right)\frac{1}{\sigma_+}\sin\sigma_+ t \\ & + i\left(4z\kappa^2 - 4\Delta\kappa^2 + 3\Delta z^2 - 4z\Delta^2 + \Delta b\right)\frac{1}{\sigma_-}\sin\sigma_- t\Bigg] \end{aligned} \tag{6.95}$$

$$G_{34} = iz\kappa^2\frac{e^{-\bar{\Gamma}t}}{2b}\left[\frac{1}{\sigma_+}\sin\left(\sigma_+ t\right) - \frac{1}{\sigma_-}\sin\left(\sigma_- t\right)\right]. \tag{6.96}$$

6.5.2 Pulsed solutions

As inputting a pulsed pump into the coupled ring system gives a non-steady state solution, giving a time-dependent effective Hamiltonian as well as meaning that section 6.2.1 no longer applies, this is solved by taking the Fourier transform of the effective Hamiltonian and taking a perturbative solution as in [76]. That is, the Fourier transform

$$\bar{b}_J\left(t\right) = \frac{1}{\sqrt{2\pi}}\int \bar{b}_J\left(k\right)e^{-ikv_J t}\,dk \tag{6.97}$$

is taken and applied to the equations of motion in section 6.2.

To zeroth order, in the semi-classical approximation, with $v_{P1} = v_{P2} = v_P$ and $\bar{\Gamma}_{P1} = \bar{\Gamma}_{P2} = \bar{\Gamma}_P$, we take $\eta = \zeta = 0$ in the FWM equations of motion to give that the pump solutions for both SPDC and FWM are given by

$$\left(-ikv_P+\bar{\Gamma}_{P1}\right)\bar{\beta}_{P1}^{(0)}(k)=-i\gamma_{P1}^{*}\alpha_{P1}(k)-i\kappa\bar{\beta}_{P2}^{(0)}(k) \tag{6.98}$$
$$\left(-ikv_P+\bar{\Gamma}_{P2}\right)\bar{\beta}_{P2}^{(0)}(k)=-i\gamma_{P2}^{*}\alpha_{P2}(k)-i\kappa^{*}\bar{\beta}_{P1}^{(0)}(k), \tag{6.99}$$

which gives the pump solutions

$$\begin{aligned}\left[\left(-ikv_P+\bar{\Gamma}_{P1}\right)\left(-ikv_P+\bar{\Gamma}_{P2}\right)+|\kappa|^2\right]\bar{\beta}_{P1}^{(0)}(k)=&\\ -i\gamma_{P1}^{*}\left(-ikv_P+\bar{\Gamma}_{P2}\right)\alpha_{P1}(k)-\kappa\gamma_{P2}^{*}\alpha_{P2}(k)&\end{aligned} \tag{6.100}$$
$$\begin{aligned}\left[\left(-ikv_P+\bar{\Gamma}_{P1}\right)\left(-ikv_P+\bar{\Gamma}_{P2}\right)+|\kappa|^2\right]\bar{\beta}_{P2}^{(0)}(k)=&\\ -i\gamma_{P2}^{*}\left(-ikv_P+\bar{\Gamma}_{P1}\right)\alpha_{P2}(k)-\kappa^{*}\gamma_{P1}^{*}\alpha_{P1}(k).&\end{aligned} \tag{6.101}$$

This process can be repeated for $\bar{b}_{I1}^{(0)}$, $\bar{b}_{I2}^{(0)}$, $\bar{b}_{S1}^{(0)}$ and $\bar{b}_{S2}^{(0)}$ to get

$$\begin{aligned}\left[\left(-ikv_J+\bar{\Gamma}_n\right)\left(-ikv_J+\bar{\Gamma}_m\right)+|\kappa|^2\right]\bar{b}_{Jn}^{(0)}(k)=&\\ \left(-ikv_J+\bar{\Gamma}_m\right)\left(-i\gamma_{Jn}\bar{\psi}_{Jn<}(k)-i\mu_{Jn}\bar{\phi}_{Jn<}(k)\right)-\kappa\gamma_{Jm}\bar{\psi}_{Jm<}(k)-\kappa\mu_{Jm}\bar{\phi}_{Jm<}(k)&,\end{aligned} \tag{6.102}$$

for $J=S\,(I)$, $K=I\,(S)$ and $n=1\,(2)$, $m=2\,(1)$. These zeroth order equations similarly hold for both SPDC and FWM. These then give the first order correction terms for SPDC

$$\begin{aligned}\left(-ikv_J+\bar{\Gamma}_n\right)\bar{b}_{Jn}^{(1)}(k)=-i\gamma_{Jn}\bar{\psi}_{Jn<}(k)-i\mu_{Jn}\bar{\phi}_{Jn<}(k)-i\kappa\bar{b}_{Jm}^{(1)}(k)&\\ -i\Lambda\int F_{Jn}\left(k,k'\right)\bar{b}_{Kn}^{(0)\dagger}\left(k'\right)\,dk',&\end{aligned} \tag{6.103}$$

where $F_{Sn}(k,k')$ and $F_{In}(k,k')$ are defined as

$$F_{Sn,SPDC}\left(k,k'\right)=\frac{1}{\sqrt{2\pi}}\int\bar{\beta}_{Pn}^{(0)}(k_P)\,\delta\left(kv_S-k_Pv_P+k'v_I+\Delta\right)\,dk_P \tag{6.104}$$
$$F_{In,SPDC}\left(k,k'\right)=\frac{1}{\sqrt{2\pi}}\int\bar{\beta}_{Pn}^{(0)}(k_P)\,\delta\left(kv_I-k_Pv_P+k'v_S+\Delta\right)\,dk_P. \tag{6.105}$$

This gives the solution to the frequency equations of motion in terms of the zeroth order terms, to first order, as

$$\begin{aligned}\bar{b}_{Jn}^{(1)}(k)=\bar{b}_{Jn}^{(0)}(k)-\frac{\kappa\Lambda\int F_{Jm}(k,k')\,\bar{b}_{Km}^{(0)\dagger}(k')\,dk'}{\left[\left(-ikv_J+\bar{\Gamma}_n\right)\left(-ikv_J+\bar{\Gamma}_m\right)+|\kappa|^2\right]}&\\ -\frac{i\Lambda\left(-ikv_J+\bar{\Gamma}_m\right)\int F_{Jn}(k,k')\,\bar{b}_{Kn}^{(0)\dagger}(k')\,dk'}{\left[\left(-ikv_J+\bar{\Gamma}_n\right)\left(-ikv_J+\bar{\Gamma}_m\right)+|\kappa|^2\right]},&\end{aligned} \tag{6.106}$$

where again, for $J=S\,(I)$, $K=I\,(S)$ and for $n=1\,(2)$, $m=2\,(1)$. Equation 6.21 then allows this to be considered as the pulsed Fourier transformed version of equation 6.22. This can then be substituted into the frequency versions of the correlation functions defined in section 6.4 to give the first order semiclassical pulsed solution.

This can also be repeated for FWM to give the similar equations

$$\begin{aligned}\left[\left(-ikv_J+\bar{\Gamma}_n\right)\left(-ikv_J+\bar{\Gamma}_m\right)+|\kappa|^2\right]\bar{b}^{(1)}_{Jn}(k) &= \left[\left(-ikv_J+\bar{\Gamma}_n\right)\left(-ikv_J+\bar{\Gamma}_m\right)+|\kappa|^2\right]\bar{b}^{(0)}_{Jn}(k)\\ &-\frac{i\zeta}{2\pi}\int \bar{\beta}^{\dagger(0)}_{Pn}\left(k'_P\right)\bar{\beta}^{(0)}_{Pn}(k_P)\,\bar{b}^{(0)}_{Jn}\left(k+\frac{v_P}{v_J}\left(k'_P-k_P\right)\right)dk_P\,dk'_P\left(-ikv_J+\bar{\Gamma}_m\right)\\ &-\frac{\kappa\zeta}{2\pi}\int \bar{\beta}^{\dagger(0)}_{Pm}\left(k'_P\right)\bar{\beta}^{(0)}_{Pm}(k_P)\,\bar{b}^{(0)}_{Jm}\left(k+\frac{v_P}{v_J}\left(k'_P-k_P\right)\right)dk_P\,dk'_P\\ &-\kappa\Lambda\int F_{Jm}\left(k,k'\right)\bar{b}^{(0)\dagger}_{Km}\left(k'\right)\,dk'-i\Lambda\left(-ikv_J+\bar{\Gamma}_m\right)\int F_{Jn}\left(k,k'\right)\bar{b}^{(0)\dagger}_{Kn}\left(k'\right)\,dk',\end{aligned}\tag{6.107}$$

where $F_{Sn}\left(k,k'\right)$ and $F_{In}\left(k,k'\right)$ are defined here as

$$F_{Sn,FWM}\left(k,k'\right)=\frac{1}{2\pi}\int \bar{\beta}^{(0)}_{Pn}(k_P)\,\bar{\beta}^{(0)}_{Pn}\left(k'_P\right)\delta\left(kv_S-k_Pv_P-k'_Pv_P+k'v_I+\Delta\right)dk_P\,dk'_P \tag{6.108}$$

$$F_{In,FWM}\left(k,k'\right)=\frac{1}{2\pi}\int \bar{\beta}^{(0)}_{Pn}(k_P)\,\bar{\beta}^{(0)}_{Pn}\left(k'_P\right)\delta\left(kv_I-k_Pv_P-k'_Pv_P+k'v_S+\Delta\right)dk_P\,dk'_P. \tag{6.109}$$

This can be simplified by neglecting the XPM terms, by setting $\zeta=0$, which reduces the FWM solutions to the SPDC solutions, except that $F_{Jn,FWM}$ definitions are used instead of $F_{Jn,SPDC}$.

6.6 Calculating Correlation Functions

6.6.1 Continuous Solution

Appendix D gives the integrals for the different terms that appear in calculating the correlation functions $G^{(1)}_m$ and A_m, which are in turn used in calculating the other correlation functions of section 6.4. Fourier transforming then gives these correlation functions in frequency space. Throughout this section, we assumme that the pump is resonant only with the first ring. We give the analytic formula for the FWM solution given in section 6.5.1, having used the formulas in appendix D. These apply when the total loss in the first ring equals the total loss in the second ring, $\bar{\Gamma}_1=\bar{\Gamma}_2$. However, when this does not apply, the matrix elements are considerably longer, so we calculate these numerically.

In addition, there are other potiential issues in comparing a single ring to coupled rings that are more noticeable when the input pump is CW. The easiest way of comparing a single ring to coupled rings is by saying that each of the coupled rings have the same loss, which is equal to the loss of the single ring. However, in doing this, because the coupled rings are individually only coupled to a single waveguide, this is implicitly saying that the single ring only couples to a single waveguide when comparing like-for-like. However, especially in the case of a CW input, having two waveguides coupled to the system considerably changes its behaviour. One particular example is that the second waveguide allows for considerably larger amounts of destructive interference of the pump with istelf at the point of coupling to/from the input waveguide/ring, allowing the ring to be used as a add-drop filter, such as in [82]. As such, having two waveguides potentially allows the system to perform different functions, or the same functions in different ways. As this is the case, the fairest way to compare the systems would be to compare the coupled rings (when there are also two waveguides) with both a single ring coupled to a single waveguide and a single ring coupled to two waveguides.

We start with the un-normalised, unheralded first order correlation function given by equation 6.71,

$$G_m^{(1)}\left(t_l, t_p\right) = 4\Gamma_m e^{-i\Delta_p\left(t_l - t_p\right)} \int \sum_n \bar{\Gamma}_n G_{SmIn}^*\left(t_l - t'\right) G_{SmIn}\left(t_p - t'\right) dt'. \tag{6.110}$$

Valid for $\sigma_\pm < \bar{\Gamma}$, this gives the output photon numbers

$$\begin{aligned} J_1 = \Gamma z^2 &\left[\left(\sigma_-^2 + \bar{\Gamma}^2\right)\left(\sigma_+^2 + \bar{\Gamma}^2\right)\left(\left(\sigma_- - \sigma_+\right)^2 + 4\bar{\Gamma}^2\right)\left(\left(\sigma_- + \sigma_+\right)^2 + 4\bar{\Gamma}^2\right)\right]^{-1} \\ &\Big[\sigma_-^4\left(\sigma_+^2 + \bar{\Gamma}^2\right) + \bar{\Gamma}^2\sigma_+^4 + \left(8\bar{\Gamma}^4 + \kappa^2\left(3\bar{\Gamma}^2 + \Delta_p^2\right) - 2\bar{\Gamma}^2\Delta_p^2 + \Delta_p^4\right)\sigma_+^2 \\ &+ \sigma_-^2\left(2\left(4\bar{\Gamma}^2 - 2\Delta_p^2 + \kappa^2\right)\sigma_+^2 + \sigma_+^4 + 8\bar{\Gamma}^4 + \kappa^2\left(3\bar{\Gamma}^2 + \Delta_p^2\right) - 2\bar{\Gamma}^2\Delta_p^2 + \Delta_p^4\right) \\ &+ 2\bar{\Gamma}^2\left(8\bar{\Gamma}^4 + \bar{\Gamma}^2\left(8\Delta_p^2 + 6\kappa^2\right) + 5\Delta_p^2\left(\Delta_p^2 + \kappa^2\right)\right)\Big] \end{aligned} \tag{6.111}$$

$$J_2 = \Gamma\kappa^2 z^2 \frac{\sigma_-^2\left(8\sigma_+^2 + 12\bar{\Gamma}^2 + 4\Delta_p^2 + \kappa^2\right) + \left(12\bar{\Gamma}^2 + 4\Delta_p^2 + \kappa^2\right)\sigma_+^2 + 48\bar{\Gamma}^4 + 10\bar{\Gamma}^2\left(4\Delta_p^2 + \kappa^2\right)}{4\left(\sigma_-^2 + \bar{\Gamma}^2\right)\left(\sigma_+^2 + \bar{\Gamma}^2\right)\left(\left(\sigma_- - \sigma_+\right)^2 + 4\bar{\Gamma}^2\right)\left(\left(\sigma_- + \sigma_+\right)^2 + 4\bar{\Gamma}^2\right)}. \tag{6.112}$$

However, shown in figure 6.10, for a single ring, this simplifies to

$$J_{\text{single}} = J_1\left(\kappa = 0\right) = \frac{z^2\Gamma}{3z^2 + \bar{\Gamma}^2 - 4z\Delta_p + \Delta_p^2}, \tag{6.113}$$

which is valid for $-3z^2 + 4z\Delta_p - \Delta_p^2 < \bar{\Gamma}^2$. Beyond this point, the effect of Optical Parametric Oscillation (OPO) occurs, where the photons in the system oscillate between being at the pump photons and signal/idler photons, directly meaning that the number of pump photons in the systems oscillates with time, so no steady state solution exists. Although simply maximising the output (average) photon number is (at least equivalent or similar to) maximising the squeezing produced, this may or may not be the desired outcome. However, being able to produce the same brightness with less pump power is a more efficient system. As such, we start by plotting the rate of output photons J_1 for a single ring in figure 6.10 and for equivalent coupled rings in figure 6.12. From these graphs, while the output rate of photons from the coupled rings can be greater than the equivalent single ring for particular detunings, at the optimum detuning $\Delta = \sqrt{3}\bar{\Gamma}$, the output from a single ring is maximised at a lower value of z than the coupled rings. From this, the output rate from a single ring can always be saturated with a lower input power than the equivalent coupled rings. This is true even at the EP surface, plotted in figure 6.11. However, unlike with a pulsed input, with a CW input, the EP can be adiabatically explored, which may be of interest in $\mathcal{PT}$-symmetry experiments. In contrast with section 6.6.2, only having a single waveguide coupled to the system, so that the second ring has lower loss, the coupled ring system is still no better than the single ring, as shown in figure 6.13.

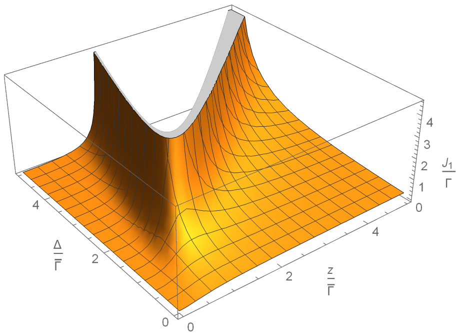

Figure 6.10: Graph of the average photon number output J of FWM in a single ring. This shows the bistability at $\Delta_P > \sqrt{3}\bar{\Gamma}$, where there is a range of invalid stable solutions for z, which coincides with the phenomenon of Optical Paramtric Oscillation (OPO).

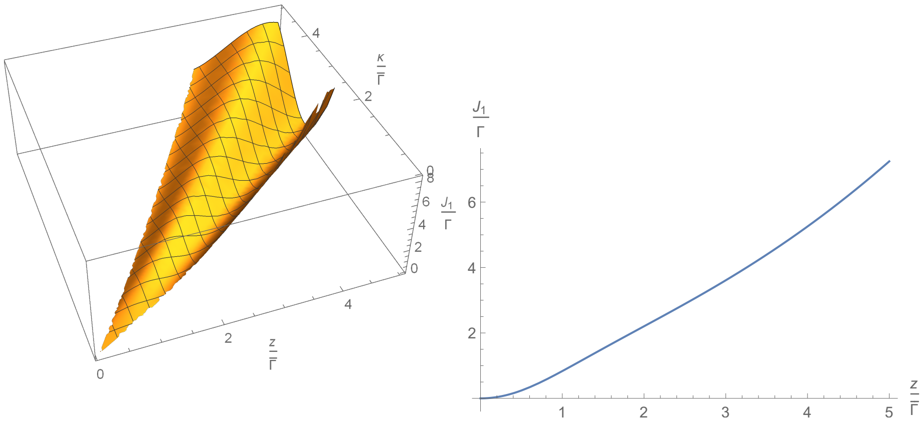

Figure 6.11: Graph of the average photon number output J of FWM along the lossy EP2 given by equation 6.60 (left) and additionally along the line $z = \Delta_P$ (right). While this region is always stable and also shows an almost linear increase with z for (approximately) $\bar{\Gamma} < z < 4\bar{\Gamma}$, it offers none of the typical enhancements of an EP, although as this is an EP surface, may be of theoretical interest in e.g. adiabatically exploring phases in the EP.

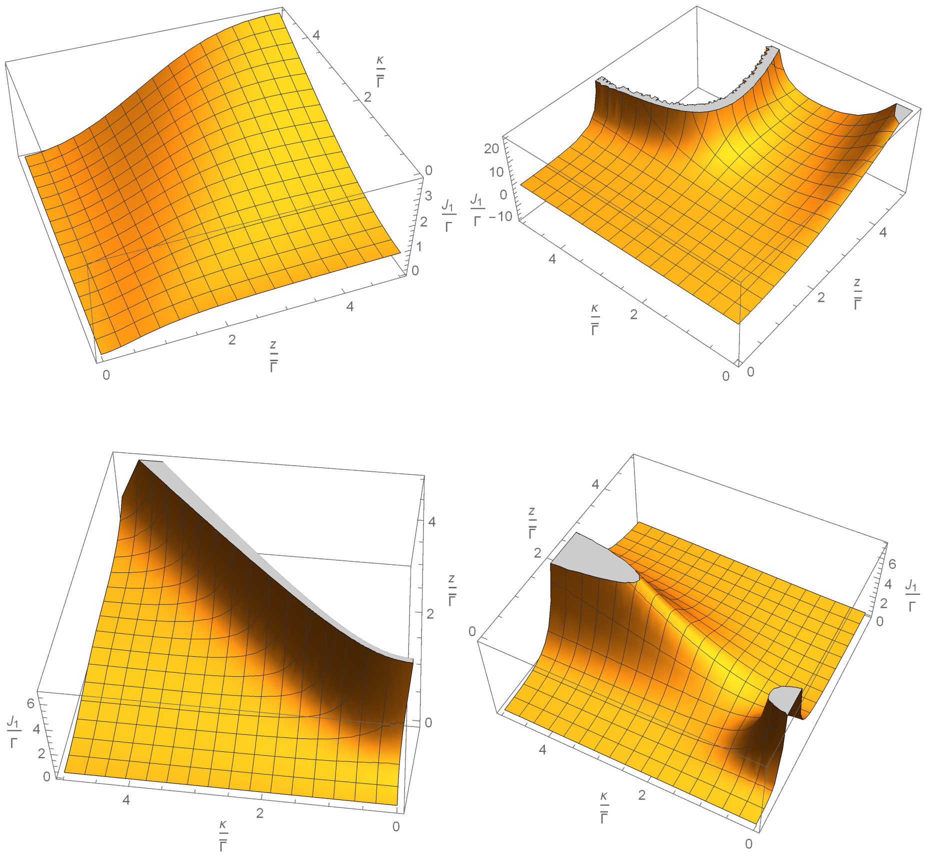

Figure 6.12: Graph of the average photon number output J of FWM in a coupled rings. Top left has $2\Delta_P = z$ and top right has $\Delta_P = z$. These top graphs give regimes where having 2 rings (and larger coupling) improves the rate of single photons output. However, the bottom graphs show the opposite, where the equivalent single ring (or, smaller coupling) coupled to a single waveguide gives a larger output. Bottom left shows $2\Delta_P = 3z$ and bottom right shows the critical detuning $\Delta_P = \sqrt{3}\Gamma$.

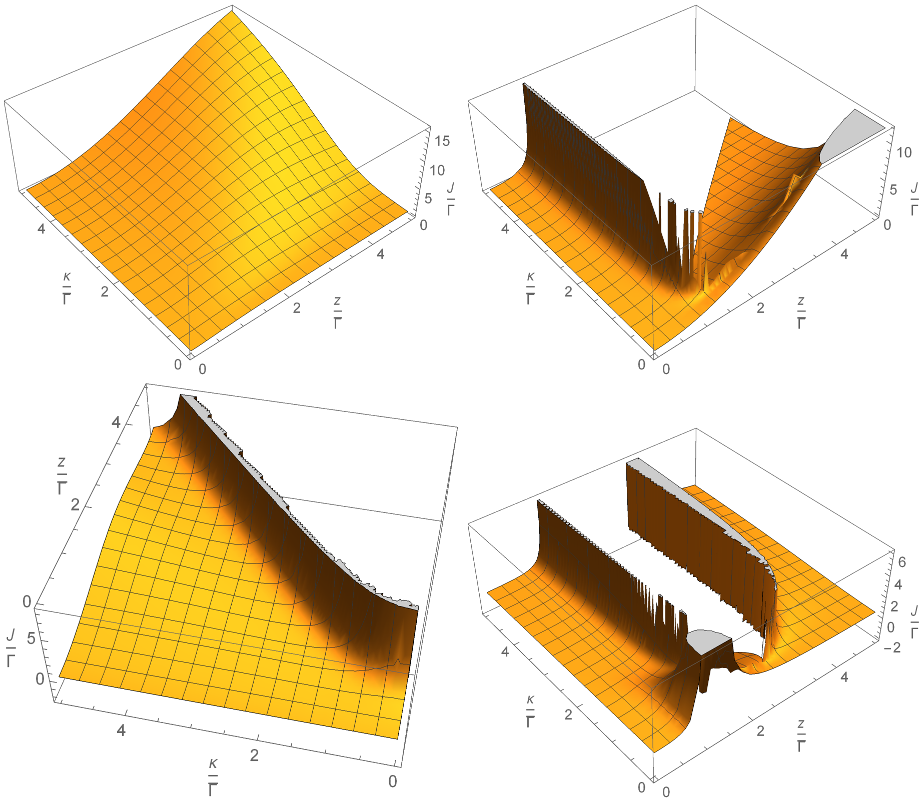

Figure 6.13: Numerically calculated graph of the average photon number output J of FWM in a coupled rings where the second ring remains uncoupled to any waveguides and has a loss rate $\bar{\Gamma}_2 = M_2 = \bar{\Gamma}_1/100$. Top left has $2\Delta_P = z$ and top right has $\Delta_P = z$. As in figure 6.12, these top graphs give regimes where having 2 rings (and larger coupling) improves the rate of single photons output. However, the bottom graphs still show the opposite, where the single ring system coupled to a single waveguide gives a larger output. Bottom left shows $2\Delta_P = 3z$ and bottom right shows the critical detuning $\Delta_P = \sqrt{3}\bar{\Gamma}$. As this is numerically calculated, errors near the transition point between stable and unstable regions occur.

This can also be looked at with a system with a CW input that undergoes SPDC, as in figure 6.14 for rings with equal loss and figure 6.15 for rings with $\bar{\Gamma}_1 = 100\bar{\Gamma}_2$. This again demonstrates that a single ring undergoing SPDC has the ability to produce a similar number of output photons (i.e. the same amount of squeezing) as the coupled rings, although at a lower input pump power. This also holds even when the rate of loss in the second ring is much smaller than the rate of loss in the first ring.

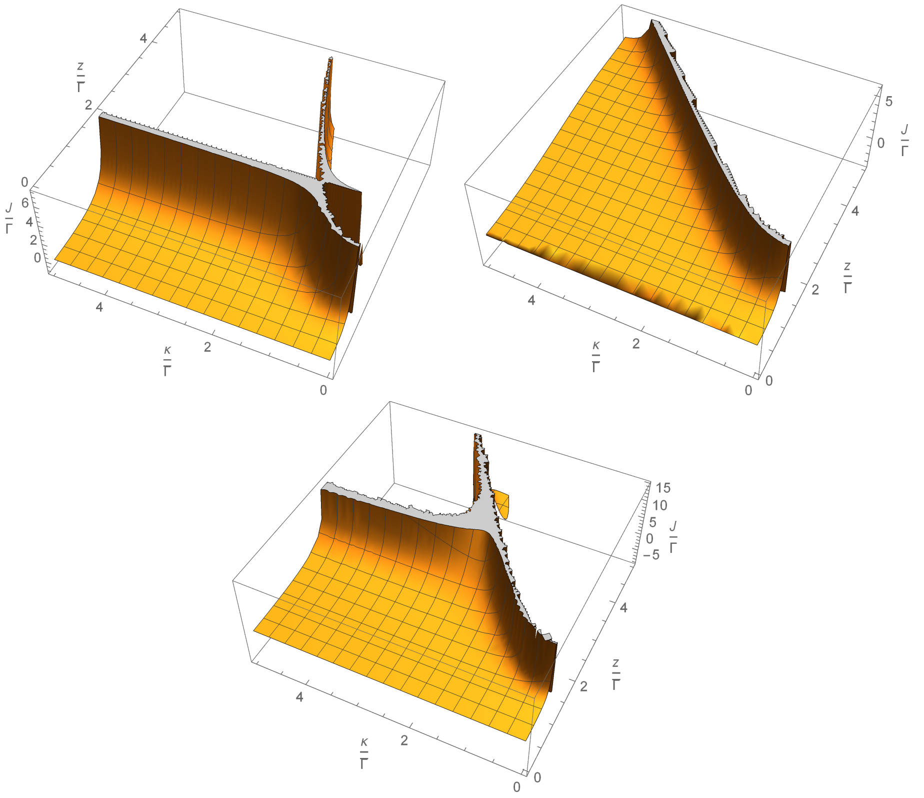

Figure 6.14: Numerically calculated graph of the average photon number output J_1 of SPDC in a coupled ring system with $\bar{\Gamma}_1 = \bar{\Gamma}_2$ (and $z_2 = 0$). Top left has $\Delta_P = 0$ and top right has $2\Delta_P = z_1$. Bottom graphs shows $4\Delta_P = \left(\sqrt{5} - 1\right) z_1$. This shows that the single ring system coupled to a single waveguide gives a similar output to the coupled ring system at a lower pump input power.

While this gives the rate of getting photons output from the system, the distribution of these photons is also an important property. As such, the first order correlation function G_1 is plotted in frequency space in figure for rings with equal loss undergoing FWM. This shows that coupled rings can cause frequency splitting, although this does not always necessarily occur. While coupled rings have parameters that give large narrow spikes in the correlation function (indicating a large squeezing parameter), this also occurs in single ring systems. This indicates that a CW input into coupled rings has a similar qualitative effect to a CW input to a single ring, although may be of theoretical interest in exploring $\mathcal{PT}$-symmetric systems.

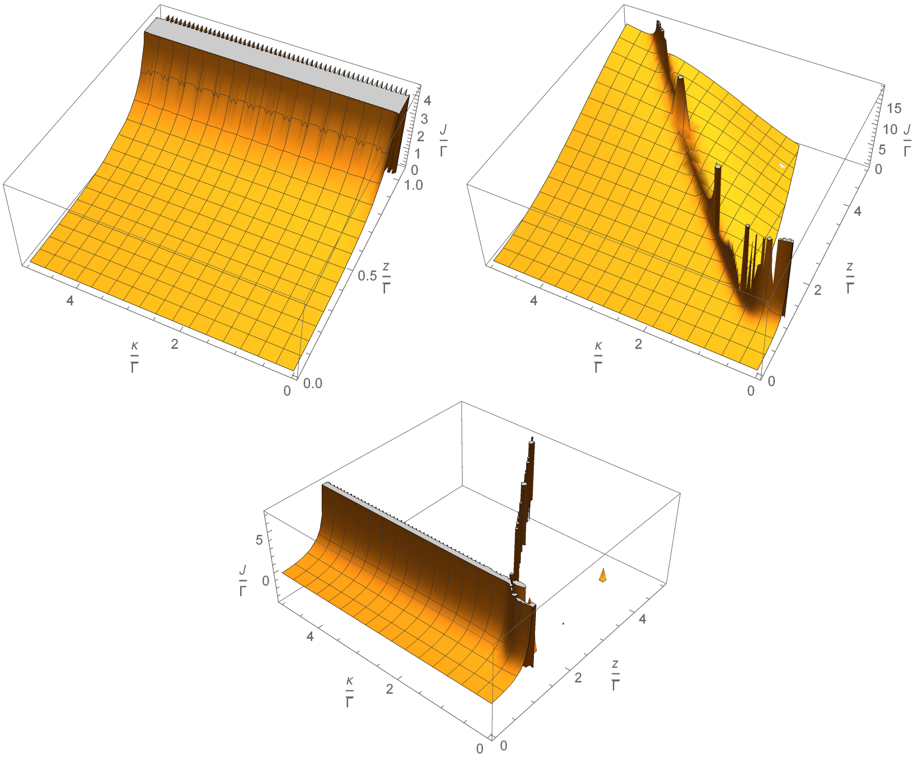

Figure 6.15: Numerically calculated graph of the average photon number output J_1 of SPDC in a coupled ring system with $\bar{\Gamma}_1 = 100\bar{\Gamma}_2$ (and $z_2 = 0$). Top left has $\Delta_P = 0$ and top right has $2\Delta_P = z_1$. Bottom graphs shows $4\Delta_P = \left(\sqrt{5} - 1\right) z_1$. As with figure 6.14, this shows that the single ring system coupled to a single waveguide gives a similar output to the coupled ring system at a lower pump input power.

Rings with a CW input may be of theoretical interest and have applications, such as exploring the high squeezing limit and the threshold between quantum and classical behaviour, or the breakdown of the undepleted pump approximation. However, a CW input generally creates less than ideal single photons, when the aim is to, for example, interact photons from different sources. This can be shown by calculating the Joint Spectral Intensity (JSI) with the aim of finding unentangled photons/a highly pure state. From section 6.4.2, we already have that the Joint Temporal Intensity depends on both $G^{(1)}$ and A correlation functions. As done in [77] for a single ring, this results in a highly correlated term in the Joint Spectral Intensity that cannot be ignored. As such, a CW input is rarely considered a good single photon source when interfering multiple photons from different sources as the (heralded) single photon purity is much lower than other sources, or the same source with a pulsed input.

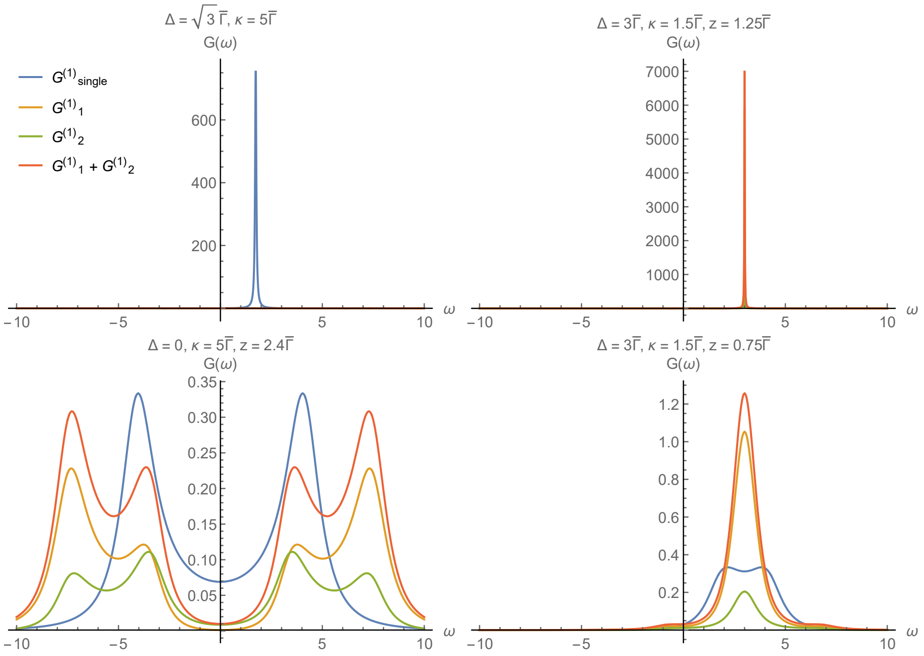

Figure 6.16: Graphs show the first order correlaton function $G^{(1)}(\omega)$ for a variety of parameters for both single and coupled rings. This shows that, although the calculated quantitative numbers are different, both single and coupled rings have similar qualitative features in their outputs. Top graphs show that both single and coupled rings can have large spikes in their output at a single frequency, potentially indicating the approach of instability (or OPO) as well as breakdown of the undepleted pump approximation. Bottom graphs show that, at the single photon output level, both the single ring and coupled rings can have single frequency peaks as well as multiple peaks, depending on the parameters, although coupled rings can have extra peaks due to the frequency splitting from both coupling between rings and detuning.

6.6.2 Pulsed Solution

Taking the definition of Joint Spectral Intensity (JSI) as

$$G^{(2)}_{si,m}\left(k,k'\right) = v_S v_I \left\langle \bar{\psi}^{\dagger}_{Im>}\left(k\right) \bar{\psi}^{\dagger}_{Sm>}\left(k'\right) \bar{\psi}_{Sm>}\left(k'\right) \bar{\psi}_{Im>}\left(k\right) \right\rangle \tag{6.114}$$

and using

$$\bar{\psi}_{Jm>}\left(k\right) = \bar{\psi}_{Jm<}\left(k\right) - \frac{i\gamma_{Jm}}{v_J}\bar{b}_{Jm}\left(k\right) \tag{6.115}$$

immediately gives

$$G^{(2)}_{si,m}\left(k,k'\right) = 2\bar{\Gamma}_{Im} v_S \left\langle \bar{b}^{\dagger}_{Im}\left(k\right) \bar{\psi}^{\dagger}_{Sm>}\left(k'\right) \bar{\psi}_{Sm>}\left(k'\right) \bar{b}_{Im}\left(k\right) \right\rangle . \tag{6.116}$$

This is further expanded by using the property that, to first order,

$$\begin{aligned}
&\bar{b}_{Im}^{(0)}\left(k\right)\left|\mathrm{vac}\right\rangle = 0 && (6.117)\\
\implies &\bar{b}_{Im}^{(1)}\left(k\right)\left|\mathrm{vac}\right\rangle = -\frac{\kappa\Lambda}{\left[\left(-ikv_J+\bar{\Gamma}_n\right)\left(-ikv_J+\bar{\Gamma}_m\right)+|\kappa|^2\right]}\int F_{In}\left(k,k'\right)\bar{b}_{Sn}^{(0)\dagger}\left(k'\right)\,dk'\\
&\qquad -\frac{i\Lambda\left(-ikv_I+\bar{\Gamma}_n\right)}{\left[\left(-ikv_J+\bar{\Gamma}_n\right)\left(-ikv_J+\bar{\Gamma}_m\right)+|\kappa|^2\right]}\int F_{Im}\left(k,k'\right)\bar{b}_{Sm}^{(0)\dagger}\left(k'\right)\,dk', && (6.118)
\end{aligned}$$

which gives

$$\begin{aligned}
&\bar{\psi}_{Sm<}\left(k'\right)\bar{b}_{Im}^{(1)}\left(k\right)\left|\mathrm{vac}\right\rangle =\\
&\quad\frac{\gamma_{Sm}^{*}\Lambda\left[\left(-ikv_I+\bar{\Gamma}_n\right)\left(ik'v_S+\bar{\Gamma}_n\right)F_{Im}\left(k,k'\right)+\kappa^2F_{In}\left(k,k'\right)\right]}{\left[\left(-ikv_I+\bar{\Gamma}_n\right)\left(-ikv_I+\bar{\Gamma}_m\right)+|\kappa|^2\right]\left[\left(ik'v_S+\bar{\Gamma}_n\right)\left(ik'v_S+\bar{\Gamma}_m\right)+|\kappa|^2\right]}\left|\mathrm{vac}\right\rangle \qquad (6.119)
\end{aligned}$$

and similarly using

$$\begin{aligned}
&\bar{b}_{Jm}^{(0)}\left(k'\right)\bar{b}_{Jm}^{(0)\dagger}\left(k\right)\left|\mathrm{vac}\right\rangle =\\
&\quad\frac{2v_J\bar{\Gamma}_m\left[\left(-ik'v_J+\bar{\Gamma}_n\right)\left(ikv_J+\bar{\Gamma}_n\right)-\kappa^2\right]\delta\left(k-k'\right)}{\left[\left(-ik'v_J+\bar{\Gamma}_n\right)\left(-ik'v_J+\bar{\Gamma}_m\right)+|\kappa|^2\right]\left[\left(ikv_J+\bar{\Gamma}_n\right)\left(ikv_J+\bar{\Gamma}_m\right)+|\kappa|^2\right]} \qquad (6.120)\\
&\bar{b}_{Jn}^{(0)}\left(k'\right)\bar{b}_{Jm}^{(0)\dagger}\left(k\right)\left|\mathrm{vac}\right\rangle =\\
&\quad\frac{2v_J^2\kappa\left(k'\bar{\Gamma}_n+k\bar{\Gamma}_m\right)\delta\left(k-k'\right)}{\left[\left(-ik'v_J+\bar{\Gamma}_n\right)\left(-ik'v_J+\bar{\Gamma}_m\right)+|\kappa|^2\right]\left[\left(ikv_J+\bar{\Gamma}_n\right)\left(ikv_J+\bar{\Gamma}_m\right)+|\kappa|^2\right]} \qquad (6.121)
\end{aligned}$$

gives

$$\begin{aligned}
&\bar{b}_{Sm}^{(0)}\left(k'\right)\bar{b}_{Im}^{(1)}\left(k\right)\left|\mathrm{vac}\right\rangle =\\
&\quad-\frac{2v_S\Lambda\left[i\bar{\Gamma}_m\left(-ikv_I+\bar{\Gamma}_n\right)\left(k'^2v_S^2+\bar{\Gamma}_n^2-\kappa^2\right)F_{Im}\left(k,k'\right)+\kappa^2v_Sk'\left(\bar{\Gamma}_m+\bar{\Gamma}_n\right)F_{In}\left(k,k'\right)\right]}{\left[\left(-ikv_I+\bar{\Gamma}_n\right)\left(-ikv_I+\bar{\Gamma}_m\right)+|\kappa|^2\right]\left|\left(ik'v_S+\bar{\Gamma}_n\right)\left(ik'v_S+\bar{\Gamma}_m\right)+|\kappa|^2\right|^2} \qquad (6.122)\\
&\bar{b}_{Sn}^{(0)}\left(k'\right)\bar{b}_{Im}^{(1)}\left(k\right)\left|\mathrm{vac}\right\rangle =\\
&\quad-\frac{2\kappa\Lambda\bar{\Gamma}v_S\left[\left(k'^2v_S^2+\bar{\Gamma}^2-\kappa^2\right)F_{In}\left(k,k'\right)+2iv_Sk'\left(-ikv_J+\bar{\Gamma}\right)F_{Im}\left(k,k'\right)\right]}{\left[\left(-ikv_I+\bar{\Gamma}_n\right)\left(-ikv_I+\bar{\Gamma}_m\right)+|\kappa|^2\right]\left|\left(ikv_S+\bar{\Gamma}_n\right)\left(ikv_S+\bar{\Gamma}_m\right)+|\kappa|^2\right|^2}. \qquad (6.123)
\end{aligned}$$

At this point, the effects of XPM are often ignored by setting $\zeta = 0$. While the XPM term is larger than (although the same order of magnitude as) the FWM term Λ, this can be shown as a valid approximation by calculating the Joint Spectral Amplitude (JSA) to first order in Λ to get

$$\bar{b}_{Sm}\left(k'\right)\bar{b}_{Im}\left(k\right)\left|\mathrm{vac}\right\rangle \approx \bar{b}_{Sm}^{(1)}\left(k'\right)\bar{b}_{Im}^{(1)}\left(k\right)\left|\mathrm{vac}\right\rangle = \bar{b}_{Sm}^{(0)}\left(k'\right)\bar{b}_{Im}^{(1)}\left(k\right)\left|\mathrm{vac}\right\rangle + \mathcal{O}\left(\zeta\Lambda\right) + \mathcal{O}\left(\Lambda^2\right). \qquad (6.124)$$

While the higher order terms are necessary for higher order expansions (such as for large amounts of squeezing), when creating individual pairs of photons, these higher order terms are small, the XPM terms (as well as the terms involving higher orders of Λ) can therefore be ignored here. Assuming $\gamma_S = \gamma_I = \gamma$ and $v_S = v_I = v$, this gives

$$\begin{aligned} G^{(2)}_{si,m}\left(k,k'\right) &= \\ &4v_S^2 \Gamma_m \bar{\Gamma}_m \left|\Lambda\right|^2 \left| \frac{\left(-ikv_I + \bar{\Gamma}_n\right)\left(ik'v_S + \bar{\Gamma}_n\right) F_{Im}\left(k,k'\right) + \kappa^2 F_{In}\left(k,k'\right)}{\left[\left(-ikv_I + \bar{\Gamma}_n\right)\left(-ikv_I + \bar{\Gamma}_m\right) + \left|\kappa\right|^2\right]\left[\left(ik'v_S + \bar{\Gamma}_n\right)\left(ik'v_S + \bar{\Gamma}_m\right) + \left|\kappa\right|^2\right]} \right. \\ &\left. - 2\frac{\bar{\Gamma}_m\left(-ikv_I + \bar{\Gamma}_n\right)\left(k'^2 v_S^2 + \bar{\Gamma}_n^2 - \kappa^2\right) F_{Im}\left(k,k'\right) - i\kappa^2 v_S k'\left(\bar{\Gamma}_m + \bar{\Gamma}_n\right) F_{In}\left(k,k'\right)}{\left[\left(-ikv_I + \bar{\Gamma}_n\right)\left(-ikv_I + \bar{\Gamma}_m\right) + \left|\kappa\right|^2\right]\left|\left(ik'v_S + \bar{\Gamma}_n\right)\left(ik'v_S + \bar{\Gamma}_m\right) + \left|\kappa\right|^2\right|^2} \right|^2 . \end{aligned} \tag{6.125}$$

We first plot this for typically coupled rings with a Q factor of $Q \sim 10^6$, with pump resonant in both rings and input into both waveguides to give an example of a typical system and compare this with an equivalent single ring (using equation 6.127 below) in figure 6.17. However, this system is worse than the equivalent single ring, so we now aim to optimise parameters and try to find an enhancement typical of (at least classical) $\mathcal{PT}$-symmetric systems.

Alternatively, as picking a value of coupling to match the loss in the ring gives an output worse than that of a single ring, in order to help compare coupled rings with a single ring more effectively, the case where the pump is resonant only a single ring (here, the first) can be considered, to give

$$\begin{aligned} G^{(2)}_{si,m}\left(k,k'\right) &= 4v_S^2 \Gamma_m \bar{\Gamma}_m \left|\Lambda\right|^2 \cdot \\ &\left| \frac{\left(-ikv_I + \bar{\Gamma}_n\right) F_{Im}\left(k,k'\right)\left[\left(ik'v_S + \bar{\Gamma}_n + 2\bar{\Gamma}_m\right)\left|\kappa\right|^2 - \left(k'^2 v_S^2 + \bar{\Gamma}_n^2\right)\left(ik'v_S + \bar{\Gamma}_m\right)\right]}{\left[\left(-ikv_I + \bar{\Gamma}_n\right)\left(-ikv_I + \bar{\Gamma}_m\right) + \left|\kappa\right|^2\right]\left|\left(ik'v_S + \bar{\Gamma}_n\right)\left(ik'v_S + \bar{\Gamma}_m\right) + \left|\kappa\right|^2\right|^2} \right|^2 . \end{aligned} \tag{6.126}$$

In the limit of zero coupling between rings ($\kappa = 0$), we obtain the JTI of a single ring (setting $\bar{\Gamma} = \bar{\Gamma}_1$)

$$G^{(2)}_{si,1}\left(k,k'\right) = 4v_S^2 \Gamma \bar{\Gamma} \left|\Lambda\right|^2 \left| \frac{F_{Im}\left(k,k'\right)}{\left(ikv_I + \bar{\Gamma}\right)\left(ik'v_S + \bar{\Gamma}\right)} \right|^2 . \tag{6.127}$$

This allows for defining an 'enhancement' factor (which may or may not be an enhancement) by taking the ratio of multiple rings to a single ring, which is here independent of the process (SPDC or FWM) used,

$$\begin{aligned} &\left| \frac{\left(-ikv_I + \bar{\Gamma}_n\right)\left(ikv_I + \bar{\Gamma}_1\right)\left(ik'v_S + \bar{\Gamma}_1\right)}{\left[\left(-ikv_I + \bar{\Gamma}_n\right)\left(-ikv_I + \bar{\Gamma}_m\right) + \left|\kappa\right|^2\right]\left|\left(ik'v_S + \bar{\Gamma}_n\right)\left(ik'v_S + \bar{\Gamma}_m\right) + \left|\kappa\right|^2\right|^2} \cdot \right. \\ &\qquad \left. \left[\left(ik'v_S + \bar{\Gamma}_n + 2\bar{\Gamma}_m\right)\left|\kappa\right|^2 - \left(k'^2 v_S^2 + \bar{\Gamma}_n^2\right)\left(ik'v_S + \bar{\Gamma}_m\right)\right] \right|^2 . \end{aligned} \tag{6.128}$$

At the central frequency $k = k' = 0$, this then becomes

$$E_0 = \left| \frac{\bar{\Gamma}_n \bar{\Gamma}_1^2 \left[\left(\bar{\Gamma}_n + 2\bar{\Gamma}_m \right) |\kappa|^2 - \bar{\Gamma}_n^2 \bar{\Gamma}_m \right]}{\left[\bar{\Gamma}_n \bar{\Gamma}_m + |\kappa|^2 \right]^3} \right|^2 . \tag{6.129}$$

Plotting this, as in figure 6.18, makes it apparent that having a large difference in loss parameters is important, to the extent that the most effective method is to remove the second waveguide from the system entirely, so that the only loss in the second ring is the intrinsic loss M_2, which we here assume is equal to $M_1 = M$. From that, the value of the coupling rate that gives the largest enhancement in brightness then depends on the loss rates of the rings.

We then plot the JSIs of the coupled rings at the approximate value of coupling, κ, that maximises the enhancement factor in figure 6.19 for SPDC and figure 6.20 for FWM. This shows that the idea of $\mathcal{PT}$-symmetry that maximising the brightness also narrows the distribution into an output resembling that of an EP, giving much higher purities holds even for this type of quantum $\mathcal{PT}$-symmetric system. In comparison with coupled rings with randomly chosen parameters, which have lower purities and brightness than their equivalent single ring counterpart, coupled rings at an EP regime show an increased brightness of potentially several orders of magnitude (depending on the intrinsic loss M) and a purity that gets arbitrarily close to 1, also depending on the intrinsice loss. However, in practice, this will likely not hold exactly due to other effects such as backscattering and the effect of higher order terms not calculated here. As such, while it is reasonable to expect coupled rings at an EP to have a considerably higher purity than the equivalent single ring (which also suffers from the same theoretical approximations), the maximum limit of purity is highly likely to be < 1. These graphs also show an asymmetry in the calculated JSI with respect to the photon frequency. As such, as the photon modes chosen to be signal and idler are arbitrary, the true JSI will be the frequency-symmetric version $\mathrm{Sym}\left[G^{(2)}_{si,m}\left(k,k'\right)\right] = \frac{1}{2}\left(G^{(2)}_{si,m}\left(k,k'\right) + G^{(2)}_{is,m}\left(k',k\right)\right)$. While filtering can be used to recreate the JSIs shown in figures 6.19 and 6.20, this is shown explicitly in figure 6.21 for FWM with $\bar{\Gamma}_1 = 100\bar{\Gamma}_2$. However, the (numerically calculated) purity remains unchanged from the unsymmetrised version.

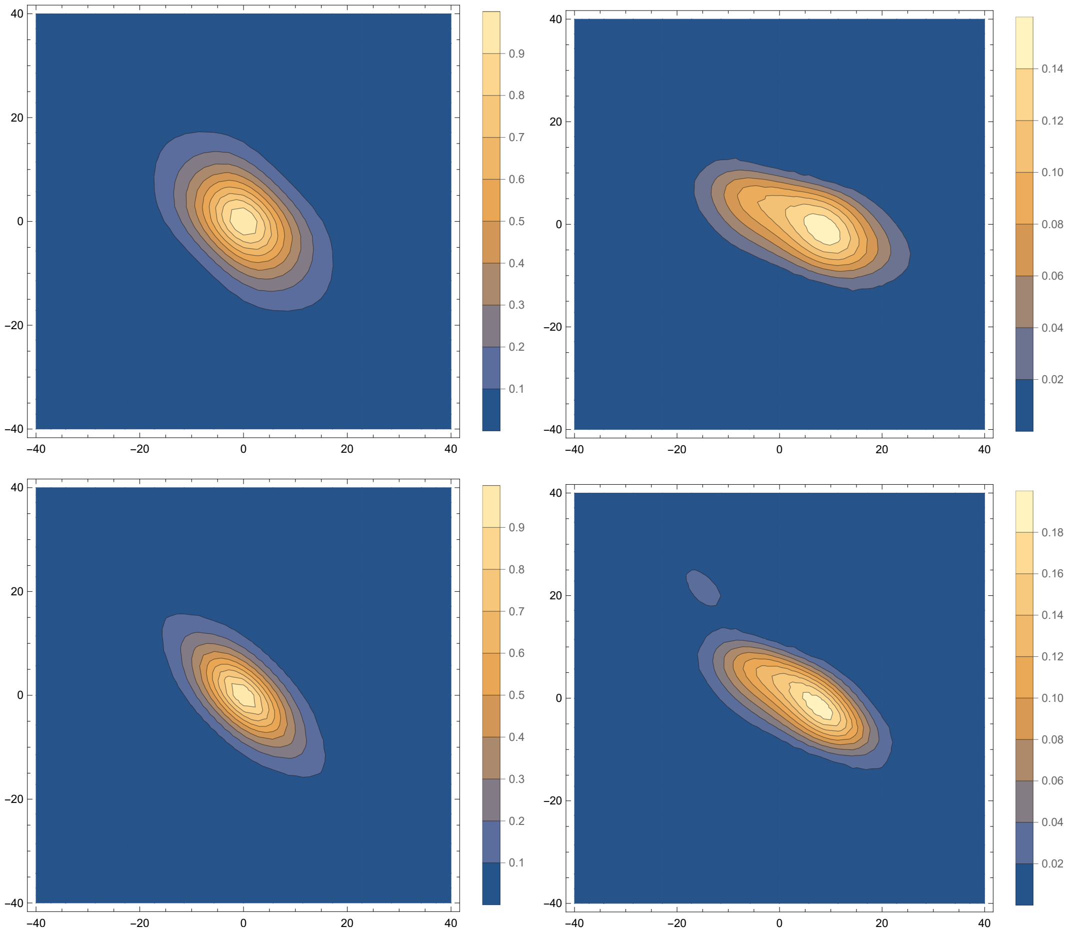

Figure 6.17: Graph of the Joint Spectral Intensity (JSI) of (top) FWM and (bottom) SPDC of a single ring (left) coupled to a single waveguide with a single pump input and (right) equivalent coupled rings with equal loss $\bar{\Gamma}$ equal to the coupling rate κ and two pumps coupled in through two waveguides. As the value of intensity scales with α_P^4 for FWM and α_P^2 for SPDC, the actual value is arbitrary, so both graphs are normalised to the peak brightness of the output of the relevant single ring. This gives several features: As the (normalised) output is independent of the input pump strength, this is not reminiscent of a typical $\mathcal{PT}$-symmetric system, where the gain is matched to the loss of the system. The brightness of the coupled rings is lower than the single ring despite having effectively twice the input pump power and twice the number of rings FWM/SPDC can occur in. The relatively large value of coupling between rings causes the central frequency to shift. While it's possible that this has other uses outside of typical single photon production, the purity of this system is $\sim 79\%$ for FWM and $\sim 68\%$ for SPDC, in comparison with the single ring purity of $\sim 88\%$ for FWM and $\sim 76\%$ for SPDC. This shows that, in this regime, the coupled rings have no benefit over a single ring as a typical single photon emitter.

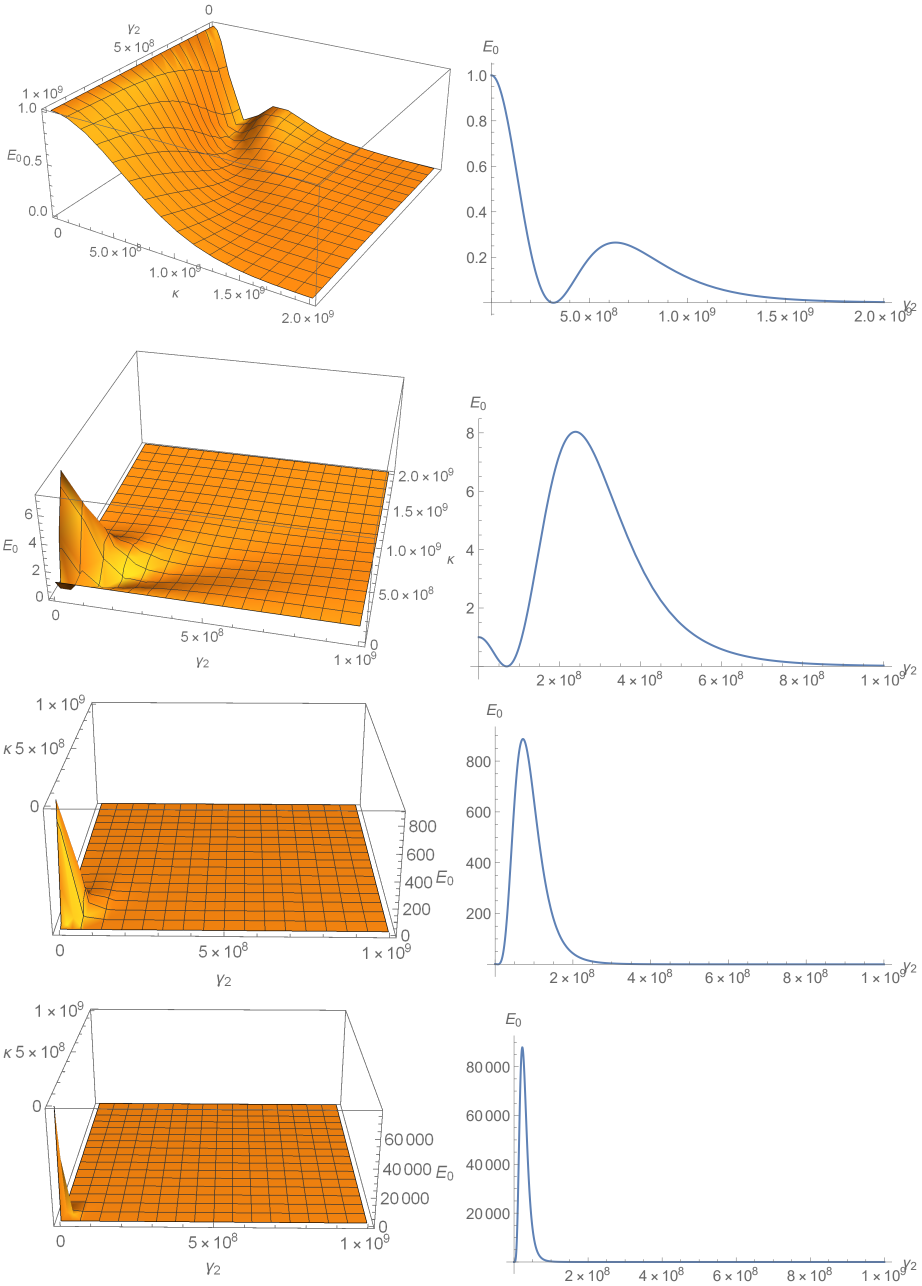

Figure 6.18: Graph of the Enhancement Factor E_0 of coupled rings compared with a single ring. Graphs are for rings with $\bar{\Gamma}_1 = 10^9$ Hz and $\mu_1 = \mu_2 = \mu$ and in order of top to bottom show loss rates M as a proportion of $\bar{\Gamma}_1$: 50%, 10%, 1% and 0.1%. Left graphs show E_0 plotted with both coupling rates γ_2 and κ. These consistently give that, when the maximum enhancement possible is greater than 1, it occurs at $\gamma_2 = 0$ (i.e. no second waveguide) and for maximum enhancement equal to 1, a single ring (being $\kappa = 0$) is optimal (for this reason, maximum enhancement cannot be < 1). Right graphs show E_0 at $\gamma_2 = 0$. This shows that, the lower the intrinsic loss rate M (i.e. the greater in difference of loss rates between rings), the larger the enhancement (up to several orders of magnitude) and the smaller the value of the coupling required to reach that enhancement.

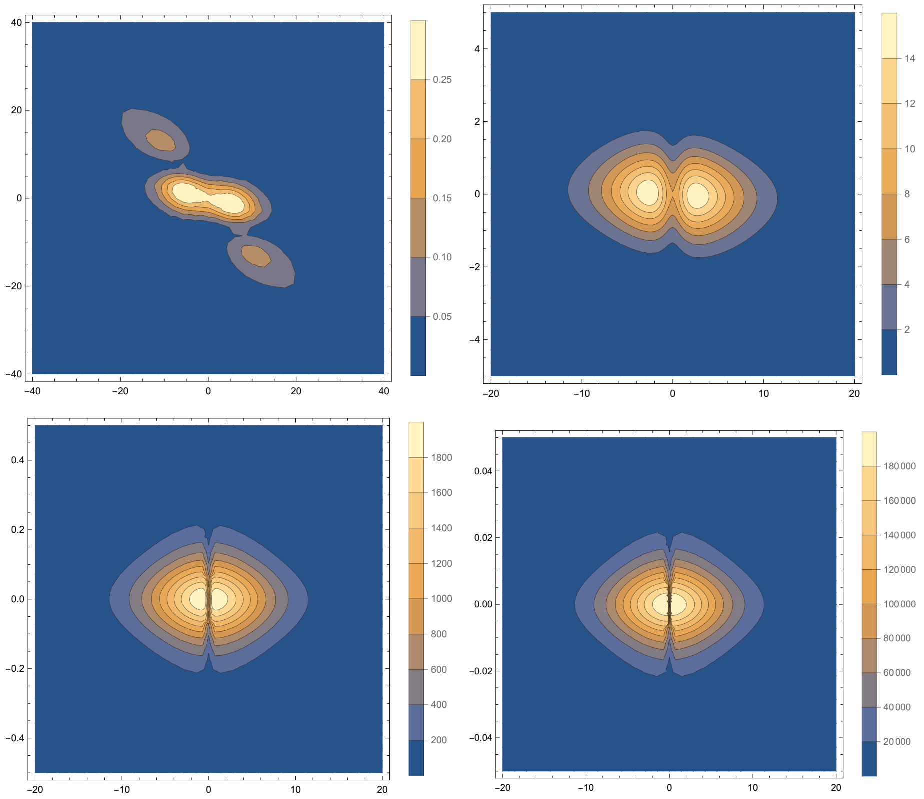

Figure 6.19: Graph of JSI of coupled rings for SPDC compared with the peak brightness of the single ring in figure 6.17. Graphs are for rings with $\bar{\Gamma}_1 = 10^9$ Hz and $\mu_1 = \mu_2 = \mu$. Loss rates M as a proportion of $\bar{\Gamma}_1$ are: (top left) 50%, (top right) 10%, (bottom left) 1% and (bottom right) 0.1%. They have respective numerically evaluated purities of: 65.0805% (as a result of frequency splitting causing multiple peaks), 99.2569%, 99.9929%, 99.9999%. While these values will likely be smaller in reality, due to other effects, such as backscattering, this demonstrates that points equivalent to EPs in physical quantum $\mathcal{PT}$-symmetric systems are possible and that here, it results in increased brightness (by orders of magnitude) and arbitrarily high purities, depending on the quality of the system.

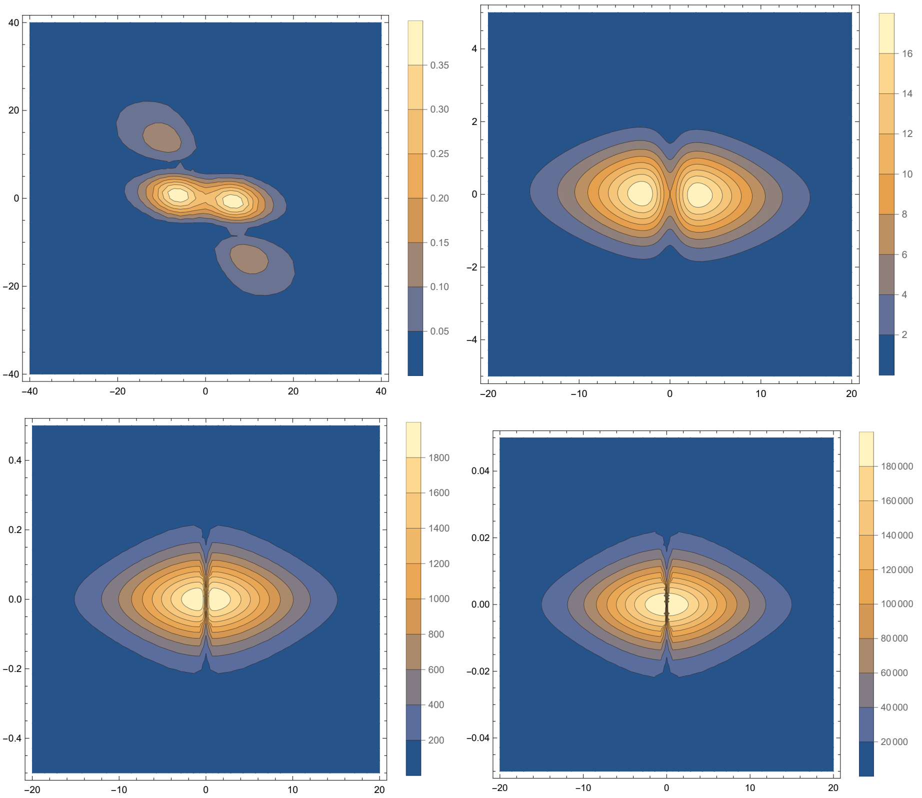

Figure 6.20: Graph of JSI of coupled rings for FWM compared with the peak brightness of the single ring in figure 6.17. Graphs are for rings with $\bar{\Gamma}_1 = 10^9$ Hz and $\mu_1 = \mu_2 = \mu$. Loss rates M as a proportion of $\bar{\Gamma}_1$ are: (top left) 50%, (top right) 10%, (bottom left) 1% and (bottom right) 0.1%. They have respective numerically evaluated purities of: 79.2902% (as a result of frequency splitting causing multiple peaks), 99.7731%, 99.9980%, 1. While these values will likely be smaller in reality, due to other effects, such as backscattering (and the last, due to numerical approximation errors), this demonstrates that, as with figure 6.19, points equivalent to EPs in physical quantum $\mathcal{PT}$-symmetric systems are possible and that here, it results in increased brightness (by orders of magnitude) and arbitrarily high purities, depending on the quality of the system.

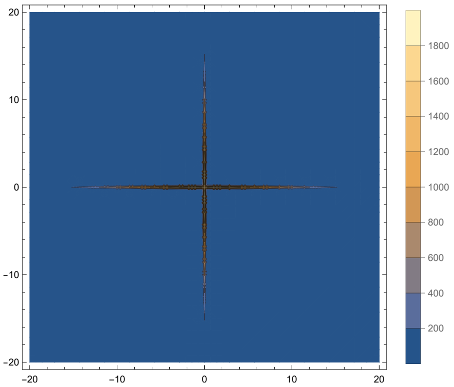

Figure 6.21: Graph of the (true) frequency-symmetrised JSI of coupled rings for FWM compared with the peak brightness of the single ring in figure 6.17. Graphs is for rings with $\bar{\Gamma}_1 = 10^9$ Hz and $\mu_1 = \mu_2 = \mu$. Loss rate is $M = \bar{\Gamma}_1/100$. The numerically evaluated purity is 99.9980%, matching that shown in figure 6.20 although this is highly likely to be smaller in reality.

6.7 Discussion and Conclusion

In this chapter, we have demonstrated the theoretical feasability of a native $\mathcal{PT}$-symmetric quantum system with both gain (which appears in the form of squeezing) and loss, which necessarily appears as the system being looked at is coupled to a waveguide which allows the output to be detected (in addition to any intrinsic loss of the system from being coupled to an environment). In this respect, both the gain and loss are required for the system to function and output to be detected, in contrast to most $\mathcal{PT}$-symmetric systems typically considered. As shown in [35], this also enforces that (Langevin) noise operators appear in the equations of motion. However, these are also necessary to the function of the system in that these noise operators are the vacuum 'fluctuations' that allow for the photons to be created.

Having shown such a system can exist, there are now two different types of this system: one exists in the steady state, with a stable solution; the other has a pulsed input making it time dependent. These approaches are different in both details and results. In the steady state with a Continuous wave input, the system can be analytically shown to have different Exceptional Points and Exceptional Point surfaces with what can be considered to be different 'backgrounds' of lossiness. In a lossy background, the Exceptional Points are little different to any other point in the parameter space and are likely only of theoretical interest in exploring $\mathcal{PT}$-symmetric quantum systems (although having the coupled rings required to create the EP allows for other possibilities that cannot occur in a single ring, such as more frequency splitting). By contrast, any point on a background of gain causes effects such as Optical Parametric Oscillations, or at least, saturation of the system, so that the system may no longer be in a steady state or the semi-classical approximation breaks down when the number of signal/idler photons approaches the number of pump photons in the system. The transition point between these (such as what can occur at the ‘neutral’ EP) is when saturation of the system is likely to occur, preventing the output from reaching an infinitely large number of photons.

The opposite approach, with a pulsed (time dependent) input, has no analytical Exceptional Points. However, this gives vastly different outputs to a pulsed input into a single ring. Where a single ring has a fundamental limit to the amount of purity that can be obtained from generating heralded single photons, this no longer applies to coupled rings. In this case, the input gain no longer appears as an important parameter in creating the effects that typically arise in $\mathcal{PT}$-symmetric systems. Instead, the difference between losses of the ring is what matters, alongside the coupling between the rings. Here, we find that when there is a large difference in the losses, there is a (numerically tractable) value of coupling that gives enhancements that typically only exist in the EP of a non-Hermitian system, that doesn’t exist for single rings. That is, a large enhancement in the efficiency of the system appears and the frequency distribution of the output becomes much narrower than the single ring. As this enhancement and narrowing is independent of the input pump strength, unlike for a continuous wave input, decreasing the pump power input allows for the same rate of photons to be output (avoiding the potential saturation problems and allowing for weaker lasers to be used) while giving improving the purity to values arbitrarily close to unity, impossible for a standard single ring. As such, we consider this as an Exceptional Point of a Quantum system that is intrinsically Parity-Time symmetric with a fundamentally important practical application, demonstrating that quantum natively $\mathcal{PT}$-symmetric systems with gain and loss can exist and even be practically advantageous.

Chapter 7

Conclusion

In this thesis, we have looked at simulating and creating $\mathcal{PT}$-symmetric quantum systems, as well as the applications of such simulation methods and systems. We have shown in chapter 4 that there are different ways of adapting the pre-existing simulation method of unitary dilation to simulate coupled non-unitary systems and that this has applications that are not typically considered in other simulation methods. In chapter 5, we showed that the idea of a unitary interferometer can be extended into a nonunitary interferometer by using a singular value decomposition and using squeezing to implement gain terms. This also demonstrated a link between $\mathcal{PT}$-symmetry and nonlinear optics. This was then used in chapter 6 to show that coupled microring resonators with gain (in the form of squeezing) and loss are $\mathcal{PT}$-symmetric and when applied to the physical process of single photon creation, the non-Hermitianity inherent in this system can be used to create large enhancements in both purity and efficiency of a single photon, in line with the exceptional points of classical $\mathcal{PT}$-symmetric systems, except here done in the quantum regime with the ability to output a highly pure quantum state of light.

In chapter 4, we started by looking at embedding purely lossy $\mathcal{PT}$-symmetric Hamiltonians into a controllable and Markovian open system and extended this idea to include simulating $\mathcal{PT}$-symmetric Hamiltonians with gain and loss using non-Markovian open systems in section 4.2.2. While this simulation method necessarily involves postselection due to jump terms in the evolution, often with low success probabilities, this is perhaps a natural way of creating systems with $\mathcal{PT}$-symmetric subsystems. The gain term in these subsystems aligns with the non-Markovianity present in the system and effects such as information retrieval are directly present, although in a limited amount. This could potentially be further adapted to look at Floquet systems where the gain and loss terms oscillate with time. Alternatively, specific examples of (potentially small) environments could be considered to demonstrate larger amounts of information retrieval that arises from the entire system behaving unitarily with only a small subsystem able to be measured. We then looked at using Halmos' unitary dilation to simulate coupled time-reversed $\mathcal{PT}$-symmetric systems in section 4.3. In this section, we looked at how a pre-existing simulation method could be adapted using various different normalisation methods. While other examples are possible and could be looked at further, we considered the specific example of 2- and 3- mode $\mathcal{PT}$-symmetric systems evolving in temporal directions that are the reverse of each other, coupled together such that the overall system remains unitary. In itself, this leads to a number of fundamental questions, including whether such a system could exist in reality. One such possible example of this is a coupled particle-antiparticle system, where the particle and antiparticle individually appear to evolve under a $\mathcal{PT}$-symmetric Hamiltonian, such as the one considered in section 4.4.2. This looked at the concept of neutral B-meson mixing (consisting of a down quark with a bottom anti-quark coupled to a bottom quark with a down anti-quark) from the context of $\mathcal{PT}$-symmetry, demonstrating that in principle, while the overall evolution remains unitary, this does not necessarily restrict the postselected individual subsystems to being Hermitian, directly reconsidering the (previously asked) question of whether, as an example, the Dirac equation must be Hermitian when it is used to describe individual particles that combine to form larger systems. We also demonstrated that the different methods of normalisation in this dilation shown in section 4.3.2 lead to different effective Hamiltonians, as in section 4.3.3. While this is an unsurprising result, this demonstrates a qualitative difference between different simulation methods, in that time-dependent normalisation leads to a steady state solution at the EP and broken regimes, while time-independent normalisation has polynomial and exponential growth and decay. This also showed that the effective Hamiltonian of the system can be discontinuous and in the case of time-dependent normalisation, can have large discontinuous spikes even when the dilated unitary is well behaved. In addition, in section 4.4.1, we demonstrated that unitary dilation can be considered as an extension of the HOM effect into multiple modes of the system. This also demonstrates that the coupling term in the dilated unitary can effectively be tuned by varying the amount of distinguishability present in the photons input into the system. This could potentially be further extended to consider more complex types of dilation involving N subsystems with N (or more) photons input, or by looking at more general states of light input into the system or by modelling loss and noise effects in the system.

In chapter 5, we then looked at extending the idea of a unitary interferometer to that of a nonunitary interferometer. In looking at the idea of an effective Hamiltonian describing the transformation given by a unitary interferometer in more detail in section 5.2, we found that the effective Hamiltonian of a unitary interferometer (consisting of beamsplitters and phase shifters) is necessarily Hermitian. We also found that the equivalent effective Hamiltonians given by squeezing operations was non-Hermitian. This idea was extended in section 5.3 to show that any symplectic transformation on the creation and annihilation operators is a $\mathcal{PT}$-symmetric transformation on the operator space of creation and annihilation operators. This allowed us to demonstrate a design of a nonunitary interferometer in section 5.4 that used nonlinear optics to, in effect, 'sandwich' the single photon creation process and create a nonunitary transformation on the heralded input state analagous to a unitary interferometer. We further showed in section 5.5 that this can be Trotterised similarly to (standard, Hermitian and local) Hamiltonian simulation albeit requiring a longer time to achieve the same error, or alternatively, in the same simulation time giving a larger error. To demonstrate that this can theoretically simulate a non-Hermitian system, we then gave a model for a 2D $\mathcal{PT}$-symmetric staggered transverse field Heisenberg spin lattice in section 5.6 where an individual spin can be parameterised by a value β and is $\mathcal{PT}$-symmetric for $\beta \in \mathbb{R}$, $\mathcal{PT}$-broken for $\beta \notin \mathbb{R}$ and at the EP when $\beta = 0$. Using a tensor network to numerically calculate the properties of the gound state of this lattice showed that, unlike a randomly chosen lattice model, the lattice remains $\mathcal{PT}$-symmetric when $\beta \in \mathrm{Re}$ and the EP stays at $\beta = 0$. Calculating the spontaneous magnetisation also showed that the critical point occurs in the Hermitian limit and can be encircled in the non-Hermitian regime. It also appears that non-Hermitian extensions to the ferromagnetic and paramagnetic phases exist within the $\mathcal{PT}$-unbroken phase. Simulating the evolution of this lattice in section 5.7 confirmed that, when $\beta \in \mathbb{R}$, the evolution is oscillatory, or stationary in the paramagnetic phase ($\beta \gg 0$). Calculating the correlations between spins showed that, in the $\mathcal{PT}$-unbroken and Hermitian phases, the correlations oscillate between being more- or less- correlated and as β gets larger in the unbroken phase, this splits, with an anti-correlation becoming larger with increasing β. At the EP, the system then becomes maximally (anti-)correlated in a steady state, with all the spins pointing in either one direction or the other. In the broken phase, the amount of (anti-)correlation then decreases.

In chapter 6, we demonstrated that a practical application of the Exceptional Point in natively $\mathcal{PT}$-symmetric quantum systems is possible, in the form of improved single photon sources. Considering squeezing as a form of $\mathcal{PT}$-symmetric gain suggested the idea of modelling a $\mathcal{PT}$-symmetric quantum system as coupled microring resonators, one with gain (i.e. squeezing), the other with loss. While loss is necessarily present in both rings, both as an intrinsic loss rate and from coupling out to the output waveguides, it can be imbalanced such that the loss in one ring is much greater than the loss in the other ring by varying the coupling to the waveguides. We considered this idea for both Continuous Wave (CW) and pulsed pump inputs and both Spontaneous Parametric Down Conversion (SPDC) and Four Wave Mixing (FWM) processes. After looking at the dynamics and steady state solution in section 6.2, showing that a pulsed input can be analytically solved in the frequency domain and the CW input in the (temporal) steady state regime, we calculated the eigenvalues and eigenvectors of this system in section 6.3, demonstrating that multiple second and fourth order EPs and EP surfaces exist, with more complex topological structures than seen in 2- and 3- dimensional $\mathcal{PT}$-symmetric systems. While this example of a quantum $\mathcal{PT}$-symmetric system could be explored in line with other $\mathcal{PT}$-symmetric systems to demonstrate e.g. Berry phases when encircling an EP, or even encircling multiple EPs, microring resonators are already commonly used as a single photon source. From this, it seems the best method to demonstrate the application of a quantum EP would be to use it to find an enhancement in single photon generation. Such an enhancement can be theoretically shown by calculating the correlation functions, such as the Joint Spectral Intensity (JSI), shown in section 6.4. This was done by solving the equations of motion from section 6.2 in section 6.5, which gave the solutions shown in section 6.6. While, for a CW input, no particular improvement over a single ring was shown (when compared with the best possible output from a single ring), for a pulsed input, calculating the JSI demonstrated that EP-like behaviour can be found by minimising the intrinsic loss rate and only coupling to a single waveguide (to give a maximum amount of difference in loss between the rings). In doing so, a coupling value can be numerically calculated that maximises the efficiency of the output state in terms of the laser power required to create that state. Calculating the JSI at this point then gave a purity well above 99%, considerably greater than that of a single ring, getting arbitrarily close to 1 for lower losses, reminiscent of the classical effect of single mode lasing at an EP. This directly demonstrates that quantum Exceptional Points can exist and can have practical applications analogous to classical Exceptional Points.

Overall, this demonstrates that, while a Hamiltonian acting on the Hilbert space of a quantum system is Hermitian, non-Hermitian and $\mathcal{PT}$-symmetric dynamics can still be found within that system. This could be from using an open or embedded system, or by using nonlinear optical transformations. While performing simulations using an open or embedded system requires some form of postselection to replicate non-Hermitian dynamics, non-Hermitian and $\mathcal{PT}$-symmetric effects can be recreated using nonlinear optics. This includes using squeezing to perform nonunitary simulations in an interferometer with the same heralding required as in the equivalent unitary interferometer. However, using nonlinear optics to recreate quantum $\mathcal{PT}$-symmetry also demonstrates that the ideas typical of $\mathcal{PT}$-symmetry can then be used in quantum optical applications, such as in efficient generation of ultra pure single photon states.

Appendix A

Simulation Code for 2D $\mathcal{PT}$-symmetric lattice

```
from thewalrus.quantum import pure_state_amplitude

import matplotlib.pyplot as plt

import math
import numpy as np
from numpy import sqrt
from scipy.linalg import expm

#parameters
gamma = 0.0
hFieldStrength = 1.0
jFieldStrength = 1.0
mode = 1 #input mode
N = 500 #number of time steps
dt = 0.1
#probability of heralded single photons = sinh^2 r < 1/10
avgPhotonNo = 1/100
noOfSpins = 4
size = 2**noOfSpins
noOfHeraldModes = 1

#creates file
f = open("PTEvolution.txt", "w+")
```

```
#definitions

#Creates arrays for G (non-unitary evolution matrix) and state for each
#time step
GArray = np.zeros((N, size, size), dtype=complex)
GArray[0] = np.eye(size)
stateArray = np.zeros((N, size), dtype=complex)
stateArray[0, mode-1] = 1.0
actualStateProb = np.zeros((size, N), dtype=complex)

#creates arrays for the singular value decomposition udv^\dagger = ud(vh)
uArray = np.zeros((N+1, size, size), dtype=complex)
uArray[0] = np.eye(size)
dArray = np.zeros((N+1, size), dtype=float)
dArray[0] = np.ones(size)
vhArray = np.zeros((N+1, size, size), dtype=complex)
vhArray[0] = np.eye(size)

#creates array for squeezing and loss:
#when element is > 1, gives squeezing, < 1 is loss
squeezingLossArray = np.zeros((N+1, size), dtype = float)
lossTransmission = np.zeros((N+1, size), dtype = float)
lossReflection = np.zeros((N+1, size), dtype = float)

#Defines the n-mode PT-symmetric Hamiltonian HPT
HPT  = np.zeros((size, size), dtype=complex)

#1D PT-symmetric spin-chain (time independent), Heisenberg/Ising model
#hPTFieldStrength = gamma
#sigmaX = [[0, 1.0], [1.0, 0]]
#HIsing2 = \
#    jFieldStrength*np.kron([[1.0, 0], [0, -1.0]], [[1.0, 0], [0, -1.0]])
#for n in range(0, noOfSpins):
#    HIsing1 = [[0, hFieldStrength+((-1.0)**n)*hPTFieldStrength],\
#                    [hFieldStrength-((-1.0)**n)*hPTFieldStrength, 0]]
#    HPT += np.kron(np.identity(2**n, dtype=complex),\
#                    np.kron(HIsing1, np.identity(2**(noOfSpins-n-1),\
```

```
#dtype=complex)))
#for n in range(0, noOfSpins-1):
#    HPT += np.kron(np.identity(2**n, dtype=complex),\
#                   np.kron(HIsing2, np.identity(2**(noOfSpins-n-2),\
#                       dtype=complex)))

#2D PT-symmetric spin-chain (time independent), Heisenberg/Ising model
hPTFieldStrength = gamma
sigmaX = [[0, 1.0], [1.0, 0]]
HIsing2 = jFieldStrength*np.kron([[1.0, 0], [0, -1.0]], [[1.0, 0], [0, -1.0]])
HIsing3 = jFieldStrength*np.kron([[1.0, 0], [0, -1.0]],\
                np.kron([[1.0, 0], [0, 1.0]], [[1.0, 0], [0, -1.0]]))
for n in range(0, noOfSpins):
    HIsing1 = [[0, hFieldStrength+((-1.0)**n)*hPTFieldStrength],\
                   [hFieldStrength-((-1.0)**n)*hPTFieldStrength, 0]]
    HPT += np.kron(np.identity(2**n, dtype=complex),\
                        np.kron(HIsing1, np.identity(2**(noOfSpins-n-1),\
                        dtype=complex)))
for n in range(0, (noOfSpins-1)//2):
    HPT += np.kron(np.identity(2**(2*n), dtype=complex),\
                        np.kron(HIsing2, np.identity(2**(noOfSpins-(2*n)-2),\
                        dtype=complex)))
for n in range(0, noOfSpins-2):
    HPT += np.kron(np.identity(2**n, dtype=complex),\
                        np.kron(HIsing3, np.identity(2**(noOfSpins-n-3),\
                        dtype=complex)))

#classical precomputation

hadamardSingle = [[1/sqrt(2), 1/sqrt(2)], [-1.0/sqrt(2), 1.0/sqrt(2)]]
hadamardFull = hadamardSingle
for n in range(0, noOfSpins-1):
    hadamardFull = np.kron(hadamardFull, hadamardSingle)

#at each time step, calculates the value of G and the 'state'
#after such an evolution
for n in range(0, N):
        #G = exp(-iHt)
```

```
    GArray[n] = expm(-1.0j*HPT*n*dt)
        #basis change
    #GArray[n] = np.dot(hadamardFull.T, np.dot(GArray[n], hadamardFull))
    stateArray[n] = np.dot(GArray[n], stateArray[0])
    for m in range(0,size):
        actualStateProb[m, n] = np.abs(stateArray[n, m])**2

#quantum circuit precomputation

maxSqueezingValue = 0.0
#circuit parameters depend on the singular value decomposition
for n in range(1, N):
    uArray[n], dArray[n], vhArray[n] = np.linalg.svd(GArray[n],\
    full_matrices=True)
    for k in range(0, size):
        if dArray[n, k] > 1.0: #squeezing when singular value > 1
            squeezingLossArray[n, k] = np.arccosh(dArray[n, k])
            print(str(n) + ": " + str(squeezingLossArray[n, k]) +\
                ", " + str(dArray[n,k]))
            if squeezingLossArray[n, k] > maxSqueezingValue:
                maxSqueezingValue = squeezingLossArray[n, k]
        elif dArray[n, k] < 1.0: #loss when singular value < 1
            lossTransmission[n, k] = sqrt(dArray[n,k])
            lossReflection[n,k] = sqrt(1-dArray[n,k])

#sets number of qumodes (number of modes in system)
#+ (number of heralding modes)
noOfModes = int(size + noOfHeraldModes)

#Defines matrices for the mean and covariance
muArray = np.zeros((N+1, 2*noOfModes), dtype=float)
covArray = np.zeros((N+1, 2*noOfModes, 2*noOfModes),dtype=float)

#transformation matrix giving 2-mode squeezing for photon generation
S2PhotonGeneration = np.identity(2*noOfModes, dtype=complex)
S2PhotonGenerationDiag = np.identity(2*noOfModes, dtype=complex)
S2PhotonGenerationBS = np.identity(2*noOfModes, dtype=complex)
```

```
S2PhotonGenerationDiag[mode-1, mode-1] = np.exp(-photonSqueezingValue)
S2PhotonGenerationDiag[mode+size, mode+size] = np.exp(photonSqueezingValue)
S2PhotonGenerationDiag[size, size] = np.exp(photonSqueezingValue)
S2PhotonGenerationDiag[2*size+1, 2*size+1] = np.exp(-photonSqueezingValue)

S2PhotonGenerationBS[mode-1, mode-1] = 1.0/sqrt(2)
S2PhotonGenerationBS[mode-1, size] = -1.0/sqrt(2)
S2PhotonGenerationBS[mode+size, mode+size] = 1.0/sqrt(2)
S2PhotonGenerationBS[mode+size, 2*size+1] = -1.0/sqrt(2)
S2PhotonGenerationBS[size, size] = 1.0/sqrt(2)
S2PhotonGenerationBS[size, mode-1] = 1.0/sqrt(2)
S2PhotonGenerationBS[2*size+1, 2*size+1] = 1.0/sqrt(2)
S2PhotonGenerationBS[2*size+1, mode+size] = 1.0/sqrt(2)

S2PhotonGeneration = np.matmul(S2PhotonGenerationBS.T,\
                    np.matmul(S2PhotonGenerationDiag, S2PhotonGenerationBS))

#transforms between quadrature and creation/annihilation operator spaces
hadamardComplex = [[1/sqrt(2), 1/sqrt(2)], [1.0j/sqrt(2), -1.0j/sqrt(2)]]
hadamardComplex = np.kron(hadamardComplex,\
    np.identity(noOfModes, dtype=complex))

#creating the quantum circuit

#quantum circuit initialised in vacuum state by default
#modes 0 to size-1 are computational modes, size is heralding modes

for n in range(0, N):
    print("t = " + str(n*dt))

    gainLossMat = np.identity(2*(noOfModes+size), dtype=float)
    gainLossDaggerMat = np.identity(2*(noOfModes+size), dtype=float)
    gainLossTransform = np.identity(2*(noOfModes+size), dtype = complex)
    gainLossDaggerTransform = np.identity(2*(noOfModes+size), dtype = complex)
        #additional size modes for loss
    uTransformMat = np.identity(2*noOfModes, dtype=complex)
    vTransformMat = np.identity(2*noOfModes, dtype=complex)
    vTempTransformMat = np.identity(2*noOfModes, dtype=complex)
```

```
    uTempTransformMat = np.identity(2*size, dtype=complex)
    vhTempTransformMat = np.identity(2*size, dtype=complex)
    uhTempTransformMat = np.identity(2*size, dtype=complex)
    uhTransformMat = np.identity(2*noOfModes, dtype=complex)
    vhTransformMat = np.identity(2*noOfModes, dtype=complex)
    transformation = np.identity(2*noOfModes, dtype = complex)

    #apply Clements decomposition of uh
    uhTransformMat[0:size, 0:size] = uArray[n].conj().T
    uhTransformMat[noOfModes:noOfModes+size, noOfModes:noOfModes+size]\
        = uArray[n].T
    uhTransformMat = np.matmul(hadamardComplex,\
                        np.matmul(uhTransformMat, hadamardComplex.conj().T))
    transformation = np.matmul(uhTransformMat,\
                        np.matmul(transformation, uhTransformMat.T))

    #apply gain (squeezing) corresponding to d
    for k in range(0, size):
        if dArray[n, k] > 1.0:
            gainLossDaggerMat[k, k] = np.exp(squeezingLossArray[n, k])
            gainLossDaggerMat[k+noOfModes+size, k+noOfModes+size] =\
                np.exp(-squeezingLossArray[n, k])
        elif dArray[n, k] == 1.0:
            gainLossDaggerMat[k, k] = 1.0
            gainLossDaggerMat[k+noOfModes+size, k+noOfModes+size] = 1.0
    gainLossDaggerTransform[0:noOfModes, 0:noOfModes] =\
        transformation[0:noOfModes, 0:noOfModes]
    gainLossDaggerTransform[noOfModes+size:2*noOfModes+size,\
        noOfModes+size:2*noOfModes+size] =\
        transformation[noOfModes:2*noOfModes, noOfModes:2*noOfModes]
    gainLossDaggerTransform =\
        np.matmul(gainLossDaggerMat, np.matmul(gainLossDaggerTransform,\
            gainLossDaggerMat.T))
    transformation[0:noOfModes, 0:noOfModes] =\
        gainLossDaggerTransform[0:noOfModes, 0:noOfModes]
    transformation[noOfModes:2*noOfModes, noOfModes:2*noOfModes] =\
        gainLossDaggerTransform[noOfModes+size:2*noOfModes+size,\
            noOfModes+size:2*noOfModes+size]
```

```
#apply v
vTransformMat[0:size, 0:0+size] = vhArray[n].conj().T
vTransformMat[noOfModes:noOfModes+size, noOfModes:noOfModes+size] =\
    vhArray[n].T
vTransformMat =\
    np.matmul(hadamardComplex, np.matmul(vTransformMat,\
        hadamardComplex.conj().T))
transformation = np.matmul(vTransformMat, np.matmul(transformation,\
    vTransformMat.T))

#create an approximate single photon state using 2-mode squeezing
#and heralding
#using input mode
transformation = np.matmul(S2PhotonGeneration, np.matmul(transformation,\
    S2PhotonGeneration.T))

#apply clements decomposition of v
vhTransformMat[0:size, 0:size] = vhArray[n]
vhTransformMat[noOfModes:noOfModes+size, noOfModes:noOfModes+size] =\
    vhArray[n].conj()
vhTransformMat =\
    np.matmul(hadamardComplex, np.matmul(vhTransformMat,\
        hadamardComplex.conj().T))
transformation = np.matmul(vhTransformMat, np.matmul(transformation,\
    vhTransformMat.T))

#apply gain (squeezing) and loss (beamsplitter coupled to vacuum mode)
#corresponding to d
for k in range(0, size):
    if dArray[n, k] > 1.0:
        gainLossMat[k, k] = np.exp(-squeezingLossArray[n, k])
        gainLossMat[noOfModes+size+k, noOfModes+size+k] =\
            np.exp(squeezingLossArray[n, k])
    if dArray[n, k] < 1.0:
        gainLossMat[k, k] = lossTransmission[n,k]
        gainLossMat[k+noOfModes, k+noOfModes] = lossTransmission[n,k]
        gainLossMat[k+noOfModes+size, k+noOfModes+size] =\
```

```
            lossTransmission[n,k]
        gainLossMat[k+2*noOfModes+size, k+2*noOfModes+size] =\
            lossTransmission[n,k]
        gainLossMat[k, k+noOfModes+size] = -lossReflection[n,k]
        gainLossMat[k+noOfModes+size, k] = lossReflection[n,k]
        gainLossMat[k+noOfModes, k+2*noOfModes+size] =\
            -lossReflection[n,k]
        gainLossMat[k+2*noOfModes+size, k] = lossReflection[n,k]
    elif dArray[n, k] == 1.0:
        gainLossMat[k, k] = 1.0
        gainLossMat[noOfModes+size+k, noOfModes+size+k] = 1.0
gainLossTransform[0:noOfModes, 0:noOfModes] =\
    transformation[0:noOfModes, 0:noOfModes]
gainLossTransform[noOfModes+size:2*noOfModes+size,\
    noOfModes+size:2*noOfModes+size] =\
        transformation[noOfModes:2*noOfModes, noOfModes:2*noOfModes]
gainLossTransform = np.matmul(gainLossMat, np.matmul(gainLossTransform,\
    gainLossMat.T))
transformation[0:noOfModes, 0:noOfModes] =\
    gainLossTransform[0:noOfModes, 0:noOfModes]
transformation[noOfModes:2*noOfModes, noOfModes:2*noOfModes] =\
    gainLossTransform[noOfModes+size:2*noOfModes+size,\
        noOfModes+size:2*noOfModes+size]

#apply Clements decomposition of u
uTransformMat[0:size, 0:size] = uArray[n]
uTransformMat[noOfModes:noOfModes+size, noOfModes:noOfModes+size] =\
    uArray[n].conj()
uTransformMat = np.matmul(hadamardComplex, np.matmul(uTransformMat,\
    hadamardComplex.conj().T))
transformation = np.matmul(uTransformMat, np.matmul(transformation,\
    uTransformMat.T))

covArray[n] = transformation
```

Appendix B

Heisenberg Equations of Motion for Coupled Rings

This appendix contains the Heisenberg Equations of Motion in the rotated basis (using operators $\bar{A}$) for coupled rings undergoing the processes of SPDC and FWM respectively. These are

$$\left(\frac{d}{dt}+\bar{\Gamma}_{P1}\right)\bar{b}_{P1}\left(t\right)=-i\gamma_{P1}^{*}\bar{\psi}_{P1<}\left(0,t\right)-i\mu_{P1}^{*}\bar{\phi}_{P1<}\left(0,t\right)-i\Lambda^{*}\bar{b}_{S1}\left(t\right)\bar{b}_{I1}\left(t\right)e^{-i\Delta t}-i\kappa\bar{b}_{P2}\left(t\right) \tag{B.1}$$

$$\left(\frac{d}{dt}+\bar{\Gamma}_{S1}\right)\bar{b}_{S1}\left(t\right)=-i\gamma_{S1}^{*}\bar{\psi}_{S1<}\left(0,t\right)-i\mu_{S1}^{*}\bar{\phi}_{S1<}\left(0,t\right)-i\Lambda\bar{b}_{P1}\left(t\right)\bar{b}_{I1}^{\dagger}\left(t\right)e^{i\Delta t}-i\kappa\bar{b}_{S2}\left(t\right) \tag{B.2}$$

$$\left(\frac{d}{dt}+\bar{\Gamma}_{I1}\right)\bar{b}_{I1}\left(t\right)=-i\gamma_{I1}^{*}\bar{\psi}_{I1<}\left(0,t\right)-i\mu_{I1}^{*}\bar{\phi}_{I1<}\left(0,t\right)-i\Lambda\bar{b}_{P1}\left(t\right)\bar{b}_{S1}^{\dagger}\left(t\right)e^{i\Delta t}-i\kappa\bar{b}_{I2}\left(t\right) \tag{B.3}$$

$$\left(\frac{d}{dt}+\bar{\Gamma}_{P2}\right)\bar{b}_{P2}\left(t\right)=-i\gamma_{P2}^{*}\bar{\psi}_{P2<}\left(0,t\right)-i\mu_{P2}^{*}\bar{\phi}_{P2<}\left(0,t\right)-i\Lambda^{*}\bar{b}_{S2}\left(t\right)\bar{b}_{I2}\left(t\right)e^{-i\Delta t}-i\kappa^{*}\bar{b}_{P1}\left(t\right) \tag{B.4}$$

$$\left(\frac{d}{dt}+\bar{\Gamma}_{S2}\right)\bar{b}_{S2}\left(t\right)=-i\gamma_{S2}^{*}\bar{\psi}_{S2<}\left(0,t\right)-i\mu_{S2}^{*}\bar{\phi}_{S2<}\left(0,t\right)-i\Lambda\bar{b}_{P2}\left(t\right)\bar{b}_{I2}^{\dagger}\left(t\right)e^{i\Delta t}-i\kappa^{*}\bar{b}_{S1}\left(t\right) \tag{B.5}$$

$$\left(\frac{d}{dt}+\bar{\Gamma}_{I2}\right)\bar{b}_{I2}\left(t\right)=-i\gamma_{I2}^{*}\bar{\psi}_{I2<}\left(0,t\right)-i\mu_{I2}^{*}\bar{\phi}_{I2<}\left(0,t\right)-i\Lambda\bar{b}_{P2}\left(t\right)\bar{b}_{S2}^{\dagger}\left(t\right)e^{i\Delta t}-i\kappa^{*}\bar{b}_{I1}\left(t\right). \tag{B.6}$$

for SPDC and

$$\begin{aligned}\left(\frac{d}{dt}+\bar{\Gamma}_{P1}+2i\eta\bar{b}_{P1}^{\dagger}\left(t\right)\bar{b}_{P1}\left(t\right)\right)\bar{b}_{P1}\left(t\right)&=-i\gamma_{P1}^{*}\bar{\psi}_{P1<}\left(0,t\right)-i\mu_{P1}^{*}\bar{\phi}_{P1<}\left(0,t\right)\\&\quad-2i\Lambda^{*}\bar{b}_{P1}^{\dagger}\left(t\right)\bar{b}_{S1}\left(t\right)\bar{b}_{I1}\left(t\right)e^{-i\Delta t}-i\kappa\bar{b}_{P2}\left(t\right)\end{aligned}\tag{B.7}$$

$$\begin{aligned}\left(\frac{d}{dt}+\bar{\Gamma}_{S1}+i\zeta\bar{b}_{P1}^{\dagger}\left(t\right)\bar{b}_{P1}\left(t\right)\right)\bar{b}_{S1}\left(t\right)&=-i\gamma_{S1}^{*}\bar{\psi}_{S1<}\left(0,t\right)-i\mu_{S1}^{*}\bar{\phi}_{S1<}\left(0,t\right)\\&\quad-i\Lambda\bar{b}_{P1}\left(t\right)\bar{b}_{P1}\left(t\right)\bar{b}_{I1}^{\dagger}\left(t\right)e^{i\Delta t}-i\kappa\bar{b}_{S2}\left(t\right)\end{aligned}\tag{B.8}$$

$$\begin{aligned}\left(\frac{d}{dt}+\bar{\Gamma}_{I1}+\zeta\bar{b}_{P1}^{\dagger}\left(t\right)\bar{b}_{P1}\left(t\right)\right)\bar{b}_{I1}\left(t\right)&=-i\gamma_{I1}^{*}\bar{\psi}_{I1<}\left(0,t\right)-i\mu_{I1}^{*}\bar{\phi}_{I1<}\left(0,t\right)\\&\quad-i\Lambda\bar{b}_{P1}\left(t\right)\bar{b}_{P1}\left(t\right)\bar{b}_{S1}^{\dagger}\left(t\right)e^{i\Delta t}-i\kappa\bar{b}_{I2}\left(t\right)\end{aligned}\tag{B.9}$$

$$\begin{aligned}\left(\frac{d}{dt}+\bar{\Gamma}_{P2}+2i\eta\bar{b}_{P2}^{\dagger}\left(t\right)\bar{b}_{P2}\left(t\right)\right)\bar{b}_{P2}\left(t\right)&=-i\gamma_{P2}^{*}\bar{\psi}_{P2<}\left(0,t\right)-i\mu_{P2}^{*}\bar{\phi}_{P2<}\left(0,t\right)\\&\quad-2i\Lambda^{*}\bar{b}_{P2}^{\dagger}\left(t\right)\bar{b}_{S2}\left(t\right)\bar{b}_{I2}\left(t\right)e^{-i\Delta t}-i\kappa^{*}\bar{b}_{P1}\left(t\right)\end{aligned}\tag{B.10}$$

$$\begin{aligned}\left(\frac{d}{dt}+\bar{\Gamma}_{S2}+i\zeta\bar{b}_{P2}^{\dagger}\left(t\right)\bar{b}_{P2}\left(t\right)\right)\bar{b}_{S2}\left(t\right)&=-i\gamma_{S2}^{*}\bar{\psi}_{S2<}\left(0,t\right)-i\mu_{S2}^{*}\bar{\phi}_{S2<}\left(0,t\right)\\&\quad-i\Lambda\bar{b}_{P2}\left(t\right)\bar{b}_{P2}\left(t\right)\bar{b}_{I2}^{\dagger}\left(t\right)e^{i\Delta t}-i\kappa^{*}\bar{b}_{S1}\left(t\right)\end{aligned}\tag{B.11}$$

$$\begin{aligned}\left(\frac{d}{dt}+\bar{\Gamma}_{I2}+i\zeta\bar{b}_{P2}^{\dagger}\left(t\right)\bar{b}_{P2}\left(t\right)\right)\bar{b}_{I2}\left(t\right)&=-i\gamma_{I2}^{*}\bar{\psi}_{I2<}\left(0,t\right)-i\mu_{I2}^{*}\bar{\phi}_{I2<}\left(0,t\right)\\&\quad-i\Lambda\bar{b}_{P2}\left(t\right)\bar{b}_{P2}\left(t\right)\bar{b}_{S2}^{\dagger}\left(t\right)e^{i\Delta t}-i\kappa^{*}\bar{b}_{I1}\left(t\right)\end{aligned}\tag{B.12}$$

for FWM.

Appendix C

Coupled Ring Correlation Functions

This appendix contains a list of correlation functions that appear in analysing the output of SPDC and FWM in coupled rings of chapter 6.

C.1 First order Correlation Functions

un-normalised cross-correlation

Due to the symmetry of the system, where $\psi_{Sn<}$ transforms into terms involving $\psi_{Sm>}$, $\psi^\dagger_{Im>}$, $\phi_{Sm>}$, $\phi^\dagger_{Im>}$ and $\psi_{In<}$ transforms into terms involving $\psi_{Sm>}$, $\psi^\dagger_{Im>}$, $\phi_{Sm>}$, $\phi^\dagger_{Im>}$, meaning that $\psi_{Sn>}$ and $\psi^\dagger_{In>}$ commute, the cross-correlation function is 0.

$$v\left\langle \bar{\psi}^\dagger_{Im>}\left(t_l\right)\bar{\psi}_{Sm>}\left(t_2\right)\right\rangle = 0 \tag{C.1}$$

un-normalised, unheralded

These are the 'fundamental' correlation functions that other correlation functions can be written in terms of. For the output being measured in mode m,

$$\begin{aligned}
G^{(1)}_m\left(t_l,t_p\right) = \left[G^{(1)}_m\left(t_p,t_l\right)\right]^* &= v\left\langle \bar{\psi}^\dagger_{Sm>}\left(t_l\right)\bar{\psi}_{Sm>}\left(t_p\right)\right\rangle &\text{(C.2)}\\
&= \int\sum_n\left[q^*_{SmIn}\left(t_l,t'\right)q_{SmIn}\left(t_p,t'\right)+p^*_{SmIn}\left(t_l,t'\right)p_{SmIn}\left(t_p,t'\right)\right]dt' &\text{(C.3)}\\
&= \int\sum_n\frac{\bar{\Gamma}_n}{\Gamma_n}q^*_{SmIn}\left(t_l,t'\right)q_{SmIn}\left(t_p,t'\right)\,dt' &\text{(C.4)}\\
&= 4\Gamma_m e^{-i\Delta_p\left(t_l-t_p\right)}\int\sum_n\bar{\Gamma}_n G^*_{SmIn}\left(t_l-t'\right)G_{SmIn}\left(t_p-t'\right)\,dt'. &\text{(C.5)}
\end{aligned}$$

At $t_l = t_p$ this defines both a normalisation and the number of output photons,

$$J_m = G^{(1)}_m\left(t,t\right) = 4\Gamma_m\int\sum_n\bar{\Gamma}_n\left|G_{SmIn}\left(t-t'\right)\right|^2dt'. \tag{C.6}$$

in some given time-bin. Although not directly measured when measuring a single photon, we also define

$$\begin{aligned}
A_m\left(t_l,t_p\right) &= A_m^*\left(t_p,t_l\right) = v\left\langle\bar{\psi}_{Sm>}\left(t_l\right)\bar{\psi}_{Im>}\left(t_p\right)\right\rangle && \text{(C.7)}\\
&= \int\sum_n q_{SmSn}\left(t_l-t'\right)q_{ImSn}\left(t_p-t'\right)+p_{SmSn}\left(t_l-t'\right)p_{ImSn}\left(t_p-t'\right)dt' && \text{(C.8)}\\
&= 2\Gamma_m e^{-i\Delta\left(t_p+t_l\right)}\Bigg[G_{SmIm}\left(t_p-t_l\right)\\
&\qquad -2\int\sum_n\bar{\Gamma}_n G_{SmSn}\left(t_l-t'\right)G_{SmIn}\left(t_p-t'\right)dt'\Bigg]. && \text{(C.9)}
\end{aligned}$$

normalised, unheralded

Normalising gives information about the coherence time of the output photons

$$g_m^{(1)}\left(t_l,t_p;t_s\right) = \frac{\left\langle\bar{\psi}_{Sm>}^{\dagger}\left(t_l\right)\bar{\psi}_{Sm>}\left(t_p\right)\right\rangle}{\left\langle\bar{\psi}_{Sm>}^{\dagger}\left(t_s\right)\bar{\psi}_{Sm>}\left(t_s\right)\right\rangle} = \frac{G_m^{(1)}\left(t_l,t_P\right)}{J_m} \qquad \text{(C.10)}$$

un-normalised, heralded

$G^{(1)}$ can also be heralded to give

$$\begin{aligned}
G_{m;h}^{(1)}\left(t_l,t_p\right) &= v\left\langle\bar{\psi}_{Sm>}^{\dagger}\left(t_l\right)\bar{\psi}_{Sm>}\left(t_p\right)\right\rangle_h && \text{(C.11)}\\
&= v\frac{\left\langle\bar{\psi}_{Im>}^{\dagger}\left(t_i\right)\bar{\psi}_{Sm>}^{\dagger}\left(t_l\right)\bar{\psi}_{Sm>}\left(t_p\right)\bar{\psi}_{Im>}\left(t_i\right)\right\rangle}{\left\langle\bar{\psi}_{Im>}^{\dagger}\left(t_i\right)\bar{\psi}_{Im>}\left(t_i\right)\right\rangle} && \text{(C.12)}\\
&= \frac{A_m^*\left(t_l,t_i\right)A_m\left(t_p,t_i\right)}{J_m}+G_m^{(1)}\left(t_l,t_p\right). && \text{(C.13)}
\end{aligned}$$

The subscript h represents that the expectation value is taken with respect to the heralded photon. At $t_l=t_p=t$, we further have

$$G_{m;h}^{(1)}\left(t,t\right) = \frac{\left|A_m\left(t,t_i\right)\right|^2}{J_m}+J_m, \qquad \text{(C.14)}$$

which gives the number of heralded output photons.

normalised, heralded

$$g^{(1)}_{m,h}\left(t_l,t_p\right) = \frac{\left\langle \bar{\psi}^{\dagger}_{Sm>}\left(t_l\right)\bar{\psi}_{Sm>}\left(t_p\right)\right\rangle_h}{\left\langle \bar{\psi}^{\dagger}_{Sm>}\left(t_s\right)\bar{\psi}_{Sm>}\left(t_s\right)\right\rangle_h} \tag{C.15}$$

$$= \frac{\left\langle \bar{\psi}^{\dagger}_{Im>}\left(t_i\right)\bar{\psi}^{\dagger}_{Sm>}\left(t_l\right)\bar{\psi}_{Sm>}\left(t_p\right)\bar{\psi}_{Im>}\left(t_i\right)\right\rangle}{\left\langle \bar{\psi}^{\dagger}_{Im>}\left(t_i\right)\bar{\psi}^{\dagger}_{Sm>}\left(t_s\right)\bar{\psi}_{Sm>}\left(t_s\right)\bar{\psi}_{Im>}\left(t_i\right)\right\rangle} \tag{C.16}$$

$$= \frac{A^*_m\left(t_l,t_i\right)A_m\left(t_p,t_i\right)+J_mG^{(1)}_m\left(t_l,t_p\right)}{\left|A_m\left(t_s,t_i\right)\right|^2+J_m^2} \tag{C.17}$$

C.2 Second order Correlation Functions

Similar to the first order correlation functions, these can be heralded or unheralded and normalised or unnormalised.

un-normalised, unheralded

$$G^{(2)}_m\left(t_1,t_2,t_3,t_4\right) = v^2\left\langle \bar{\psi}^{\dagger}_{Sm>}\left(t_1\right)\bar{\psi}^{\dagger}_{Sm>}\left(t_2\right)\bar{\psi}_{Sm>}\left(t_3\right)\bar{\psi}_{Sm>}\left(t_4\right)\right\rangle \tag{C.18}$$

$$= G^{(1)}_m\left(t_2,t_3\right)G^{(1)}_m\left(t_1,t_4\right)+G^{(1)}_m\left(t_1,t_3\right)G^{(1)}_m\left(t_2,t_4\right). \tag{C.19}$$

At $t_1 = t_4 = t$ and $t_2 = t_3 = t'$, this becomes

$$G^{(2)}_m\left(t,t'\right) = J_m^2 + |G^{(1)}_m\left(t,t'\right)|^2. \tag{C.20}$$

normalised, unheralded

$$g^{(2)}_m\left(t_1,t_2,t_3,t_4;t_{s_1},t_{s_2}\right) = \frac{\left\langle \bar{\psi}^{\dagger}_{Sm>}\left(t_1\right)\bar{\psi}^{\dagger}_{Sm>}\left(t_2\right)\bar{\psi}_{Sm>}\left(t_3\right)\bar{\psi}_{Sm>}\left(t_4\right)\right\rangle}{\left\langle \bar{\psi}^{\dagger}_{Sm>}\left(t_{s_1}\right)\bar{\psi}_{Sm>}\left(t_{s_1}\right)\right\rangle\left\langle \bar{\psi}^{\dagger}_{Sm>}\left(t_{s_2}\right)\bar{\psi}_{Sm>}\left(t_{s_2}\right)\right\rangle} \tag{C.21}$$

$$= \frac{G^{(1)}_m\left(t_2,t_3\right)G^{(1)}_m\left(t_1,t_4\right)+G^{(1)}_m\left(t_1,t_3\right)G^{(1)}_m\left(t_2,t_4\right)}{J_m^2} \tag{C.22}$$

When $t_1 = t_2 = t_3 = t_4 = t$, this gives $g^{(2)}\left(t\right) = 2$ as expected. Alternatively, setting $t_1 = t_4 = t$ and $t_2 = t_3 = t'$ gives

$$g^{(2)}_m\left(t,t'\right) = 1 + |g^{(1)}_m\left(t,t'\right)|^2 \implies 1 \le g^{(2)}_m\left(t,t'\right) \le 2, \tag{C.23}$$

showing that unheralded single photons from such a source cannot be used as a good source of single photons as they are equivalent to a thermal state in this correlation function.

un-normalised, heralded

$$G^{(2)}_{m,h}\left(t_1,t_2,t_3,t_4\right) = v^2\left\langle \bar{\psi}^\dagger_{Sm>}\left(t_1\right)\bar{\psi}^\dagger_{Sm>}\left(t_2\right)\bar{\psi}_{Sm>}\left(t_3\right)\bar{\psi}_{Sm>}\left(t_4\right)\right\rangle_h \tag{C.24}$$

$$= v^2\frac{\left\langle \bar{\psi}^\dagger_{Im>}\left(t_i\right)\bar{\psi}^\dagger_{Sm>}\left(t_1\right)\bar{\psi}^\dagger_{Sm>}\left(t_2\right)\bar{\psi}_{Sm>}\left(t_3\right)\bar{\psi}_{Sm>}\left(t_4\right)\bar{\psi}_{Im>}\left(t_i\right)\right\rangle}{\left\langle \bar{\psi}^\dagger_{Im>}\left(t_i\right)\bar{\psi}_{Im>}\left(t_i\right)\right\rangle} \tag{C.25}$$

$$\begin{aligned}
&= \frac{1}{J_m}\big[A^*_m\left(t_2,t_i\right)A_m\left(t_4,t_i\right)G^{(1)}_m\left(t_1,t_3\right) + A^*_m\left(t_2,t_i\right)A_m\left(t_3,t_i\right)G^{(1)}_m\left(t_1,t_4\right)\\
&\quad + A^*_m\left(t_1,t_i\right)A_m\left(t_4,t_i\right)G^{(1)}_m\left(t_2,t_3\right) + A^*_m\left(t_1,t_i\right)A_m\left(t_3,t_i\right)G^{(1)}_m\left(t_2,t_4\right)\\
&\quad + G^{(1)}_m\left(t_1,t_4\right)G^{(1)}_m\left(t_2,t_3\right)G^{(1)}_m\left(t_i,t_i\right)\\
&\quad + G^{(1)}_m\left(t_1,t_3\right)G^{(1)}_m\left(t_2,t_4\right)G^{(1)}_m\left(t_i,t_i\right)\big].
\end{aligned} \tag{C.26}$$

setting $t_2 = t_3 = t'$ and $t_1 = t_4 = t$ gives

$$\begin{aligned}
G^{(2)}_{m,h}\left(t,t'\right) &= 2\frac{\Re\left[A^*_m\left(t',t_i\right)A_m\left(t,t_i\right)G^{(1)}_m\left(t,t'\right)\right]}{J_m}\\
&\quad + \left|A_m\left(t',t_i\right)\right|^2 + \left|A_m\left(t,t_i\right)\right|^2 + J^2_m + \left|G^{(1)}_m\left(t,t'\right)\right|^2
\end{aligned} \tag{C.27}$$

normalised, heralded

$$g^{(2)}_{m,h}\left(t_1,t_2,t_3,t_4;t_{s_1},t_{s_2}\right) = \frac{\left\langle \bar{\psi}^\dagger_{Sm>}\left(t_1\right)\bar{\psi}^\dagger_{Sm>}\left(t_2\right)\bar{\psi}_{Sm>}\left(t_3\right)\bar{\psi}_{Sm>}\left(t_4\right)\right\rangle_h}{\left\langle \bar{\psi}^\dagger_{Sm>}\left(t_{s_1}\right)\bar{\psi}_{Sm>}\left(t_{s_1}\right)\right\rangle_h\left\langle \bar{\psi}^\dagger_{Sm>}\left(t_{s_2}\right)\bar{\psi}_{Sm>}\left(t_{s_2}\right)\right\rangle_h}$$

$$= \frac{\left\langle \bar{\psi}^\dagger_{Im>}\left(t_i\right)\bar{\psi}^\dagger_{Sm>}\left(t_1\right)\bar{\psi}^\dagger_{Sm>}\left(t_2\right)\bar{\psi}_{Sm>}\left(t_3\right)\bar{\psi}_{Sm>}\left(t_4\right)\bar{\psi}_{Im>}\left(t_i\right)\right\rangle\left\langle \bar{\psi}^\dagger_{Im>}\left(t_i\right)\bar{\psi}_{Im>}\left(t_i\right)\right\rangle}{\left\langle \bar{\psi}^\dagger_{Im>}\left(t_i\right)\bar{\psi}^\dagger_{Sm>}\left(t_{s_1}\right)\bar{\psi}_{Sm>}\left(t_{s_1}\right)\bar{\psi}_{Im>}\left(t_i\right)\right\rangle\left\langle \bar{\psi}^\dagger_{Im>}\left(t_i\right)\bar{\psi}^\dagger_{Sm>}\left(t_{s_2}\right)\bar{\psi}_{Sm>}\left(t_{s_2}\right)\bar{\psi}_{Im>}\left(t_i\right)\right\rangle}.$$

Using

$$\left\langle \bar{\psi}^\dagger_{Im>}\left(t_i\right)\bar{\psi}^\dagger_{Sm>}\left(t_s\right)\bar{\psi}_{Sm>}\left(t_s\right)\bar{\psi}_{Im>}\left(t_i\right)\right\rangle = A^*_m\left(t_s,t_i\right)A_m\left(t_s,t_i\right) + G^{(1)}_m\left(t_i,t_i\right)G^{(1)}_m\left(t_s,t_s\right) \tag{C.28}$$

$$= \left|A_m\left(t_s,t_i\right)\right|^2 + J^2_m \tag{C.29}$$

and setting $t_2 = t_3 = t'$ and $t_1 = t_4 = t$ gives

$$g^{(2)}_{m,h}\left(t,t';t_{s_1},t_{s_2}\right) = \frac{2J_m\Re\left[A^*_m\left(t',t_i\right)A_m\left(t,t_i\right)G^{(1)}_m\left(t,t'\right)\right]}{\left(\left|A_m\left(t_{s_1},t_i\right)\right|^2 + J^2_m\right)\left(\left|A_m\left(t_{s_2},t_i\right)\right|^2 + J^2_m\right)} \tag{C.30}$$

$$+ \frac{J^2_m\left[\left|A_m\left(t',t_i\right)\right|^2 + \left|A_m\left(t,t_i\right)\right|^2 + J^2_m + \left|G^{(1)}_m\left(t,t'\right)\right|^2\right]}{\left(\left|A_m\left(t_{s_1},t_i\right)\right|^2 + J^2_m\right)\left(\left|A_m\left(t_{s_2},t_i\right)\right|^2 + J^2_m\right)}. \tag{C.31}$$

At $t = t_{s_1} = t_{s_2} = t'$, this simplifies to

$$g^{(2)}_{m,h}\left(t, t; t_{s_1}, t_{s_2}\right) = 2J_m^2 \frac{2|A_m\left(t, t_i\right)|^2 + J_m^2}{\left(|A_m\left(t, t_i\right)|^2 + J_m^2\right)^2}. \tag{C.32}$$

For a pure single photon source, this is 0, so the aim is often to get this value to be as close to 0 as possible.

un-normalised Joint Temporal Intensity

$$\begin{aligned} G^{(2)}_{si,m}\left(t_1, t_2, t_3, t_4\right) &= v^2 \left\langle \bar{\psi}^\dagger_{Im>}\left(t_1\right) \bar{\psi}^\dagger_{Sm>}\left(t_2\right) \bar{\psi}_{Sm>}\left(t_3\right) \bar{\psi}_{Im>}\left(t_4\right) \right\rangle &\text{(C.33)}\\ &= A^*_m\left(t_2, t_1\right) A_m\left(t_3, t_4\right) + G^{(1)}_m\left(t_1, t_4\right) G^{(1)}_m\left(t_2, t_3\right). &\text{(C.34)}\end{aligned}$$

As with the heralded $G^{(1)}_m$, setting $t_1 = t_4 = t_i$ and $t_2 = t_3 = t_s$ gives

$$G^{(2)}_{si,m}\left(t_i, t_s\right) = |A_m\left(t_s, t_i\right)|^2 + J_m^2. \tag{C.35}$$

However, the normalisation of the JTI is different to the other correlation functions and it is also not usually heralded, as it is already a function of both the signal and idler photons.

normalised Joint Temporal Intensity

$$\begin{aligned} g^{(2)}_{si,m;h}\left(t_1, t_2, t_3, t_4\right) &= \frac{\left\langle \bar{\psi}^\dagger_{Im>}\left(t_1\right) \bar{\psi}^\dagger_{Sm>}\left(t_2\right) \bar{\psi}_{Sm>}\left(t_3\right) \bar{\psi}_{Im>}\left(t_4\right) \right\rangle}{\left\langle \bar{\psi}^\dagger_{Im>}\left(t_1\right) \bar{\psi}_{Im>}\left(t_4\right) \right\rangle \left\langle \bar{\psi}^\dagger_{Sm>}\left(t_2\right) \bar{\psi}_{Sm>}\left(t_3\right) \right\rangle} &\text{(C.36)}\\ &= \frac{A^*_m\left(t_2, t_1\right) A_m\left(t_3, t_4\right) + G^{(1)}_m\left(t_1, t_4\right) G^{(1)}_m\left(t_2, t_3\right)}{G^{(1)}\left(t_1, t_4\right) G^{(1)}\left(t_2, t_3\right)}. &\text{(C.37)}\end{aligned}$$

Setting $t_1 = t_4 = t_i$ and $t_2 = t_3 = t_s$ gives

$$g^{(2)}_{si,m}\left(t_i, t_s\right) = 1 + \frac{|A_{si,m}\left(t_s, t_i\right)|^2}{J_m^2}. \tag{C.38}$$

From [81], we also have that

$$g^{(2)}_h\left(t, t; t, t\right) = \frac{2}{g^{(2)}_{si,m}\left(t, t\right)} \left(2 - \frac{1}{g^{(2)}_{si,m}\left(t, t\right)}\right). \tag{C.39}$$

Appendix D

Integrals for Coupled Rings

This appendix contains a list of integrals useful in calculating integrals that appear in the coupled rings equations of chapter 6, especially in section 6.6

$$\int e^{-\bar{\Gamma}(t_j+t_k-2t')} \sin\left(\sigma_\pm \left(t_j - t'\right)\right) \sin\left(\sigma_\pm \left(t_k - t'\right)\right) dt'$$
$$= \frac{\sigma_\pm e^{-\bar{\Gamma}|t_j-t_k|}}{4\bar{\Gamma}\left(\bar{\Gamma}^2+\sigma_\pm^2\right)} \left[\bar{\Gamma}\sin\left(\sigma_\pm|t_j-t_k|\right) + \sigma_\pm \cos\left(\sigma_\pm|t_j-t_k|\right)\right],$$

$$\int e^{-\bar{\Gamma}(t_j+t_k-2t')} \left[\sin\left(\sigma_+ \left(t_j - t'\right)\right) \sin\left(\sigma_- \left(t_k - t'\right)\right) + \sin\left(\sigma_- \left(t_j - t'\right)\right) \sin\left(\sigma_+ \left(t_k - t'\right)\right)\right] dt'$$
$$= \frac{1}{2} e^{-\bar{\Gamma}|t_j-t_k|} \Big\{$$
$$\frac{2\bar{\Gamma}\left[\cos\left(\sigma_+|t_j-t_k|\right) + \cos\left(\sigma_-|t_j-t_k|\right)\right] + \left(\sigma_+ - \sigma_-\right)\left[\sin\left(\sigma_-|t_k-t_j|\right) - \sin\left(\sigma_+|t_k-t_j|\right)\right]}{\left(\sigma_+ - \sigma_-\right)^2 + 4\bar{\Gamma}^2}$$
$$+ \frac{\left(\sigma_+ + \sigma_-\right)\left[\sin\left(\sigma_+|t_j-t_k|\right) + \sin\left(\sigma_-|t_j-t_k|\right)\right] - 2\bar{\Gamma}\left[\cos\left(\sigma_+|t_j-t_k|\right) + \cos\left(\sigma_-|t_j-t_k|\right)\right]}{\left(\sigma_+ + \sigma_-\right)^2 + 4\bar{\Gamma}^2} \Big\},$$

$$\int e^{-\bar{\Gamma}(t_j+t_k-2t')} \cos\left(\sigma_\pm \left(t_j - t'\right)\right) \cos\left(\sigma_\pm \left(t_k - t'\right)\right) dt'$$
$$= \frac{e^{-\bar{\Gamma}|t_j-t_k|}}{4\bar{\Gamma}\left(\bar{\Gamma}^2+\sigma_\pm^2\right)} \left[\left(\sigma_\pm^2 + 2\bar{\Gamma}^2\right)\cos\left(\sigma_\pm|t_j-t_k|\right) - \sigma_\pm\bar{\Gamma}\sin\left(\sigma_\pm|t_j-t_k|\right)\right],$$

$$\int e^{-\bar{\Gamma}(t_j+t_k-2t')}\big[\cos\left(\sigma_+\left(t_j-t'\right)\right)\cos\left(\sigma_-\left(t_k-t'\right)\right)+\cos\left(\sigma_-\left(t_j-t'\right)\right)\cos\left(\sigma_+\left(t_k-t'\right)\right)\big]\,dt'$$

$$=\frac{1}{2}e^{-\bar{\Gamma}|t_j-t_k|}\Big\{$$

$$\frac{2\bar{\Gamma}\left[\cos\left(\sigma_+|t_j-t_k|\right)+\cos\left(\sigma_-|t_j-t_k|\right)\right]+\left(\sigma_+-\sigma_-\right)\left[\sin\left(\sigma_-|t_k-t_j|\right)-\sin\left(\sigma_+|t_k-t_j|\right)\right]}{\left(\sigma_+-\sigma_-\right)^2+4\bar{\Gamma}^2}$$

$$+\frac{2\bar{\Gamma}\left[\cos\left(\sigma_+|t_j-t_k|\right)+\cos\left(\sigma_-|t_j-t_k|\right)\right]-\left(\sigma_++\sigma_-\right)\left[\sin\left(\sigma_+|t_j-t_k|\right)+\sin\left(\sigma_-|t_j-t_k|\right)\right]}{\left(\sigma_++\sigma_-\right)^2+4\bar{\Gamma}^2}\Big\},$$

$$\int e^{-\bar{\Gamma}(t_j+t_k-2t')}\sin\left(\sigma_\pm\left(t_j-t'\right)\right)\cos\left(\sigma_\pm\left(t_k-t'\right)\right)dt'$$

$$=\frac{e^{-\bar{\Gamma}|t_j-t_k|}}{4\bar{\Gamma}\left(\bar{\Gamma}^2+\sigma_\pm^2\right)}\left[\bar{\Gamma}^2\sin\left(\sigma_\pm|t_j-t_k|\right)+\sigma_\pm\bar{\Gamma}\cos\left(\sigma_\pm|t_j-t_k|\right)-\left(\sigma_\pm^2+\bar{\Gamma}^2\right)\sin\left(\sigma_\pm\left(t_j-t_k\right)\right)\right],$$

$$\int e^{-\bar{\Gamma}(t_j+t_k-2t')}\big[\sin\left(\sigma_+\left(t_j-t'\right)\right)\cos\left(\sigma_-\left(t_k-t'\right)\right)+\sin\left(\sigma_-\left(t_j-t'\right)\right)\cos\left(\sigma_+\left(t_k-t'\right)\right)\big]dt'$$

$$=\frac{1}{2}e^{-\bar{\Gamma}|t_j-t_k|}\left\{\frac{2\bar{\Gamma}\left[\sin\left(\sigma_+\left(t_j-t_k\right)\right)+\sin\left(\sigma_-\left(t_j-t_k\right)\right)\right]}{\left(\sigma_+-\sigma_-\right)^2+4\bar{\Gamma}^2}+\right.$$

$$\frac{\operatorname{sgn}\left(t_j-t_k\right)\left(\sigma_+-\sigma_-\right)\left[\cos\left(\sigma_+|t_j-t_k|\right)-\cos\left(\sigma_-|t_j-t_k|\right)\right]}{\left(\sigma_+-\sigma_-\right)^2+4\bar{\Gamma}^2}$$

$$\left.+\frac{2\bar{\Gamma}\left[\sin\left(\sigma_+|t_j-t_k|\right)+\sin\left(\sigma_-|t_j-t_k|\right)\right]+\left(\sigma_++\sigma_-\right)\left[\cos\left(\sigma_+|t_j-t_k|\right)+\cos\left(\sigma_-|t_j-t_k|\right)\right]}{\left(\sigma_++\sigma_-\right)^2+4\bar{\Gamma}^2}\right\}$$

$$\int e^{-\bar{\Gamma}(t_j+t_k-2t')}\big[\sin\left(\sigma_+\left(t_j-t'\right)\right)\cos\left(\sigma_-\left(t_k-t'\right)\right)-\sin\left(\sigma_-\left(t_j-t'\right)\right)\cos\left(\sigma_+\left(t_k-t'\right)\right)\big]\,dt'$$

$$=\frac{1}{2}e^{-\bar{\Gamma}|t_j-t_k|}\Big\{$$

$$\frac{2\bar{\Gamma}\left[\sin|\sigma_+\left(t_j-t_k|\right)-\sin\left(\sigma_-|t_j-t_k|\right)\right]+\left(\sigma_+-\sigma_-\right)\left[\cos\left(\sigma_+|t_j-t_k|\right)+\cos\left(\sigma_-|t_j-t_k|\right)\right]}{\left(\sigma_+-\sigma_-\right)^2+4\bar{\Gamma}^2}$$

$$+\frac{2\bar{\Gamma}\left[\sin\left(\sigma_+\left(t_j-t_k\right)\right)-\sin\left(\sigma_-\left(t_j-t_k\right)\right)\right]}{\left(\sigma_++\sigma_-\right)^2+4\bar{\Gamma}^2}$$

$$+\frac{\operatorname{sgn}\left(t_j-t_k\right)\left(\sigma_++\sigma_-\right)\left[\cos\left(\sigma_+|t_j-t_k|\right)-\cos\left(\sigma_-|t_j-t_k|\right)\right]}{\left(\sigma_++\sigma_-\right)^2+4\bar{\Gamma}^2}$$

$$\int e^{-\bar{\Gamma}(t_j+t_k-2t')}\big[\sin\big(\sigma_\pm\big(t_j-t'\big)\big)\cos\big(A_\mp\big(t_k-t'\big)\big)-\cos\big(\sigma_\pm\big(t_j-t'\big)\big)\sin\big(A_\mp\big(t_k-t'\big)\big)\big]\,dt'$$

$$= \frac{e^{-\bar{\Gamma}|t_j-t_k|}}{\left(\sigma_+-\sigma_-\right)^2+4\bar{\Gamma}^2}\Big\{$$

$$\big[2\bar{\Gamma}\sin\left(A_\mp\left(t_j-t_k\right)\right)+\left(\sigma_\pm-A_\mp\right)\cos\left(A_\mp|t_j-t_k|\right)\big]\,\Theta\left(t_k-t_j\right)$$

$$+\big[2\bar{\Gamma}\sin\left(\sigma_\pm\left(t_j-t_k\right)\right)+\left(\sigma_\pm-A_\mp\right)\cos\left(\sigma_\pm|t_j-t_k|\right)\big]\,\Theta\left(t_j-t_k\right)\Big\}$$

$$= \frac{1}{2}\frac{e^{-\bar{\Gamma}|t_j-t_k|}}{\left(\sigma_+-\sigma_-\right)^2+4\bar{\Gamma}^2}\Big\{$$

$$2\bar{\Gamma}\left[\sin\left(\sigma_+\left(t_j-t_k\right)\right)+\sin\left(\sigma_-\left(t_j-t_k\right)\right)\right]+2\bar{\Gamma}\left[\sin\left(\sigma_+|t_j-t_k|\right)-\sin\left(\sigma_-|t_j-t_k|\right)\right]$$

$$+\left(\sigma_\pm-A_\mp\right)\left[\cos\left(\sigma_+|t_j-t_k|\right)+\cos\left(\sigma_-|t_j-t_k|\right)\right]$$

$$+\operatorname{sgn}\left(t_j-t_k\right)\left(\sigma_+-\sigma_-\right)\left[\cos\left(\sigma_+|t_j-t_k|\right)-\cos\left(\sigma_-|t_j-t_k|\right)\right]\Big\}$$

$$\int e^{-\bar{\Gamma}(t_j+t_k-2t')}\big[\sin\big(\sigma_\pm\big(t_j-t'\big)\big)\cos\big(A_\mp\big(t_k-t'\big)\big)+\cos\big(\sigma_\pm\big(t_j-t'\big)\big)\sin\big(A_\mp\big(t_k-t'\big)\big)\big]\,dt'$$

$$= \frac{e^{-\bar{\Gamma}|t_j-t_k|}}{\left(\sigma_++\sigma_-\right)^2+4\bar{\Gamma}^2}\Big\{$$

$$\big[2\bar{\Gamma}\sin\left(A_\mp|t_j-t_k|\right)+\left(\sigma_++\sigma_-\right)\cos\left(A_\mp|t_j-t_k|\right)\big]\,\Theta\left(t_k-t_j\right)$$

$$+\big[2\bar{\Gamma}\sin\left(\sigma_\pm|t_j-t_k|\right)+\left(\sigma_++\sigma_-\right)\cos\left(\sigma_\pm|t_j-t_k|\right)\big]\,\Theta\left(t_j-t_k\right)\Big\}$$

$$= \frac{e^{-\bar{\Gamma}|t_j-t_k|}}{\left(\sigma_++\sigma_-\right)^2+4\bar{\Gamma}^2}\Big\{$$

$$2\bar{\Gamma}\left[\sin\left(\sigma_+|t_j-t_k|\right)+\sin\left(\sigma_-|t_j-t_k|\right)\right]+2\bar{\Gamma}\left[\sin\left(\sigma_\pm\left(t_j-t_k\right)\right)-\sin\left(A_\mp\left(t_j-t_k\right)\right)\right]+$$

$$\left(\sigma_++\sigma_-\right)\cos\left(A_\mp|t_j-t_k|\right)\Theta\left(t_k-t_j\right)$$

$$+\big[2\bar{\Gamma}\sin\left(\sigma_\pm|t_j-t_k|\right)+\left(\sigma_++\sigma_-\right)\cos\left(\sigma_\pm|t_j-t_k|\right)\big]\,\Theta\left(t_j-t_k\right)\Big\}$$

Bibliography

[1] C. M. Bender and S. Boettcher, "Real spectra in non-hermitian hamiltonians having p t symmetry," *Physical Review Letters*, vol. 80, no. 24, p. 5243, 1998.

[2] A. Mostafazadeh, "Pseudo-hermiticity versus pt symmetry: the necessary condition for the reality of the spectrum of a non-hermitian hamiltonian," *Journal of Mathematical Physics*, vol. 43, no. 1, pp. 205–214, 2002.

[3] A. Mostafazadeh, "Pseudo-hermiticity versus pt-symmetry. ii. a complete characterization of non-hermitian hamiltonians with a real spectrum," *Journal of Mathematical Physics*, vol. 43, no. 5, pp. 2814–2816, 2002.

[4] A. Mostafazadeh, "Pseudo-hermiticity versus pt-symmetry iii: Equivalence of pseudo-hermiticity and the presence of antilinear symmetries," *Journal of Mathematical Physics*, vol. 43, no. 8, pp. 3944–3951, 2002.

[5] K. Kawabata, Y. Ashida, and M. Ueda, "Information retrieval and criticality in parity-time-symmetric systems," *Physical review letters*, vol. 119, no. 19, p. 190401, 2017.

[6] B. Gardas, S. Deffner, and A. Saxena, "Pt-symmetric slowing down of decoherence," *Physical Review A*, vol. 94, no. 4, p. 040101, 2016.

[7] Y. Wu, W. Liu, J. Geng, X. Song, X. Ye, C.-K. Duan, X. Rong, and J. Du, "Observation of parity-time symmetry breaking in a single-spin system," *Science*, vol. 364, no. 6443, pp. 878–880, 2019.

[8] U. Günther and B. F. Samsonov, "Naimark-dilated p t-symmetric brachistochrone," *Physical review letters*, vol. 101, no. 23, p. 230404, 2008.

[9] S. Dogra, A. A. Melnikov, and G. S. Paraoanu, "Quantum simulation of parity–time symmetry breaking with a superconducting quantum processor," *Communications Physics*, vol. 4, no. 1, pp. 1–8, 2021.

[10] A. Guo, G. Salamo, D. Duchesne, R. Morandotti, M. Volatier-Ravat, V. Aimez, G. Siviloglou, and D. Christodoulides, "Observation of p t-symmetry breaking in complex optical potentials," *Physical review letters*, vol. 103, no. 9, p. 093902, 2009.

[11] C. E. Rüter, K. G. Makris, R. El-Ganainy, D. N. Christodoulides, M. Segev, and D. Kip, "Observation of parity–time symmetry in optics," *Nature physics*, vol. 6, no. 3, pp. 192–195, 2010.

[12] A. Regensburger, C. Bersch, M.-A. Miri, G. Onishchukov, D. N. Christodoulides, and U. Peschel, "Parity–time synthetic photonic lattices," *Nature*, vol. 488, no. 7410, pp. 167–171, 2012.

[13] J. Zhu, S. K. Ozdemir, Y.-F. Xiao, L. Li, L. He, D.-R. Chen, and L. Yang, "On-chip single nanoparticle detection and sizing by mode splitting in an ultrahigh-q microresonator," *Nature photonics*, vol. 4, no. 1, pp. 46–49, 2010.

[14] M. Brandstetter, M. Liertzer, C. Deutsch, P. Klang, J. Schöberl, H. E. Türeci, G. Strasser, K. Unterrainer, and S. Rotter, "Reversing the pump dependence of a laser at an exceptional point," *Nature communications*, vol. 5, no. 1, pp. 1–7, 2014.

[15] B. Peng, Ş. Özdemir, S. Rotter, H. Yilmaz, M. Liertzer, F. Monifi, C. Bender, F. Nori, and L. Yang, "Loss-induced suppression and revival of lasing," *Science*, vol. 346, no. 6207, pp. 328–332, 2014.

[16] B. Peng, Ş. K. Özdemir, F. Lei, F. Monifi, M. Gianfreda, G. L. Long, S. Fan, F. Nori, C. M. Bender, and L. Yang, "Parity–time-symmetric whispering-gallery microcavities," *Nature Physics*, vol. 10, no. 5, pp. 394–398, 2014.

[17] L. Chang, X. Jiang, S. Hua, C. Yang, J. Wen, L. Jiang, G. Li, G. Wang, and M. Xiao, "Parity–time symmetry and variable optical isolation in active–passive-coupled microresonators," *Nature photonics*, vol. 8, no. 7, pp. 524–529, 2014.

[18] H. Hodaei, M.-A. Miri, M. Heinrich, D. N. Christodoulides, and M. Khajavikhan, "Parity-time–symmetric microring lasers," *Science*, vol. 346, no. 6212, pp. 975–978, 2014.

[19] L. Feng, Z. J. Wong, R.-M. Ma, Y. Wang, and X. Zhang, "Single-mode laser by parity-time symmetry breaking," *Science*, vol. 346, no. 6212, pp. 972–975, 2014.

[20] B. Peng, Ş. K. Özdemir, M. Liertzer, W. Chen, J. Kramer, H. Yılmaz, J. Wiersig, S. Rotter, and L. Yang, "Chiral modes and directional lasing at exceptional points," *Proceedings of the National Academy of Sciences*, vol. 113, no. 25, pp. 6845–6850, 2016.

[21] L. Xiao, X. Zhan, Z. Bian, K. Wang, X. Zhang, X. Wang, J. Li, K. Mochizuki, D. Kim, N. Kawakami, *et al.*, "Observation of topological edge states in parity–time-symmetric quantum walks," *Nature Physics*, vol. 13, no. 11, pp. 1117–1123, 2017.

[22] J. Li, A. K. Harter, J. Liu, L. de Melo, Y. N. Joglekar, and L. Luo, "Observation of parity-time symmetry breaking transitions in a dissipative floquet system of ultracold atoms," *Nature communications*, vol. 10, no. 1, pp. 1–7, 2019.

[23] Y. N. Joglekar and A. K. Harter, "Passive parity-time-symmetry-breaking transitions without exceptional points in dissipative photonic systems," *Photonics Research*, vol. 6, no. 8, pp. A51–A57, 2018.

[24] C.-K. Hong, Z.-Y. Ou, and L. Mandel, "Measurement of subpicosecond time intervals between two photons by interference," *Physical review letters*, vol. 59, no. 18, p. 2044, 1987.

[25] M. A. Nielsen and I. L. Chuang, *Quantum Computation and Quantum Information: 10th Anniversary Edition.* Cambridge University Press, 2010.

[26] L. D. Landau and E. Lifshitz, "Quantum mechanics, vol. 3," *Course of theoretical physics*, vol. 3, 1965.

[27] C. M. Bender, "Introduction to $\mathcal{PT}$-symmetric quantum theory," *Contemporary physics*, vol. 46, no. 4, pp. 277–292, 2005.

[28] G. Lindblad, "On the generators of quantum dynamical semigroups," *Communications in Mathematical Physics*, vol. 48, no. 2, pp. 119–130, 1976.

[29] C. M. Bender, D. C. Brody, and H. F. Jones, "Must a hamiltonian be hermitian?," *American Journal of Physics*, vol. 71, no. 11, pp. 1095–1102, 2003.

[30] A. Fring and R. Tenney, "Exactly solvable time-dependent non-hermitian quantum systems from point transformations," *arXiv preprint arXiv:2105.01486*, 2021.

[31] Y. Ashida, Z. Gong, and M. Ueda, "Non-hermitian physics," *Advances in Physics*, vol. 69, no. 3, pp. 249–435, 2020.

[32] C. Dembowski, B. Dietz, H.-D. Gräf, H. Harney, A. Heine, W. Heiss, and A. Richter, "Encircling an exceptional point," *Physical Review E*, vol. 69, no. 5, p. 056216, 2004.

[33] F. Klauck, L. Teuber, M. Ornigotti, M. Heinrich, S. Scheel, and A. Szameit, "Observation of pt-symmetric quantum interference," *Nature Photonics*, vol. 13, no. 12, pp. 883–887, 2019.

[34] Y.-C. Lee, M.-H. Hsieh, S. T. Flammia, and R.-K. Lee, "Local p t symmetry violates the no-signaling principle," *Physical review letters*, vol. 112, no. 13, p. 130404, 2014.

[35] S. Scheel and A. Szameit, "$\mathcal{PT}$-symmetric photonic quantum systems with gain and loss do not exist," *EPL (Europhysics Letters)*, vol. 122, no. 3, p. 34001, 2018.

[36] M. Srednicki, *Quantum field theory.* Cambridge University Press, 2007.

[37] M. Fox, *Quantum optics: an introduction*, vol. 15. OUP Oxford, 2006.

[38] M. Reck, A. Zeilinger, H. J. Bernstein, and P. Bertani, “Experimental realization of any discrete unitary operator,” *Physical review letters*, vol. 73, no. 1, p. 58, 1994.

[39] W. R. Clements, P. C. Humphreys, B. J. Metcalf, W. S. Kolthammer, and I. A. Walmsley, “Optimal design for universal multiport interferometers,” *Optica*, vol. 3, no. 12, pp. 1460–1465, 2016.

[40] R. W. Boyd, *Nonlinear optics.* Academic press, 2020.

[41] N. Maraviglia, *Simulating open quantum systems in integrated photonics.* PhD thesis, University of Bristol, 2020.

[42] N. Maraviglia, P. Yard, R. Wakefield, J. Carolan, C. Sparrow, L. Chakhmakhchyan, C. Harrold, T. Hashimoto, N. Matsuda, A. K. Harter, Y. N. Joglekar, and A. Laing, “Photonic quantum simulations of coupled pt-symmetric hamiltonians,” *Physical Review Research*, vol. 4, no. 1, p. 013051, 2022.

[43] P. Yard, *time as a resource in integrated quantum photonics.* PhD thesis, University of Bristol, 2021.

[44] P. Yard, N. Maraviglia, R. Wakefield, J. Carolan, C. Sparrow, L. Chakhmakhchyan, C. Harrold, T. Hashimoto, N. Matsuda, A. K. Harter, Y. N. Joglekar, and A. Laing, “Coherence optimisation with pt-symmetric hamiltonians,” 2021. In Preparation.

[45] M. A. Quiroz-Juárez, J. L. Domínguez-Juárez, R. Quintero-Torres, J. L. Aragón, A. K. Harter, Y. N. Joglekar, *et al.*, “Observation of slowly decaying eigenmodes without exceptional points in floquet dissipative synthetic circuits,” *Communications Physics*, vol. 1, no. 1, 2018.

[46] V. V. Albert, “Lindbladians with multiple steady states: theory and applications,” *arXiv preprint arXiv:1802.00010*, 2018.

[47] J. Muga, J. Palao, B. Navarro, and I. Egusquiza, “Complex absorbing potentials,” *Physics Reports*, vol. 395, no. 6, pp. 357–426, 2004.

[48] R. Di Candia, J. S. Pedernales, A. Del Campo, E. Solano, and J. Casanova, “Quantum simulation of dissipative processes without reservoir engineering,” *Scientific reports*, vol. 5, no. 1, pp. 1–7, 2015.

[49] A. Rivas, S. F. Huelga, and M. B. Plenio, "Quantum non-markovianity: characterization, quantification and detection," *Reports on Progress in Physics*, vol. 77, no. 9, p. 094001, 2014.

[50] P. Halmos, "Normal dilations and extensions of operators," *Summa Brasiliensis Math*, 1950.

[51] C. Sparrow, E. Martín-López, N. Maraviglia, A. Neville, C. Harrold, J. Carolan, Y. N. Joglekar, T. Hashimoto, N. Matsuda, J. L. O'Brien, *et al.*, "Simulating the vibrational quantum dynamics of molecules using photonics," *Nature*, vol. 557, no. 7707, pp. 660–667, 2018.

[52] B. C. Sanders, S. D. Bartlett, T. Rudolph, and P. L. Knight, "Photon-number superselection and the entangled coherent-state representation," *Physical Review A*, vol. 68, no. 4, p. 042329, 2003.

[53] S. D. Bartlett, T. Rudolph, and R. W. Spekkens, "Reference frames, superselection rules, and quantum information," *Reviews of Modern Physics*, vol. 79, no. 2, p. 555, 2007.

[54] P. S. Turner, "Postselective quantum interference of distinguishable particles," *arXiv preprint arXiv:1608.05720*, 2016.

[55] S. Stanisic and P. S. Turner, "Discriminating distinguishability," *Physical Review A*, vol. 98, no. 4, p. 043839, 2018.

[56] A. E. Moylett, R. García-Patrón, J. J. Renema, and P. S. Turner, "Classically simulating near-term partially-distinguishable and lossy boson sampling," *Quantum Science and Technology*, vol. 5, no. 1, p. 015001, 2019.

[57] A. J. Menssen, A. E. Jones, B. J. Metcalf, M. C. Tichy, S. Barz, W. S. Kolthammer, and I. A. Walmsley, "Distinguishability and many-particle interference," *Physical review letters*, vol. 118, no. 15, p. 153603, 2017.

[58] M. C. Tichy, "Sampling of partially distinguishable bosons and the relation to the multidimensional permanent," *Physical Review A*, vol. 91, no. 2, p. 022316, 2015.

[59] K. Jones-Smith and H. Mathur, "Relativistic non-hermitian quantum mechanics," *Physical Review D*, vol. 89, no. 12, p. 125014, 2014.

[60] M. Artuso, E. Barberio, and S. Stone, "B meson decays," *PMC Physics A*, vol. 3, no. 1, pp. 1–82, 2009.

[61] F. L. Semião and M. Paternostro, "Quantum circuits for spin and flavor degrees of freedom of quarks forming nucleons," *Quantum Information Processing*, vol. 11, no. 1, pp. 67–75, 2012.

[62] R. Wakefield, Y. N. Joglekar, and A. Laing, "Pt-symmetry in nonlinear quantum optics," 2021. In Preparation.

[63] N. Tischler, C. Rockstuhl, and K. Słowik, "Quantum optical realization of arbitrary linear transformations allowing for loss and gain," *Phys. Rev. X*, vol. 8, p. 021017, Apr 2018.

[64] W. So and R. C. Thompson, "Singular values of matrix exponentials," *Linear and Multilinear Algebra*, vol. 47, no. 3, pp. 249–258, 2000.

[65] C. Li, G. Zhang, X. Z. Zhang, and Z. Song, "Conventional quantum phase transition driven by a complex parameter in a non-hermitian $\mathcal{PT}-$ symmetric ising model," *Phys. Rev. A*, vol. 90, p. 012103, Jul 2014.

[66] A. Galda and V. M. Vinokur, "Parity-time symmetry breaking in spin chains," *Phys. Rev. B*, vol. 97, p. 201411, May 2018.

[67] G. Vidal, "Efficient simulation of one-dimensional quantum many-body systems," *Phys. Rev. Lett.*, vol. 93, p. 040502, Jul 2004.

[68] G. Evenbly, "Gauge fixing, canonical forms, and optimal truncations in tensor networks with closed loops," *Phys. Rev. B*, vol. 98, p. 085155, Aug 2018.

[69] F. Verstraete and J. I. Cirac, "Renormalization algorithms for quantum-many body systems in two and higher dimensions," *arXiv preprint cond-mat/0407066*, 2004.

[70] N. Killoran, J. Izaac, N. Quesada, V. Bergholm, M. Amy, and C. Weedbrook, "Strawberry fields: A software platform for photonic quantum computing," *Quantum*, vol. 3, p. 129, 2019.

[71] T. R. Bromley, J. M. Arrazola, S. Jahangiri, J. Izaac, N. Quesada, A. D. Gran, M. Schuld, J. Swinarton, Z. Zabaneh, and N. Killoran, "Applications of near-term photonic quantum computers: software and algorithms," *Quantum Science and Technology*, vol. 5, no. 3, p. 034010, 2020.

[72] R. Wakefield, Y. N. Joglekar, and A. Laing, "Creating pure single photons with pt-symmetric microring resonators," 2021. In Preparation.

[73] H. Ramezani, T. Kottos, R. El-Ganainy, and D. N. Christodoulides, "Unidirectional nonlinear pt-symmetric optical structures," *Physical Review A*, vol. 82, no. 4, p. 043803, 2010.

[74] Y. Wu, B. Zhu, S.-F. Hu, Z. Zhou, and H.-H. Zhong, "Floquet control of the gain and loss in a pt-symmetric optical coupler," *Frontiers of Physics*, vol. 12, no. 1, pp. 1–7, 2017.

[75] S. Altinisik, D. Dizdarevic, and J. Main, “Balanced gain and loss in spatially extended non-pt-symmetric multiwell potentials,” *Physical Review A*, vol. 100, no. 6, p. 063639, 2019.

[76] Z. Vernon and J. E. Sipe, “Spontaneous four-wave mixing in lossy microring resonators,” *Physical Review A*, vol. 91, no. 5, p. 053802, 2015.

[77] Z. Vernon and J. Sipe, “Strongly driven nonlinear quantum optics in microring resonators,” *Physical Review A*, vol. 92, no. 3, p. 033840, 2015.

[78] F. A. Sabattoli, H. El Dirani, L. Youssef, F. Garrisi, D. Grassani, L. Zatti, C. Petit-Etienne, E. Pargon, J. E. Sipe, M. Liscidini, C. Sciancalepore, D. Bajoni, and M. Galli, “Suppression of parasitic nonlinear processes in spontaneous four-wave mixing with linearly uncoupled resonators,” *Phys. Rev. Lett.*, vol. 127, p. 033901, Jul 2021.

[79] P. M. Alsing and E. E. Hach III, “Photon-pair generation in a lossy microring resonator. i. theory,” *Physical Review A*, vol. 96, no. 3, p. 033847, 2017.

[80] U. B. Hoff, B. M. Nielsen, and U. L. Andersen, “Integrated source of broadband quadrature squeezed light,” *Opt. Express*, vol. 23, pp. 12013–12036, May 2015.

[81] M. Razavi, I. Söllner, E. Bocquillon, C. Couteau, R. Laflamme, and G. Weihs, “Characterizing heralded single-photon sources with imperfect measurement devices,” *Journal of Physics B: Atomic, Molecular and Optical Physics*, vol. 42, no. 11, p. 114013, 2009.

[82] T. Barwicz, M. A. Popovic, P. T. Rakich, M. R. Watts, H. A. Haus, E. P. Ippen, and H. I. Smith, “Microring-resonator-based add-drop filters in sin: fabrication and analysis,” *Optics express*, vol. 12, no. 7, pp. 1437–1442, 2004.